Eur. Phys. J. A (2023) 59:131
https://doi.org/10.1140/epja/s10050-023-01034-3

THE EUROPEAN PHYSICAL JOURNAL A

Review

TALYS: modeling of nuclear reactions

Arjan Koning[1,a], **Stephane Hilaire**[2,3,b], **Stephane Goriely**[4,c]

[1] Nuclear Data Section, IAEA, Wagrammerstrasse 5, Vienna 1400, Austria
[2] DIF, CEA, Arpajon 91297, France
[3] Université Paris-Saclay, CEA, LMCE, 91680 Bruyères-le-Châtel, France
[4] Institut d'Astronomie et d'Astrophysique, Université Libre de Bruxelles, Campus de la Plaine, CP-226, Brussels 1050, Belgium

Received: 16 February 2023 / Accepted: 6 May 2023

Communicated by Nicolas Alamanos

Abstract TALYS is a software package for the simulation of nuclear reactions below 200 MeV. It is used worldwide for the analysis and prediction of nuclear reactions and is based on state-of-art nuclear structure and nuclear reaction models. A general overview of the implemented physics and capabilities of TALYS is given. The general nuclear reaction mechanisms described are the optical model, direct reactions, compound nucleus model, pre-equilibrium reactions and fission. The most important nuclear structure models are those for masses, discrete levels, level densities, photon strength functions and fission barriers. A wide variety of nuclear reactions simulated with TALYS will be demonstrated, ranging from low-energy neutron cross sections, astrophysics, high-energy charged particle reactions and other reactions. TALYS is a nuclear reaction software which aims to give a complete description of nuclear reaction observables, and to be an important link between fundamental nuclear physics and applications.

Contents

[a] e-mail: A.Koning@iaea.org (corresponding author)
[b] e-mail: Stephane.Hilaire@cea.fr
[c] e-mail: Stephane.Goriely@ulb.be

Published online: 14 June 2023

1 Introduction

The fundamentals of nuclear models for low and intermediate energy nuclear reactions were laid down around 60 to 80 years ago and we still make use of their basic features. Our compact, subjective list of important nuclear models developed in history would include the liquid drop model for mass and fission predictions, the Fermi gas model of nuclear level densities and the Breit-Wigner model to describe neutron resonance reactions, which stem from before the 1940s. The optical model for nucleon scattering and statistical compound nucleus model date from the 1950s and these models still represent the foundation of the current nuclear reaction modeling in the fast energy range. Important additions from the 1960s are the width fluctuation corrections to the statistical model, the coupled-channels model for direct reactions and the pre-equilibrium nuclear reaction mechanism.

Today, one can state that nuclear reaction mechanisms can be broadly divided into direct and compound nucleus reaction processes with pre-equilibrium reactions as an inter-

mediate phenomenon between those two. For these reaction models to correctly predict nuclear reaction observables, they need to be combined with nuclear structure information, in particular nuclear masses, deformation parameters, discrete level information, level densities, photon strength functions, optical potentials and fission paths. All the aforementioned models have been modernized by the nuclear physics community in the past decades and the purpose of this paper is to show that these models, including most of the essential refinements, have been implemented into one consistent computational scheme called TALYS.

Besides the gradual advance in nuclear theories and the availability of more and more precise experimental data for their validation, an important revolution for nuclear reaction modeling that has taken place in the past decades is the exponential increase in computer power, in particular for the possibility

- to analyze not only one nuclear reaction channel, but all competing reaction reaction channels, for many energies and nuclides simultaneously,
- to implement nuclear models with less and less approximations,
- to obtain basic ingredients for nuclear reaction calculations from fundamental nuclear structure models,
- to implement nuclear models in a readable and structured way enabling future generations of computer scientists to understand and reuse them,
- to use a more systematic, standardized interface for data to other software, enlarging the possibilities and applications for nuclear reaction model codes.

The above outline of the essentials of nuclear reaction modeling provided the motivation to develop TALYS, which is a computer program for the analysis and prediction of nuclear reactions that involve photons, neutrons, protons, deuterons, tritons, ^{3}He- and alpha-particles as projectiles, in the 0–200 MeV energy range for almost the entire nuclide chart. We have implemented a large suite of nuclear reaction models into a single software package to ensure that this entire particle-nuclide-energy domain is covered.

There are two main purposes of TALYS, which are strongly connected. First, it is a *nuclear physics* tool that can be used for the analysis of nuclear reaction experiments. The interplay between experiment and theory gives us insight in the fundamental interaction between particles and nuclei, and precise measurements enable us to constrain our models. In return, when the resulting nuclear models are believed to have sufficient predictive power, they can give an indication of the reliability of measurements. Currently, TALYS has been used, or at least cited, in about 6000 different papers, and

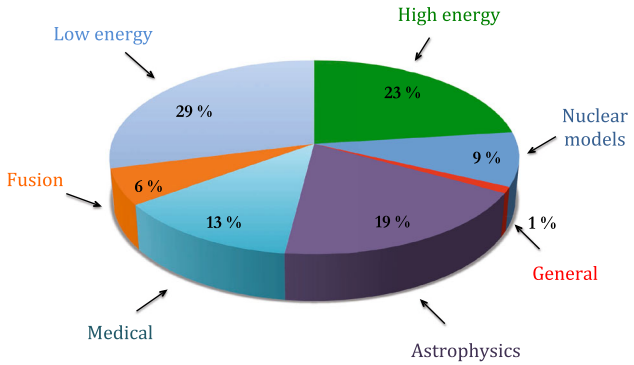

Fig. 1 Current segmentation of TALYS publications by application area

a significant part of them concerns the analysis of existing or new measurements. It is clear that our software project would be nowhere without an extensive and high-quality experimental database for validation of nuclear models and their parameters.

After the nuclear physics stage comes the second function of TALYS, namely as a *nuclear data* tool. Either in a default mode, when no measurements are available, or after fine-tuning adjustable parameters of the various reaction models to match experimental data, TALYS can *generate* nuclear data for all open reaction channels, on a user-defined projectile-target-energy-angle grid. Accurate, reliable nuclear data is essential for existing and new nuclear technologies. Important applications that rely directly or indirectly on data generated by nuclear reaction simulation codes like TALYS are: the entire fuel cycle of conventional and future nuclear power reactors, medical isotope production, nuclear fusion, accelerator applications, various branches of astrophysics, space applications, homeland security, radiotherapy, single-event upsets in microprocessors, geophysics and many more. Figure 1 gives an arbitrary division of the current use of TALYS in various fields.

The TALYS code project started around 2000, when two research organisations, NRG Petten, the Netherlands and CEA-DAM Bruyères-le-Châtel, France, decided to implement their combined knowledge of nuclear models into one single software package. Since then, virtually all TALYS development has taken place at NRG and CEA-DAM, later also at the Université Libre de Bruxelles (Belgium), and in recent years at the IAEA in Vienna.

In its first decade, the development of TALYS used to follow the "first completeness, then quality" principle. With that, we certainly never suggested that we were using toy models to arrive at some quick and dirty results, since several reaction mechanisms coded in TALYS are based on sophisticated theoretical models whose implementation is only possible with the current-day computer power. It rather means that, in our quest for completeness, we try to divide

our effort equally among all nuclear reaction types. The precise description of *all* possible reaction channels in a single calculational scheme is such an enormous task that we have chosen, to put it bluntly, not to devote several years to the theoretical research and absolutely perfect implementation of one particular reaction channel which accounts for only a small part of the total reaction cross section. Instead, we aim to enhance the quality of TALYS equally over the whole application range and always search for the largest shortcoming that remains after the last improvement. We now think that "completeness *and* quality" has been accomplished for several important parts of the program. The reward of this approach is that with TALYS we can cover the whole path from fundamental nuclear reaction models to the creation of complete data libraries for nuclear applications, with the obvious side note that the implemented nuclear models will always need to be upgraded using better physics. An additional objective since the beginning of TALYS development is full transparency of the implemented nuclear models, in other words, an *understandable* source program, and coding structure as modular as possible.

The idea to construct a computer program that gives a simultaneous prediction of many nuclear reaction channels, rather than a very detailed description of only one or a few reaction channels, is not new. Well-known examples of all-in-one open source codes from the past century are GNASH [1], ALICE [2], STAPRE [3], and EMPIRE [4]. They have been, and are still, used not only for research but also for the creation of the nuclear data libraries that exist around the world. All these codes have helped to shape the ideas for the development of TALYS.

TALYS is newer in the sense that it has been written entirely from scratch in the 21st century (with the exception of one very essential module, the coupled-channels code ECIS-06 [5]), using a consistent set of programming procedures and a strong focus on validation and reproducibility. To complete our list of nuclear model reaction codes we also mention other important codes of the past decades which are currently in use: CoH3 [6], Ccone [7] and YAHFC [8], which like TALYS are designed around the optical and statistical model. To our knowledge, not all these codes are (yet) open source however.

What probably sets TALYS apart is the very large user database, currently leading to more than 6000 publications in which TALYS is cited, and which also provided feedback over the years to help us make the code more user-friendly and robust.

As specific features of the TALYS package we mention

- In general, an exact implementation of many of the latest nuclear models for direct, compound, pre-equilibrium and fission reactions.
- A continuous, smooth description of reaction mechanisms over a wide energy and mass range. A safe statement is that these limits are 0.001–200 MeV and $12 < A < 339$, but it is computationally possible to go beyond that.
- Completely integrated optical model and coupled-channels calculations by the ECIS-06 code [5].
- Incorporation of optical model parameterisations for many nuclei, both phenomenological, optionally including dispersion relations, and microscopic, and for actinides from the IAEA Reference Input Parameter Library [9] (RIPL).
- Total and partial cross sections, energy spectra, angular distributions, double-differential spectra and recoils.
- Discrete and continuum photon production cross sections.
- Excitation functions for residual nuclide production, including isomeric cross sections.
- An exact modeling of exclusive channel cross sections, e.g. $(n, 2np)$, and spectra.
- Automatic reference to nuclear structure parameters as masses, discrete levels, resonances, level density parameters, deformation parameters, fission barrier and gamma-ray parameters, generally from the RIPL database but also beyond that.
- Various width fluctuation models for binary compound reactions and, at higher energies, multiple Hauser-Feshbach emission until all reaction channels are closed.
- Various phenomenological and microscopic models for ground-state properties, level densities, photon strength functions, optical model potentials, and fission properties.
- Various fission models to predict cross sections, fission fragment and product yields, neutron and gamma multiplicities, and prompt fission neutron and gamma spectra.
- Models for pre-equilibrium reactions, and multiple pre-equilibrium emission up to any order.
- Generation of parameters for the unresolved resonance range.
- Reconstruction of resonance range into pointwise cross sections using tabulated resonance parameters.
- Calculation of astrophysical reaction rates based on a Maxwell-Boltzmann distribution for incident projectiles (or a Planck distribution for incident photons).
- Option to start with an excitation energy distribution instead of a projectile-target combination, helpful for coupling TALYS with intranuclear cascade codes or fission fragment analyses, or for calculating β-delayed processes.
- Use of systematics if an adequate theory for a particular reaction mechanism is not yet available or implemented, or simply as a predictive alternative for more physical nuclear models.

- Medical isotope production yields as a function of accelerator energy and beam current.
- Output files for automatic generation of nuclear data in ENDF-6 format [10] using the TEFAL program [11].
- Flexible input and output to enable automatic optimization to experimental data and generation of covariance data by the TASMAN program [11] using Monte Carlo techniques.
- A transparent source program.
- Input/output communication that is easy to use and understand.
- An extensive tutorial and descriptive manual.
- A large collection of sample cases.
- Publicly available, regularly updated, and major upgrades bi-annually released.

The last 7 items in the above list will not be further discussed in the remaining Sections of this paper, since this is not a tutorial but a TALYS review paper, focussing on the physics. The central message is that we always provide a complete set of answers for a nuclear reaction, for all open channels and all associated cross sections, spectra, angular distributions, etc. It depends on the current status of nuclear reaction theory, and our ability to implement that theory, whether these answers are generated by sophisticated physical methods or by a simpler empirical approach.

This paper consists globally of three parts:

- **Nuclear reaction models**
  In Sect. 2 we will first give a global introduction of TALYS, including a general discussion of nuclear reactions and the types of observables that can be obtained. After that we will focus on the nuclear reaction models: the optical model in Sect. 3, direct reactions in Sect. 4, compound nucleus reactions in Sect. 5, pre-equilibrium reactions in Sect. 6, direct capture in Sect. 7, and multiple emission in Sect. 8.
- **Nuclear structure ingredients**
  Nuclear structure models for masses and deformations are discussed in Sect. 9, discrete levels in Sect. 10, level densities in Sect. 11, photon strength functions in Sect. 12 and fission in Sect. 13.
- **TALYS applications**
  Astrophysics will be discussed in Sect. 15 and fission yields in Sect. 14. An illustration of the use of TALYS for several nuclear reaction calculations will be given in Sect. 16. The use of TALYS in a wider application system will be discussed in Sect. 17.

We end this paper with an outlook in Sect. 18.

2 Nuclear reactions

An outline of the general theory and modeling of nuclear reactions can be given in many ways. A common classification is in terms of time scales: short reaction times are associated with direct reactions and long reaction times with compound nucleus processes. At intermediate time scales, pre-equilibrium processes occur. An alternative, more or less equivalent, classification can be given with the number of intranuclear collisions, which is one or two for direct reactions, a few for pre-equilibrium reactions and many for compound reactions, respectively. As a consequence, the coupling between the incident and outgoing channels decreases with the number of collisions and the statistical nature of the nuclear reaction theories increases with the number of collisions. Figures 2 and 3 explain the role of the different reaction mechanisms during an arbitrary nucleon-induced reaction in a schematic manner. They will all be discussed in this paper.

The collection of nuclear models and their inputs are summarized in the TALYS flowchart of Fig. 4. After the discussion of the basic reaction mechanisms below, we return to the most important theoretical aspects of the nuclear models implemented in TALYS in later sections.

When discussing nuclear reactions in the context of a computer code, as in this paper, a different starting point is more appropriate. We think it is best illustrated by Fig. 5. A particle incident on a target nucleus will induce several *binary* reactions which are described by the various competing reaction mechanisms that were mentioned above. The end products of the binary reaction are the emitted particle and the corresponding recoiling residual nucleus. In general this is, however, not the end of the process. A total nuclear reaction may involve a whole sequence of residual nuclei, especially

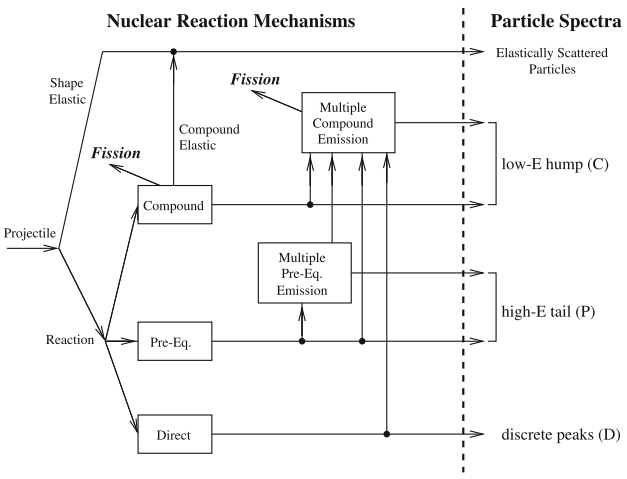

Fig. 2 The role of direct, pre-equilibrium and compound processes in the description of a nuclear reaction and the outgoing particle spectra. The C, P and D labels correspond to those in Fig. 3

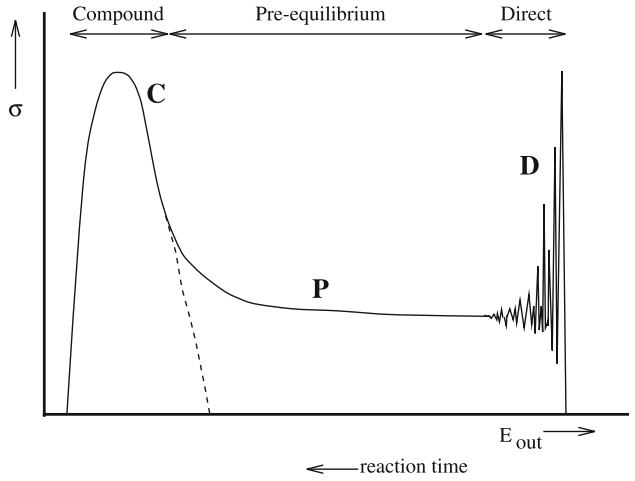

Fig. 3 Schematic drawing of an outgoing particle spectrum. The energy regions to which direct (D), pre-equilibrium (P) and compound (C) mechanisms contribute are indicated. The dashed curve distinguishes the compound contribution from the rest in the transitional energy region

at higher energies, resulting from multiple particle emission. All these residual nuclides have their own separation energies, optical model parameters, level densities, fission barriers, gamma strength functions, etc. that must properly be taken into account along the reaction chain. The implementation of this entire reaction chain forms the backbone of TALYS. The program has been written in a way that enables a clear and easy inclusion of all possible nuclear model ingredients for any number of nuclides in the reaction chain. Of course, in this whole chain the target and primary compound nucleus have a special status, since they are subject to *all* reaction mechanisms, i.e. direct, pre-equilibrium, compound and fission and, at low incident energies, width fluctuation corrections in compound nucleus decay. Also, at incident energies below a few MeV, only binary reactions take place and the target and compound nucleus are often the only two nuclei involved in the whole reaction. Historically, it is for the binary reactions that most of the theoretical methods have been developed and refined, mainly because their validity, and their relation with nuclear structure, could best be tested with exclusive measurements. In general, however, Fig. 5 should serve as the illustration of a total nuclear reaction at any incident energy. The projectile, in this case a neutron, and the target $(Z_C, N_C - 1)$ form a compound nucleus (Z_C, N_C) with a total energy

$$E^{tot} = E_{CM} + S_n(Z_{CN}, N_{CN}) + E_x^0, \tag{1}$$

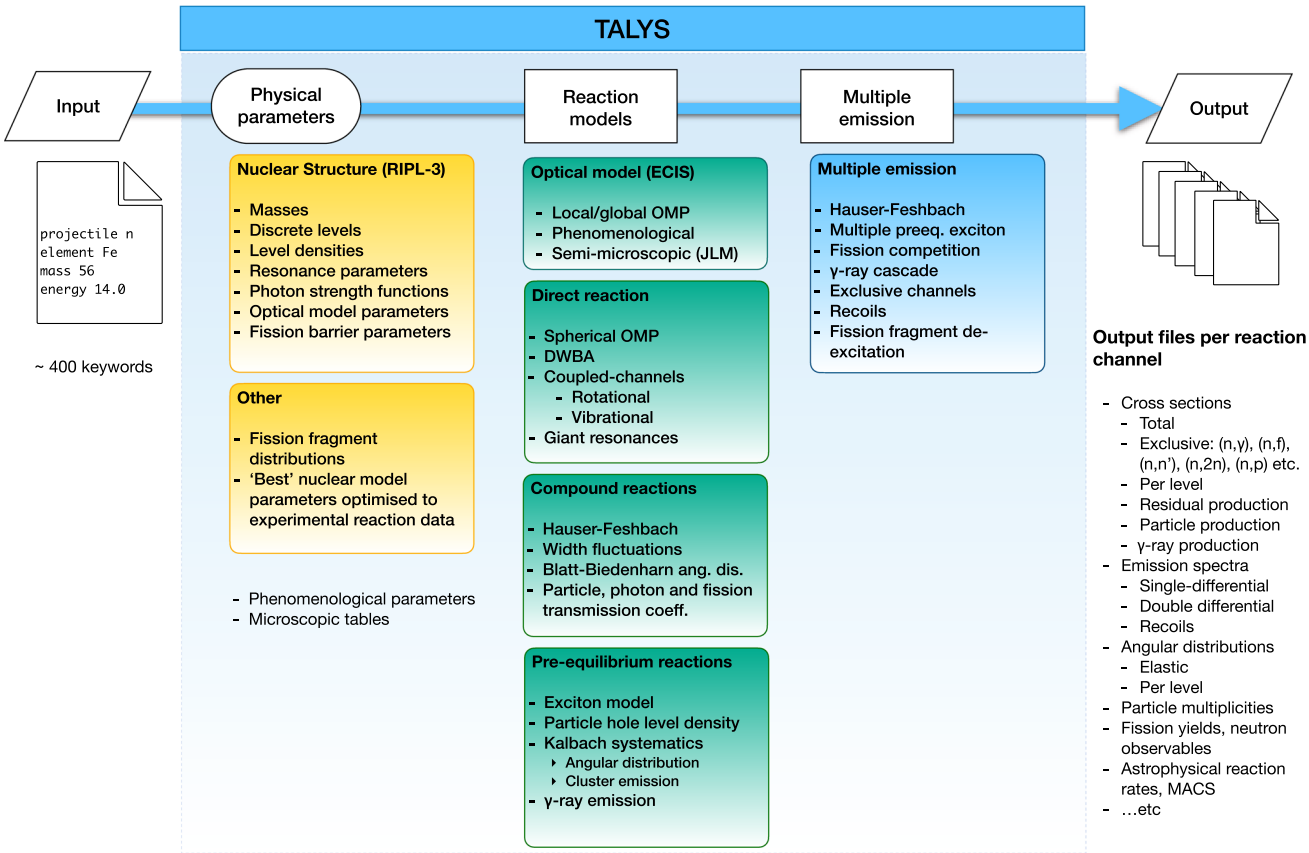

Fig. 4 Schematic illustration of TALYS flowchart, including input, nuclear models, and output of TALYS. See text for more details

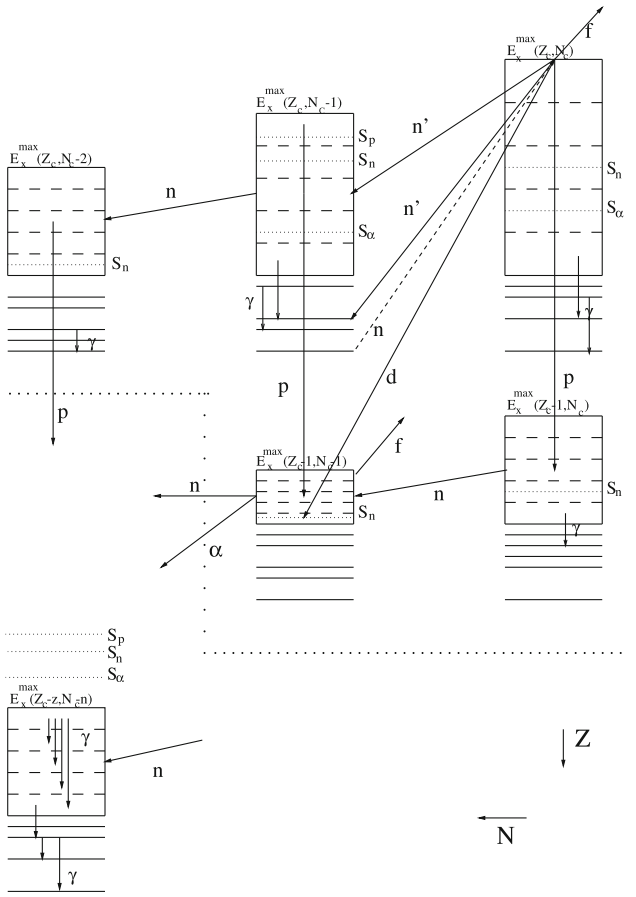

Fig. 5 Schematic representation of a neutron-induced reaction on a nucleus $(Z_c, N_c - 1)$. The dashed arrow represents the incident channel, while the continuous arrows represent the various decay possibilities. E_x^{max} denotes the maximal excitation energy possibly reached in each residual nucleus and S_k the particle separation energy for particle k. For each nucleus a few discrete levels are drawn, together with a few continuum energy bins. Spin and parity degrees of freedom are left out of this figure for simplicity. Fission is indicated by an f

where E_{CM} is the incident energy in the CM frame, S_n is the neutron separation energy of the compound nucleus, and E_x^0 the excitation energy of the target, which is often zero, i.e. representing the ground state. The compound nucleus is described by a range of possible spin (J) and parity (Π) combinations, which for simplicity are left out of Fig. 5. From this state, transitions to all open channels may occur by means of direct, pre-equilibrium and compound processes. The residual nuclei formed by these binary reactions may be populated in the discrete level part and in the continuum part of the available excitation energy range. In Fig. 5, we have only drawn three binary channels, namely the $(Z_C, N_C - 1)$, $(Z_C - 1, N_C)$ and $(Z_C - 1, N_C - 1)$ nuclei that result from binary neutron, proton and deuteron emission, respectively. Each nucleus is characterized by a separation energy per possible ejectile. If the populated residual nucleus has a maximal excitation energy $E_x^{max}(Z, N)$ that is still above the separation energies for one or more different particles for that nucleus, further emission of these particles may occur and nuclei with lower Z and N will be populated. At the end of the nuclear reaction (left bottom part of Fig. 5), all the reaction population is below the lowest particle separation energy, and the residual nucleus $(Z_C - z, N_C - n)$ can only decay to its ground or isomeric states by means of gamma decay. In a computer program, the continuum must be discretized in excitation energy (E_x) bins. We can take these bins equidistant (the default) or non-equidistant, although we already want to stress the important fact here that the *emission* energy grid for the outgoing particles is non-equidistant in TALYS. After the aforementioned binary reaction, every continuum excitation energy bin will be further depleted by means of particle emission, gamma decay or fission. Computationally, this process starts at the initial compound nucleus and its highest energy bin, i.e. the bin just below $E_x^{max}(Z_C, N_C) = E^{tot}$, and subsequently in order of decreasing energy bin/level, decreasing N and decreasing Z. Inside each continuum bin, there is an additional loop over all possible J and Π, whereas for each discrete level, J and Π have unique values. Hence, a bin/level is characterized by the set $\{Z, N, E_x, J, \Pi\}$ and by means of gamma or particle emission, it can decay into all accessible $\{Z', N', E_{x'}, J', \Pi'\}$ bins/levels. In this way, the whole reaction chain is followed until all bins and levels are depleted and thus all channels are closed. In the process, all particle production cross sections and residual production cross sections are accumulated to their final values.

In the rest of this Section, we will zoom in on the various parts of Fig. 5 to describe the various stages of the reaction, depending on the incident energy, and we will mention the nuclear reaction mechanisms that apply.

2.1 Observables

After this short introduction of the sequence of particle emission, it is appropriate to list all the different observables that TALYS can calculate. As output, for a single projectile + target combination and a range of incident energies, TALYS produces cross sections (assuming incident neutrons here, but similar for other all other projectiles) for:

- total (n, tot), elastic (n, el), reaction $(n, reac)$ and non-elastic (n, non) reactions,
- radiative capture channel (n, γ),
- single particle production channels (n, n'), (n, p), (n, d), (n, t), (n, h), (n, α),
- discrete level inelastic reactions, (n, n'_1), (n, n'_2), etc. and the continuum (n, n'_{cont}), and similarly for all other ejectiles,
- multi-particle reactions $(n, 2n)$, (n, np), etc,
- total fission (n, f) reaction and its subdivision into first, second, etc. chance partial fission,

- residual production $(n, x)^A_Z$El, mostly relevant at higher energies, as far as not yet covered by the exclusive channels mentioned above,
- production of the ground state and isomers, if present, e.g. $(n, n')^{A(g)}_Z$El, $(n, n')^{A(m)}_Z$El, and similarly for all other channels and residual production at higher energies, e.g. $(p, x)^{A(m)}_Z$El,
- total particle production (n, xn), (n, xp), etc, mostly relevant at higher energies.

As for secondary distributions, TALYS produces:

- the elastic scattering angular distribution,
- the angular distributions for inelastic scattering per discrete level, and similarly for the other ejectiles,
- double-differential emission spectra for all outgoing particles,
- recoil distributions for the residual nuclides,
- particle production yields,
- discrete and continuum gamma-ray distributions for all open channels, including gamma production cross sections.

This is a rather complete list of nuclear reaction observables which can be validated with the associated experimental data. Moreover, this output is required to fill a complete nuclear data library in the fast energy range for technological applications. The capabilities of TALYS do not stop here however. Additional simulated quantities are:

- Maxwellian-averaged cross sections (MACS) and astrophysical reaction rates,
- fission yields, isomeric ratios and related neutron and gamma observables: average total number of prompt fission neutrons, $\bar{\nu}$, per mass, $\nu(A)$, and per number, P(ν), prompt fission neutron and gamma spectra(PFNS and PFGS, respectively), etc,
- reproduction of pointwise cross sections from resonance parameters,
- production yields and spectra from an excited nucleus as starting condition, i.e. without specifying a projectile,
- complete tables of nuclear structure information: discrete level scheme, level densities, photon strength functions and fission properties, optical potentials, etc..

2.2 Reaction mechanisms

In the projectile energy range between 1 keV and several hundreds of MeV, the importance of a particular nuclear reaction mechanism appears and disappears upon varying the incident energy. We will now describe the particle decay scheme that typically applies in the various energy regions. Because of the Coulomb barrier for charged particles, it will be clear that the discussion for low-energy reactions usually concerns incident neutrons. In general, however, what follows can be generalized to incident charged particles. The energy ranges mentioned in each paragraph heading are just meant as helpful indications, which apply to a typical medium mass nucleus.

2.2.1 Low energies

Elastic scattering and capture ***($E < 0.2$ MeV)***

If the energy of an incident neutron is below the excitation energy of the first inelastic level, and if there are no (n, p), etc. reactions that are energetically possible, then the only reaction possibilities are elastic scattering, neutron capture and for actinides, fission. At these low energies, only the $(Z_C, N_C - 1)$ and (Z_C, N_C) nuclides of Fig. 5 are involved, see Fig. 6. First, the shape (or direct) elastic scattering cross section can directly be determined from the optical model, which will be discussed in Sect. 3. The compound nucleus is formed at one single energy $E^{tot} = E_x^{max}(Z_C, N_C)$ and a range of J, Π-values. This compound nucleus either decays by means of compound elastic scattering back to the initial state of the target nucleus, or by means of neutron capture, after which gamma decay follows to the continuum and to discrete states of the compound nucleus. The competition between the compound elastic and capture channels is described by the compound nucleus theory, which we will discuss in Sect. 5. It should be clear that this model only covers the case where the levels in the compound nucleus have a dense spacing, which generally holds for a few to a few tens of keV of incident neutron energy. At lower energies, resonance reaction theory applies. The elastic and capture processes comprise the first *binary* reaction. To complete the description of the total reaction, the excited (Z_C, N_C) nucleus, which is populated over its whole excitation energy range by the primary gamma emission, must complete its decay. The highest continuum bin is depleted first, for all J and Π. The subsequent gamma decay increases the population of the lower bins, before the latter are depleted themselves. Also, continuum bins that are above the neutron separation energy S_n of the compound nucleus contribute to the feeding of the $(n, \gamma n)$ channel. This results in a weak continuous neutron spectrum, even though the elastic channel is the only true binary neutron channel that is open. The continuum bins and the discrete levels of the compound nucleus are depleted one by one, in decreasing order, until the ground or an isomeric state of the compound nucleus is reached by subsequent gamma decay. If a nuclide is fissile, fission may compete as well, both from the initial compound state $E_x^{max}(Z_C, N_C)$ and from the continuum bins of the compound nucleus, the latter resulting in a $(n, \gamma f)$ cross section. Both contributions add up to the so-called first-chance fission cross section.

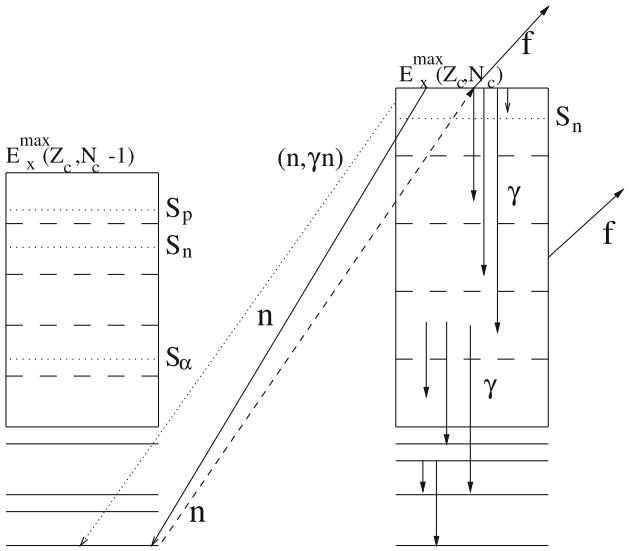

Fig. 6 Same as Fig. 5 for the neutron-induced reaction at low energy. The dashed arrow represents the incident channel, while the continuous arrow represents the elastic channel. The only possibilities are elastic scattering and capture of the neutron in the compound nucleus, with subsequent decay to the ground state or an isomeric state of the compound nucleus. A small part of the population may decay back to the target nucleus by means of the $(n, \gamma n)$ channel (dotted arrow). For fissile nuclei, fission may be another open channel

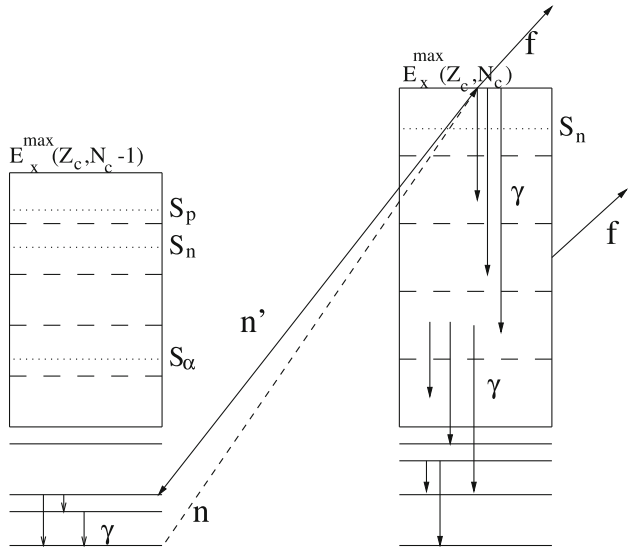

Fig. 7 Same as Fig. 6 for neutron-induced reaction at somewhat higher energy. The dashed arrow represents the incident channel, while the continuous arrows represent the decay possibilities. In addition to the possibilities sketched in Fig. 6, there is now inelastic scattering followed by gamma decay in the target nucleus

Inelastic scattering to discrete states ***(***$0.2 < E < 4$ ***MeV)***
At somewhat higher incident energies, the first inelastic channels open up, see Fig. 7. Reactions to these discrete levels have a compound and a direct component. The former is again described by the compound nucleus theory, while the latter is described by the Distorted Wave Born Approximation (DWBA) for spherical nuclei and by coupled-channels equations for deformed nuclei, see Sect. 4. When the incident energy crosses an inelastic threshold, the compound inelastic contribution generally rises rapidly and predominates, whereas the direct component increases more gradually. Obviously, the elastic scattering, capture and fission processes described in the previous subsection also apply here. In addition, there is now gamma decay to an isomeric state or the ground state in the target nucleus after inelastic scattering. When there are several inelastic levels open to decay, the compound contribution to each individual level is still significant. However, the effect of the width fluctuation correction on the compound cross section is already small in this case, as will be outlined in Sect. 5.

2.2.2 *High energies*

Pre-equilibrium reactions ***(***$E > 4$ ***MeV)***
At higher incident energies, inelastic cross sections to both the discrete states and the continuum are possible, see Fig. 5. Like reactions to discrete states, reactions to the continuum also have a compound and a direct-like component. The latter are usually described by pre-equilibrium reactions which, by definition, include direct reactions to the continuum. They will be discussed in Sect. 6. Also non-elastic channels to other nuclides, through charge-exchange, e.g. (n, p), and transfer reactions, e.g. (n, α), generally open up at these energies, and reactions to these nuclides can take place by the same direct, pre-equilibrium and compound mechanisms. Again, the channels described in the previous subsections also apply here. In addition, gamma decay to ground and isomeric states of all residual nuclides occurs. When many channels open up, particle decay to individual states, e.g. compound elastic scattering, rapidly becomes negligible. For the excitation of a discrete state, the direct component now becomes predominant, since that involves no statistical competition with the other channels. At about 15 MeV, the *total* compound cross section, i.e. summed over all final discrete states and the excited continuum, is however still larger than the summed direct and pre-equilibrium contributions.

Multiple compound emission ***(***$E > 8$ ***MeV)***
At incident energies above about the neutron separation energy, the residual nuclides formed after the first binary reaction contain enough excitation energy to enable further decay by compound nucleus particle emission or fission. This gives rise to multiple reaction channels such as $(n, 2n)$, (n, np), etc. For higher energies, this picture can be generalized to many residual nuclei, and thus more complex reaction channels, see Fig. 5. If fission is possible, this may occur for all residual nuclides, which is known as multiple chance fission. All excited nuclides will eventually decay to their isomeric and ground states.

Multiple pre-equilibrium emission ($E > 40$ MeV)
At still higher incident energies, above several tens of MeV, the residual nuclides formed after binary emission may contain so much excitation energy that the presence of further fast particles inside the nucleus becomes possible. These can be imagined as strongly excited particle-hole pairs resulting from the first binary interaction with the projectile. The residual system is then clearly non-equilibrated and the excited particle that is high in the continuum may, in addition to the first emitted particle, also be emitted on a short time scale. This so-called multiple pre-equilibrium emission forms an alternative theoretical picture of the intra-nuclear cascade process, whereby now not the exact location and momentum of the particles is followed, but instead the total energy of the system and the number of particle-hole excitations (exciton number). In TALYS, this process can be generalized to any number of multiple pre-equilibrium stages in the reaction by keeping track of all successive particle-hole excitations, see Sect. 8.2. For these incident energies, the binary compound cross section becomes small: the non-elastic cross section is almost completely exhausted by direct reactions and primary pre-equilibrium emission. Of course, the reaction process will end with multiple compound decay. Again, Fig. 5 applies.

2.3 Cross section definitions

In TALYS, cross sections for reactions to all open channels are calculated. Although the types of most of these partial cross sections are generally well known, it is appropriate to define them for completeness and to outline the book-keeping of the various cross sections, including all the sum rules they obey. The particular nuclear models that are needed to obtain the cross sections are described later in terms of more fundamental quantities. Unless otherwise stated, we use incident neutrons as example in what follows and we consider only photons (γ), neutrons (n), protons (p), deuterons (d), tritons (t), helium-3 particles (h) and alpha particles (α) as competing particles. Also, to avoid an overburdening of the notation and the explanation, we will postpone the competition of fission to the last part of this subsection.

Total cross sections
The most basic nuclear reaction calculation is that with the optical model, which will be explained in more detail in Sect. 3. Here, it is sufficient to summarize the relations that can be found in many nuclear reaction textbooks, namely that the optical model yields the reaction cross section σ_{reac} and, in the case of neutrons, the total cross section σ_{tot} and the shape-elastic cross section $\sigma_{shape-el}$. They are related by

$$\sigma_{tot} = \sigma_{shape-el} + \sigma_{reac}. \tag{2}$$

If the elastic channel is, besides shape elastic scattering, also fed by compound nucleus decay, the latter component is a part of the reaction cross section and is called the compound elastic cross section $\sigma_{comp-el}$. With this, we can define the total elastic cross section σ_{el},

$$\sigma_{el} = \sigma_{shape-el} + \sigma_{comp-el}, \tag{3}$$

and the non-elastic cross section σ_{non-el},

$$\sigma_{non-el} = \sigma_{reac} - \sigma_{comp-el}, \tag{4}$$

so that we can combine these equations to give

$$\sigma_{tot} = \sigma_{el} + \sigma_{non-el}. \tag{5}$$

The last equation contains the quantities that can actually be measured. We also note that the competition between the many compound nucleus decay channels ensures that $\sigma_{comp-el}$ rapidly diminishes for incident neutron energies above a few MeV, in which case σ_{non-el} becomes practically equal to σ_{reac}.

A further subdivision of the outcome of a nuclear reaction concerns the breakdown of σ_{non-el}: this cross section contains all the partial cross sections. For this we introduce the exclusive cross sections, from which all other cross sections of interest can be derived.

2.3.1 Exclusive cross sections

In this paper, we call a cross section *exclusive* when the outgoing channel is precisely specified by the type and number of outgoing particles (plus any number of photons). Well-known examples are the inelastic or (n, n') cross section and the $(n, 2n)$ cross section, which corresponds with two, *and only* two, neutrons (plus accompanying photons) in the outgoing channel. We denote the exclusive cross section as $\sigma^{ex}(i_n, i_p, i_d, i_t, i_h, i_\alpha)$, where i_k stands for the number of ejectiles of type k. In this notation, where the incident particle is assumed implicit, e.g. the $(n, 2np)$ cross section is given by $\sigma^{ex}(2, 1, 0, 0, 0, 0)$, for which we will also use the shorthand notation $\sigma_{n,2np}$. For a non-fissile nucleus, the sum over all exclusive cross sections is equal to the non-elastic cross section

$$\sigma_{non-el} = \sum_{i_n=0}^{\infty}\sum_{i_p=0}^{\infty}\sum_{i_d=0}^{\infty}\sum_{i_t=0}^{\infty}\sum_{i_h=0}^{\infty}\sum_{i_\alpha=0}^{\infty} \sigma^{ex}(i_n, i_p, i_d, i_t, i_h, i_\alpha), \tag{6}$$

where it should be understood that $\sigma^{ex}(1, 0, 0, 0, 0, 0)$ is the inelastic cross section $\sigma_{n,n'}$, i.e. it does not include elastic scattering.

The precise calculation of exclusive cross sections and spectra is a complicated book-keeping problem. We will describe the exact formalism here. In what follows we use quantities with a prime for daughter nuclides and quantities without a prime for mother nuclides in a decay chain. Consider an excitation energy bin or discrete level E_x in a nucleus (Z, N). Let $P(Z, N, E_x)$ represents the population of this bin/level before it decays. Let $s_k(Z, N, E_x, E_{x'})$ be the part of the population that decays from the (Z, N, E_x) bin/level to the residual $(Z', N', E_{x'})$ bin/level, whereby (Z, N) and (Z', N') are connected through the particle type k, with the index k running from γ-rays up to α-particles. With these definitions, we can link the various residual nuclides while keeping track of all intermediate particle emissions. A special case for the population is the initial compound nucleus (Z_C, N_C), which contains the entire initial reaction population at its total excitation energy E_x^{max} (projectile energy + binding energy), i.e.

$$P(Z_C, N_C, E_x^{max}) = \sigma_{non-el}, \tag{7}$$

while the populations to all the other bins/levels are zero. For the initial compound nucleus, $s_k(Z_C, N_C, E_x^{max}, E_{x'})$ represents the binary feeding to the excitation energy bins of the first set of residual nuclides. This term generally consists of direct, pre-equilibrium and compound components.

The population of any bin in the decay chain is equal to the sum of the decay parts for all particles that can reach this bin from the associated mother bins, i.e.

$$P(Z', N', E_{x'}(i')) = \sum_{k=\gamma,n,p,d,t,h,\alpha} \sum_{i} s_k(Z, N, E_x(i), E_{x'}(i')), \tag{8}$$

where the sum over i runs over discrete level and continuum energy bins in the energy range from $E_{x'}(i') + S_k$ to $E_x^{max}(Z, N)$, where S_k is the separation energy of particle k so that the sum only includes decay that is energetically allowed, and $E_x^{max}(Z, N)$ is the maximum possible excitation energy of the (Z, N) nucleus. Note again that the particle type k determines (Z, N).

To obtain the exclusive cross sections, we need to start with the initial compound nucleus and work our way down to the last nucleus that can be reached. First, consider a daughter nucleus (Z', N') somewhere in the reaction chain. We identify all exclusive channels $(i_n, i_p, i_d, i_t, i_h, i_\alpha)$ that lead to this residual (Z', N') nucleus, i.e. all channels that satisfy

$$\begin{aligned} i_n + i_d + 2i_t + i_h + 2i_\alpha &= N_C - N' \\ i_p + i_d + i_t + 2i_h + 2i_\alpha &= Z_C - Z'. \end{aligned} \tag{9}$$

For each of these channels, the *inclusive* cross section per excitation energy bin, S, is equal to the sum of the feeding from all possible mother bins, i.e.

$$\begin{aligned} S(i_n, i_p, i_d, i_t, i_h, i_\alpha, E_{x'}(i')) = & \sum_{k=\gamma,n,p,d,t,h,\alpha} \\ & \sum_i \frac{s_k(Z, N, E_x(i), E_{x'}(i'))}{P(Z, N, E_x(i))} \\ & \times S(i_n - \delta_{nk}, i_p - \delta_{pk}, i_d - \delta_{dk}, i_t - \delta_{tk}, i_h - \delta_{hk}, \\ & i_\alpha - \delta_{\alpha k}, E_x(i)), \end{aligned} \tag{10}$$

where we introduce Kronecker delta's, with characters as subscript, as

$$\begin{aligned} \delta_{nk} &= 1 \text{ if } k = n \text{ (neutron)} \\ &= 0, \text{ otherwise,} \end{aligned} \tag{11}$$

and similarly for the other particles. Note that S is still inclusive in the sense that it is not yet depleted for further decay. The summation runs over the excitation energies of the mother bin from which decay into the $E_{x'}(i')$ bin of the residual nucleus is energetically allowed. Feeding by gamma decay from bins above the $(Z', N', E_{x'}(i'))$ bin is taken into account by the $k = \gamma$ term, in which case all of the Kronecker delta's in Eq. (11) are zero.

With Eq. (7) as initial condition, the recursive procedure is completely defined. For a fixed nucleus, Eq. (10) is calculated for all excitation energy bins, in decreasing order, until the remaining population is in an isomeric or ground state of the nucleus. When there is no further decay possible, the exclusive cross section per ground state/isomer, numbered by i, can be identified,

$$\sigma_i^{ex}(i_n, i_p, i_d, i_t, i_h, i_\alpha) = S(i_n, i_p, i_d, i_t, i_h, i_\alpha, E_i). \tag{12}$$

The total exclusive cross section for a particular channel is then calculated as

$$\sigma^{ex}(i_n, i_p, i_d, i_t, i_h, i_\alpha) = \sum_{i=0,isomers} \sigma_i^{ex}(i_n, i_p, i_d, i_t, i_h, i_\alpha). \tag{13}$$

The procedure outlined above automatically sorts and stores all exclusive cross sections, irrespective of the order of particle emission within the reaction chain. For example, the (n, np) and (n, pn) channels are automatically added. The above formalism holds *exactly* for an arbitrary number of emitted particles.

We stress that keeping track of the excitation energy E_x throughout this formalism is essential to get the exact exclusive cross sections for two reasons:

(i) the exact determination of the branching ratios for exclusive isomeric ratios. The isomeric ratios for different exclusive reactions that lead to the same residual product, e.g. (n, np) and (n, d), both leading to $(Z_C - 1, N_C - 1)$,

are generally different from each other and thus also from the isomeric ratios of the total residual product. Hence, it would be an approximation to apply isomeric branching ratios for residual products, obtained after the full reaction calculation, a posteriori on the exclusive channels. This is avoided with our method,.

(ii) the exclusive spectra, which we will explain in Sect. 2.4.2.

When TALYS computes the binary reaction models and the multiple pre-equilibrium and Hauser-Feshbach models, it stores both $P(Z, N, E_x)$ and $s_k(Z, N, E_x, E_{x'})$ for all residual nuclei and particles. This temporary storage enables us to first complete the full reaction calculation, including all its physical aspects, until all channels are closed. Then, we turn to the exclusive cross section and spectra problem afterwards. It can thus be considered as an isolated book-keeping problem.

2.3.2 Binary cross sections

Some of the exclusive channels need, and get, more attention than others. The exclusive binary cross sections, for reactions that are characterized by one, and only one, particle out are special in the sense that they comprise both discrete and continuous energy transitions. Inelastic scattering can occur through both direct collective and compound transitions to the first few excited levels and through pre-equilibrium and compound reactions to the continuum. Let us assume that for a target nucleus the basic structure properties like spin, parity, etc. of the first N levels are known. Then, the inelastic cross section, $\sigma_{n,n'}$ is the sum of the total discrete inelastic cross section $\sigma_{n,n'}^{disc}$ and the continuum inelastic cross section $\sigma_{n,n'}^{cont}$

$$\sigma_{n,n'} = \sigma_{n,n'}^{disc} + \sigma_{n,n'}^{cont}, \tag{14}$$

where $\sigma_{n,n'}^{disc}$ is the sum over the inelastic cross sections for all the individual discrete states

$$\sigma_{n,n'}^{disc} = \sum_{i=1}^{N} \sigma_{n,n'}^{i}. \tag{15}$$

A further breakdown of each term is possible by means of reaction mechanisms. The inelastic cross section for each individual state i has a direct and a compound contribution:

$$\sigma_{n,n'}^{i} = \sigma_{n,n'}^{i,direct} + \sigma_{n,n'}^{i,comp}, \tag{16}$$

where the direct component comes from DWBA or coupled-channels calculations, see Sect. 4. Similarly, for the inelastic scattering to the continuum we can consider a pre-equilibrium and a compound contribution

$$\sigma_{n,n'}^{cont} = \sigma_{n,n'}^{\text{preeq}} + \sigma_{n,n'}^{cont,comp}. \tag{17}$$

The set of definitions (Eqs. 14-17) can be given in a completely analogous way for the other binary channels $\sigma_{n,p}$, i.e. $\sigma^{ex}(0, 1, 0, 0, 0, 0)$, $\sigma_{n,d}$, $\sigma_{n,t}$, $\sigma_{n,h}$ and $\sigma_{n,\alpha}$. For the depletion of the reaction population that goes into the pre-equilibrium channels, which will be discussed in Sect. 6, it is helpful to define here the total discrete direct cross section,

$$\sigma^{disc,direct} = \sum_{i} \sum_{k=n',p,d,t,h,\alpha} \sigma_{n,k}^{i,direct}. \tag{18}$$

We mention here that the entire formalism above also applies to so-called super-elastic scattering, in which the target nucleus is in an excited state, transfers its energy to the projectile and falls back to the ground state. Finally, we also consider an alternative division for the non-elastic cross section. It is equal to the sum of the *inclusive* binary cross sections

$$\sigma_{non-el} = \sum_{k=\gamma,n',p,d,t,h,\alpha} \sigma_{n,k}^{inc,bin}, \tag{19}$$

where again at the present stage of the outline we do not consider fission and ejectiles heavier than α-particles. This is what we actually use in the inclusive nuclear reaction calculations. With the direct, pre-equilibrium and compound models, several residual nuclides can be formed after the binary reaction, with a total population per nucleus that is equal to the terms of Eq. (19). The residual nuclides then decay further until all channels are closed. Note that $\sigma^{inc,bin}$ is not a "true" cross section in the sense of a quantity for a final combination of a product and light particle(s).

2.3.3 Total particle production cross sections

Especially for incident energies higher than about 10 MeV, it is appropriate to define the composite or total neutron production cross section, $\sigma_{n,xn}$. It can be expressed in terms of the exclusive cross sections as follows

$$\sigma_{n,xn} = \sum_{i_n=0}^{\infty} \sum_{i_p=0}^{\infty} \sum_{i_d=0}^{\infty} \sum_{i_t=0}^{\infty} \sum_{i_h=0}^{\infty} \sum_{i_\alpha=0}^{\infty} i_n \sigma^{ex}(i_n, i_p, i_d, i_t, i_h, i_\alpha), \tag{20}$$

i.e. in the more common notation,

$$\sigma_{n,xn} = \sigma_{n,n'} + 2\sigma_{n,2n} + \sigma_{n,np} + 2\sigma_{n,2np} + ... \tag{21}$$

Again, $\sigma_{n,xn}$ is not a true cross section since the incident and outgoing channels are not exactly defined by its individual reaction components. The neutron multiplicity, or yield, Y_n is defined as

$$Y_n = \frac{\sigma_{n,xn}}{\sigma_{non-el}}. \tag{22}$$

Similarly, the total proton production cross section, $\sigma_{n,xp}$ is defined as

$$\sigma_{n,xp} = \sum_{i_n=0}^{\infty}\sum_{i_p=0}^{\infty}\sum_{i_d=0}^{\infty}\sum_{i_t=0}^{\infty}\sum_{i_h=0}^{\infty}\sum_{i_\alpha=0}^{\infty} i_p \sigma^{ex}(i_n, i_p, i_d, i_t, i_h, i_\alpha), \quad (23)$$

and the proton multiplicity, or yield, Y_p is defined as

$$Y_p = \frac{\sigma_{n,xp}}{\sigma_{non-el}}, \quad (24)$$

and similarly for the other particles. We note that we do not, in practice, use Eq. (20) to calculate the composite particle production cross section. Instead, we first calculate the inclusive binary cross section of Eq. (19) and then, during the depletion of each residual nucleus by further decay we directly add the reaction flux, equal to the $s_k(Z, N, E_x, E_{x'})$ term of Eq. (8), to $\sigma_{n,xn}$, $\sigma_{n,xp}$, etc. This procedure has already been sketched in the multiple decay scheme at the beginning of this Section.

2.3.4 Residual production cross sections

We can define another important type of derived cross section using the exclusive cross section, namely the residual production cross section σ_{prod}. All exclusive cross sections with the same number of neutron and proton units in the outgoing channel sum up to the same residual nucleus production cross section for the final nucleus (Z, N), i.e.

$$\sigma_{prod}(Z, N) = \sum_{i_n=0}^{\infty}\sum_{i_p=0}^{\infty}\sum_{i_d=0}^{\infty}\sum_{i_t=0}^{\infty}\sum_{i_h=0}^{\infty}\sum_{i_\alpha=0}^{\infty} \sigma^{ex}(i_n, i_p, i_d, i_t, i_h, i_\alpha)\delta_N\delta_Z, \quad (25)$$

where the Kronecker delta's are defined by

$$\begin{aligned} \delta_N &= 1 \text{ if } i_n + i_d + 2i_t + i_h + 2i_\alpha = N_C - N \\ &= 0 \text{ otherwise,} \\ \delta_Z &= 1 \text{ if } i_p + i_d + i_t + 2i_h + 2i_\alpha = Z_C - Z \\ &= 0 \text{ otherwise,} \end{aligned} \quad (26)$$

where the first compound nucleus that is formed from the projectile and target nucleus is denoted by (Z_C, N_C). As an example, consider the $n + {}^{56}\text{Fe} \rightarrow {}^{54}\text{Mn} + x$ reaction. The exclusive cross sections that add up to the ^{54}Mn production cross section are $\sigma_{n,2np}$, $\sigma_{n,nd}$, and $\sigma_{n,t}$, or $\sigma^{ex}(2, 1, 0, 0, 0, 0)$, $\sigma^{ex}(1, 0, 1, 0, 0, 0)$, and $\sigma^{ex}(0, 0, 0, 1, 0, 0)$, respectively.

Since all exclusive cross sections contribute to the residual production cross section for one nuclide (Z, N) only, Eq. (6) automatically implies

$$\sigma_{non-el} = \sum_Z \sum_N \sigma_{prod}(Z, N). \quad (27)$$

Similar to Eq. (13), Eq. (25) is separated per isomer

$$\sigma_{prod,i}(Z, N) = \sum_{i_n=0}^{\infty}\sum_{i_p=0}^{\infty}\sum_{i_d=0}^{\infty}\sum_{i_t=0}^{\infty}\sum_{i_h=0}^{\infty}\sum_{i_\alpha=0}^{\infty} \sigma_i^{ex}(i_n, i_p, i_d, i_t, i_h, i_\alpha)\delta_N\delta_Z, \quad (28)$$

and the equivalent of Eq. (13) is

$$\sigma_{prod}(Z, N) = \sum_{i=0, isomers} \sigma_{prod,i}(Z, N). \quad (29)$$

Also here, we do not calculate σ_{prod} and $\sigma_{prod,i}$ using Eqs. (25) and (28), although optionally TALYS includes it as a numerical check in the output for residual nuclides close to the target. Analogous to the total particle production, we determine the residual production cross section, for both the isomers and the ground state, after the complete decay of each nucleus by means of an inclusive calculation.

2.3.5 Gamma-ray production cross sections

As mentioned at the end of Sect. 2.3.1, while the reaction flux goes through the entire decay chain, TALYS also does the book-keeping of all gamma decays between discrete levels via branching ratios (to be discussed in Sect. 10). This means we have the decay branches $s_\gamma(Z, N, E_P, E_D)$ for any nuclide, where E_P and E_D are the excitation energies of the parent and daughter level, respectively. Again, this is computed for exclusive and inclusive cross sections and any pair of P and D which are connected through non-zero branching ratios, e.g. for $\sigma^{disc}_{n,n'\gamma}(P \rightarrow D)$, $\sigma^{disc}_{n,2n\gamma}(P \rightarrow D)$ etc. and also for $\sigma_{prod,\gamma}(Z, N)(P \rightarrow D)$.

2.3.6 Fission cross sections

For clarity, we have kept the fission channel out of the discussion so far. The generalization to a picture in which fission is possible is however not too difficult. For fissile nuclides, the first expression that needs generalization is that of the non-elastic cross section expressed as a sum of exclusive cross sections, Eq. (6). It reads

$$\sigma_{non-el} = \sum_{i_n=0}^{\infty}\sum_{i_p=0}^{\infty}\sum_{i_d=0}^{\infty}\sum_{i_t=0}^{\infty}\sum_{i_h=0}^{\infty}\sum_{i_\alpha=0}^{\infty} \sigma^{ex}(i_n, i_p, i_d, i_t, i_h, i_\alpha) + \sigma_f, \quad (30)$$

where the total fission cross section σ_f is the sum over exclusive fission cross sections

$$\sigma_f = \sum_{i_n=0}^{\infty}\sum_{i_p=0}^{\infty}\sum_{i_d=0}^{\infty}\sum_{i_t=0}^{\infty}\sum_{i_h=0}^{\infty}\sum_{i_\alpha=0}^{\infty} \sigma_f^{ex}(i_n, i_p, i_d, i_t, i_h, i_\alpha), \quad (31)$$

where $\sigma_f^{ex}(i_n, i_p, i_d, i_t, i_h, i_\alpha)$ represents the cross section for fissioning *after* the emission of i_n neutrons, i_p protons, etc. Well-known special cases are $\sigma_{n,f} = \sigma_f^{ex}(0,0,0,0,0,0)$, $\sigma_{n,nf} = \sigma_f^{ex}(1,0,0,0,0,0)$ and $\sigma_{n,2nf} = \sigma_f^{ex}(2,0,0,0,0,0)$, which are also known as first-chance, second-chance and third-chance fission cross section, respectively. Equation (31) is more general in the sense that it also includes cases where particles other than neutrons can be emitted before the residual nucleus fissions, e.g. (n, npf), which may occur at higher incident energies.

The generalization of the non-elastic cross section of Eq. (19) is

$$\sigma_{non-el} = \sum_{k=\gamma,n',p,d,t,h,\alpha} \sigma_{n,k}^{inc,bin} + \sigma_f^{bin}, \quad (32)$$

where σ_f^{bin} represents fission from the initial compound state. Note that the fission term here excludes the $(n, \gamma f)$ process since that is treated as a subchannel after the binary capture reaction.

Analogous to Eq. (25), we can define a cross section for each fissioning residual product

$$\sigma_{prod}^{fis}(Z,N) = \sum_{i_n=0}^{\infty}\sum_{i_p=0}^{\infty}\sum_{i_d=0}^{\infty}\sum_{i_t=0}^{\infty}\sum_{i_h=0}^{\infty}\sum_{i_\alpha=0}^{\infty} \sigma_f^{ex}(i_n, i_p, i_d, i_t, i_h, i_\alpha)\delta_N\delta_Z. \quad (33)$$

At higher energies, the meaning of $\sigma_{prod}^{fis}(Z,N)$ is more relevant than the exclusive fission cross sections. Consequently, for the total fission cross section we have

$$\sigma_f = \sum_Z \sum_N \sigma_{prod}^{fis}(Z,N). \quad (34)$$

What remains to be explained is how σ_f^{ex} is computed. First, we need to add to Eq. (8) a term we denote by $s_f(Z,N,E_x(i))$, which is the part of the population that fissions from the $(Z,N,E_x(i))$ bin. Hence, for fissile nuclides we have

$$P(Z,N,E_x(i)) = s_f(Z,N,E_x(i)) + \sum_{k=\gamma,n,p,d,t,h,\alpha} \sum_i s_k(Z,N,E_x(i),E_{x'}(i')). \quad (35)$$

where in this case the sum over i runs over discrete levels and continuum bins from 0 to $E_x(i) - S_k$. The exclusive fission cross section σ_f^{ex} is

$$\sigma_f^{ex}(i_n, i_p, i_d, i_t, i_h, i_\alpha) = \sum_i \frac{s_f(Z,N,E_x(i))}{P(Z,N,E_x(i))} \times S(i_n, i_p, i_d, i_t, i_h, i_\alpha, E_x(i)), \quad (36)$$

where i runs from 0 to $E_x^{max}(Z,N)$. The rest of the calculation of the exclusive particle cross section proceeds exactly as before. Equation (10) is now automatically depleted from the fission cross section (36), in the sense that the s_k terms alone, summed over γ and particles only, no longer add up to the population P.

2.4 Spectra and angular distributions

In addition to cross sections, TALYS also computes energy spectra, angular distributions and energy-angle distributions.

2.4.1 Discrete angular distributions

The elastic angular distribution $\frac{d\sigma^{el}}{d\Omega}$ has a direct and a compound component:

$$\frac{d\sigma^{el}}{d\Omega} = \frac{d\sigma^{shape-el}}{d\Omega} + \frac{d\sigma^{comp-el}}{d\Omega}, \quad (37)$$

where the shape-elastic part comes directly from the optical model while the compound part comes from compound nucleus theory. An analogous relation holds for inelastic scattering to a single discrete state i

$$\frac{d\sigma_{n,n'}^{i}}{d\Omega} = \frac{d\sigma_{n,n'}^{i,direct}}{d\Omega} + \frac{d\sigma_{n,n'}^{i,compound}}{d\Omega}, \quad (38)$$

where the direct component comes from DWBA or coupled-channels calculations. For charge exchange, we can write

$$\frac{d\sigma_{n,p}^{i}}{d\Omega} = \frac{d\sigma_{n,p}^{i,direct}}{d\Omega} + \frac{d\sigma_{n,p}^{i,compound}}{d\Omega}, \quad (39)$$

and analogous expressions can be written for the other binary reactions (n,d), etc.

Of course, the integration over solid angle of every angular distribution defined here must be equal to the corresponding cross section, e.g.

$$\sigma_{n,n'}^{i,direct} = \int d\Omega \frac{d\sigma_{n,n'}^{i,direct}}{d\Omega}. \quad (40)$$

In the output of TALYS, we use a representation in terms of outgoing angle and one in terms of Legendre coefficients, i.e. Equation (37) can also be written as

$$\frac{d\sigma^{el}}{d\Omega} = \sum_L (C_L^{shape-el} + C_L^{comp-el}) P_L(\cos\Theta), \quad (41)$$

where P_L are Legendre polynomials. For inelastic scattering we have

$$\frac{d\sigma^i_{n,n'}}{d\Omega} = \sum_L (C_L^{i,direct} + C_L^{i,comp}) P_L(\cos\Theta), \tag{42}$$

and similarly for the other binary channels. The Legendre expansion is required for the storage of the results in nuclear data libraries.

2.4.2 Exclusive spectra

An exclusive spectrum is not only specified by the exact number of emitted particles, but also by their outgoing energies.

In TALYS, exclusive spectra are calculated in the same loops that take care of the exclusive cross sections. The inclusive continuum spectra are obtained by taking the derivative of the inclusive cross sections per excitation energy of Eq. (10) with respect to the outgoing particle energy $E_{k'}$,

$$E_{k'} = E_x - E_{x'}(i') - S_{k'}, \tag{43}$$

where $S_{k'}$ is the separation energy for outgoing particle k'. Note that since the inclusive cross section per excitation energy S depends on $E_{k'}$ via s_k, the product rule of differentiation applies to Eq. (10). Therefore, the inclusive spectrum per excitation energy for an outgoing particle k' of a given $(i_n, i_p, i_d, i_t, i_h, i_\alpha)$ channel is

$$\begin{aligned}\frac{dS}{dE_{k'}}(i_n, i_p, i_d, i_t, i_h, i_\alpha, E_{x'}(i')) = \sum_{k=\gamma,n,p,d,t,h,\alpha} \\ \sum_i \Bigg[\frac{s_k(Z, N, E_x(i), E_{x'}(i'))}{P(Z, N, E_x(i))} \\ \times \frac{dS}{dE_{k'}}(i_n - \delta_{nk}, \ldots, i_\alpha - \delta_{\alpha k}, E_x(i)) \\ + \delta_{kk'} \frac{ds_k(Z, N, E_x(i), E_{x'}(i'))}{dE_{k'}} \\ \times \frac{S(i_n - \delta_{nk}, \ldots, i_\alpha - \delta_{\alpha k}, E_x(i))}{P(Z, N, E_x(i))} \Bigg],\end{aligned} \tag{44}$$

where, as initial condition, the derivatives of $s_k(Z_C, N_C, E_x^{max}, E_{x'}(i'))$ are the binary emission spectra. The first term on the right-hand side corresponds to the spectrum of the feeding channel and the second term denotes the contribution of the last emitted particle. The calculation of Eq. (44) can be done simultaneously with the exclusive cross section calculation, i.e. we follow exactly the same recursive procedure. The final exclusive spectrum for outgoing particle k' is given by

$$\begin{aligned}\frac{d\sigma^{ex}}{dE_{k'}}(i_n, i_p, i_d, i_t, i_h, i_\alpha) \\ = \sum_{i=0,isomers} \frac{dS}{dE_{k'}}(i_n, i_p, i_d, i_t, i_h, i_\alpha, E_i),\end{aligned} \tag{45}$$

The terms on the right hand side are the exclusive spectra per ground state or isomer. The latter naturally result from our method, even though only the total exclusive spectra of the left hand side are of interest.

We stress that for a given $(i_n, i_p, i_d, i_t, i_h, i_\alpha)$ channel, Eq. (44) is calculated for *every* outgoing particle k' (i.e. n, p, d, t, h and α). Hence, e.g. the $(n, 2np\alpha)$ channel is characterized by only one exclusive cross section, $\sigma_{n,2np\alpha}$, but by three spectra, one for outgoing neutrons, protons and alpha's, respectively, whereby all three spectra are constructed from components from the first up to the fourth particle emission (i.e. the α can have been emitted in each of the four stages). In practice, this means that all spectra have a first order pre-equilibrium component (and for higher energies also multiple pre-equilibrium components), and a compound component from multiple emission. Upon integration over outgoing energy, the exclusive cross sections may be obtained,

$$\begin{aligned}\sigma^{ex}(i_n, i_p, i_d, i_t, i_h, i_\alpha) \\ = \frac{1}{i_n + i_p + i_d + i_t + i_h + i_\alpha} \sum_{k'=n,p,d,t,h,\alpha} \\ \int dE_{k'} \frac{d\sigma^{ex}}{dE_{k'}}(i_n, i_p, i_d, i_t, i_h, i_\alpha).\end{aligned} \tag{46}$$

Finally, the exclusive fission cross sections are also accompanied by spectra. For example, the first two neutrons emitted in the $(n, 2nf)$ channel (third-chance fission) are described by an outgoing neutron spectrum. The exclusive spectrum of outgoing particle k' in a fission channel is

$$\begin{aligned}\frac{d\sigma^{ex}_f}{dE_{k'}}(i_n, i_p, i_d, i_t, i_h, i_\alpha) = \sum_i \frac{s_f(Z, N, E_x(i))}{P(Z, N, E_x(i))} \\ \times \frac{dS}{dE_{k'}}(i_n, i_p, i_d, i_t, i_h, i_\alpha),\end{aligned} \tag{47}$$

while the exclusive particle spectra are again described by Eq. (44). For double-differential spectra, the usual generalization holds. We also repeat here that the total (observable) fission cross section is always calculated by letting reaction population go into the fission channel from each (Z, N, E_x, J, Π) channel until all nuclides have ended up in their ground or isomeric states, irrespective of the user request for an exclusive channel calculation. Also, it should be clear, the formalism described above does not include neutrons produced by the fissioning nucleus itself. We describe that in Sect. 14.

2.4.3 Binary spectra

Similar to the cross sections, the exclusive spectra determine various other specific spectra of interest. The exclusive inelastic spectrum is a special case of Eq. (45)

$$\frac{d\sigma_{n,n'}}{dE_{n'}} = \frac{d\sigma^{ex}}{dE_{n'}}(1,0,0,0,0,0). \tag{48}$$

Since Eq. (44) represents an energy spectrum, it includes by definition only continuum transitions, i.e. it does not include the binary reactions to discrete states. Hence, upon integration, Eq. (48) only gives the continuum inelastic cross section of Eq. (14):

$$\sigma^{cont}_{n,n'} = \int dE_{n'} \frac{d\sigma_{n,n'}}{dE_{n'}}. \tag{49}$$

Similar relations hold for the binary (n, p), (n, d), (n, t), (n, h) and (n, α) spectra. The contributions to the binary spectra generally come from pre-equilibrium and continuum compound spectra.

2.4.4 Total particle production spectra

Similar to the total particle production cross sections, the composite or total neutron spectrum can be expressed in terms of exclusive spectra as follows

$$\frac{d\sigma_{n,xn}}{dE_{n'}} = \sum_{i_n=0}^{\infty}\sum_{i_p=0}^{\infty}\sum_{i_d=0}^{\infty}\sum_{i_t=0}^{\infty}\sum_{i_h=0}^{\infty}\sum_{i_\alpha=0}^{\infty} \frac{d\sigma^{ex}}{dE_{n'}}(i_n, i_p, i_d, i_t, i_h, i_\alpha), \tag{50}$$

i.e. in the other notation,

$$\frac{d\sigma_{n,xn}}{dE_{n'}} = \frac{d\sigma_{n,n'}}{dE_{n'}} + \frac{d\sigma_{n,2n}}{dE_{n'}} + \frac{d\sigma_{n,np}}{dE_{n'}} + \frac{d\sigma_{n,2np}}{dE_{n'}} + \ldots. \tag{51}$$

Similar relations hold for the (n, xp), etc. spectra. Note that, in contrast with Eq. (20), the multiplicity is already implicit in the exclusive spectra.

Again, in practice we do not use Eq. (50) to calculate the composite spectra but instead add the $ds_k(Z, N, E_x, E_{x'})/dE_{k'}$ term that appears in Eq. (44) to the composite spectra while depleting all nuclides in an inclusive calculation. We do use Eq. (50) as a numerical check in the case of a few outgoing particles. Finally, integration of the total neutron spectrum and addition of the binary discrete cross section give the total particle production cross section

$$\sigma_{n,xn} = \int dE_{n'} \frac{d\sigma_{n,xn}}{dE_{n'}} + \sigma^{disc}_{n,n'}, \tag{52}$$

and similarly for the other particles.

2.4.5 Double-differential cross sections

The generalization of the exclusive spectra to angular dependent cross sections is done by means of the exclusive double-differential cross sections

$$\frac{d^2\sigma^{ex}}{dE_{k'}d\Omega}(i_n, i_p, i_d, i_t, i_h, i_\alpha), \tag{53}$$

which are obtained by either physical models or systematics. Integration over angles yields the exclusive spectrum

$$\frac{d\sigma^{ex}}{dE_{k'}}(i_n, i_p, i_d, i_t, i_h, i_\alpha) = \int d\Omega \frac{d^2\sigma^{ex}}{dE_{k'}d\Omega}(i_n, i_p, i_d, i_t, i_h, i_\alpha). \tag{54}$$

The other relations are analogous to those of the spectra, e.g. the inelastic double-differential cross section for the continuum is

$$\frac{d^2\sigma_{n,n'}}{dE_{n'}d\Omega} = \frac{d^2\sigma^{ex}}{dE_{n'}d\Omega}(1,0,0,0,0,0), \tag{55}$$

and the total neutron double-differential cross section can be expressed as

$$\frac{d^2\sigma_{n,xn}}{dE_{n'}d\Omega} = \sum_{i_n=0}^{\infty}\sum_{i_p=0}^{\infty}\sum_{i_d=0}^{\infty}\sum_{i_t=0}^{\infty}\sum_{i_h=0}^{\infty}\sum_{i_\alpha=0}^{\infty} \frac{d^2\sigma^{ex}}{dE_{n'}d\Omega}(i_n, i_p, i_d, i_t, i_h, i_\alpha). \tag{56}$$

For the *exclusive* calculation, the angular information is only tracked for the first particle emission. The reason is that for incident energies up to about 20 to 30 MeV, only the first emitted particle deviates from an isotropic angular distribution. Multiple compound emission to the continuum is essentially isotropic. The isotropic contribution to the exclusive double-differential spectrum is then simply determined by the part of the corresponding cross section that comes from Hauser-Feshbach decay. At higher incident energies, where the approximation of only one forward-peaked particle becomes incorrect, the interest in exclusive spectra, or for that matter, the computational check of Eq. (56), is no longer there. The presence of multiple pre-equilibrium emission at energies above several tens of MeV requires that we include angular information for every emitted particle in the *total* double-differential cross section, i.e. the left-hand side of Eq. (56). Again, this is all tracked correctly in the full inclusive calculation.

2.4.6 Recoils

Qualitative analysis

In a nuclear reaction code, the calculations are usually performed in the center of mass (CM) frame, while the experimental data are obtained in the Laboratory (LAB) frame. It is therefore necessary to perform a transformation either by (i) expressing the experimental data in the CM frame or by (ii) expressing the CM model results in the LAB frame. Of course, the cross sections are the same in both frames, but the spectra are certainly different. The best example is given by the elastic peak in an emission spectrum which is a Dirac delta peak in the CM frame and rather looks like a Gaussian when measured experimentally. The reason for this, apart from the fact that the projectile beam is not perfectly monoenergetic, is that the composite system has a velocity in the LAB frame before decay occurs. Consequently if one considers the emission of an ejectile with a well defined energy in the CM frame, the ejectile energy in the LAB frame will not be unique because of all the CM emission angles. More precisely, a maximum ejectile energy will be obtained when the emission occurs at 0°, and a minimum will be obtained at 180°, together with all the intermediate situations. Dealing with this situation is simple if only one nucleus decays, but if two particles are sequentially emitted, the first emission probabilities create a velocity distribution of the residual nuclei in the LAB frame. One must first loop over these velocities before one can compute the secondary emission.

General method

As mentioned in Sect. 2.3.1, in TALYS each nucleus that can decay is described by an array $P(Z, N, E_x)$ which gives the population in a bin/level with excitation energy E_x of the nucleus (Z, N). A special case is the initial compound nucleus which contains all the initial reaction population at its total excitation energy E_x^{max}. For the kinematics of the binary reactions, it is necessary to keep track of the velocities and moving directions of these nuclei in the LAB frame, so that we can reconstruct the LAB spectra from the decays in the CM frame. We therefore have to add in principle three dimensions to the P array. The first one to keep track of the recoil energy, and the two other ones for the emission angles. However, such book-keeping would become very time consuming, especially for high energies.

Hence, we only take into account the recoil energies and the usual Θ_r angle and define another array $P_{rec}(Z, N, E_x, E_r, \Theta_r)$ which indicates the fraction of the total population $P(Z, N, E_x)$ moving with the kinetic energy E_r in the direction Θ_r with respect to the beam direction in the LAB frame. Obviously,

$$P(Z, N, E_x) = \sum_{E_r, \Theta_r \; bins} P_{rec}(Z, N, E_x, E_r, \Theta_r). \quad (57)$$

Again, the initial compound nucleus (Z_C, N_C) is a special one. Its kinetic energy E_r^0 in the LAB frame is unique and is given by

$$E_r^0 = \sqrt{(E_p^2 + 2M_p E_p + M_C^2)} - M_C, \quad (58)$$

where E_p is the projectile kinetic energy in the LAB, M_p the projectile mass and M_C the compound nucleus mass, and it moves in the beam direction (i.e. 0°). Before any emission is calculated, the initial reaction population is stored in the array element $P_{rec}(Z_c, N_c, E_x^{max}, E_r^0, 0)$. As explained before, the population of the residual nuclei bins are calculated by looping over all possible ejectiles, emission energies and angles in the CM frame. Therefore, each time we decay from a mother bin to a residual bin, we know exactly what fraction of the total bin population is emitted in a given CM (energy, angle) bin. We then simply couple the CM emission energies and angles with the CM kinetic energy and moving direction in the LAB frame to determine simultaneously the ejectile double-differential spectrum in the LAB and the residual nucleus population in the corresponding LAB (energy, angle) bin. This may seem simple from a qualitative point of view, it is however not trivial to implement numerically and can be time consuming.

Quantitative analysis

From now on, for simplicity, we assume that the kinematics of the binary reactions can be considered as a classical process, i.e. we exclude γ decay and relativistic kinematics in the recoil calculation. We here consider the emission of a given ejectile from a given energy bin i of the decaying nucleus (Z, N) which moves with a given velocity v_{cm} (or kinetic energy E_{cm}) in the direction Θ_{cm} with respect to the beam direction. The total population that is going to decay is $P(Z, N, E_i)$ and the fraction of this population moving with the velocity v_{cm} in the direction Θ_{cm} is given by $P_{rec}(Z, N, E_i, E_{cm}, \Theta_{cm})$. We can determine the total emitted flux for a given emission energy and a given emission angle in the CM frame. In practice, we rather decay from a initial bin to a residual bin in a given angular bin in the CM frame. If recoil effects are neglected we directly derive from such a decay an energy bin $[E_{low}^{CM}, E_{up}^{CM}]$ and an angular bin $[\Theta_{low}^{CM}, \Theta_{up}^{CM}]$ in which the total flux Φ_{ej}^{CM} is emitted. Accounting for recoil effects requires an intermediate step to share the available energy ΔE (difference between the energy bins of the initial nucleus and final nucleus) among the ejectile with mass m_{ej} and the residual nucleus with mass M_R.

To do this, we use the classical relation

$$\vec{v}_{ej}^{\,LAB} = \vec{v}_{cm} + \vec{v}_{ej}^{\,CM}, \quad (59)$$

which connects the LAB velocity $\overrightarrow{v}_{ej}^{LAB}$ of the ejectile with its velocity $\overrightarrow{v}_{ej}^{CM}$ in the CM frame and the CM frame velocity $\overrightarrow{v}_{cm}$. We need to connect $\overrightarrow{v}_{ej}^{CM}$ with ΔE.

This can be done upon writing

$$\Delta E = \frac{1}{2} m_{ej} (\overrightarrow{v}_{ej}^{CM})^2 + \frac{1}{2} M_R (\overrightarrow{v}_{R}^{CM})^2, \tag{60}$$

where $\overrightarrow{v}_{R}^{CM}$ is the residual nucleus velocity in the CM frame, and using the relation

$$m_{ej} \overrightarrow{v}_{ej}^{CM} + m_R \overrightarrow{v}_{R}^{CM} = \overrightarrow{0}. \tag{61}$$

Combining (60) and (61) yields

$$v_{ej}^{CM} = \sqrt{2 \frac{M_R}{m_{ej}(m_{ej} + M_R)} \Delta E}, \tag{62}$$

which reduces to the classical relation

$$v_{ej}^{CM} = \sqrt{\frac{2\Delta E}{m_{ej}}}, \tag{63}$$

if recoil effects are neglected (i.e. in the limit $M_R \to +\infty$).

Once this connection is established, Eq. (59) is used to determine the velocity and angle of both the emitted light particle and the residual nucleus by simple projections on the LAB axis.

Hence, given a decay situation in the CM frame, we can reconstruct both the energy and angle of emission in the LAB frame. We now have to determine the link between the double-differential decay characteristics in both frames. The solution is well known (see Ref. [12] for instance) and consists of using a Jacobian which accounts for the modification of an elementary solid angle $d\Omega$ in the CM frame when going into the LAB frame. However, in TALYS we have to employ another method because we do not generally calculate decays for well defined energies and angles but rather for a given energy bin and angular bin. Moreover, since we do not account for the azimuthal angle, we may also encounter some problems when calculating recoil for secondary emission. Indeed, only the first binary process has the azimuthal symmetry with respect to the beam direction.

The recoil treatment in TALYS

We here detail the way the double-differential spectra are calculated by TALYS in the LAB frame from those obtained in the CM frame. We consider the flux $\Phi(i, j)$ emitted in the CM frame in an energy-angular bin (i, j). Since $\Phi(i, j)$ is connected with the double differential cross section $xs(i, j)$ by

$$\Phi(i, j) = xs(i, j) \Delta E(i) \Delta cos\Theta(j), \tag{64}$$

the four grid points defining the coordinates of the bin in the CM frame form a rectangle in a energy-cosine grid. Coupling the CM motion (kinetic energy and angle) with these four CM bin coordinates enables one to determine four corresponding points in the LAB frame. However, the surface defined by these LAB coordinates will be different from a rectangle and each limiting grid points will be located in different outgoing energy-angle bins. The CM flux of a single bin must thus be distributed over several bins when going to the LAB frame.

The approximation made, to be able (i) to calculate the area covered in the LAB frame and (ii) the way this global area is distributed over the bins it partially covers, consists in neglecting the deformation of the area reached in the LAB frame which is therefore assumed to be a trapezoid. In other words, we make the assumption that a triangle in the CM frame is transformed into a triangle when going in the LAB frame. This is helpful since the area of a triangle is given by a simple analytic expression as function of the coordinates of the summits of the triangle. Therefore, we divide the starting energy-cosine rectangular CM bins into two triangles to determine the two triangles obtained in the LAB frame. With such a method, the whole problem can be solved and the decay calculated in the CM frame can be transformed to the LAB frame without any further approximations.

However, in practice, coupling the angular direction (in the LAB) of the nucleus that decays with the ejectile emission angle in the CM frame, while neglecting the azimuthal angle, gives double differential ejectile spectra in the LAB which are generally not correct. In fact, we believe that it is better not to account for the angular distribution of the decaying nucleus unless both Θ and ϕ are explicitly treated. Fortunately, the final angular distribution of the recoiling nucleus is seldom of interest.

Method of average velocity

As mentioned above, we do not loop over the angular distribution of the decaying nucleus. This is equivalent to replacing the array $P_{rec}(Z, N, E_i, E_r, \Theta_r)$ by $P_{rec}(Z, N, E_i, E_r)$. Then, we only have to keep track of the velocities of the nucleus that is going to decay, i.e. we have to loop over the E_r bins to reconstruct both the ejectile and residual nuclei spectra. Another approximation that we have implemented as an option, consists of using an average velocity before this reconstruction, a method first applied by Chadwick et al. [13,14]. This approach avoids the loop over the E_r bins altogether and reduces the calculation time. However, for high energies, this might be too crude an approximation.

Figure 8 gives an indication of the difference between this average energy approximation and the exact calculation. Apparently, properly including the energy bins of the recoiling nucleus E_r in the calculation leads to smearing out of var-

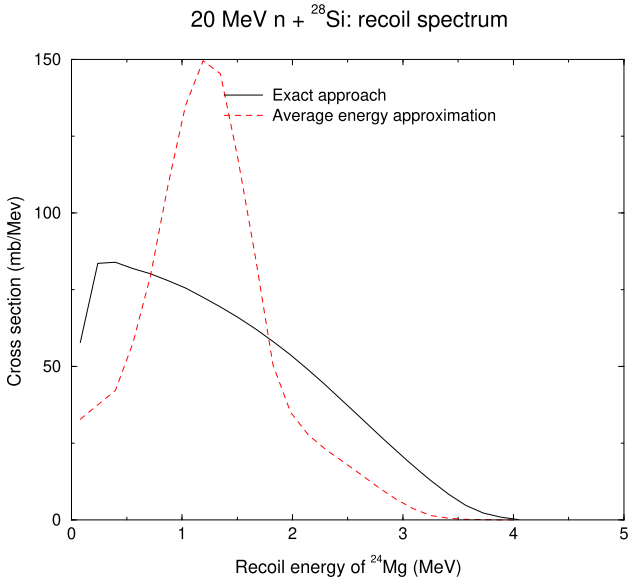

Fig. 8 Example of the difference between exact and approximative recoil treatment in TALYS

ious contributions to the final recoil spectrum. By default, we always apply the exact approach, although in cases of high incident energies the computation time may get significant.

Approximative recoil correction for binary ejectile spectra it is also possible to avoid a full recoil calculation, and merely correct the outgoing particle spectra for the recoil of the nucleus. In that case the following method is available.

The assumptions are made that (*i*) only binary emission takes place, and that (*ii*) emission only occurs under 0^o. Hence, this approximation is basically expected to be valid for angle-integrated spectra only. The CM to LAB conversion of the ejectile spectra takes under these conditions the following simple form:

$$E_{ej}^{lab} = \frac{M_R}{M_C}\,\Delta E + \frac{m_{ej} M_p}{M_C^2}\,E_p + 2\sqrt{\frac{m_{ej} M_R M_p}{M_C^3}\,E_p\,\Delta E}, \tag{65}$$

in which E_{ej}^{lab} is the LAB ejectile energy. This correction is applied to the full ejectile spectrum including the multiple emission contributions. This approximation is rather crude, but saves a lot of computer time. Since the high-energy tail originates completely from binary emission, this tail is correctly converted to the LAB system. Furthermore, the correction is small at low energies, which has the largest contributions from multiple emission.

3 Optical model

The optical model is often regarded as the most essential ingredient of nuclear reaction modeling for energies up to a few hundreds of MeV. The central assumption underlying the optical model is that the complicated interaction between an incident particle and a nucleus can be represented by a complex mean-field potential, which divides the reaction flux into a part covering shape elastic scattering and a part describing all competing non-elastic channels. Solving the Schrödinger equation numerically with this optical model potential (OMP) yields quantities which are used throughout TALYS for its reaction calculations, such as

- the basic observables: the total, shape elastic and reaction cross sections,
- the elastic angular distribution and polarisation,
- for low energies, the s, p-wave strength functions and the potential scattering radius R',
- transmission coefficients used for compound nucleus decay,
- distorted wave functions that are used for direct inelastic reactions, yielding cross sections and angular distributions, and for transitions to the continuum that describe statistical or collective multi-step direct reactions,
- inverse reaction cross sections for the pre-equilibrium model.

The essential value of a good optical model is that it can reliably predict these quantities for a wide range of energies and nuclides, while its parameters may be determined by the available experimental data for the basic reaction observables.

All optical model calculations are performed by the coupled-channels code ECIS-06 [5], which is used as a subroutine in TALYS.

3.1 Spherical OMP: neutrons and protons

The default OMP used in TALYS are the local and global parameterisations of Koning and Delaroche [15], often abbreviated as KD03. The phenomenological OMP for nucleon-nucleus scattering, $\mathcal{U}$, is defined as:

$$\mathcal{U}(r,E) = -\mathcal{V}_V(r,E) - i\mathcal{W}_V(r,E) - i\mathcal{W}_D(r,E) + \mathcal{V}_{SO}(r,E).\mathbf{l}.\sigma + i\mathcal{W}_{SO}(r,E).\mathbf{l}.\sigma + \mathcal{V}_C(r), \tag{66}$$

where $\mathcal{V}_{V,SO}$ and $\mathcal{W}_{V,D,SO}$ are the real and imaginary components of the volume-central (V), surface-central (D) and spin-orbit (SO) potentials, respectively. E is the LAB energy of the incident particle in MeV and r the radial coordinate. All components are separated in energy-dependent well depths,

V_V, W_V, W_D, V_{SO}, and W_{SO}, and energy-independent radial parts f, namely

$$\begin{aligned}
\mathcal{V}_V(r,E) &= V_V(E) f(r, R_V, a_V),\\
\mathcal{W}_V(r,E) &= W_V(E) f(r, R_V, a_V),\\
\mathcal{W}_D(r,E) &= -4a_D W_D(E) \frac{d}{dr} f(r, R_D, a_D),\\
\mathcal{V}_{SO}(r,E) &= V_{SO}(E) \left(\frac{\hbar}{m_\pi c}\right)^2 \frac{1}{r}\frac{d}{dr} f(r, R_{SO}, a_{SO}),\\
\mathcal{W}_{SO}(r,E) &= W_{SO}(E) \left(\frac{\hbar}{m_\pi c}\right)^2 \frac{1}{r}\frac{d}{dr} f(r, R_{SO}, a_{SO}).
\end{aligned} \tag{67}$$

The form factor $f(r, R_i, a_i)$ is a Woods-Saxon shape

$$f(r, R_i, a_i) = (1 + \exp[(r - R_i)/a_i])^{-1}, \tag{68}$$

where the geometry parameters are the radius $R_i = r_i A^{1/3}$, with A being the atomic mass number, and the diffuseness parameters a_i. For charged projectiles, the Coulomb term $\mathcal{V}_C$, as usual, is given by that of a uniformly charged sphere

$$\begin{aligned}
\mathcal{V}_C(r) &= \frac{Zze^2}{2R_C}\left(3 - \frac{r^2}{R_C^2}\right), \quad \text{for } r \le R_C\\
&= \frac{Zze^2}{r}, \quad \text{for } r \ge R_C,
\end{aligned} \tag{69}$$

with $Z(z)$ the charge of the target (projectile), and $R_C = r_C A^{1/3}$ the Coulomb radius.

The functional forms for the potential depths depend on $(E - E_f)$, where E_f, the Fermi energy, is defined as the energy halfway between the last occupied and the first unoccupied shell of the nucleus,

$$\begin{aligned}
E_f^n &= -\frac{1}{2}[S_n(Z,N) + S_n(Z,N+1)],\\
E_f^p &= -\frac{1}{2}[S_p(Z,N) + S_p(Z+1,N)],
\end{aligned} \tag{70}$$

with S_n (S_p) the neutron (proton) separation energy for a nucleus with proton number Z and neutron number N.

The KD03 OMP parameterisation for either incident neutrons or protons is

$$\begin{aligned}
V_V(E) &= v_1[1 - v_2(E - E_f) + v_3(E - E_f)^2\\
&\quad - v_4(E - E_f)^3]\\
W_V(E) &= w_1 \frac{(E - E_f)^2}{(E - E_f)^2 + (w_2)^2}\\
r_V &= \text{constant}\\
a_V &= \text{constant}\\
W_D(E) &= d_1 \frac{(E - E_f)^2}{(E - E_f)^2 + (d_3)^2} \exp[-d_2(E - E_f)]\\
r_D &= \text{constant}\\
a_D &= \text{constant}\\
V_{SO}(E) &= v_{so1} \exp[-v_{so2}(E - E_f)]\\
W_{SO}(E) &= w_{so1} \frac{(E - E_f)^2}{(E - E_f)^2 + (w_{so2})^2}\\
r_{SO} &= \text{constant}\\
a_{SO} &= \text{constant}\\
r_C &= \text{constant},
\end{aligned} \tag{71}$$

where $E_f = E_f^n$ for incident neutrons and $E_f = E_f^p$ for incident protons. This representation is valid for incident energies from 1 keV up to 200 MeV. Note that V_V and W_V share the same geometry parameters r_V and a_V, and likewise for the spin-orbit terms. This effectively reduces the number of free parameters.

In general, all parameters (v_i, w_i, d_i, $v_{so,i}$, $w_{so,i}$) appearing in Eq. (71) differ from nucleus to nucleus. When enough experimental scattering data of a certain nucleus is available, a so-called local OMP can be constructed. TALYS retrieves all the parameters of these local OMPs automatically from the nuclear structure and model parameter database, which contains the same information as the various tables of Ref. [15]. If a local OMP parameterisation is not available in the database, the built-in global optical models using parameters taken as functionals of Z and A are automatically used. A flag exists to overrule the local OMP by the global OMP.

The spherical optical model described above provides the transmission coefficients, DWBA cross sections, total and elastic cross sections, etc. mentioned in the beginning of this section. For deformed nuclides, strongly coupled collective levels need to be included, as explained later.

3.1.1 Dispersive OMP: neutrons

The theory of the nuclear optical model can be reformulated in terms of dispersion relations that connect the real and imaginary parts of the optical potential, and TALYS contains dispersive spherical neutron OMP parameterizations for about 70 nuclides (unpublished) as the default if it is available for the target nuclide. These dispersion relations are a natural result of the causality principle that a scattered wave cannot be emitted before the arrival of the incident wave. The dispersion component stems directly from the absorptive part of the potential,

$$\Delta\mathcal{V}(r,E) = \frac{\mathcal{P}}{\pi}\int_{-\infty}^{\infty} \frac{\mathcal{W}(r,E')}{E' - E} dE', \tag{72}$$

where $\mathcal{P}$ denotes the principal value, see e.g. Ref. [16–18]. The total real central potential can be written as the sum of a Hartree-Fock term $\mathcal{V}_{HF}(r,E)$ and the total dispersion potential $\Delta\mathcal{V}(r,E)$

$$\mathcal{V}(r,E) = \mathcal{V}_{HF}(r,E) + \Delta\mathcal{V}(r,E). \tag{73}$$

Since $\mathcal{W}(r, E)$ has a volume and a surface component, the dispersive addition is,

$$\begin{aligned}\Delta\mathcal{V}(r, E) &= \Delta\mathcal{V}_V(r, E) + \Delta\mathcal{V}_D(r, E)\\ &= \Delta V_V(E) f(r, R_V, a_V)\\ &\quad -4a_D \Delta V_D(E) \frac{d}{dr} f(r, R_D, a_D),\end{aligned} \tag{74}$$

where the volume dispersion term is given by

$$\Delta V_V(E) = \frac{\mathcal{P}}{\pi} \int_{-\infty}^{\infty} \frac{W_V(E')}{E' - E} dE', \tag{75}$$

and the surface dispersion term is given by

$$\Delta V_D(E) = \frac{\mathcal{P}}{\pi} \int_{-\infty}^{\infty} \frac{W_D(E')}{E' - E} dE'. \tag{76}$$

Hence, the real volume well depth of Eq. (67) becomes

$$V_V(E) = V_{HF}(E) + \Delta V_V(E), \tag{77}$$

and the real surface well depth is

$$V_D(E) = \Delta V_D(E). \tag{78}$$

In general, Eqs. (75)–(76) cannot be solved analytically. However, under certain plausible conditions, analytical solutions exist. Under the assumption that the imaginary potential is symmetric with respect to the Fermi energy E_F,

$$W(E_F - E) = W(E_F + E), \tag{79}$$

where W denotes either the volume or surface term, we can rewrite the dispersion relation as,

$$\begin{aligned}\Delta V(E) &= \frac{2}{\pi}(E - E_F)\\ &\quad \mathcal{P} \int_{E_F}^{\infty} \frac{W(E')}{(E' - E_F)^2 - (E - E_F)^2} dE',\end{aligned} \tag{80}$$

from which it easily follows that $\Delta V(E)$ is skew-symmetric around E_F,

$$\Delta V(E + E_F) = -\Delta V(E - E_F), \tag{81}$$

and hence $\Delta V(E_F) = 0$. This can then be used to rewrite Eq. (72) as

$$\begin{aligned}\Delta V(E) &= \Delta V(E) - \Delta V(E_F)\\ &= \frac{\mathcal{P}}{\pi} \int_{-\infty}^{\infty} W(E') \left(\frac{1}{E' - E} - \frac{1}{E' - E_F} \right) dE'\\ &= \frac{E - E_F}{\pi} \int_{-\infty}^{\infty} \frac{W(E')}{(E' - E)(E' - E_F)} dE'.\end{aligned} \tag{82}$$

For the Hartree-Fock term we adopt the usual form for $V_V(E)$ given in Eq. (71). The dispersion integrals for the functions for absorption can be calculated analytically and are included as options in ECIS-06. This makes the use of a dispersive optical model parameterization completely equivalent to that of a non-dispersive OMP: the dispersive contributions are calculated automatically once the OMP parameters are given. Upon comparison with a non-dispersive parameterization, we find that v_1 is rather different, as expected, see Refs. [19, 20], and that r_V, a_V, v_2, v_3, w_1 and w_2 are slightly different.

3.1.2 Semi-microscopic JLMB OMP

Besides the above-described phenomenological OMP, it is also possible to perform TALYS calculations with the semi-microscopic nucleon-nucleus spherical OMP derived in Refs. [21–24] from the Brückner–Hartree–Fock approximation using a Reid's hard core nucleon–nucleon interaction. More specifically, the OMP for finite nuclei is obtained by folding the OMP in nuclear matter with the target radial matter density on the basis of the local density approximation. This so-called Jeukenne–Lejeune–Mahaux (JLM) potential has been updated by Bauge et al. [25,26] through an empirical renormalization of the energy dependence of the potential depth in order to reproduce scattering and reaction observables for spherical and quasi-spherical nuclei between ^{40}Ca and ^{209}Bi in a large energy range from the keV region up to 200 MeV. Several prescriptions for the local density approximation were also tested [25] to provide the best overall description of elastic scattering and reaction measurements. The corresponding JLMB energy-dependent parameterization of the nucleon-nucleus depths is Lane consistent (i.e. isospin symmetric) and is characterized by an enhancement of the isovector components with respect to the original JLM approach that is needed in order to account simultaneously for (p, p) and (n, n) elastic scattering as well as $(p, n)_{IAS}$ quasi-elastic scattering to the isobaric analog states. The potential reads

$$\begin{aligned}U(E) &= \lambda_V(E) \left[V_0(\tilde{E}) \pm \lambda_{V1}(E) \alpha V_1(\tilde{E}) \right]\\ &\quad + i\lambda_W(E) \left[W_0(\tilde{E}) \pm \lambda_{W1}(E) \alpha W_1(\tilde{E}) \right],\end{aligned} \tag{83}$$

where $\alpha = (\rho_n - \rho_p)/\rho$ is the density asymmetry and $\rho = \rho_n + \rho_p$ is the total nuclear density of neutrons plus protons. E is the incident projectile energy and $\tilde{E} = E - \mathcal{V}_C$ is the incident energy shifted by the Coulomb potential $\mathcal{V}_C$ for incoming protons only. The energy-dependent parameters λ_V, λ_W, λ_{V1} and λ_{W1} are the real isoscalar, imaginary isoscalar, real isovector, and imaginary isovector potential depth normalization factors, respectively. The energy-dependent expressions for λ_V, λ_{V1}, λ_W, and λ_{W1} can be found in Ref. [26] and are illustrated in Fig. 9. In particular,

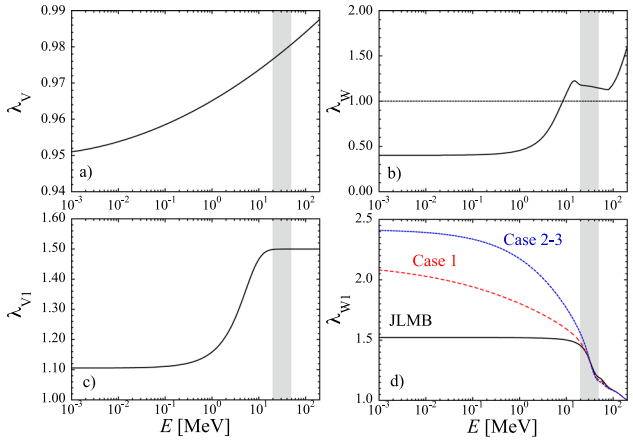

Fig. 9 Energy-dependent parameters **a** λ_V, **b** λ_W, **c** λ_{V1}, and **d** λ_{W1} of the JLMB OMP included in TALYS. The hatched zones represent the 20–50 MeV range of maximum confidence [26]. For the λ_{W1} parameter, 2 variants (Case 1–3) from Ref. [27] are also made available

the λ_{W1} phenomenological expression reads

$$\lambda_{W_1}(E) = \left[1.1 + \omega_1 \left[1 + \left(e^{\frac{E-40}{50.9}}\right)^4\right]^{-1}\right] \times \left[1 - 0.065\, e^{-\left(\frac{E-40}{13}\right)^2}\right] \times \left[1 - 0.083\, e^{-\left(\frac{E-200}{80}\right)^2}\right], \quad (84)$$

with the energy E expressed in MeV. In Eq. (84), ω_1 characterizes the low-energy amplitude for which the value of 0.44 was estimated in Ref. [26].

The resulting JLMB potential and its extension to deformed and unstable nuclei has been widely tested [26,28–31]. As stated in Ref. [26], in the 20 to 50 MeV range, the uncertainties related to λ_V, λ_{V1}, λ_W, and λ_{W1} are estimated to be 1.5%, 10%, 10%, and 10%, respectively. Outside this energy range, uncertainties are estimated to be 1.5 times larger. In the present version of TALYS, only the spherical JLMB OMP is included and feeds the ECIS-06 routine to compute observables by solving the Schrödinger equation for the interaction of the projectile. All JLMB OMP parameters can be altered via adjustable parameters.

However, while most of the JLMB renormalization factors are rather well constrained by experimental data, this is not the case for the isovector λ_{W1} contribution to the imaginary part of the potential at low energies. In the JLMB approach, the major constraint imposed on the OMP isovector component comes from the quasi-elastic (p, n) scattering data as well as the angle-integrated quasi-elastic (p, n) cross sections to the isobaric analog states at energies above some 20 MeV. For lower energies, the λ_{W_1} factor was extrapolated from the confident region around 20 MeV to a constant value of approximately 1.5 (see in particular Fig. 1 of Ref. [26]). Due to the lack of scattering data in the keV region, the low-energy extrapolation of the λ_{W_1} factor remains essentially unconstrained. This drawback was cured by an adjustment on experimental s- and p-wave neutron strength function data between 1 and 100 keV [27]. To reproduce the isospin dependence found in such data and to study the impact on cross sections, three cases corresponding to three modified renormalizations of the JLMB imaginary potential were proposed and included in TALYS, see also Fig. 9,

- Case 1 corresponds to a modified value of λ_{W_1} adopting for the parameter ω_1 the energy dependence $\omega_1 = 1.1\ \exp(-0.4E^{1/4})$ and therefore a λ_{W_1} increase by 30% at 100 keV,
- Case 2 assumes $\omega_1 = 1.25\ \exp(-0.2E^{1/2})$, i.e. a λ_{W_1} about 50% larger than the JLMB value at 100 keV,
- Case 3 corresponds to the same λ_{W_1} as in Case 2, but with a λ_W value, affecting both the isoscalar and isovector parts of the imaginary potential, see Eq. (83) twice larger than the JLMB value for energies below 1 MeV.

The resulting modified JLMB* potential has a drastic impact on the radiative neutron capture cross sections of exotic neutron-rich nuclei for which the isovector component becomes important, see Eq.(83). At large neutron excesses, the imaginary component is indeed reduced, lowering the neutron absorption channel, and consequently the radiative neutron capture cross section and astrophysical rates [27].

3.1.3 Extension to 1 GeV

To be able to predict the total, elastic and non-elastic cross sections up to 1 GeV, the OMP described above has been extended by Koning et al. [32]. It is emphasized here that this was just done to test at which energy the validity of TALYS in predicting other (residual) cross sections would fail. We are well aware of the fact that the usual Schrödinger picture of the OMP is valid up to about 180 MeV, and should then be taken over by a Dirac approach. Nevertheless, a functional form was constructed which leaves all KD03 parameter values below a joining energy E_J, at or around 200 MeV, unaltered while smoothly extending the energy dependence above E_J. This was only applied to the real, V_V, and imaginary, W_V, volume parts of the potential. For that, the KD03 OMP for neutrons below E_J reads [15],

$$V_V(E) = v_1^n[1 - v_2^n(E - E_f^n) + v_3^n(E - E_f^n)^2 - v_4^n(E - E_f^n)^3]$$
$$W_V(E) = w_1^n \frac{(E - E_f^n)^2}{(E - E_f^n)^2 + (w_2^n)^2}, \quad (85)$$

where E_f^n is the Fermi energy. For V_V, we assume that the exponential decrease should continue beyond E_J. After all, the KD03 form of Eq. (85) for V_V is just a Taylor expansion of the exponential function, in which we gave ourselves the freedom to alter the individual coefficients v_1, etc. Also, following studies like those of Typel et al. [33] and Chiba et al. [34], we assume that it converges to a negative value V_∞ at high incident energies. Hence, the form chosen for $E > E_J$ is

$$V_V(E) = V_\infty + b.\exp(-c(E - E_f^n)). \tag{86}$$

We determine the new parameters b and c by calculating the value at $E = E_f^n$, giving

$$b = V_V(E_f^n) - V_\infty. \tag{87}$$

Hence,

$$V_V(E) = V_\infty + (V_V(E_f^n) - V_\infty)\exp(-c(E - E_f^n)). \tag{88}$$

Next, c can be determined by requiring that the high-energy potential is equal to that of the low energy expression Eq. (85) at the joining energy:

$$V_V(E_J) = V_\infty + (V_V(E_f^n) - V_\infty)\exp(-c(E_J - E_f^n)), \tag{89}$$

giving

$$c = -\frac{1}{(E_J - E_f^n)}\log\left(\frac{V_V(E_J) - V_\infty}{V_V(E_f^n) - V_\infty}\right). \tag{90}$$

For W_V it is expected that at high energies new absorption channels, such as pion production, emerge and that W_V will show another smooth increase as function of energy. Hence, the form of W_V for $E > E_J$ is

$$W_V(E) = w_3^n\frac{(E - E_f^n)^4}{(E - E_f^n)^4 + (w_4^n)^4} + d, \tag{91}$$

where we find that a power of 4, instead of the usual 2, gives a better description of experimental data. Also here, a parameter d was added to ensure a value exactly equal to KD03 at E_J, i.e. at $E = E_J$ we have

$$d = W_V(E_J) - w_3^n\frac{(E_J - E_f^n)^4}{(E_J - E_f^n)^4 + (w_4^n)^4} \tag{92}$$

In sum, we have the following extension of the KD03 OMP for $E > E_J$:

$$V_V(E) = V_\infty + (V_V(E_f^n) - V_\infty) \times \exp\left(\frac{E - E_f^n}{E_J - E_f^n}.\log(\frac{V_V(E_J) - V_\infty}{V_V(E_f^n) - V_\infty})\right)$$

$$W_V(E) = W_V(E_J) - w_3^n\frac{(E_J - E_f^n)^4}{(E_J - E_f^n)^4 + (w_4^n)^4} + w_3^n\frac{(E - E_f^n)^4}{(E - E_f^n)^4 + (w_4^n)^4}, \tag{93}$$

which joins smoothly with the KD03 expression of Eq. (85) for $E < E_J$. The following, preliminary, values were obtained from a fit to neutron total and proton non-elastic cross sections up to 1 GeV:

$$\begin{aligned} E_J &= 200. \\ V_\infty &= -30. \\ w_3^n &= 25. - 0.0417A \\ w_4^n &= 250. \end{aligned} \tag{94}$$

All parameters can be adjusted with keywords to provide the best fit for individual nuclides. In Eq. (93), $V_V(E_f)$, $V_V(E_J)$ and $W_V(E_J)$ are obtained from Eq. (85). The above extension, and parameters, also hold for incident protons.

3.2 Deformed OMP: neutrons

By default, TALYS uses the global optical model by Capote et al. [35] for actinides. These parameters are directly retrievable from the RIPL database. For rotational non-fissile nuclides, if no specific potential is specified through one of the various input methods, we take our local or global spherical potential and subtract 15% from the imaginary surface potential parameter d_1, if rotational or vibrational levels are included in the coupling scheme. Again, TALYS provides ample adjustment possibilities to tailor the OMP parameters to available experimental data.

3.3 Spherical OMP: complex particles

As a baseline model, for deuterons, tritons, Helium-3 and alpha particles, we use a simplification of the folding approach of Watanabe [36], see also Madland [37]. We take the KD03 OMPs described in the previous section, either local or global, as the basis for these complex particle potentials. However, as this approach has only been tested to a limited extent with mixed results, in TALYS these OMPs may be overruled by other OMPs, often in restricted energy ranges, which have been published in the past. Below we describe the particular functional form for the potentials from the folding approach for each particle, but also mention other choices for the OMP. Indeed, for deuterons and alpha particles, the default OMP is not the folding potential.

3.3.1 Deuterons

For deuterons, the real central potential depth at incident energy E is

$$V_V^d(E) = V_V^n(E/2) + V_V^p(E/2), \tag{95}$$

and similarly for W_V and W_D. For the spin-orbit potential depth we have

$$V_{SO}^d(E) = (V_{SO}^n(E) + V_{SO}^p(E))/2, \tag{96}$$

and similarly for W_{SO}. For the radius and diffuseness parameters of the real central potential we have

$$\begin{aligned} r_V^d &= (r_V^n + r_V^p)/2, \\ a_V^d &= (a_V^n + a_V^p)/2, \end{aligned} \tag{97}$$

and similarly for the geometry parameters of the other potentials.

We are well aware of the fact that others have constructed specific potentials for deuterons that probably outperform the Watanabe-type potential described here (a systematic study still needs to be done for complex particle potentials). Therefore, we have also added the deuteron potentials of Daehnick et al. [38], Bojowald et al. [39], Han et al. [40], and An et al. [41] as options. The potential of Han et al. is currently the default in TALYS, awaiting an independent comparison of all global OMPs with all available experimental data.

3.3.2 Tritons

For tritons, the real central potential depth at incident energy E is

$$V_V^t(E) = 2V_V^n(E/3) + V_V^p(E/3), \tag{98}$$

and similarly for W_V and W_D. For the spin-orbit potential depth we have

$$V_{SO}^t(E) = (V_{SO}^n(E) + V_{SO}^p(E))/6, \tag{99}$$

and similarly for W_{SO}. For the radius and diffuseness parameters of the real central potential we have

$$\begin{aligned} r_V^t &= (2r_V^n + r_V^p)/3, \\ a_V^t &= (2a_V^n + a_V^p)/3, \end{aligned} \tag{100}$$

and similarly for the geometry parameters of the other potentials.

3.3.3 Helium-3

For Helium-3, the real central potential depth at incident energy E is

$$V_V^h(E) = V_V^n(E/3) + 2V_V^p(E/3), \tag{101}$$

and similarly for W_V and W_D. For the spin-orbit potential depth we have

$$V_{SO}^h(E) = (V_{SO}^n(E) + V_{SO}^p(E))/6, \tag{102}$$

and similarly for W_{SO}. For the radius and diffuseness parameters of the real central potential we have

$$\begin{aligned} r_V^h &= (r_V^n + 2r_V^p)/3, \\ a_V^h &= (a_V^n + 2a_V^p)/3, \end{aligned} \tag{103}$$

and similarly for the geometry parameters of the other potentials.

3.3.4 Alpha particles

For α-particles, within the folding approach [36], the real central potential depth at incident energy E is given by

$$V_V^\alpha(E) = 2V_V^n(E/4) + 2V_V^p(E/4), \tag{104}$$

and similarly for W_V and W_D. No spin-orbit potential is included, so that the depth

$$V_{SO}^\alpha(E) = W_{SO}^\alpha(E) = 0. \tag{105}$$

For the radius and diffuseness parameter of the real central potential we have

$$\begin{aligned} r_V^\alpha &= (r_V^n + r_V^p)/2, \\ a_V^\alpha &= (a_V^n + a_V^p)/2, \end{aligned} \tag{106}$$

and similarly for the geometry parameters of the other potentials.

Additional local or global α-nucleus optical potentials are available and have been included in TALYS. They have been essentially derived from fits to elastic α-nucleus scattering data at energies above $E \simeq 80$ MeV or, in some cases, to (n, α) cross sections at lower energies. These concern in particular the Wood-Saxon-type optical potential of McFadden and Satchler [42], Nolte et al. [43], or Avrigeanu et al. [44]. However, the imaginary component is known to be strongly energy dependent at energies below the Coulomb barrier. For this reason, available α-particle elastic-scattering and reaction cross sections around the Coulomb barrier on medium- and heavy-mass nuclei were used to improve previous global optical potentials, essentially fitted at higher

energies [45,46]. The Avrigeanu et al. Woods-Saxon-type model from 2014 designed for targets with $45 \leq A \leq 209$ mass number is the TALYS default potential.

In contrast to the phenomenological approach, the real component of the potential of Dimitrou et al. [45] is based on the double folding model obtained from a realistic nucleon-nucleon interaction. From this, three different types of energy-dependent imaginary potentials have been constructed from the assumption of volume or surface absorption, or from the adoption of the dispersion relations that link the real and imaginary parts of the potential see Sect. 3.1.1). The three corresponding optical potentials have been constrained in order to reproduce at best scattering and reaction data at energies below typically $E \simeq 20$ MeV and are included in TALYS.

3.4 OMP continuity and parameter adjustment

The original KD03 OMP has been designed to cover the entire 0–200 MeV range. We are well aware of the fact that other OMPs, often designed for more restricted energy or nuclide ranges, may be superior for particular cases. Important examples are deformed OMPs for actinides, and the above mentioned deuteron and alpha OMPs. Since TALYS is designed to produce credible results for its entire energy and nuclide domain, we need to ensure a smooth transition between an OMP for a restricted energy range to an OMP for the entire energy range. Since we always have the KD03 or KD03-based folding potentials as a baseline, we have built in an interpolation scheme for any alternative OMP and the KD03 OMP. In practice, we join all 18 OMP parameters smoothly from the alternative OMP and KD03, using a sufficiently large energy interval in which the interpolation takes place. In general, we set two energies, E_A, up to which the alternative OMP (alt) is completely adopted and E_B, after which the KD03 OMP is completely adopted. Then the OMP parameters at any energy become

$$\begin{aligned} V_V(E) &= R.V^{\mathrm{alt}}(E) + (1-R).V^{\mathrm{KD03}}(E) \\ r_V(E) &= R.r_V^{\mathrm{alt}}(E) + (1-R).r_V^{\mathrm{KD03}}(E) \\ &\ldots \end{aligned} \tag{107}$$

where

$$\begin{aligned} &R = 1 \quad \text{for} \quad E < E_A, \\ &R = 1 - \frac{E - E_A}{E_B - E_A} \quad \text{for} \quad E_A \leq E \leq E_B, \\ &R = 0 \quad \text{for} \quad E > E_B. \end{aligned} \tag{108}$$

The above mechanism is for example used for an extension of the alpha OMP of Avrigeanu which is known to perform well up to 25 MeV, and for that OMP we set $E_A = 25$ MeV and $E_B = 50$ MeV, which is a large enough energy range to ensure a smooth transition between both OMPs.

All optical model parameters can be altered via adjustable parameters with which the standard values can be multiplied. Also local energy-dependent adjustment of the geometry is possible to fit data. Such adjustment is already implicit in the dispersive OMPs that we use, and therefore theoretically justified, although an ad-hoc arbitrary energy-dependent form of e.g. the radius and diffuseness parameters in practice means one uses TALYS as a very complicated fitting function for the sake of reproducing experimental data. Hence, this is only applied as a last resort.

4 Direct reactions

Various models for direct reactions are included in the program: DWBA for (near-)spherical nuclides, coupled-channels for deformed nuclides, the weak-coupling model for odd nuclei, and also a giant resonance contribution in the continuum. In all cases, TALYS drives the ECIS-06 code to perform the calculations. The results are presented as discrete state cross sections and angular distributions, or as contributions to the continuum.

4.1 Distorted Wave Born Approximation

The DWBA is only valid for small deformations. Until the emergence of the more general coupled-channels formalism, it was the common method to describe inelastic scattering, for both weakly and strongly coupled levels. Nowadays, we see DWBA as a first order vibrational model for near-spherical nuclides, with only a single iteration to be performed for the coupled-channels solution. (See, however Satchler [47] for the exact difference between this so-called distorted wave method and DWBA). The interaction between the projectile and the target nucleus is modeled by the derivative of the OMP for elastic scattering times a strength parameter. The latter, the deformation parameter β_λ, is then often used to vary the overall magnitude of the cross section, which is proportional to β_λ^2.

In TALYS, we use DWBA

(a) if a deformed OMP and a coupling scheme is not available. This applies for the spherical OMPs mentioned in the previous section, which are all based on elastic scattering observables only. Hence, if we have not constructed a coupled-channels potential, TALYS will automatically use tabulated or systematical deformation parameters for DWBA calculations.
(b) if a deformed OMP is used for the first excited states only. For the levels that do not belong to that basic coupling scheme, e.g. for the many states at somewhat higher excitation energy, we use DWBA with (very) small deformation parameters.

4.2 Deformed nuclei: Coupled channels

The formalism outlined for the spherical OMP (Sect. 3) and DWBA (Sect. 4.1) works theoretically for nuclides which are spherical and in practice for nuclides which are not too strongly deformed. In general, however, the more general coupled-channels method should be invoked to describe simultaneously the elastic scattering channel and the low-lying states which are, due to their collective nature, strongly excited by inelastic scattering. These collective excitations can be described as the result of static or dynamic deformations, which cause the homogeneous neutron-proton fluid to rotate or vibrate. The associated deformation parameters can be predicted from a (semi-)microscopic model or can be derived from an analysis of the experimental angular distributions.

We already discussed the OMPs which are required to describe reactions on deformed nuclides. These OMPs need to be combined with a particular coupling scheme. The coupled-channels formalism for scattering and reaction studies is well known and will not be described here. For a detailed presentation, we refer to Tamura [48]. We will only state the main aspects here to put the formalism into practice. The analyses of Delaroche et al. [49] and Olsson et al. [50] have been used as guidance, as these papers explain clearly how to translate collective effects of various nuclides into ECIS calculations. In general various different channels, usually the ground state and several inelastic states, are included in a coupling scheme while the associated coupled equations are solved. In ECIS-06, this is done in a so-called sequential iterative approach by Raynal [5]. Besides Ref. [5], Carlson's lecture [51] is also recommended for more insight in the use of the ECIS code.

Various collective models for deformed nuclei exist. Note that the spherical optical model of Eq. (67) is described in terms of the nuclear radius $R_i = r_i A^{1/3}$. For deformed nuclei, this expression is generalized to include collective motions. Various models have been implemented in ECIS-06, which enables us to cover many nuclides of interest. We mention here that this does not exhaust all the possible coupled-channels models that currently exist. For example, the soft-rotor model as implemented in the OPTMAN code [52], which has been successfully applied to describe various deformed nuclides and especially actinides, is not covered by ECIS-06 and therefore not available here (as long as we do not implement the OPTMAN code as an option in TALYS). Hence, we will only describe the ones that can be invoked by TALYS. The collective models are automatically applied upon reading the deformation parameter database and coupling scheme, see Sect. 10.

4.2.1 Symmetric rotational model

In the symmetric rotational model, the radii of the different terms of the OMP are expressed as

$$R_i = r_i A^{1/3} \left[1 + \sum_{\lambda=2,4,....} \beta_\lambda Y_\lambda^0(\Omega) \right], \tag{109}$$

where the β_λ's are permanent, static deformation parameters, and the Y functions are spherical harmonics. The quadrupole deformation β_2 plays a leading role in the interaction process. Higher order deformations β_λ (with $\lambda = 4, 6, ...$) are systematically smaller in magnitude than β_2. The inclusion of β_4 and β_6 deformations in coupled-channels calculations produces changes in the predicted observables, but in general, only β_2 and β_4 are important in describing inelastic scattering to the first few levels in a rotational band. For even-even nuclides like ^{184}W and ^{232}Th, the symmetric rotational model provides a good description of the lowest 0^+, 2^+, 4^+, 6^+, 8^+, … rotational band. The nuclear model and parameter database of TALYS specifies whether a rotational model can be used for a particular nucleus, together with the included coupled levels and deformation parameters. Either a deformation parameter β_λ or a deformation length $\delta_\lambda = \beta_\lambda r_i A^{1/3}$ may be given. The latter one is generally recommended since it should not depend on incident energy (while r_i may, in some optical models, depend on energy). We take δ_λ equal for the three OMP components V_V, W_V and W_D and take the spin-orbit potential undeformed. The same holds for the vibrational and other collective models.

4.2.2 Harmonic vibrational model

A vibrational nucleus possesses a spherically symmetric ground state. Its excited states undergo shape oscillations about the spherical equilibrium shape. In the harmonic vibrational model, the radii of the different terms of the OMP are expressed as

$$R_i = r_i A^{1/3} \left[1 + \sum_{\lambda\mu} \alpha_{\lambda\mu} Y_\lambda^\mu(\Omega) \right], \tag{110}$$

where the $\alpha_{\lambda\mu}$ operators can be related to the coupling strengths β_λ, describing the vibration amplitude with multipolarity λ. Expanding the OMP to first or second order with this radius gives the OMP expressions for the excitation of one-phonon (first order vibrational model) and two-phonon (second order vibrational model) states [5]. For vibrational nuclei, the minimum number of states to couple is two. For even-even nuclei, we generally use the $(0^+, 2^+)$ coupling, where the 2^+ level is a one-quadrupole phonon excitation. The level scheme of a vibrational nucleus (e.g. ^{110}Pd)

often consists of a one-phonon state (2^+) followed by a (0^+, 2^+, 4^+) triplet of two-phonon states. When this occurs, all levels are included in the coupling scheme with the associated deformation length δ_2 (or deformation parameter β_2). If the 3^- and 5^- states are strongly collective excitations, that is when β_3 and β_5 are larger than 0.1, these levels may also be included in the coupling scheme. An example is ^{120}Sn [53], where the low lying (0^+, 2^+, 3^-, 4^+, 5^-) states can all be included as one-phonon states in a single coupling scheme.

4.2.3 Vibration-rotational model

For certain nuclides, the level scheme consists not only of one or more rotational bands, but also of one or more vibrational bands that can be included in the coupling scheme. An example is ^{238}U, where many vibrational bands can be coupled [54,55]. Depending on the number of levels included, the calculations can be time-consuming.

4.2.4 Asymmetric rotational model

In the asymmetric rotational model, in addition to the spheroidal equilibrium deformation, the nucleus can oscillate such that ellipsoidal shapes are produced. In this model the nucleus has rotational bands built on the statically deformed ground state and on the γ-vibrational state. The radius is now angular dependent,

$$R_i(\Theta) = r_i A^{1/3}[1 + \beta_2 \cos\gamma Y_2^0(\Omega) + \sqrt{\frac{1}{2}}\beta_2 \sin\gamma (Y_2^2(\Omega) + Y_2^{-2}(\Omega)) + \beta_4 Y_4^0(\Omega)], \quad (111)$$

where we restrict ourselves to a few terms. The deformation parameters β_2, β_4 and γ need to be specified. ^{24}Mg is an example of a nucleus that can be analyzed with the asymmetric rotational model. Mixing between bands is not yet automated as an option in TALYS.

4.3 Odd nuclei: Weak coupling

Direct inelastic scattering off odd-A nuclei can be described by the weak-coupling model [56], which assumes that a valence particle or hole interacts only weakly with a collective core excitation. Hence the model implies that the nucleon inelastic scattering by the odd-A nucleus is very similar to that by the even core alone, i.e. the angular distributions have a similar shape. Let L be the spin of the even core state, and J_0 and J the spin of the ground and excited states, respectively, of the odd-A nucleus, resulting from the angular momentum coupling. Then, the spins J of the multiplet states in the odd-A nucleus range from $\mid L - J_0 \mid$ to $(L + J_0)$. If the strength of the inelastic scattering is characterized by the square of the deformation parameters $\beta^2_{L,J}$, then the sum of all $\beta^2_{L,J}$ or $\sigma(E)$ for the transitions in the odd-A nucleus should be equal to the value β^2_L or $\sigma(E)$ for the single transition in the even core nucleus:

$$\sum_J \beta^2_{L,J} = \beta^2_L, \quad \sum_J \sigma_{J_0 \to J} = \sigma_{0 \to L}, \quad (112)$$

where the symbol $0 \to L$ indicates a transition between the ground state to the excited state with spin L in the even core nucleus. The deformation parameters $\beta^2_{L,J}$ are now given by

$$\beta^2_{L,J} = \frac{2J+1}{(2J_0+1)(2L+1)}\beta^2_L. \quad (113)$$

In practice, the DWBA cross sections are calculated for the real mass of the target nucleus and at the exact excitation energies of the odd-A states, but for the even-core spin L and with deformation parameters $\beta_{L,J}$.

We stress that our weak-coupling model is not full-proof. First of all, there are always two choices for the even-even core. The default used in TALYS is to use the even-even core obtained by subtracting a nucleon, but the other choice, to obtain the even-even core by adding a nucleon, may sometimes be more appropriate. The next uncertainty is the choice of levels in the odd-A core. We select the levels that are the closest to the excitation energy of the even-spin state of the even-even core.

4.4 Giant resonances

The high-energy part of the continuum spectra are generally described by pre-equilibrium models. These models are essentially of a single-particle nature. Upon inspection of continuum spectra, some structure in the high-energy tail is observed that cannot be accounted for by the smooth background of the single-particle pre-equilibrium model. For example, many 14 MeV inelastic neutron spectra show a little hump at excitation energies around 6–10 MeV. This structure is due to collective excitations of the nucleus that are known as giant resonances [57,58]. We use a macroscopic, phenomenological model to describe giant resonances in the inelastic channel. For each multipolarity, an energy-weighted sum rule (EWSR) S_ℓ applies,

$$S_\ell = \sum_i E_{\ell,i}\beta^2_{\ell,i} = 57.5A^{-5/3}l(2l+1) \quad \text{MeV}, \quad (114)$$

where $E_{\ell,i}$ is the excitation energy of the i-th state with multipolarity ℓ. The summation includes all the low-lying collective states, for each ℓ, that have already been included in the coupled-channels or DWBA formalism. The EWSR thus determines the remaining collective strength that is spread over the continuum. Our treatment is phenomenological in the sense that we perform a DWBA calculation with ECIS-06

for each giant resonance state and spread the cross section over the continuum with a Gaussian distribution of width $\Gamma_{\rm Gauss} = 0.42\Gamma_\ell$, where the Γ_ℓ for each multipolarity are given below. The central excitation energy for these states and the spreading width is different for each multipolarity and has been empirically determined. For the giant monopole resonance (GMR) EWSR we have

$$S_0 = 23A^{-5/3} \ \text{MeV}, \tag{115}$$

with excitation energy and width

$$\begin{aligned} E_{0,GMR} &= 18.7 - 0.025A \ \text{MeV}, \\ \Gamma_{GMR} &= 3 \ \text{MeV}. \end{aligned} \tag{116}$$

The EWSR for the giant quadrupole resonance (GQR) is

$$S_2 = 575A^{-5/3} \ \text{MeV}, \tag{117}$$

with

$$\begin{aligned} E_{0,GQR} &= 65A^{-1/3} \ \text{MeV}, \\ \Gamma_{GQR} &= 85A^{-2/3} \ \text{MeV}. \end{aligned} \tag{118}$$

The EWSR for the giant octupole resonance is

$$S_3 = 1208A^{-5/3} \ \text{MeV}, \tag{119}$$

which has a low-energy (LEOR) and a high-energy (HEOR) component. Following Kalbach [58], we assume

$$S_{3,LEOR} = 0.3S_3, \quad S_{3,HEOR} = 0.7S_3, \tag{120}$$

with excitation energy and width

$$\begin{aligned} E_{0,LEOR} &= 31A^{-1/3} \ \text{MeV}, \\ \Gamma_{LEOR} &= 5 \ \text{MeV}, \end{aligned} \tag{121}$$

and

$$\begin{aligned} E_{0,HEOR} &= 115A^{-1/3} \ \text{MeV}, \\ \Gamma_{HEOR} &= 9.3 - A/48 \ \text{MeV}, \end{aligned} \tag{122}$$

respectively.

The contribution from giant resonances is automatically included in the total inelastic cross section. The effect is most noticeable in the single- and double-differential energy spectra.

5 Compound nucleus reactions

The term compound nucleus reaction is often used for two different mechanisms: (i) the process of the capture of the projectile in the target nucleus to form a compound nucleus, which subsequently emits a particle or gamma, (ii) the multiple emission process of highly excited residual nuclei formed after the binary reaction. The latter, which is known as multiple compound emission, will be explained in Sect. 8. In either case, the basic description is given by the Hauser-Feshbach model [59]. We first treat the binary compound nucleus reaction that plays a role at low incident energy. It differs from the multiple compound emission at two important points: (a) the presence of width fluctuation corrections (WFC) and (b) non-isotropic, though still symmetric, angular distributions.

5.1 Binary compound cross section and angular distribution

In the compound nucleus picture, the projectile and the target nucleus form a compound nucleus with a total energy E^{tot} and a range of values for the total spin J and parity Π. The following energy, angular momentum and parity conservation laws need to be obeyed,

$$\begin{aligned} E_a + E_x + S_a &= E_{a'} + E_{x'} + S_{a'} = E^{tot} \\ s + I + l &= s' + I' + l' = J \\ \pi_0\Pi_0(-1)^l &= \pi_f\Pi_f(-1)^{l'} = \Pi. \end{aligned} \tag{123}$$

The Hauser-Feshbach formula for the binary cross section is given by

$$\begin{aligned} \sigma^{comp}_{\alpha\alpha'} = D^{comp}\frac{\pi}{k^2} &\sum_{J=mod(I+s,1)}^{l_{max}+I+s} \sum_{\Pi=-1}^{1} \frac{2J+1}{(2I+1)(2s+1)} \\ &\times \sum_{j=|J-I|}^{J+I} \sum_{l=|j-s|}^{j+s} \sum_{j'=|J-I'|}^{J+I'} \sum_{l'=|j'-s'|}^{j'+s'} \delta_\pi(\alpha)\delta_\pi(\alpha') \\ &\times \frac{T^J_{\alpha l j}(E_a)\left\langle T^J_{\alpha' l' j'}(E_{a'})\right\rangle}{\sum_{\alpha'',l'',j''}\delta_\pi(\alpha'')\left\langle T^J_{\alpha'' l'' j''}(E_{a''})\right\rangle} W^J_{\alpha l j \alpha' l' j'}, \end{aligned} \tag{124}$$

where all the symbols are defined in Table 1. Note that the formula automatically applies to (isomeric) target states, which is made explicit by the target excitation energy E_x in Eq. (123). In order to let Eq. (124) represent the general case, we have denoted the outgoing transmission coefficient by $\left\langle T^J_{\alpha' l' j'}\right\rangle$. For this, two cases can be distinguished. If the excitation energy $E_{x'}$, that is implicit in the definition of channel α', corresponds to a discrete state of the final nucleus, then we simply have

$$\left\langle T^J_{\alpha' l' j'}(E_{a'})\right\rangle = T^J_{\alpha' l' j'}(E_{a'}), \tag{125}$$

and $E'_{a'}$ is exactly determined by Eq. (123). For α' channels in which $E_{x'}$ is in the continuum, we have an effective transmission coefficient for an excitation energy bin with width

Table 1 Description of the symbols entering Eq. (124)

E_a	Projectile energy
s	Spin of the projectile
π_0	Parity of the projectile
l	Orbital angular momentum of the projectile
j	Total angular momentum of the projectile
$\delta_\pi(\alpha)$	1, if $(-1)^l \pi_0 \Pi_0 = \Pi$ and 0 otherwise
α	Channel designation of the initial system of projectile and target nucleus: $\alpha = \{a, s, E_a, E_x, I, \Pi_0\}$, where a is the projectile type
E_x	Excitation energy of the target nucleus (usually zero)
l_{max}	Maximum l-value for projectile, determined by OMP
S_a	Separation energy
$E_{a'}$	Ejectile energy
s'	Spin of the ejectile
π_f	Parity of the ejectile
l'	Orbital angular momentum of the ejectile
j'	Total angular momentum of the ejectile
$\delta_\pi(\alpha')$	1, if $(-1)^{l'} \pi_f \Pi_f = \Pi$ and 0 otherwise
α'	Channel designation of the final system of ejectile and residual nucleus: $\alpha' = \{a', s', E_{a'}, E_{x'}, I', \Pi_f\}$, where a' is the ejectile type
$E_{x'}$	Excitation energy of the residual nucleus
I	Spin of the target nucleus
Π_0	Parity of the target
I'	Spin of the residual nucleus
Π_f	Parity of the residual nucleus
Π	Parity of the compound system
J	Total angular momentum of the compound system
D^{comp}	Depletion factor to account for direct and Pre-equilibrium effects
k	Wave number of relative motion
T	Transmission coefficient
W	WFC factor

$\Delta E_{x'}$,

$$\left\langle T^J_{\alpha' l' j'}(E_{a'}) \right\rangle = \int_{E_{x'}-\frac{1}{2}\Delta E_{x'}}^{E_{x'}+\frac{1}{2}\Delta E_{x'}} dE_{x''} \rho(E_{x''}, J, \Pi) \times T^J_{\alpha' l' j'}(E_{a'}), \quad (126)$$

where ρ is the level density, see Sect. 11, and T is evaluated at an emission energy $E_{a'}$ that corresponds to the middle of the excitation energy bin, i.e. $E_{a'} = E^{tot} - E_{x'} - S_{a'}$. Hence, both transitions to discrete states and transitions to the whole accessible continuum are covered by the sum over α' in Eq. (124). The normalization factor D^{comp} is

$$D^{comp} = [\sigma_{reac} - \sigma^{disc,direct} - \sigma^{\text{preeq}}]/\sigma_{reac}. \quad (127)$$

This indicates that in the current version of TALYS we assume that direct and compound contributions can be added separately. This formula for D^{comp} is only applied for weakly coupled channels that deplete the flux, such as contributions from DWBA or pre-equilibrium reactions. In the case of coupled-channels calculations for the discrete collective states, the transmission coefficients of Eq. (124) are automatically reduced to account for direct effects and TALYS only subtracts the direct cross section for the weakly coupled levels (DWBA) and the pre-equilibrium component, i.e. if

$$\sigma^{disc,direct} = \sigma^{disc,cc} + \sigma^{disc,DWBA}, \quad (128)$$

then

$$D^{comp} = [\sigma_{reac} - \sigma^{disc,DWBA} - \sigma^{\text{preeq}}]/\sigma_{reac}. \quad (129)$$

The compound nucleus formula for the angular distribution is given by

$$\frac{d\sigma^{comp}_{\alpha\alpha'}(\theta)}{d\Omega} = \sum_L C^{comp}_L P_L(\cos\Theta), \quad (130)$$

where P_L are Legendre polynomials. The Legendre coefficients C^{comp}_L are given by

$$C^{comp}_L = D^{comp} \frac{\pi}{k^2} \sum_{J,\Pi} \frac{2J+1}{(2I+1)(2s+1)} \times \sum_{j=|J-I|}^{J+I} \sum_{l=|j-s|}^{j+s} \sum_{j'=|J-I'|}^{J+I'} \sum_{l'=|j'-s'|}^{j'+s'} \times \delta_\pi(\alpha)\delta_\pi(\alpha') \times \frac{T^J_{\alpha l j}(E_a) \left\langle T^J_{\alpha' l' j'}(E_{a'}) \right\rangle}{\sum_{\alpha'', l'', j''} \delta_\pi(\alpha'') \left\langle T^J_{\alpha'' l'' j''}(E_{a''}) \right\rangle} \times W^J_{\alpha l j \alpha' l' j'} A^J_{I l j I' l' j'; L}, \quad (131)$$

where the Blatt-Biedenharn factor A is given by [60]

$$A^J_{I l j I' l' j'; L} = \frac{(-1)^{I'-s'-I+s}}{4\pi} (2J+1)(2j+1) \times (2l+1)(2j'+1)(2l'+1)\,(l l 0 0 \mid L 0) \times \mathcal{W}(J j J j; I L)\mathcal{W}(j j l l; L s)\left(l' l' 0 0 \mid L 0\right) \times \mathcal{W}(J j' J j'; I' L)\mathcal{W}(j' j' l' l'; L s'), \quad (132)$$

where $(\quad \mid \quad)$ are Clebsch-Gordan coefficients and $\mathcal{W}$ are Racah coefficients.

Formulae (124) and (130–132) show that the WFC factors and the angular distribution factors depend on all the angular momentum quantum numbers involved, and thus have to be re-evaluated each time inside all the summations. We generally need these formulae for relatively low incident energy,

where the WFC has a significant impact and where the compound nucleus cross section to each individual discrete state is large enough to make its angular distribution of interest. For projectile energies above several MeV (we generally take the neutron separation energy for safety), the width fluctuations have disappeared, meaning that $W^J_{\alpha l j \alpha' l' j'} = 1$ for all channels. Then for the angle-integrated compound cross section, instead of performing the full calculation, Eq. (124) can be decoupled into two parts that represent the incoming and outgoing reaction flux, respectively. It simplifies to

$$\sigma^{comp}_{\alpha\alpha'} = \sum_{J=mod(I+s,1)}^{l_{max}+I+s} \sum_{\Pi=-1}^{1} \sigma^{CF}_{J\Pi}(E^{tot}) \times \frac{\Gamma_{\alpha'}(E^{tot}, J, \Pi \longrightarrow E_{x'}, I', \Pi_f)}{\Gamma^{tot}(E^{tot}, J, \Pi)}, \tag{133}$$

where $\sigma^{CF}_{J\Pi}$ is the compound formation cross section per spin and parity:

$$\sigma^{CF}_{J\Pi}(E^{tot}) = D^{comp} \frac{\pi}{k^2} \frac{2J+1}{(2I+1)(2s+1)} \times \sum_{j=|J-I|}^{J+I} \sum_{l=|j-s|}^{j+s} T^J_{\alpha l j}(E_a) \delta_\pi(\alpha), \tag{134}$$

which itself obeys

$$\sum_{J=mod(I+s,1)}^{l_{max}+I+s} \sum_{\Pi=-1}^{1} \sigma^{CF}_{J\Pi}(E^{tot}) = D^{comp} \sigma_{reac}. \tag{135}$$

The partial decay widths are

$$\Gamma_{\alpha'}(E^{tot}, J, \Pi \longrightarrow E_{x'}, I', \Pi_f) = \frac{1}{2\pi\rho(E^{tot}, J, \Pi)} \times \sum_{j'=|J-I'|}^{J+I'} \sum_{l'=|j'-s'|}^{j'+s'} \delta_\pi(\alpha') \left\langle T^J_{\alpha' l' j'}(E'_{a'}) \right\rangle, \tag{136}$$

and the total decay width is

$$\Gamma^{tot}(E^{tot}, J, \Pi) = \sum_{\alpha''} \Gamma_{\alpha''}(E^{tot}, J, \Pi \longrightarrow E_{x'}, I'', \Pi_f), \tag{137}$$

where we sum over all possible states in the residual nuclides through the sum over α''. Note that the term with the compound nucleus level density, $2\pi\rho$, is present in both Eqs. (136) and (137) and therefore does not need to be calculated in practice for Eq. (133). A formula similar to Eq. (133) is used for multiple emission, see Sect. 8.

In sum, we use Eqs. (124) and (131) if either width fluctuations or compound angular distributions are to be calculated and the more time-efficient Eq. (133) if they are both of no interest.

5.2 Width fluctuation correction factor

The WFC factor W accounts for the correlations that exist between the incident and outgoing waves. From a qualitative point of view, these correlations enhance the elastic channel and accordingly decrease the other open channels. We are aware that a more complete description of the WFC mechanism requires inclusion of the Engelbrecht-Weidenmüller transformation which includes direct-compound reaction interference, see Refs. [61,62]. This is under construction. Above a few MeV of projectile energy, when many competing channels are open, the WFC factor can be neglected and the simple Hauser-Feshbach model is adequate to describe the compound nucleus decay. To explain the WFC factors, we now switch to a more compact notation in which we leave out J and define $a = \{\alpha, l, j\}$ and $b = \{\alpha', l', j'\}$. With such a notation the compound nucleus cross section can be written in the compact form

$$\sigma_{ab} = \frac{\pi}{k_a^2} \frac{T_a T_b}{\sum_c T_c} W_{ab}, \tag{138}$$

for each combination of a and b. In general, the WFC factor may be calculated using three different expressions, which have all been implemented in TALYS: The Hofmann-Richert-Tepel-Weidenmüller (HRTW) model [63–65], the Moldauer model [66,67], and the model using the Gaussian Orthogonal Ensemble (GOE) of Hamiltonian matrices [68]. A comparison between the three models is given by Hilaire et al. [69].

For each expression, flux conservation implies that

$$T_a = \sum_b \frac{T_a T_b}{\sum_c T_c} W_{ab}. \tag{139}$$

This equation can be used to check the numerical accuracy of the WFC calculation.

5.2.1 The HRTW method

The simplest approach is the HRTW method. It is based on the assumption that the main effect of the correlation between incident and outgoing waves is in the elastic channel. In that case, it is convenient to express the compound nucleus cross section (138) as

$$\sigma_{ab} = \frac{\pi}{k^2} \frac{V_a V_b}{\sum_c V_c} \left[1 + \delta_{ab}(W_a - 1)\right], \tag{140}$$

where the V_i's are effective transmission coefficients that take into account the correlations.

This expression means that only the elastic channel enhancement is described since for $a = b$, Eq. (140) becomes

$$\sigma_{aa} = \frac{\pi}{k_a^2} \frac{V_a^2}{\sum_c V_c} W_a, \tag{141}$$

while for $a \neq b$,

$$\sigma_{ab} = \frac{\pi}{k_a^2} \frac{V_a V_b}{\sum_c V_c}. \tag{142}$$

An expression for the V_i values can be determined from the flux conservation condition

$$\sum_b \sigma_{ab} = \frac{\pi}{k_a^2} T_a, \tag{143}$$

which yields using Eq. (140)

$$T_a = V_a + (W_a - 1) \frac{V_a^2}{\sum_c V_c}, \tag{144}$$

or

$$V_a = \frac{T_a}{1 + \frac{(W_a - 1) V_a}{\sum_c V_c}}. \tag{145}$$

The only required information is thus the expression for W_a, which can be derived from an analysis using random matrix calculations. In TALYS, the expression of Ref. [65] is used. The result for V_a is then obtained after iterating Eq. (145) several times, starting from the initial value

$$V_a(i = 0) = \frac{T_a}{1 + (W_a - 1) \frac{T_a}{\sum_c T_c}}, \tag{146}$$

and calculating $V_a(i + 1)$ using

$$V_a(i + 1) = \frac{T_a}{1 + (W_a - 1) \frac{V_a(i)}{\sum_c V_c(i)}}, \tag{147}$$

until $V_a(i + 1) \approx V_a(i)$. In a calculation, a few tens of iterations are generally required to reach a stable result.

For each J and Π, expressions (145)–(147) only need to be evaluated once. The WFC factor can then be derived from Eqs. (138) and (140),

$$W_{ab} = \frac{V_a V_b}{\sum_c V_c} [1 + \delta_{ab}(W_a - 1)] \frac{\sum_c T_c}{T_a T_b}. \tag{148}$$

5.2.2 Moldauer expression

This is the default option for the WFC in TALYS. Moldauer's expression for W_{ab} is based on the assumption that a χ^2 law with ν degrees of freedom applies for the partial widths Γ, which can be calculated from a Porter-Thomas distribution. These are associated with transmission coefficients as

$$T = \frac{2\pi \langle \Gamma \rangle}{D}, \tag{149}$$

provided $\langle \Gamma \rangle << D$, where D is the mean level spacing. The WFC factor W_{ab} reads

$$W_{ab} = \left(1 + \frac{2\delta_{ab}}{\nu_a}\right) \times \int_0^{+\infty} \prod_c \left(1 + \frac{2T_c\, x}{\nu_c \sum_i T_i}\right)^{-(\delta_{ac} + \delta_{bc} + \nu_c/2)} dx, \tag{150}$$

Moldauer has parameterised ν using Monte Carlo calculations, giving

$$\nu_a = 1.78 + \left(T_a^{1.212} - 0.78\right) \exp\left(-0.228 \sum_c T_c\right). \tag{151}$$

Also, alternative parameterizations for ν_a are included in TALYS, notably that of Ernebjerg and Herman [70] and Kawano and Talou [71]. The integral in Eq. (150) is evaluated numerically. For this, the Gauss-Laguerre method is used and we find that 40 integration points are enough to reach convergence, the criterion being the flux conservation of Eq. (139).

Equation (150) involves a product over all possible open channels. When the number of channels is large, the product calculation drastically increases the time of computation, forcing us to consider another method. Many open channels are considered for capture reactions and reactions to the continuum.

A. Capture reactions

If the projectile is captured by the target nucleus, the compound nucleus is formed with an excitation energy at least equal to the projectile separation energy in the compound system. Since the γ transmission coefficient calculation involves all the possible states to which a photon can be emitted from the initial compound nucleus state, the number of radiative open channels is almost infinite, but each has a very small transmission coefficient. Following Ref. [72], the product over the radiative channels in Eq. (150) can be transformed as

$$\prod_{c \in \gamma} \left(1 + \frac{2T_c\, x}{\nu_c \sum_i T_i}\right)^{-\nu_c/2}$$

$$\approx \lim_{\nu_\gamma \to +\infty} \left(1 + \frac{2T_\gamma\, x}{\bar{\nu}_\gamma \sum_i T_i}\right)^{-\bar{\nu}_\gamma/2} = \exp\left(-\frac{T_\gamma^{eff}\, x}{\sum_i T_i}\right), \tag{152}$$

where T_γ^{eff} is given by the procedure sketched in Sect. 12. The derivation is based on the hypothesis that all the individual T_γ are almost identical to 0. Therefore, to calculate W_{ab} when b denotes the gamma channel, we set $T_b = 0$ in Eqs. (150) and use Eqs. (152) to calculate the product for γ channels.

B. Continuum reactions

For high excitation energies, it is impossible to describe all the open channels individually. It is then necessary to introduce energy bins to discretize the continuum of levels and define continuum (or effective) transmission coefficients as

$$T_{eff}(U) = \int_{E_{min}}^{E_{max}} \rho(\varepsilon) T(\varepsilon) d\varepsilon, \tag{153}$$

where U is generally taken as the middle of the interval $[E_{min}, E_{max}]$ and ρ is the density of levels under consideration. This effective transmission coefficient corresponds to an effective number of channels $N_{eff}(U)$, given by

$$N_{eff}(U) = \int_{E_{min}}^{E_{max}} \rho(\varepsilon) d\varepsilon. \tag{154}$$

Calculating the product term in Eq. (150) is tedious, unless one assumes that the energy variation of $T(\varepsilon)$ is smooth enough to warrant that each of the $N_{eff}(U)$ channels has the same average transmission coefficient

$$T_{mean}(U) = \frac{T_{eff}(U)}{N_{eff}(U)}. \tag{155}$$

Then, the product over the channels c belonging to such a continuum bin in the Moldauer integral Eq. (150) can be replaced by a single term, i.e.

$$\prod_c \left(1 + \frac{2T_c}{\nu_c \sum_i T_i} x\right)^{-\nu_c/2} \approx \left(1 + \frac{2T_{mean}(U)}{\nu_{mean} \sum_i T_i} x\right)^{-N_{eff}(U)\nu_{mean}/2}, \tag{156}$$

where

$$\nu_{mean} = 1.78 + \left(T_{mean}^{1.212} - 0.78\right) \exp\left(-0.228 \sum_c T_c\right). \tag{157}$$

C. Fission reactions

The fission reaction is treated as one global channel, regardless of the nature of the fission fragments that result from fission. In Sect. 13, it is explained how the global fission transmission coefficient is calculated. It is however important to state here that the fission transmission coefficient is generally greater than 1 since it results from a summation over several fission paths and can therefore be defined as

$$T_{fis}(U) = \int_{E_{min}}^{E_{max}} \rho_{fis}(\varepsilon) T_f(\varepsilon) d\varepsilon. \tag{158}$$

Of course, $0 \leq T_f(\varepsilon) \leq 1$, but one cannot assume that T_f is constant over the whole integration energy range as in the case of continuum reactions. To bypass this problem, instead of using a global fission transmission coefficient, we have grouped the various components of Eq. (158) according to their values. Instead of dealing with a global fission transmission coefficient, we use N different global transmission coefficients (where N is an adjustable parameter) such that

$$T_{fis}(U) = \sum_{i=0}^{N} T_{fis}(i, U), \tag{159}$$

where

$$T_{fis}(i, U) = \int_{E_{min}}^{E_{max}} \rho_{fis}(\varepsilon) T_f(\varepsilon) \delta_{i,N} d\varepsilon, \tag{160}$$

and $\delta_{i,N} = 1$ if $i/N \leq T_f(\varepsilon) \leq (i+1)/N$ and 0 otherwise.

In this case one can define, as for continuum reactions, an effective number of channels $N_{fis}(i, U)$, and use N average fission transmission coefficients defined by

$$T_{fismean}(i) = \frac{T_{fis}(i, U)}{N_{fis}(i, U)}. \tag{161}$$

If N is large enough, these N average coefficients can be used for the WFC calculation without making a too crude approximation.

5.2.3 The GOE triple integral

The two previously described methods to obtain W_{ab} are readily obtained since both are relatively simple to implement. However, in each case, a semi-empirical parameterisation is used. The GOE formulation avoids such a parameterisation, in which sense it is a more general expression. We refer to the numerical method employed to compute this complicated triple integral to Hilaire et al. [69]. An important conclusion from that paper is that for most cases, the Moldauer expression gives a very good approximation to the

exact GOE result. This is important since a GOE calculation is very time consuming.

5.3 Thermal and resonance energy range

The introduction of this paper states that TALYS is meant for the analysis of data up to 200 MeV. To be more precise, we should state that the *physics* implemented in TALYS starts to be applicable after a few keV, or more accurately, above the resolved resonance range. The energy where the unresolved resonance starts varies from nucleus to nucleus and is related to the average resonance spacing D_0 or, equivalently, the level density at the binding energy. Generally, the starting energy region is higher for light nuclides than for heavy nuclides. Only beyond this energy, the optical and statistical models implemented in TALYS are expected to yield reasonable results, at least for the non-fluctuating cross sections. The lower energies are the domain of R-matrix theory, which describes the individual resonances. Nevertheless, it would be useful to have a first-order estimate of the non-threshold reactions, not only for the obvious neutron capture channel, but also for the exothermal (n, p), (n, α) and fission channels. The fact that a nuclear model calculation in TALYS is only performed down to about a few keV should not prevent us to give at least an estimate of the $1/v$-like and resonance behaviour of the excitation function down to 10^{-5} eV (the lower energy limit in ENDF-6 nuclear data libraries). TALYS contains databases for data in the low-energy range:

- evaluated thermal neutron cross sections from the TARES database [73],
- evaluated neutron resonance parameters from the TARES database [73],
- average neutron s-wave resonance spacings, D_0, from the RIPL database [9].

One can now proceed in two ways.

Simple method: Linear interpolation

The simple method consists of using tabulated thermal cross section and D_0 values. First, we decide on the lower energy of validity of a TALYS nuclear model calculation E_L. Somewhat arbitrarily, we set as default $E_L = D_0$, where D_0 is taken from the evaluated database or, if not available, derived from the level density. E_L can also be entered as input. Next, we determine the neutron capture cross section at the thermal energy $E_{th} = 0.0253$ eV, either from the experimental database or, if not available, from the systematic relation [74]

$$\sigma_{n,\gamma}(E_{th}) = 1.5 \times 10^{-3} a (S_n - \Delta)^{3.5} \text{ mb}, \quad (162)$$

with a the level density parameter at the neutron separation energy S_n and Δ the pairing energy in MeV. We assign a $1/v$, i.e. $1/\sqrt{E}$, dependence to the cross section from 10^{-5} eV to an upper limit $E_{1/v}$ which we set, again arbitrarily, at $E_{1/v} = 0.2E_L$. The $1/v$ line obviously crosses $\sigma_{n,\gamma}(E_{th})$ at the thermal energy E_{th}. The points at $E_{1/v}$ and E_L are connected by a straight line. The resulting capture cross section is illustrated in Fig. 11. In reality, the region between $E_{1/v}$ and E_L is filled with resolved resonances, which is why we also implemented in TALYS a more physical method which has been available for several years now, as shortly discussed below. For other reactions with positive Q-values, such as (n, p) and (n, α), only a few experimental values at thermal energy are available and a systematic formula as for (n, γ) is hard to construct. If thermal cross sections are available for these reactions, the same method as for the radiative capture is followed. If not, we assume, e.g. in the (n, p) case that the ratio between the gamma decay width and the proton decay width is constant for incident energies up to E_L. Hence, we determine the ratio $R_p = \sigma_{n,p}/\sigma_{n,\gamma}$ at E_L from the TALYS calculation, and since we know the thermal (n, γ) value we can produce the (n, p) excitation function down to 10^{-5} eV by multiplying the capture cross section by R_p. A similar procedure is applied to all other non-threshold reactions.

High-Fidelity Resonance method: resonance reconstruction

For the TENDL project [11], a complete set of resonance parameters for all nuclides is considered, either from available compilations [75,76] or from the various nuclear data libraries around the world. This leads to a recommended set of resonance parameters which is used to create the low-energy part of the database. All this is provided in the TARES code [73]. TARES is not a resonance (analysis) code but rather collects and analyses resonance data, produces uncertainty and covariance data and produces data in pointwise form as e.g. a total cross section. To provide low-energy cross section data for all resonance channels we have integrated into TALYS three codes from the PREPRO-package [77], namely RECENT, SIGMA1 and GROUPIE, to reproduce the pointwise cross sections from the resonance parameters (RECENT), to broaden it in case of a desired temperature by the user (SIGMA1) and to group pointwise data to get a more compact groupwise representation (GROUPIE). The resulting reconstructed cross sections in the resonance range are then merged with the TALYS nuclear model result at higher energies. An example is given in Fig. 10 for resonance parameters available from experiment for ^{122}Te(n,γ). As advocated in Ref. [78], the average resonance parameters as predicted by TALYS can be used to generate statistical resonances. These average parameters are then derived from theoretical level densities and photon strength functions which are used to estimate strength functions and average radiative widths.

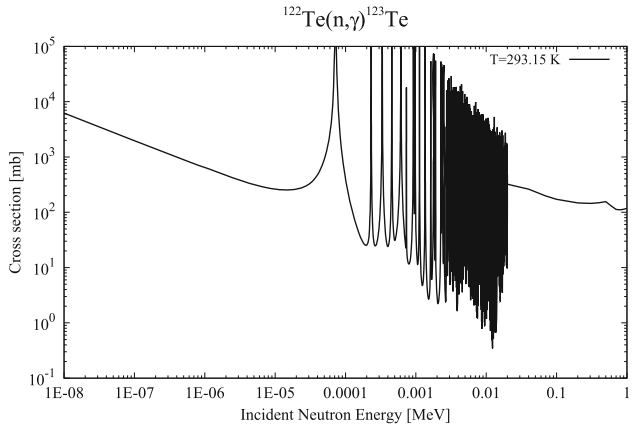

Fig. 10 Reconstruction of cross section data in the resonance range and transition into the unresolved range for ^{122}Te(n,γ). A pointwise calculation at a temperature of $T = 293.15$ K is shown

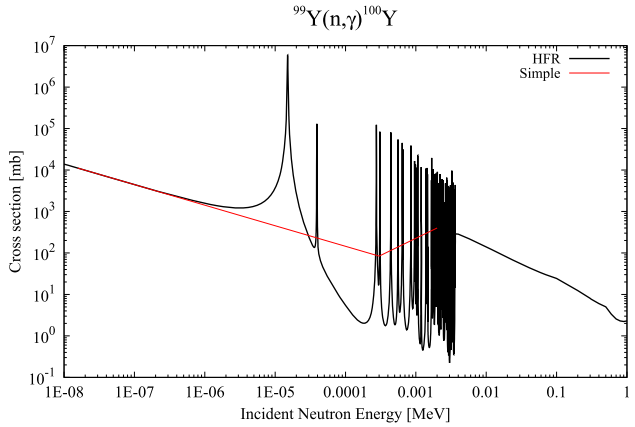

Fig. 11 Reconstruction of cross section data in the resonance range and transition into the unresolved range for ^{99}Y(n,γ) for a temperature $T = 293.15$ K, for the High-Fidelity Resonance method, compared with the simple method of linear interpolation

An example is given in Fig. 11 for the neutron-rich nucleus ^{99}Y for which no experimental data is available. Again, the difference with Fig. 11 is obvious: the fact that resonances have not been measured does not mean that they do not exist. It is therefore seen as a reasonable option to generate them on the basis of TALYS parameters from the statistical reaction range. The individual energies and widths may not be correct, but on average they follow well-established theoretical statistical estimates. In Ref. [78], such a transition from the resolved resonance regime to the unresolved range is applied to exotic neutron-rich nuclides within this so-called High-Fidelity Resonance framework and shown to have important implications, especially for astrophysical applications.

6 Pre-equilibrium reactions

It is now well known that the separation of nuclear reaction mechanisms into direct and compound is too simplistic. As Fig. 3 shows, the cross section as predicted by the pure compound process is too small with respect to measured continuum spectra, and the direct processes described in the previous section only excite the discrete levels at the highest outgoing energies. Furthermore, the measured angular distributions in the region between direct and compound are anisotropic, see e.g. Ref. [79], indicating the existence of a memory-preserving, direct-like reaction process. A third important indicator of the pre-equilibrium mechanism is the impact on excitation functions. If pre-equilibrium reactions would not exist, the compound nucleus would evaporate more particles before decaying to the ground state with gamma emission. Pre-equilibrium emission takes away the energy in the binary reaction process, which is confirmed by Fig. 12. The high-energy part of the spectrum of Fig. 3 is consistent with the excitation function above 15 MeV of Fig. 12. Instead of rapidly decreasing to zero, the excitation function has a tail towards high incident energies as the nucleus can no longer emit further particles.

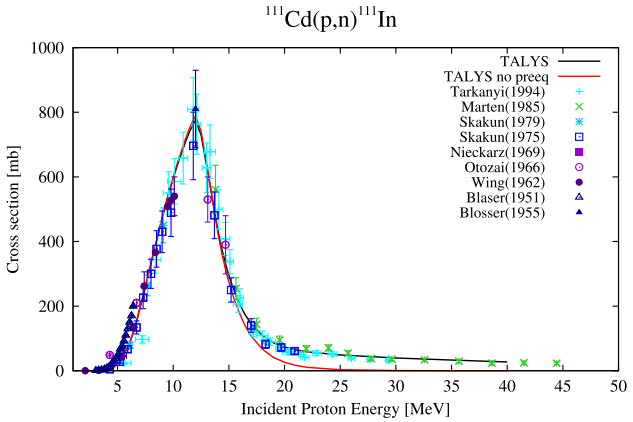

Fig. 12 Impact of pre-equilibrium mechanism on description of (p,n) cross section. The experimental data are obtained from the EXFOR database [80]

It is now well understood that, as an intermediate between the two extremes, there exists a reaction mechanism that embodies both direct- and compound-like features. These reactions are referred to as *pre-equilibrium, pre-compound* or, when discussed in a quantum-mechanical context, *multi-step processes*. Pre-equilibrium emission takes place after the first stage of the reaction but long before statistical equilibrium of the compound nucleus is attained. It is imagined that the incident particle step-by-step creates more complex states in the compound system and gradually loses its memory of the initial energy and direction. Pre-equilibrium processes cover a sizable part of the reaction cross section for incident energies between 10 and (at least) 200 MeV. Pre-equilibrium reactions have been modeled both classically and quantum-mechanically and both options are included in TALYS.

6.1 Two-component exciton model

In the exciton model [81] (see also Refs. [82,83] for extensive reviews), the nuclear state is characterized at any moment during the reaction by the total energy E^{tot} and the total number of particles above and holes below the Fermi surface. Particles (p) and holes (h) are indiscriminately referred to as excitons. Furthermore, it is assumed that all possible ways of sharing the excitation energy between different p-h configurations with the same exciton number $n = p+h$ have equal a-priori probability. To keep track of the evolution of the scattering process, one merely traces the temporal development of the exciton number, which changes in time as a result of intranuclear two-body collisions. The basic starting point of the exciton model is a time-dependent master equation, which describes the probability of transitions to more and less complex p-h states as well as transitions to the continuum, leading to emission. Upon integration over time, the energy-averaged emission spectrum is obtained. These assumptions makes the exciton model amenable for practical calculations. The price to be paid however is the introduction of a free parameter, namely the average matrix element of the residual two-body interaction, occurring in the transition rates between two exciton states. When this matrix element is properly parameterized, a very powerful model is obtained.

Qualitatively, the equilibration process of the excited nucleus is imagined to proceed as follows, see Fig. 13. After entering the target nucleus, the incident particle collides with one of the nucleons of the Fermi sea, with depth E_F. The formed state with $n = 3$ (2p1h), in the case of a nucleon-induced reaction, is the first that is subject to particle emission, confirming the picture of the exciton model as a compound-like model rather than a direct-like model. Subsequent interactions result in changes in the number of excitons, characterized by $\Delta n = +2$ (a new p-h pair) or $\Delta n = -2$ (annihilation of a p-h pair) or $\Delta n = 0$ (creation of a different configuration with the same exciton number). In the first stage of the process, corresponding to low exciton numbers, the $\Delta n = +2$ transitions are predominant. Apart from transitions to more complex or less complex exciton states, at any stage there is a non-zero probability that a particle is emitted. Should this happen at an early stage, it is intuitively clear that the emitted particle retains some "memory" of the incident energy and direction: the hypothesis of a fully equilibrated compound nucleus is not valid. This phase is called the pre-equilibrium phase, and it is responsible for the experimentally observed high-energy tails and forward-peaked angular distributions. If emission does not occur at an early stage, the system eventually reaches a (quasi-) equilibrium. The equilibrium situation, corresponding to high exciton numbers, is established after a large number of interactions, i.e. after a long lapse of time, and the system has "forgotten"

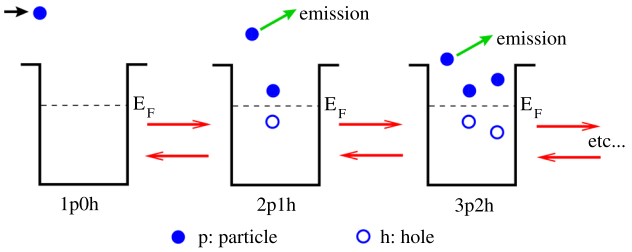

Fig. 13 Reaction flow in exciton model

about the initial state. Accordingly, this stage may be called the compound or evaporation stage. Hence, in principle the exciton model enables to compute the emission cross sections in a unified way, without introducing adjustments between equilibrium and pre-equilibrium contributions. However, in practical cases it turns out that it is simpler and even more accurate to distinguish between a pre-equilibrium and an equilibrium phase and to perform the latter with the usual Hauser-Feshbach formalism, as described in Sect. 5. This is the approach followed in TALYS.

Two versions of the exciton model are implemented in TALYS: The default is the two-component model in which the neutron or proton types of particles and holes are followed throughout the reaction, and that will be described here. For the simpler, and more generally known, one-component model we refer to Ref. [81].

In the following reaction equations, we use a notation in which p_π (p_ν) is the proton (neutron) particle number and h_π (h_ν) the proton (neutron) hole number. From this, we define the proton exciton number $n_\pi = p_\pi + h_\pi$ and the neutron exciton number $n_\nu = p_\nu + h_\nu$. Then, we can construct the charge-independent particle number $p = p_\pi + p_\nu$, the hole number $h = h_\pi + h_\nu$ and the exciton number $n = n_\pi + n_\nu$.

The temporal development of the system can be described by a master equation, describing the gain and loss terms for a particular class of exciton states [81]. Integrating the master equation over time up to the equilibration time yields the mean lifetime of the exciton state τ that can be used to calculate the differential cross section [84]. The primary pre-equilibrium differential cross section for the emission of a particle k with emission energy E_k can then be expressed in terms of τ, the composite-nucleus formation cross section σ^{CF}, and an emission rate W_k,

$$\frac{d\sigma_k^{\mathrm{preeq}}}{dE_k} = \sigma^{\mathrm{CF}} \sum_{p_\pi=p_\pi^0}^{p_\pi^{\max}} \sum_{p_\nu=p_\nu^0}^{p_\nu^{\max}} W_k(p_\pi, h_\pi, p_\nu, h_\nu, E_k) \times \tau(p_\pi, h_\pi, p_\nu, h_\nu) P(p_\pi, h_\pi, p_\nu, h_\nu), \quad (163)$$

where the factor P represents the part of the pre-equilibrium population that has survived emission from the previous states and now passes through the $(p_\pi, h_\pi, p_\nu, h_\nu)$ configurations, averaged over time. Expressions for all quantities appearing in this expression will be briefly summarized

below. The initial proton and neutron particle numbers are $p_\pi^0 = Z_p$, and $p_\nu^0 = N_p$, respectively with Z_p (N_p) the proton (neutron) number of the projectile. For any exciton state in the reaction process, $h_\pi = p_\pi - p_\pi^0$ and $h_\nu = p_\nu - p_\nu^0$, so that for primary pre-equilibrium emission the initial hole numbers are $h_\pi^0 = h_\nu^0 = 0$. For e.g. a neutron-induced reaction, the initial exciton number is given by $n^0 = n_\nu^0 = 1$ ($0p_\pi 0h_\pi 1p_\nu 0h_\nu$), but only pre-equilibrium gamma emission can occur from this state, while nucleon emission from this state is essentially elastic scattering and this is already covered by the optical model. Particle emission only occurs from $n = 3$ ($2p1h$) and higher exciton states. We use a hardwired value of $p_\pi^{\max} = p_\nu^{\max} = 6$ as the upper limit of the summation [81], and in addition the never-come-back approximation, i.e. throughout the cascade one neglects the interactions that decrease the exciton number, although the adopted solution of Eq. (163) includes transitions that convert a proton p-h pair into a neutron pair and vice versa. The maximum values $p_\pi^{\max}$ and $p_\nu^{\max}$ thus entail an automatic separation of the pre-equilibrium population and the compound nucleus population. The latter is then handled by the more adequate Hauser-Feshbach mechanism. We now discuss the various ingredients of Eq. (163).

A. Reaction cross sections

The basic feeding term for pre-equilibrium emission is the composite formation cross section σ^{CF}, which is given by

$$\sigma^{\mathrm{CF}} = \sigma_{\mathrm{reac}} - \sigma_{\mathrm{direct}}, \tag{164}$$

where the reaction cross section σ_{reac} is directly obtained from the optical model and σ_{direct} is the sum of the cross sections for direct reactions to discrete states $\sigma^{disc,direct}$ as defined in Eq. (18), and for giant resonances, see Sect. 4.4.

B. Emission rates and p-h state densities

The emission rate W_k has been derived by Cline and Blann [85] from the principle of microreversibility, and can easily be generalized to a two-component version as shown by Dobeš and Běták [86]. The emission rate for an ejectile k with relative mass μ_k and spin s_k is

$$W_k(p_\pi, h_\pi, p_\nu, h_\nu, E_k) = \frac{2s_k+1}{\pi^2\hbar^3}\mu_k E_k \sigma_{k,\mathrm{inv}}(E_k) \times \frac{\omega(p_\pi - Z_k, h_\pi, p_\nu - N_k, h_\nu, E^{\mathrm{tot}} - E_k)}{\omega(p_\pi, h_\pi, p_\nu, h_\nu, E^{\mathrm{tot}})}, \tag{165}$$

where $\sigma_{k,\mathrm{inv}}(E_k)$ is the inverse reaction cross section, again calculated with the optical model, Z_k (N_k) is the charge (neutron) number of the ejectile and E^{tot} is the total energy of the composite system.

For the p-h state density $\omega(p_\pi, h_\pi, p_\nu, h_\nu, E_x)$ we use the expression of Běták and Dobeš [86,87]. Their formula is based on the assumption of equidistant level spacing and is corrected for the effect of the Pauli exclusion principle and for the finite depth of the potential well. The two-component p-h state density is

$$\omega(p_\pi, h_\pi, p_\nu, h_\nu, E_x) = \frac{g_\pi^{n_\pi} g_\nu^{n_\nu}}{p_\pi! h_\pi! p_\nu! h_\nu! (n-1)!} \times (U - A(p_\pi, h_\pi, p_\nu, h_\nu))^{n-1} f(p, h, U, V), \tag{166}$$

where g_π and g_ν are the single-particle state densities, A the Pauli correction, f the finite well function, and $U = E_x - P_{p,h}$ with $P_{p,h}$ the pairing correction [88]. We refer to Ref. [81] for the expressions for $P_{p,h}$ and $A(p_\pi, h_\pi, p_\nu, h_\nu)$. For the single-particle state densities we take

$$g_\pi = Z/15, \qquad g_\nu = N/15, \tag{167}$$

which is, through the relationship $g = 6a/\pi^2$, in line with the values for our total level density parameter a, see Eq. (227), and also provides a globally better description of spectra than $g = A/13$, used in several older exciton model parameterizations.

The finite well function $f(p, h, E_x, V)$ accounts for the fact that a hole cannot have an energy below that of the bottom of the potential well depth V. It is given by

$$f(p, h, E_x, V) = 1 + \sum_{i=1}^{h} (-1)^i \binom{h}{i} \left[\frac{E_x - iV}{E_x}\right]^{n-1} \times \Theta(E_x - iV), \tag{168}$$

where Θ is the unit step function. Note that f is different from 1 only for excitation energies greater than V. In the original version of Běták and Dobeš [87], V is given by the depth E_f of the Fermi well. This was generalized by Kalbach [58,89] to obtain an effective method to include surface effects in the first stage of the interaction, leading to a harder pre-equilibrium spectrum. For the first stage the maximum depth of the hole should be significantly reduced, since in the surface region the potential is shallower than in the interior. This automatically leaves more energy to be adopted by the excited particle, yielding more emission at the highest outgoing energies. We use the following functional form for V in terms of the projectile energy E_p and the mass A,

$$\begin{aligned} V &= 22 + 16\frac{E_p^4}{E_p^4 + (450/A^{1/3})^4}\ \mathrm{MeV\ for} \\ &\quad h = 1 \text{ and incident protons}, \\ V &= 12 + 26\frac{E_p^4}{E_p^4 + (245/A^{1/3})^4}\ \mathrm{MeV\ for} \\ &\quad h = 1 \text{ and incident neutrons}, \\ V &= E_f = 38\ \mathrm{MeV\ for}\ h > 1, \end{aligned} \tag{169}$$

see Ref. [81] for a further justification of this parameterisation.

C. Lifetimes

The lifetime τ of exciton state $(p_\pi, h_\pi, p_\nu, h_\nu)$ in Eq. (163) is defined as the inverse sum of the total emission rate and the various internal transition rates,

$$\tau(p_\pi, h_\pi, p_\nu, h_\nu) = [\lambda^+_\pi(p_\pi, h_\pi, p_\nu, h_\nu) + \lambda^+_\nu(p_\pi, h_\pi, p_\nu, h_\nu) + \lambda^0_{\pi\nu}(p_\pi, h_\pi, p_\nu, h_\nu) + \lambda^0_{\nu\pi}(p_\pi, h_\pi, p_\nu, h_\nu) + W(p_\pi, h_\pi, p_\nu, h_\nu)]^{-1}, \quad (170)$$

where λ^+_π (λ^+_ν) is the internal transition rate for proton (neutron) p-h pair creation, $\lambda^0_{\pi\nu}$ ($\lambda^0_{\nu\pi}$) is the rate for the conversion of a proton (neutron) p-h pair into a neutron (proton) p-h pair, and λ^-_π (λ^-_ν) is the rate for p-h annihilation. The total emission rate W is the integral of Eq. (165) over all outgoing energies, summed over all outgoing particles,

$$W(p_\pi, h_\pi, p_\nu, h_\nu) = \sum_{k=\gamma,n,p,d,t,h,\alpha} \int dE_k W_k(p_\pi, h_\pi, p_\nu, h_\nu, E_k). \quad (171)$$

Expressions for the internal transition rates λ and the pre-equilibrium population P in Eq. (163) are rather extensive and are given in Ref. [81].

D. Internal transition rates

The transition rates λ^+ (λ^0) for the creation (conversion) of a p-h pair are expressed in terms of a collision probability per unit time, which contains the main parameter that drives the pre-equilibrium strength.

We distinguish between two options for the collision probabilities. The best known is to express them in terms of an effective squared matrix element M^2, as used in many exciton model analyses. This matrix element thus represents an effective residual interaction, whereby all individual residual interactions taking place inside the nucleus can be cast into an average form for the squared matrix element to which one assigns a global energy dependence.

The average residual interaction inside the nucleus is not necessarily the same for like and unlike nucleons, and therefore the two-component exciton model contains 4 different matrix elements. They all relate to the following semi-empirical expression which has been shown to work for incident energies up to 200 MeV [81]:

$$M^2 = \frac{C_1 A_p}{A^3}\left[7.48C_2 + \frac{4.62\times10^5}{(\frac{E^{\rm tot}}{n.A_p} + 10.7C_3)^3}\right]. \quad (172)$$

where E^{tot} is the total energy of the system and C_1, C_2 and C_3 are adjustable constants that are all equal to 1 by default, and A_p is the mass number of the projectile, which allows generalization for complex-particle reactions. Equation (172) is slightly different (10%) from the expression given in Ref. [81] to allow for better fits of excitation functions.

We also emphasize that the above parameterization has been fine-tuned to experimental particle emission spectra as these form the most exclusive type on information to constrain the pre-equilibrium models. This does not necessarily give the optimal solution for cross section excitation functions and recently more attempts have been made to establish new trends for M^2 on the basis of excitation functions [90].

Instead of modeling the intranuclear transition rate by an average squared matrix element, one may also relate the transition rate to an *effective* imaginary optical potential [81] related to nucleon-nucleon collisions in nuclear matter:

$$W_i^{\rm eff}(E) = C^{\rm omp}\ W_i(E). \quad (173)$$

We use as best overall parameter $C^{\rm omp} = 0.55$. Apart from $C^{\rm omp}$, this constitutes a parameter-free model. When experimental data from the EXFOR database [80] become programmatically available, an interesting future study is to see which of the two options for the transition rates gives the best trend and whether our parameterizations can be improved.

6.2 Photon exciton model

For pre-equilibrium photon emission, we have implemented the model of Akkermans and Gruppelaar [91]. This model gives a simple but powerful simulation of the direct and semi-direct capture process within the framework of the exciton model. Analogous to the particle emission rates, the continuum γ-ray emission rates may be derived from the principle of detailed balance or microscopic reversibility, assuming that only $E1$-transitions contribute. This yields for the two-component emission rate

$$W_\gamma\left(p_\pi, h_\pi, p_\nu, h_\nu, E_\gamma\right) = \frac{E_\gamma^2}{\pi^2\hbar^3c^2} \times \frac{\sigma_{\gamma,abs}(E_\gamma)}{\omega(p_\pi, h_\pi, p_\nu, h_\nu, E^{tot})} \frac{1}{g(n-2)+g^2E_\gamma} \times \left(g^2E_\gamma\frac{1}{2}\left[\omega(p_\pi-1, h_\pi-1, p_\nu, h_\nu, E_x-E_\gamma) + \omega\left(p_\pi, h_\pi, p_\nu-1, h_\nu-1, E_x-E_\gamma\right)\right] + \frac{gn\omega(p_\pi, h_\pi, p_\nu, h_\nu, E_x-E_\gamma)}{gn+g^2E_\gamma}\right), \quad (174)$$

where g is the single-particle state density, n the exciton number and $\sigma_{\gamma,abs}(E_\gamma)$ is the photon absorption cross section of Eq. (294). The initial p-h configuration is $n_0 = 1$ $(1p0h)$ for photon emission. For "direct" γ-ray emission in nucleon-induced reactions only the second term between brackets $(n = 1)$ contributes. The "semi-direct" γ-ray emission $(n = 3)$ consists of both terms.

The emission rate (174) is included in Eq. (163), so that the pre-equilibrium photon cross section automatically emerges.

6.3 Pre-equilibrium spin distribution

Since the exciton model described above does not provide a spin distribution for the residual states after pre-equilibrium emission, a model needs to be adopted that provides the spin population in the continuum after binary reactions and further pre-equilibrium stages. TALYS provides two options for this. The default is to adopt the compound nucleus spin distribution (described in Sect. 5) also for the excited states resulting from pre-equilibrium emission. Another option that has been quite often used in the past is to assign a spin distribution to the p-h state density. For that, we adopt the usual decomposition of the state density into a J-dependent part and an energy-dependent part,

$$\rho(p_\pi, h_\pi, p_\nu, h_\nu, J, E_x) = (2J+1)R_n(J) \times \omega(p_\pi, h_\pi, p_\nu, h_\nu, E_x). \tag{175}$$

The function $R_n(J)$ represents the spin distribution of the states in the continuum. It is given by

$$R_n(J) = \frac{2J+1}{\pi^{1/2} n^{3/2} \sigma^3} \exp\left[-\frac{(J+\frac{1}{2})^2}{n\sigma^2}\right]. \tag{176}$$

where the spin cut-off parameter σ is given by Ref. [92],

$$\sigma^2 = C_p n A^{\frac{2}{3}}, \tag{177}$$

where A is the mass number of the nucleus and by default $C_p = 0.24$. In practice, with this option the residual states formed by pre-equilibrium reactions would be multiplied by R_n a posteriori. The default in TALYS is still to use the compound nucleus spin distribution. There has been quite some debate about the correct spin distributions for pre-equilibrium reactions, see e.g. Ref. [83] and updated versions of Eq. (175) will be reserved for future pre-equilibrium models which consistently take the spin into account throughout the entire formalism. There are several indications that the spin-distribution should be narrower than the one prescribed by Eq.(177), and as an example Ref. [93] provides a discussion of this issue for ^{238}U$(n, n'\gamma)$ reactions.

6.4 Continuum stripping, pick-up, break-up and knock-out reactions

For pre-equilibrium reactions involving deuterons, tritons, Helium-3 and alpha particles, a contribution from the exciton model is automatically calculated with the formalism of the previous subsections. It is however well known that for nuclear reactions involving composite projectiles and ejectiles, mechanisms like stripping, pick-up, break-up and knock-out play an important role and these direct-like reactions are not covered by the exciton model. Therefore, Kalbach [94,95] developed a phenomenological contribution for these mechanisms, which we have included in TALYS. In total, the pre-equilibrium cross section for these reactions is given by the sum of an exciton model (EM), nucleon transfer (NT), knock-out (KO) and break-up (BU) contribution:

$$\frac{d\sigma_k^{\text{preeq}}}{dE_k} = \frac{d\sigma_k^{EM}}{dE_k} + \frac{d\sigma_k^{NT}}{dE_k} + \frac{d\sigma_k^{KO}}{dE_k} + \frac{d\sigma_k^{BU}}{dE_k}, \tag{178}$$

where the contribution from the exciton model was outlined in the previous subsection.

6.4.1 *Transfer reactions*

The general differential cross section formula for a nucleon transfer reaction of the type $A(a,b)B$ is

$$\frac{d\sigma_{a,b}^{NT}}{dE_b} = \frac{2s_b+1}{2s_a+1}\frac{A_b}{A_a}\frac{E_b\sigma_{b,inv}(E_b)}{A_a} K \left(\frac{A_a}{E_a+V_a}\right)^{2n} \times \left(\frac{C_a}{A_B}\right)^n N_a \left(\frac{2Z_A}{A_A}\right)^{2(Z_a+2)h_\pi+2p_\nu} \times \omega_{NT}(p_\pi, h_\pi, p_\nu, h_\nu, U), \tag{179}$$

where

$$\begin{aligned} C_a &= 5500 \text{ for incident neutrons,} \\ &= 3800 \text{ for incident charged particles,} \\ N_a &= \frac{1}{80E_a} \text{ for pickup,} \\ &= \frac{1}{580\sqrt{E_a}} \text{ for stripping,} \\ &= \frac{1}{1160\sqrt{E_a}} \text{ for exchange.} \end{aligned} \tag{180}$$

K is an enhancement factor taking into account the fact that d, t and 3-He are loosely bound:

$$\begin{aligned} K &= 12 \text{ for } (N,\alpha), \\ &= 12 - 11\frac{E_a-20}{E_a} \text{ for } (\alpha, N) \text{ and } E_a > 20, \\ &= 1 \text{ otherwise,} \end{aligned} \tag{181}$$

where N stands for either neutron or proton. The well depth V_a is set at

$$V_a = 12.5A_a \text{ MeV}, \tag{182}$$

and represents the average potential drop seen by the projectile between infinity and the Fermi level. The possible degrees of freedom for the reaction are all included in the residual state density $\omega_{NT}(p_\pi, h_\pi, p_\nu, h_\nu, U)$. Since we do not use

this model to describe exchange reactions in inelastic scattering, there is no need to sum the various terms of Eq. (179) over p_π, as in Ref. [94]. The exciton numbers are automatically determined by the transfer reaction, i.e. $n = \mid A_a - A_b \mid$, $n_\pi = h_\pi = \mid Z_a - Z_b \mid$, $n_\nu = h_\nu = \mid N_a - N_b \mid$, $p_\pi = p_\nu = 0$. The accessible state density that is directly determined by the reaction is $\omega(p_\pi, h_\pi, p_\nu, h_\nu, U)$, given by Eq. (166). The total residual state density however also takes into account more complex configurations that can be excited by the transfer reaction. It is given by

$$\begin{aligned}\omega_{NT}(p_\pi, h_\pi, p_\nu, h_\nu, U) &= \sum_{i=0}^{3}\sum_{j=0}^{3-i}(X_{NT})^{i+j} \\ &\times\omega(p_\pi + i, h_\pi + i, p_\nu + j, h_\nu + j, U) \\ &+ \sum_{i=0}^{p_\pi}\sum_{j=0}^{h_\pi}\sum_{k=0}^{p_\nu}\sum_{l=0}^{h_\nu}\Theta\left(i + j + k + l - \frac{1}{2}\right) \\ &\times\omega(p_\pi - i, h_\pi - j, p_\nu - k, h_\nu - l, U). \end{aligned} \tag{183}$$

The first term allows that up to three p-h pairs can be excited in a transfer reaction. The factor X_{NT} represents the probability for exciting such a pair and is given by

$$X_{NT} = \frac{7\sqrt{E_a/A_a}}{V_1 A_A^2}(p_\nu^2 + p_\pi^2 + h_\nu^2 + 1.5h_\pi^2). \tag{184}$$

For neutrons and protons we adopt for V_1 the value given by Eq. (169), for deuterons and tritons we take V_1=17 MeV, and for Helium-3 and alpha particles we take V_1=25 MeV. The finite well depth correction for Eq. (183) are made using a well depth of

$$\begin{aligned} V &= V_1\left(\frac{2Z}{A}\right) \quad \text{if} \quad n_\pi = 0 \\ &= V_1 \quad \text{otherwise.} \end{aligned} \tag{185}$$

The second term of Eq. (183) allows for transfer of nucleons at the Fermi level. Here, the Heaviside function Θ is merely used to avoid double counting of $\omega(p_\pi, h_\pi, p_\nu, h_\nu, U)$.

6.4.2 Knockout reactions

For (nucleon,α) reactions a knockout contribution is added. The general differential cross section formula for a knockout reaction of the type $A(a, b)B$ is

$$\begin{aligned}\frac{d\sigma_{a,b}^{KO}}{dE_b} &= \frac{\sigma_{a,inv}(E_a)}{14}(2s_b + 1)A_b E_b \sigma_{b,inv}(E_b) \\ &\times\frac{P_b g_a g_b\,[U - A_{KO}(p_a, h_b)]}{\sum_{c=a,b}(2s_c + 1)A_c\,\langle\sigma_c\rangle} \\ &\times\frac{1}{(E_{max} + 2B_{coul,c})(E_{max} - B_{coul,c})^2 g_a g_b^2/6g_c} \end{aligned} \tag{186}$$

where P_b is the probability of exciting a b-type p-h pair, E_{max} is the maximum emission energy, and $B_{coul,c}$ is the Coulomb barrier for a particle c. The average inverse cross section $\langle\sigma_c\rangle$ is given by

$$\langle\sigma_c\rangle = \int_{B_{coul,c}}^{E_{max}} dE\sigma_c(E). \tag{187}$$

For the knockout model, the single-particle state density parameters for the cluster degrees of freedom g represent the number of cluster states per unit energy. The relevant values are given by

$$g_n = N/13, \quad g_p = Z/13, \quad g_\alpha = A/208 \ \text{MeV}. \tag{188}$$

The Pauli correction factor A_{KO} is given by

$$A_{KO}(p_a, h_b) = \frac{1}{2g_a^2} - \frac{1}{2g_b^2}. \tag{189}$$

The probabilities for exciting the various p-h pairs are

$$\begin{aligned} P_n &= \frac{N_A - \phi Z_A}{A_A - 2\phi Z_A + \phi Z_A/2} \\ P_p &= \frac{Z_A - \phi Z_A}{A_A - 2\phi Z_A + \phi Z_A/2} \\ P_\alpha &= \frac{\phi Z_A/2}{A_A - 2\phi Z_A + \phi Z_A/2}. \end{aligned} \tag{190}$$

The factors ϕ are a kind of pre-formation parameters [94]. The following values are adopted

$$\begin{aligned} N_A \le 116 &: \phi = 0.08 \\ 116 \le N_A < 126 &: \phi = 0.02 + 0.06(126 - N_A)/10 \\ 126 \le N_A < 129 &: \phi = 0.02 + 0.06(N_A - 126)/3 \\ 129 \le N_A &: \phi = 0.08. \end{aligned} \tag{191}$$

6.4.3 Break-up reactions

For reactions induced by complex particles, break-up may play an important role. This holds especially for the weakly bound deuteron. Break-up is here defined as having a projectile fragment emerged from the reaction in a relatively narrow peak centered close to the beam velocity and strongly directed toward forward angles. For break-up reactions, the model by Kalbach [95] has been included. This leads to an extra contribution for all complex-particle induced reactions and in particular for the (d, n) and (d, p) channels.

The basic parameters for this empirical model for a projectile a and ejectile b are the centroid energy of the breakup peak given by

$$E_0 = \frac{A_b}{A_a}(E_{\text{inc}} - C_a) + C_b, \tag{192}$$

where $A_{a,b}$ is the mass number and $C_{a,b}$ the Coulomb barrier of the particles involved. Expressions for these terms are given in Ref. [95]. The break-up peak is assumed to be described by a Gaussian,

$$P(E_{\rm inc}) = \frac{1}{w\sqrt{2\pi}} \exp\left(-\frac{(E_{\rm inc}-E_0)^2}{2w^2}\right), \tag{193}$$

where the expression for w can be found in Ref. [95].

An alternative option for the break-up component in TALYS is the model by Avrigeanu et al. [96]. For that model however, contributions of explicit direct break-up reactions need to be added by other codes, to give the total (d, p) cross section.

6.5 Angular distribution systematics

A sound pre-equilibrium theory should, besides the angle-integrated spectra, also describe the smooth forward peaked angular distributions in the continuum. To do so, the multi-step direct reaction model has been included in TALYS, but only as a global collective-like method. Semi-classical models, such as the exciton model, have always had some problems to describe angular distributions, essentially because it is based on a compound-like concept instead of a direct one [97]. A powerful phenomenological method is given by Kalbach [79]. It is based on experimental information only and the insight that in general, a pre-equilibrium process consists of a forward peaked part (multi-step direct) and an isotropic part (multi-step compound), and that the angular distributions are fairly structureless and all look alike. The corresponding formula for the double-differential cross section for a projectile a and an ejectile b is

$$\frac{d^2\sigma_{a,xb}}{dE_b d\Omega} = \frac{1}{4\pi}\left[\frac{d\sigma^{\rm preeq}}{dE_b} + \frac{d\sigma^{comp}}{dE_b}\right]\frac{a}{\sinh(a)} \times[\cosh(a\cos\Theta) + f_{MSD}(E_b)\sinh(a\cos\Theta)], \tag{194}$$

where E_a and E_b are the incident and the outgoing energy, respectively, and $\frac{d\sigma^{\rm preeq}}{dE_b}$ and $\frac{d\sigma^{comp}}{dE_b}$ are the angle-integrated pre-equilibrium and compound spectra, respectively, and f_{MSD} is the so-called multi-step direct or pre-equilibrium ratio:

$$f_{MSD}(E_b) = \frac{d\sigma^{\rm preeq}}{dE_b} \Big/ \left[\frac{d\sigma^{\rm preeq}}{dE_b} + \frac{d\sigma^{comp}}{dE_b}\right], \tag{195}$$

which thus increases from practically 0 at very low emission energy to 1 at the highest emission energies. Hence, once the angle-integrated spectra are known, the parameter a determines the angular distribution. We refer to Ref. [79] for the expression for a.

Since we calculate the pre-equilibrium and compound cross sections explicitly, and actually only store f_{MSD} in data libraries, Eq. (194) can be reduced to a formula for the double-differential pre-equilibrium cross section

$$\frac{d^2\sigma^{\rm preeq}_{a,xb}}{dE_b d\Omega} = \frac{1}{4\pi}\frac{d\sigma^{\rm preeq}}{dE_b}\frac{a}{\sinh(a)}\exp(a\cos\Theta), \tag{196}$$

to which the isotropic compound angular distribution can be added. In sum, given the angle-integrated spectrum $\frac{d\sigma^{\rm preeq}}{dE_b}$ by some physics model, the double-differential cross section is returned quite simply and reasonably accurate by Eq. (196).

7 Direct capture

At relatively low energies, the reaction model described in the present sections makes the fundamental assumption that the capture process takes place with the intermediate formation of a compound nucleus in thermodynamic equilibrium. The energy of the incident particle is then shared more or less uniformly by all the nucleons before releasing the energy by particle emission or γ-de-excitation. The formation of a compound nucleus is usually justified by assuming that the nuclear level density in the compound system at the projectile incident energy is large enough to ensure an average statistical continuum superposition of available resonances [98]. However, when the number of available states in the compound system is relatively small, the validity of the Hauser-Feshbach predictions has to be questioned, the neutron capture process being possibly dominated by direct electromagnetic transitions to a bound final state rather than through a compound intermediary. The direct capture (DC) proceeds via the excitation of only a few degrees of freedom on much shorter time scales reflecting the time taken by the projectile to traverse the target. For the DC process, the mean free path of the incident particle is comparable with the size of the nucleus and the particle ejection occurs preferentially at forward angles. It has become clear, however, that the DC process is important, and often dominating at the very low energies of astrophysical interest, especially for light or exotic nuclei systems for which few, or even no resonant states are available [99–103]. This should be also the case for medium-mass or heavy neutron rich nuclei.

The DC cross section is not calculated by default at the present time, since (i) its ingredients (mainly the excited spectrum and spectroscopic factors) remain difficult to determine on theoretical grounds, (ii) most of the HF/pre-equilibrium ingredients have been tuned without including the DC contribution (even if small), and (iii) the model has not been widely tested, especially for charged-particle-induced reactions or for a large range of energies.

A TALYS calculation of the DC cross sections is done within the potential model, following the method described in Ref. [102]. This model is employed to study the neutron DC reaction describing the transition from the initial scattering state $A+n$ directly to the final nucleus B with accompanying γ-ray emission. The allowed electric dipole ($E1$), electric quadrupole ($E2$) and magnetic dipole ($M1$) transitions to the ground state as well as all possible excited states in the final nucleus are taken into account.

In the case of neutron capture, the DC cross section for $A(n,\gamma)B$ can be expressed as [104]

$$\sigma^{DC}(E) = \sum_{f=0}^{E_B^x} S_f \sigma_f^{dis}(E) + \int_{E_B^x}^{S_n} \sum_{J_f,\pi_f} \rho(E_f, J_f, \pi_f)\langle S_f\rangle \sigma_f^{cont} dE_f. \quad (197)$$

Below the level x at energy E_B^x, the sum runs over all the available discrete final states in the residual nucleus B, which are usually experimental levels if available. S_f is the spectroscopic factor describing the overlap between the antisymmetrized wave function of the initial system $A+n$ and the final state B^x. Above E_B^x, the summation is replaced by a continuous integration over a spin- and parity-dependent nuclear level density $\rho(E_f, S_f, \pi_f)$ and the spectroscopic factor by an average quantity $\langle S_f\rangle$ that can be energy-dependent. In the TALYS structure database, experimental information on discrete levels are included, whenever available (see Sect. 10). Similarly, experimental information on spectroscopic factors extracted from (d, p) reactions has been extracted from Nuclear Data Sheets journals for about 4270 nuclear levels in 146 different nuclei [105]. When not available experimentally, the level density and spectroscopic factors included in Eq. (197) are taken from either

1. the spin- and parity-dependent one-particle one-hole neutron excitations deduced from the combinatorial nuclear level density [106] with an average spectroscopic factor $\langle S_f\rangle = 1.0$; or
2. total one-particle one-hole neutron excitations deduced from the combinatorial nuclear level density [106] with an average spectroscopic factor $\langle S_f\rangle = 1.0$; or
3. the spin- and parity-dependent combinatorial nuclear level density from Ref. [106] with a simple energy-dependent prescription $\langle S_f(E_f)\rangle = 0.1+0.33\exp(-0.8E)$ (where E_f is the excitation energy in MeV) based on shell-model results [107].

In all cases, the ground state contribution in Eq. (197) is calculated with $S_f=0.347$ for even-even targets, a value deduced from the compilation of all the known spectroscopic factors [105], and with $S_f=1$ for odd-A targets. These values of S_f were shown to minimize deviations between theory and experiment in nuclei close to the valley of β-stability where the three models yield similar results [102,107].

The potential model calculates the transition matrix elements between the initial and the final states by sandwiching the electromagnetic operators in the long wave-length limit. It is usually enough to consider the $E1$, $E2$ and $M1$ transitions which is the TALYS case. The complete set of equations used to calculate the matrix elements of the electromagnetic operators can be found in Ref. [102]. The radial wave functions are obtained from the solution of the 2-body Schrödinger equation with a central potential, the same as the one used for the Hauser-Feshbach and pre-equilibrium channels. It should be emphasized that TALYS treats the three (compound nucleus, pre-equilibrium, and direct) capture mechanisms coherently, i.e they are obtained on the basis of the same nuclear ingredients, such as the optical potential and nuclear level densities. In this framework, the three components are calculated on the same footing and represent partial fluxes of the same total reaction cross section.

8 Multiple emission

At incident energies above approximately the neutron separation energy, the residual nuclides formed after the first binary reaction are populated with enough excitation energy to enable further decay by particle emission or fission. This is called multiple emission and leads to e.g. $(n, 2n)$ and more complex reaction channels (see Fig. 5). We distinguish between two mechanisms: multiple compound (Hauser-Feshbach) decay, which becomes important as soon as the incident energy is higher than the neutron separation energy and multiple pre-equilibrium decay, which becomes important above 30–40 MeV of incident energy.

8.1 Multiple Hauser–Feshbach decay

This is the conventional way, and for incident energies up to several tens of MeV sufficient, to treat multiple emission. It is assumed that direct, pre-equilibrium, and compound processes can take place in the binary reaction and that secondary and further particles are emitted by compound emission.

After the binary reaction, the residual nucleus may be left in an excited discrete state i' or an excited state within a continuum bin i' which is characterized by excitation energy $E_x(i')$, spin I' and parity Π'. The population of this state or set of states is given by a probability distribution for Hauser-Feshbach decay P^{HF} that is completely determined by the binary reaction mechanism. For a binary neutron-induced reaction to a discrete state i', i.e. when $E_x(i')$, I' and Π'

have unique values, the residual population is given by

$$P^{\mathrm{HF}}(Z', N', E_x(i'), I', \Pi') = \sigma^{i'}_{n,k'}(E^{tot}, I, \Pi \rightarrow E_x(i'), I', \Pi'), \quad (198)$$

where the non-elastic reaction cross section for a discrete state $\sigma^{i'}_{n,k'}$ was defined in Sect. 2.3.2 and where the ejectile k' connects the initial compound nucleus (Z_C, N_C) and the residual nucleus (Z', N'). For binary reactions to the continuum, the residual population of states characterised by (I', Π') per $E_x(i')$ bin is given by the sum of a pre-equilibrium and a compound contribution

$$P^{\mathrm{HF}}(Z', N', E_x(i'), I', \Pi') = \int dE_{k'} \frac{d\sigma^{comp,cont}}{dE_{k'}}(E^{tot}, I, \Pi \rightarrow E_x(i'), I', \Pi') + \mathcal{P}^{\mathrm{pre}}(Z', N', p^{max}_{\pi}+1, h^{max}_{\pi}+1, p^{max}_{\nu}+1, h^{max}_{\nu}+1, E_x(i')), \quad (199)$$

where the integration range over $dE_{k'}$ corresponds exactly with the bin width of $E^{'}_{x}(i')$ and $\mathcal{P}^{\mathrm{pre}}$ denotes the population entering the compound stage after primary pre-equilibrium emission. The expression for $\mathcal{P}^{\mathrm{pre}}$ will be given in Eq. (203) of the next subsection. Once the first generation of residual nuclides/states has been filled, the picture can be generalized to tertiary and higher order multiple emission.

In general, the population P^{HF} before decay of a level i' or a set of states $(I', \Pi', E_x(i'))$ in bin i' of a nucleus (Z', N') in the reaction chain is proportional to the feeding, through the ejectiles k', from all possible mother bins i with an energy $E_x(i)$ in the (Z, N) nuclides, i.e.

$$P^{\mathrm{HF}}(Z', N', E_x(i'), I', \Pi') = \sum_{I,\Pi}\sum_{k'}\sum_{i}[P^{\mathrm{HF}}(Z, N, E_x(i), I, \Pi) + \mathcal{P}^{\mathrm{pre}}(Z, N, p^{max}_{\pi}+1, h^{max}_{\pi}+1, p^{max}_{\nu}+1, h^{max}_{\nu}+1, E_x(i))] \times \frac{\Gamma_{k'}(E_x(i), I, \Pi \rightarrow E_x(i'), I', \Pi')}{\Gamma^{tot}(E_x(i), I, \Pi)}. \quad (200)$$

The appearance of the indices p^{max}_{π} indicates that only the reaction population that has not been emitted via the (multiple) pre-equilibrium mechanism propagates to the multiple compound stage. Similar to Eq. (136) the decay widths are given by

$$\Gamma_{k'}(E_x(i), I, \Pi \longrightarrow E_x(i'), I', \Pi') = \frac{1}{2\pi\rho(E_x(i), I, \Pi)} \times \sum_{j'=|J-I'|}^{J+I'} \sum_{l'=|j'-s'|}^{j'+s'} \delta_{\pi}(\alpha') \left\langle T^{J}_{\alpha' l' j'}(E'_{a'}) \right\rangle. \quad (201)$$

Again, the term $2\pi\rho$ (compound nucleus level density) of the decay width Eq. (201) falls out of the multiple emission equation Eq. (200) and therefore does not need to be calculated in practice. The total decay width is

$$\Gamma^{tot}(E_x(i), I, \Pi) = \sum_{k''} \sum_{I''=mod(J+s,1)}^{J+l_{max}} \sum_{\Pi''=-1}^{1} \sum_{i''} \Gamma_{k''}(E_x(i), I, \Pi \longrightarrow E_x(i''), I'', \Pi''). \quad (202)$$

In sum, the differences between binary and multiple compound emission are that width fluctuations and angular distributions do not enter the model and that the initial compound nucleus energy E^{tot} is replaced by an excitation energy bin E_x of the mother nucleus. The calculational procedure, in terms of sequences of decaying bins, was already explained in Sect. 2.

8.2 Multiple pre-equilibrium emission

At excitation energies above typically 30–40 MeV, the composite nucleus is far from equilibrated and it is obvious that the excited nucleus should be described by more degrees of freedom than just E_x, J and Π. In general, we need to keep track of the p-h configurations that are excited throughout the reaction chain and thereby calculate multiple pre-equilibrium emission up to any order. This is accomplished by treating multiple pre-equilibrium emission within the exciton model, which is the default option for multiple pre-equilibrium calculations in TALYS. The probability that a second fast particle is emitted starts to increase around 40–50 MeV of incident energy and above 100 MeV several fast particles can be emitted from the non-equilibrated nucleus, similar to the picture in high-energy intranuclear cascade models. The exciton model approach in TALYS is one of several mechanisms that have been implemented in the past to handle multiple-preequilibrium emission. In essence, it is a phase space approach towards the well known intranuclear cascade picture, in which first various fast partciles are knocked out of the nucleus before the evaporation stage. Within the preequilibrium picture, other approaches have been developed, such as the Hybrid Monte Carlo Simulation (HMS) model implemented in EMPIRE [108]. The method implemented in TALYS can be regarded as completely deterministic. The same argument as for primary pre-equilibrium emission holds: multiple pre-equilibrium emission takes away so much excitation energy that the process has a large impact on the prediction of residual production cross sections, as illustrated in Sect. 16. Besides the formulation in terms of the exciton model, TALYS also contains an alternative more approximative model for multiple pre-equilibrium emission, called the s-wave transmission coefficient method. Both approaches are discussed below.

For multiple pre-equilibrium emission within the exciton model, we introduce the pre-equilibrium population

$\mathcal{P}^{\rm pre}(Z, N, p_\pi, h_\pi, p_\nu, h_\nu, E_x(i))$ which holds the amount of the reaction population present in a (Z, N) nucleus, $(p_\pi, h_\pi, p_\nu, h_\nu)$ exciton state and excitation energy bin $E_x(i)$. A special case is the pre-equilibrium population for a particular exciton state after binary emission, which can be written as

$$\begin{aligned}&\mathcal{P}^{\rm pre}(Z', N', p_\pi - Z_{k'}, h_\pi, p_\nu - N_{k'}, h_\nu, E_x(i'))\\&\quad= \sigma^{\rm CF}(Z_C, N_C, E^{\rm tot})\\&\qquad\times W_{k'}(Z_C, N_C, E^{\rm tot}, p_\pi, h_\pi, p_\nu, h_\nu, E_{k'})\\&\qquad\times\tau(Z_C, N_C, E^{\rm tot}, p_\pi, h_\pi, p_\nu, h_\nu)\\&\qquad\times P(Z_C, N_C, E^{\rm tot}, p_\pi, h_\pi, p_\nu, h_\nu),\end{aligned}\tag{203}$$

where Z_C (N_C) again is the compound nucleus charge (neutron) number and $Z_{k'}$ ($N_{k'}$) corresponds to the ejectile charge (neutron) number. The residual excitation energy $E_x(i')$ is linked to the total energy $E^{\rm tot}$, the ejectile energy $E_{k'}$, and its separation energy $S(k')$ by $E_x(i') = E^{\rm tot} - E_{k'} - S(k')$. This $\mathcal{P}^{\rm pre}$ represents the feeding term for secondary pre-equilibrium emission. Note that for several p-h configurations this population is equal to zero.

In general, the pre-equilibrium population can be expressed in terms of the mother nucleus, excitation energy bins, and p-h configurations from which it is fed. The residual population is given by a generalization of Eq. (163), in which $\sigma^{\rm CF}(Z_C, N_C, E^{\rm tot})$ is replaced by the population of the p-h states left after the previous emission stage $\mathcal{P}^{\rm pre}(Z, N, p_\pi^0, h_\pi^0, p_\nu^0, h_\nu^0, E_x(i))$. Since several combinations of emission and internal transitions may lead to the same configuration, a summation is applied over the ejectiles treated in multiple pre-equilibrium (neutrons and protons), over the $(p_\pi^0, h_\pi^0, p_\nu^0, h_\nu^0)$ configurations with which the next step is started and over the mother excitation energy bins:

$$\begin{aligned}&\mathcal{P}^{\rm pre}(Z', N', p'_\pi, h'_\pi, p'_\nu, h'_\nu, E_x(i'))\\&= \sum_{k'=n,p}\sum_{p_\pi^0=1}^{p_\pi^{\max}}\sum_{h_\pi^0=1}^{h_\pi^{\max}}\sum_{p_\nu^0=1}^{p_\nu^{\max}}\sum_{h_\nu^0=1}^{h_\nu^{\max}}\sum_i\\&\mathcal{P}^{\rm pre}(Z, N, p_\pi^0, h_\pi^0, p_\nu^0, h_\nu^0, E_x(i))\\&\quad\times W_k(Z, N, p_\pi, h_\pi, p_\nu, h_\nu, E_x(i), E_{k'})\\&\quad\times\tau(Z, N, p_\pi, h_\pi, p_\nu, h_\nu, E_x(i))\\&\quad\times P(Z, N, p_\pi, h_\pi, p_\nu, h_\nu, E_x(i)),\end{aligned}\tag{204}$$

where the mother and daughter quantities are related by

$$\begin{aligned}Z &= Z' + Z_{k'},\\N &= N' + N_{k'},\\p_\pi &= p'_\pi + Z_{k'},\\h_\pi &= h'_\pi,\\p_\nu &= p'_\nu + N_{k'},\\h_\nu &= h'_\nu,\end{aligned}$$

$$E_x = E_x(i') + E_{k'} + S_{k'}.\tag{205}$$

In the computation, we thus need to keep track of every possible $(Z', N', p'_\pi, h'_\pi, p'_\nu, h'_\nu, E_x(i'))$ configuration, which is uniquely linked to a mother exciton state $(Z, N, p_\pi, h_\pi, p_\nu, h_\nu, E_x(i))$ through the ejectile characterized by $(Z_{k'}, N_{k'}, E_{k'})$. The term $P(Z, N, p_\pi, h_\pi, p_\nu, h_\nu, E_x(i))$ represents the part of the pre-equilibrium cross section that starts in $(Z, N, p_\pi^0, h_\pi^0, p_\nu^0, h_\nu^0, E_x(i))$ and survives emission up to a new p-h state $(Z, N, p_\pi, h_\pi, p_\nu, h_\nu, E_x(i))$. The initial condition is

$$P(Z, N, p_\pi^0, h_\pi^0, p_\nu^0, h_\nu^0, E_x(i)) = 1.\tag{206}$$

The part of $\mathcal{P}^{\rm pre}$ that does not feed a new pre-equilibrium population automatically goes to the multiple Hauser-Feshbach chain of Eq. (200).

The final expression for the multiple pre-equilibrium spectrum is very similar to Eq.(163)

$$\begin{aligned}\frac{d\sigma_k^{\rm mpreeq}}{dE_{k'}} &= \sum_{p_\pi^0=1}^{p_\pi^{\max}}\sum_{h_\pi^0=1}^{h_\pi^{\max}}\sum_{p_\nu^0=1}^{p_\nu^{\max}}\sum_{h_\nu^0=1}^{h_\nu^{\max}}\\&\quad\sum_i\mathcal{P}^{\rm pre}(Z, N, p_\pi^0, h_\pi^0, p_\nu^0, h_\nu^0, E_x(i))\\&\quad\sum_{p_\pi=p_\pi^0}^{p_\pi^{\max}}\sum_{h_\pi=h_\pi^0}^{h_\pi^{\max}}\sum_{p_\nu=p_\nu^0}^{p_\nu^{\max}}\sum_{h_\nu=h_\nu^0}^{h_\nu^{\max}}\\&\quad W_k(Z, N, p_\pi, h_\pi, p_\nu, h_\nu, E_x(i), E_{k'})\\&\quad\times\tau(Z, N, p_\pi, h_\pi, p_\nu, h_\nu, E_x(i))\\&\quad P(Z, N, p_\pi, h_\pi, p_\nu, h_\nu, E_x(i)).\end{aligned}\tag{207}$$

Apart from the exciton model TALYS offers another, slightly faster, method to determine multiple pre-equilibrium emission by Chadwick et al. [109,110], using the s-wave transmission coefficient. In this method, the multiple pre-equilibrium spectrum is given by the following expression:

$$\begin{aligned}\frac{d\sigma_k^{\rm mpreeq}}{dE_{k'}} &= \sum_{p_\pi^0=1}^{p_\pi^{\max}}\sum_{h_\pi^0=1}^{h_\pi^{\max}}\sum_{p_\nu^0=1}^{p_\nu^{\max}}\sum_{h_\nu^0=1}^{h_\nu^{\max}}\\&\sum_i\mathcal{P}^{\rm pre}(Z, N, p_\pi^0, h_\pi^0, p_\nu^0, h_\nu^0, E_x(i))\frac{1}{p_\pi^0 + p_\nu^0}\\&\quad\times\frac{\omega(Z_{k'}, h_\pi^0, N_{k'}, h_\nu^0, E_{k'} + S_{k'})}{\omega(p_\pi^0, h_\pi^0, p_\nu^0, h_\nu^0, E_x(i))}\\&\quad\times\omega(p_\pi^0 - Z_{k'}, h_\pi^0, p_\nu^0 - N_{k'}, h_\nu^0, E_x(i) - E_{k'} - S_{k'})\\&\quad\times T_s(E_{k'}).\end{aligned}\tag{208}$$

In this approach each residual p-h configuration created in the primary pre-equilibrium decay may have one or more excited particles in the continuum. Each of these excited particles can either be emitted or captured. The emission probability

is assumed to be well represented by the s-wave transmission coefficient $T_s(E_{k'})$.

8.3 Initially populated target nuclei

Usually, a TALYS calculation concerns a projectile with a certain incident energy and a target. For various applications, it is also of prime interest to introduce the possibility to start the decay from an initial population, i.e. an excited nucleus with fixed excitation energy or a population distributed over excitation energy, possibly characterized by given spin and parity distributions as well. Interesting applications concern, for example, the calculation of β-delayed processes starting from an initial β-strength function or the neutron and gamma decay from fission fragments. In the latter case, one can calculate the fragment distribution from fission, e.g. as described in Sect. 14 or from empirical methods, and assume a population per excitation energy and spin, of the excited light and heavy fission fragments. This distribution is given by

$$\sum_{I,\Pi}\sum_{i}[P^{\mathrm{HF}}(Z,N,E_x(i),I,\Pi), \tag{209}$$

and is then the starting point for a TALYS calculation. The initial population enters the Hauser-Feshbach scheme and the compound nucleus calculation proceeds as in Eq. (200). The emitted neutrons and photons can be recorded as well as the path from fission fragment to fission product. All relevant nuclear structure quantities are available since we simulate the process by a photon-induced reaction, the only difference being that we do not excite a single compound nucleus energy but directly fill the continuum bins and discrete levels according to our specified starting population. Also, there is no width fluctuation correction in this case. The initial population can be provided at two levels of detail. A full excitation energy-spin-parity population can be given, which is then interpolated on the internal excitation energy scheme of TALYS. Alternatively, only the total population per excitation energy can be given, after which the spin-parity-dependent population is determined by multiplying it with the spin distribution of Eq. (213). This option is the basis for the calculation of fission neutron observables and fission yields. There are however more applications for this feature, such as coupling a high-energy intranuclear cascade code with TALYS, the latter taking care of the low energy evaporation part including all its quantum-mechanical conservation rules.

9 Nuclear masses and deformations

At the level of nuclear physics that is relevant to TALYS, the mass can be considered as the most fundamental property of the nucleus, and directly affects all the outcomes of a nuclear reaction calculation. Separation energies and Q-values directly depend on the masses of the involved nuclides, and determine whether certain reactions can take place or not. The nuclear community has invested a lot of effort to measure, compile and evaluate experimental nuclear masses [111] and simultaneously theoretical nuclear structure models have been developed to predict as accurately and reliably as possible, masses and other nuclear structure properties, in particular for experimentally inaccessible nuclei.

In TALYS, we use both the real mass M in atomic mass units ($amu = 931.49386$ MeV) and the mass excess $\Delta M = (M - A) * amu$ in MeV from the mass tables. The latter are retrieved from tables for a more precise calculation of separation energies. For example, the neutron separation energy of a nucleus (Z, N) is

$$S_n(Z,N) = M(Z,N-1) - M(Z,N) + M(n), \tag{210}$$

but we have actually implemented

$$S_n(Z,N) = \Delta M(Z,N-1) - \Delta M(Z,N) + \Delta M(n), \tag{211}$$

where $\Delta M(n)$ is the neutron mass excess and similarly for the other light particles.

For reaction Q-values one needs the masses of two nuclides. The Q-value is the difference between two separation energies,

$$Q(a,b) = S_a(Z,N) - S_b(Z,N). \tag{212}$$

If the experimental mass excess is known for only one of the two nuclei involved, at the edge of the experimental mass table, we take both *theoretical* mass excesses to calculate the Q-value, for consistency. TALYS includes many different theoretical models for predicting nuclear masses and basic structure properties like deformations or matter densities. In practice, theoretical models are only used for exotic nuclides for which no experimental data is available. The experimental mass table contains data for 2550 nuclei. While for nuclear technology only a band of 1000–1500 nuclides around the valley of stability is relevant, the other exotic ones are essential for astrophysics.

9.1 Experimental nuclear masses

The most recent generally used Atomic Mass Evaluation (AME) is the 2020 update of Ref. [111] which provides experimental atomic masses for 2550 nuclei for TALYS. An additional 1008 atomic masses, known as "recommended" masses and extracted from the 2020 AME on the basis of the smooth property of the mass surface [111] are also included in TALYS.

Obviously, around the valley of stability we need to use experimentally determined masses and cannot afford to deviate from this, especially if we want to reproduce experimental reaction data and be credible when providing data for nuclear applications.

9.2 Theoretical nuclear masses

Theoretical masses are needed outside the range where measurements have been performed and sometimes exhibit a remarkable dispersion, especially when applied in nuclear reaction models. Despite the many mass models available [112,113], TALYS only includes a handful of those. These mass predictions are obtained with physical models that differ quite significantly in their essence and correspond to the mostly used ones for applications. They all show a relative small rms deviation $\sigma_{rms} < 0.8$ MeV with respect to the 2457 known masses with $Z, N \geq 8$ [111]. The TALYS options include

- the mean-field Skyrme-Hartree-Fock-Bogoliubov nuclear mass model (HFB24) based on the BSk24 Skyrme interaction [114] with $\sigma_{rms} = 0.56$ MeV. This is our default model for theoretical masses,
- the mean-field Gogny-Hartree-Fock-Bogoliubov nuclear mass model based on the D1M interaction [115] with $\sigma_{rms} = 0.81$ MeV,
- the macroscopic-microscopic finite-range droplet model (FRDM) [116] with $\sigma_{rms} = 0.61$ MeV,
- the 10-parameter Duflo-Zuker (DZ) mass formula [117] with $\sigma_{rms} = 0.61$ MeV, included as a subroutine in TALYS. This model is considered in particular if a nuclide is even outside the mass table requested or can be used simply as an interesting alternative.

The difference in theoretical mass estimates may have an enormous impact on cross section calculations for exotic nuclides. Figure 14 shows (n, γ) cross section ratios at 100 keV for the neutron-rich Sn isotopes, for different mass models relative to the default HFB24. Up to $A = 140$, experimental or recommended masses are available from the AME [111] and consequently differences in the cross section calculation are only due to the different deformations predicted by the various mass models. For $A > 140$ targets, major discrepancies in the radiative neutron capture cross sections are observed due to the different Q-values estimated by the various mass models. Deviations by many orders of magnitude can be obtained as soon as exotic n-rich nuclei are concerned. Apart from the TALYS mass models, also the WS4 model from Ref. [118] is included in the comparison.

Note that these (n, γ) cross sections are calculated with the HFB+combinatorial level densities, see Sect. 11 and

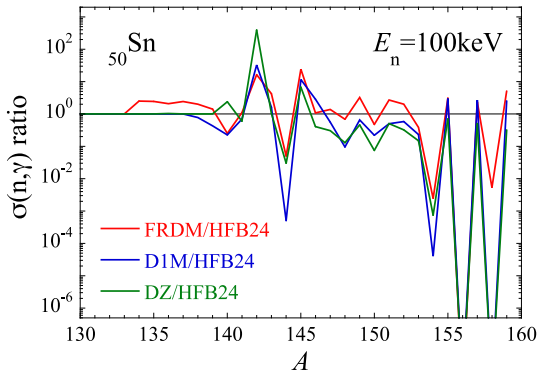

Fig. 14 Illustration for the Sn neutron-rich isotopes of the dispersion obtained in the (n, γ) cross sections calculated at $E_n = 100$ KeV with different TALYS mass models. No direct capture contribution is included

D1M+QRPA+0lim photon strength functions, see Sect. 12. No direct capture contribution is included.

9.3 Deformation parameters

Deformation parameters are needed to estimate many different quantities in TALYS. First of all, as input to OMP calculations for deformed nuclides, by means of the coupled-channels (for strong deformations) or DWBA (for weak deformations) formalism. This requires values for (at least) β_2 and for rotational nuclides also β_4 and β_6. In addition, deformation parameters are used to estimate nuclear level density parameters, giant dipole parameters, as well as moments of inertia. They are consistently taken from the same model used for the atomic mass estimates.

9.4 Isotopic abundances

TALYS can calculate nuclear reaction data for natural elements. The isotopic abundances are taken from RIPL [9] (which are equal to those of the Nuclear Wallet Cards from Brookhaven National Laboratory). For a natural target element, a TALYS calculation is performed for each stable isotope, after which the results are summed up weighted by the respective isotopic abundances.

10 Discrete levels

The discrete level scheme of a nucleus is essential for nuclear reaction simulations, as it plays a central role in both direct and compound nuclear reactions. The complete properties of each discrete level play an important role in:

- coupled-channels or DWBA calculations,

- validating of the low-energy part of the level density, and establishing the associated level density parameters,
- estimating the Hauser-Feshbach decay in which the transition to each discrete level competes with all other open channels,
- estimating the decay from higher to lower discrete levels in residual nuclides (a) for gamma-ray intensities for each transition, and (b) for the determination of the ratio between isomeric and ground state production.

For the current capabilities of TALYS, the following properties for each discrete level is required: the sequence number, energy, spin, parity, half-life (especially for long-lived isomers), number of branchings for gamma decay to lower levels, branching ratios to lower levels, and the electron conversion coefficients. More details about such properties and their availability in TALYS are given below.

10.1 Completeness and property assignment

Ideally, discrete level information would all be available from measurements, and indeed an extensive experimental discrete level compilation and evaluation can be constructed from the ENSDF [119] and NUBASE [120] databases. These two databases are the source for the RIPL database [9] for discrete levels, where NUBASE provides the most recent evaluation for ground states and isomers, while ENSDF provides the entire level scheme. Unfortunately, to have partial data about measured discrete levels is not enough for TALYS, or any nuclear model code. The information on the level scheme needs to be complete, i.e. for each discrete level all aforementioned properties need to be known, so that Hauser-Feshbach decay and gamma-ray cascade can be properly calculated, and no reaction flux remains locked up in a level that cannot decay because, for example, the corresponding spin or branching ratios remain unknown. Therefore, where information is missing in RIPL, it is added to the TALYS discrete level files with some educated guess. Each nuclide has a maximum level number until which all properties need to be known, experimentally or theoretically. Beyond that level, level densities take over for the description of the reaction process.

For nuclides far away from the valley of stability, the discrete level database has been completed with the HFB ground state estimates for spin and parity from the mass database of Ref. [121], so that at least the discrete level and mass databases span the same range of nuclides.

Each discrete level has a spin and parity. Often, the measured level scheme from ENSDF is complete in terms of levels and energies up to a certain level number, but the spin may not be specified. All one can do then is to assign the spin and try to maximize the likelihood that it is correct. For that, a histogram of the measured spins of all levels up to the level of interest with the unmeasured spin is built. Next, this histogram is compared with a Fermi gas spin distribution,

$$R_F(E_x, J) = \frac{2J+1}{2\sigma^2} \exp\left[-\frac{(J+\frac{1}{2})^2}{2\sigma^2}\right], \tag{213}$$

where

$$\sigma^2 = \left(0.83A^{0.26}\right)^2 \tag{214}$$

gives a reasonable estimate [122] for the spin distribution of discrete levels with energies up to a few MeV. The value assigned to the level with unknown spin is that of the histogram bin with measured spin values which has the largest underestimation of the theoretical spin distribution. Hence, when there are many levels with unknown spins the final distribution of measured plus assigned spins will approach the theoretical one. We stress here that the likelihood that the assigned value is wrong is large, but at least the assignment procedure is based on some physical justifications and not random. A similar procedure is followed for unknown parities, we assign the parity which leads to a more equal parity distribution for all levels up to that level. Obviously, a more rigorous fundamental approach to estimate discrete level properties based on theory e.g. on the basis of shell model calculations, including collective states, would be welcome.

In addition an assignment procedure needs to be followed for branching ratios of levels which decay to lower levels. Omission of branching ratios for a certain level, e.g. because they have not been measured, would mean that there is no gamma decay from that level, locking up the reaction flux at that level and consequently leading to an underestimate of the cross section to the low-lying levels. To assign branching ratios we make use of the downward photon strength function (PSF) $\overleftarrow{f_{X\ell}}$, which will be discussed in more detail in Sect. 12. For each initial level I, the probability of decay to a final level F is given by electric (E) or magnetic (M) radiation, with $E1$ and $M1$ as the strongest transitions. The gamma energy, multipolarity and parity are given by

$$\begin{aligned} E_\gamma &= E(I) - E(F), \\ l &= \mid J(I) - J(F) \mid, \\ P' &= (-1)^{P(I)P(F)}, \end{aligned} \tag{215}$$

leading to the transmission coefficient

$$\mathcal{T}_{X\ell}(E_\gamma, l, P') = 2\pi \overleftarrow{f_{X\ell}}(E_\gamma) E_\gamma^{2\ell+1}, \tag{216}$$

related to the PSF $\overleftarrow{f_{X\ell}}$, as defined and discussed in Sect. 12, and to the branching ratio Br to each final level through

$$Br(I \rightarrow F) = \mathcal{T}_{X\ell}(E_\gamma, l, P') / \sum_{i=1}^{I-1} \mathcal{T}_{X\ell}(E_\gamma, l, P'). \quad (217)$$

TALYS retains the 4 largest branching ratios and normalizes them to 1. Finally, the electron conversion coefficient estimates what fraction of the decay goes to electron conversion and to the gamma-ray intensity. It is specified when the branching ratio is experimentally known, in other cases TALYS keeps it at the constant value of 0.001.

Fortunately, for important nuclides, detailed information for the lowest 10–30 discrete levels is known, but there may be exceptions. Therefore, it is absolutely essential in such a combined experimental/theoretical database to record exactly when discrete level properties have been assigned using the theoretical considerations mentioned above, and this is done in the TALYS discrete level database. This also allows the user to have some adjustment freedom for fitting experimental nuclear reaction data, by e.g. changing a spin or branching ratio. Examples of level schemes with assigned values and their explanation can be found in the TALYS manual.

10.2 Coupling schemes for deformed nuclides

An important application of the discrete level scheme is the coupling scheme for coupled-channels calculations. The deformation of a nucleus can be characterized by the deformation length δ_L or deformation parameter β_L. In TALYS, the type of collectivity can be spherical, vibrational, rotational and asymmetric rotational, which corresponds with the generally used options that ECIS gives for deformed nuclides. For all stable nuclides, the coupling scheme has been specified in a database whereby the user can choose for more or less complexity by either including or excluding specific rotational and vibrational bands. For the rotational band, the deformation parameter β_2, β_4 and β_6 can be given. If these β parameters are not given they are automatically retrieved from the HFB mass directory, as described in Sect. 9 on nuclear masses. In certain cases, the deformation parameters have been adjusted to fit data, and then they are added as extra information to the coupling schemes. Also, for the first level of a vibrational band the deformation parameter is given. The vibrational-rotational model is thus invoked if within the rotational model also states belonging to a vibrational band are specified. The level of complexity of rotational or vibrational-rotational calculations can all be specified. Weakly coupled levels are treated with DWBA.

As an example, for ^{40}Ca, a coupled-channels calculation with a vibrational model will automatically be invoked. Levels 2 (3^- at 3.737 MeV, with $\delta_3 = 1.34$), 3 (2^+ at 3.904 MeV, with $\delta_2 = 0.36$), 4 (5^- at 4.491 MeV, with $\delta_5 = 0.93$), will all be coupled individually as one-phonon states. There is also an option to enforce a spherical OMP calculation. In that case all levels will be treated with DWBA.

The coupling schemes can become fairly complex. For example, for ^{238}U, the basis for the coupling scheme is a rotational model in which 6 excited levels can be coupled in one rotational band, while there are up to 5 vibrational bands which can be included [54], leading to a total of 23 coupled levels. TALYS provides various options to make such coupling schemes as simple or complex as possible. More details about coupled-channels options using a variety of vibrational and rotational coupling schemes have been discussed in Sect. 3.

11 Level densities

The nucleus is a quantum system in which the first low-energy excitations from the ground state are characterized by several discrete states with quantum numbers such as energy, spin and parity, as described in Sect. 10. Beyond several tens of discrete levels not all levels are experimentally observed and one has to resort to a statistical approach to describe the excited nucleus. Depending on the nuclide, one observes that typically somewhere between 15 and 40 levels, the measured number of cumulative discrete levels starts to deviate from the theoretical number of levels that is predicted by a quantum-statistical approach. Several models for the level density have been developed in the past, which range from phenomenological analytical expressions to tabulated level densities derived from microscopic nuclear structure models.

The *level density* $\rho(E_x, J, \Pi)$ corresponds to the number of nuclear levels per MeV around an excitation energy E_x, for a certain spin J and parity Π. The *total level density* $\rho^{\rm tot}(E_x)$ corresponds to the total number of levels per MeV around E_x, and is obtained by summing the level density over spin and parity,

$$\rho^{\rm tot}(E_x) = \sum_{J,\Pi} \rho(E_x, J, \Pi). \quad (218)$$

An important constraint for a level density model is that at an excitation energy around the neutron separation energy S_n, it reproduces the density of observed resonances obtained from low-energy neutron measurements. In particular, D_0, the average s-wave resonance spacing at S_n, which is obtained from the available experimental data set of s-wave resonances [9,75], is related to the inverse of the level density. The following equation applies,

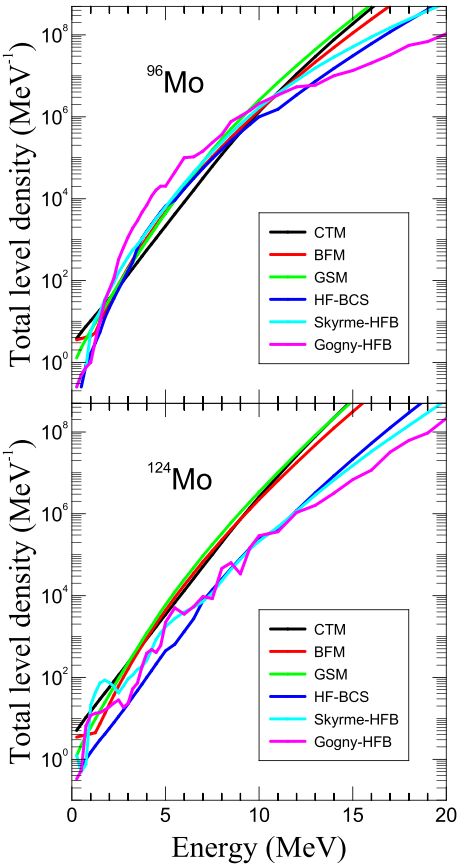

Fig. 15 Level density models implemented in TALYS for the stable ^{96}Mo and the exotic ^{124}Mo. The use of Eq. (230), enabling to adjust the level density models for ^{96}Mo, results in an overall agreement between the various models while a clear difference is observed for ^{124}Mo for which neither experimental low-lying levels nor s-wave mean spacing data are available

$$\frac{1}{D_0} = \sum_{J=|I-\frac{1}{2}|}^{J=I+\frac{1}{2}} \rho(S_n, J, \Pi), \tag{219}$$

where I is the spin of the target nucleus.

The other important constraint is that at low excitation energies, the total level density reproduces the observed number of cumulative discrete levels. This means that

$$N_U = N_L + \int_{E_L}^{E_U} dE_x \rho^{\text{tot}}(E_x), \tag{220}$$

where N_L and its corresponding energy E_L is an offset, i.e. a low-energy level which is not expected to fall within the statistical level density regime, and the total level density is required to reproduce the number of levels until a certain level N_U with energy E_U. Beyond N_U it is expected that experimental levels are missing.

As an illustration, the total level density obtained with the various models implemented in TALYS are compared in Fig. 15 for two nuclei, namely ^{96}Mo and the exotic ^{124}Mo.

The complete mathematical details of the various level density models in TALYS can be found in Ref. [122]. In order to make this paper self contained, we restrict ourselves to the formulae which have been implemented and leave out the derivation.

11.1 Phenomenological level densities

TALYS has the option to use three phenomenological level density models, namely the Constant Temperature Model (CTM) [122], the Back-shifted Fermi gas Model (BFM) [122], and the Generalized Superfluid Model (GSM) [123, 124]. Most of the phenomenological level density models developed in the past belong to one of these three categories. The objective of Ref. [122] was to produce consistent parameterizations for both the CTM and BFM based on the same experimental data set. Both models are summarized below.

When level densities are given by analytical expressions they are usually factorized as follows

$$\rho(E_x, J, \Pi) = P(E_x, J, \Pi) R(E_x, J) \rho^{\text{tot}}(E_x), \tag{221}$$

where $P(E_x, J, \Pi)$ is the parity distribution and $R(E_x, J)$ the spin distribution. In all phenomenological level density models in TALYS the parity equipartition is assumed, i.e.

$$P(E_x, J, \Pi) = \frac{1}{2}, \tag{222}$$

while the microscopic models are parity-dependent and may not have equal parity distributions.

11.1.1 The Fermi Gas Model

The Fermi Gas model (FGM) lies at the basis of all phenomenological models and is based on the assumption that the single-particle states which construct the excited levels of the nucleus are equally spaced, and that collective levels are absent. The Fermi gas level density is [125]

$$\rho_F(E_x, J, \Pi) = \frac{1}{2} \frac{2J+1}{2\sqrt{2\pi}\sigma^3} \exp\left[-\frac{(J+\frac{1}{2})^2}{2\sigma^2}\right] \times \frac{\sqrt{\pi}}{12} \frac{\exp\left[2\sqrt{aU}\right]}{a^{1/4}U^{5/4}}, \tag{223}$$

where the first factor $\frac{1}{2}$ represents the equiparity distribution and σ^2 is the spin cut-off parameter, which represents the width of the angular momentum distribution. The effective excitation energy U is defined by

$$U = E_x - \Delta, \tag{224}$$

where the energy shift Δ is the pairing energy which is included to simulate the known odd-even effects in nuclei.

The underlying idea is that Δ accounts for the fact that pairs of nucleons must be broken before each component can be excited individually. In practice, Δ plays an important role as adjustable parameter to reproduce observables, and its definition can vary depending on the level density model.

Equation (223) also contains the level density parameter a, which in practice can either be extracted, through Eq. (219), from experimental s-wave resonance spacings, if available, or if not, from global systematics. In contemporary analytical models, the a-parameter is energy-dependent to take shell (and, in some cases, pairing) effects into account. Equation (223) is a special case of the factorization given by Eq. (221) with the Fermi gas spin distribution of Eq. (231).

Summing $\rho_F(E_x, J, \Pi)$ over all spins and parities yields for the total Fermi gas level density

$$\rho_F^{\text{tot}}(E_x) = \frac{1}{\sqrt{2\pi}\sigma}\frac{\sqrt{\pi}}{12}\frac{\exp\left[2\sqrt{aU}\right]}{a^{1/4}U^{5/4}}. \tag{225}$$

These equations show that ρ_F^{tot} and ρ_F are determined by three parameters, a, σ and Δ. The first two of these have specific energy dependencies that will now be discussed separately, while we postpone the discussion of Δ to the sections on the various specific level density models.

11.1.2 The level density parameter a

For the level density parameter a we adopt the formula of Ignatyuk et al. [123], who argued that energy-dependent shell effects should be effectively included in the level density through an energy dependent expression for a. This expression takes into account the presence of shell effects at low energy [126] and their disappearance at high energy in a phenomenological manner. It reads,

$$a = a(E_x) = \tilde{a}\left(1 + \delta W\frac{1-\exp[-\gamma U]}{U}\right). \tag{226}$$

Here, $\tilde{a}$ is the asymptotic level density value one would obtain in the absence of any shell effects, i.e. $\tilde{a} = a(E_x \longrightarrow \infty)$ in general, but also $\tilde{a} = a(E_x)$ for all E_x if $\delta W = 0$. The damping parameter γ determines how rapidly $a(E_x)$ approaches $\tilde{a}$ at increasing excitation energies. Finally, δW is the shell correction energy. The absolute magnitude of δW determines how different $a(E_x)$ is from $\tilde{a}$ at low energies, while the sign of δW determines whether $a(E_x)$ decreases or increases as a function of E_x.

The asymptotic value $\tilde{a}$ is given by the smooth form

$$\tilde{a} = \alpha A + \beta A^{2/3}, \tag{227}$$

where A is the mass number, while the following systematic formula for the damping parameter is used,

$$\gamma = \frac{\gamma_1}{A^{\frac{1}{3}}} + \gamma_2. \tag{228}$$

In Eqs. (227)–(228), α, β, γ_1 and γ_2 are free parameters that have been determined to give the best global level density description over the full range of nuclides for which experimental D_0 data is available [122].

The shell correction energy δW is defined as the difference between the experimental mass of the nucleus M_{exp} and its mass according to the spherical liquid-drop model M_{LDM},

$$\delta W = M_{\text{exp}} - M_{\text{LDM}}. \tag{229}$$

The experimental mass is taken from the 2020 AME [111] and M_{LDM} from the parameterizations available in Ref. [127] or [122].

We note that the parameters $\tilde{a}$, δW and γ are all adjustable. If the level density parameter at the neutron separation energy $a(S_n)$ cannot be extracted from an experimental D_0 value, TALYS considers the above systematics (Eq. 227).

By default, TALYS considers the best nominal level density ρ_{nom} adjusted to the discrete level scheme and D_0, whenever available. However, for adjustment purposes, flexibility can be achieved either by varying directly all the related parameters or through a scaling function, i.e.

$$\rho(E_x, J, \pi) = \exp(c\sqrt{E_x - \delta})\rho_{nom}(E_x - \delta, J, \pi) \tag{230}$$

where $c = 0$ and $\delta = 0$ correspond to unaltered nominal level densities. The "pairing shift" δ simply implies obtaining the level density from the table or formula at a different energy. The parameter c plays a role similar to that of the level density parameter a within the phenomenological models (see Eq. 223). Adjusting c and δ together gives adjustment flexibility at both low and higher energies and allows the user to adjust level densities for cross section fitting.

11.1.3 The spin cut-off parameter

The spin cut-off parameter σ represents the width of the angular momentum distribution of the level density,

$$R_F(E_x, J) = \frac{2J+1}{2\sigma^2}\exp\left[-\frac{(J+\frac{1}{2})^2}{2\sigma^2}\right]. \tag{231}$$

It is given by

$$\sigma^2 = \sigma_F^2(E_x) = I_0\frac{a}{\tilde{a}}t, \tag{232}$$

with $\tilde{a}$ from Eq. (227) and

$$I_0 = \frac{\frac{2}{5} m_0 R^2 A}{(\hbar c)^2}, \tag{233}$$

where $R = 1.2A^{1/3}$ is the radius, and m_0 the neutron mass, and the thermodynamic temperature t,

$$t = \sqrt{\frac{U}{a}}. \tag{234}$$

This gives

$$\sigma_F^2(E_x) = 0.01389 \frac{A^{5/3}}{\tilde{a}} \sqrt{aU}. \tag{235}$$

Analogous to the level density parameter, we have to account for low excitation energies for which Eq. (235) is not defined ($E_x \leq \Delta$) or less appropriate. This leads to an alternative method to determine the spin cut-off parameter, namely from the spins of the low-lying discrete levels, see Ref. [122]. It can be derived that

$$\sigma_d^2 = \frac{1}{3 \sum_{i=N_L}^{N_U} (2J_i + 1)} \sum_{i=N_L}^{N_U} J_i (J_i + 1)(2J_i + 1). \tag{236}$$

where J_i is the spin of discrete level i. Extracting these spins from the discrete level file readily gives an estimate of σ_d^2. In TALYS, σ_d^2 can be used on a nucleus-by-nucleus basis, when discrete levels are known. For cases where either Eqs. (235) or (236) are not applicable, e.g. because there are no discrete levels or $U = E_x - \Delta$ is negative, TALYS adopts the systematics

$$\sigma_d^2 = \left(0.83 A^{0.26}\right)^2 \tag{237}$$

which gives a reasonable estimate for excitation energies of the order of 1–2 MeV.

The final functional form for $\sigma^2(E_x)$ is a combination of Eqs. (235) and (236). Defining $E_d = \frac{1}{2}(E_L + E_U)$ as the energy in the middle of the $N_L - N_U$ region, we assume σ_d^2 is constant up to this energy and can then be linearly interpolated to the expression given by Eq. (235). We choose the matching point to be the neutron separation energy S_n of the nucleus under consideration, i.e.

$$\begin{aligned} \sigma^2(E_x) &= \sigma_d^2 \ \text{ for } \ 0 \leq E_x \leq E_d \\ &= \sigma_d^2 + \frac{E_x - E_d}{S_n - E_d} (\sigma_F^2(E_x) - \sigma_d^2) \\ &\quad \text{for } \ E_d \leq E_x \leq S_n \\ &= \sigma_F^2(E_x) \ \text{ for } \ E_x \geq S_n. \end{aligned} \tag{238}$$

11.1.4 Constant temperature model

In the CTM, as introduced by Gilbert and Cameron [128], the excitation energy range is divided into a low energy part from 0 MeV up to a matching energy E_M, where the so-called constant temperature law applies and a high energy part above E_M, where the Fermi gas model applies. Hence, the total level density reads

$$\begin{aligned} \rho^{\text{tot}}(E_x) &= \rho_T^{\text{tot}}(E_x), \quad \text{if } E_x \leq E_M, \\ &= \rho_F^{\text{tot}}(E_x), \quad \text{if } E_x \geq E_M, \end{aligned} \tag{239}$$

and similarly for the level density

$$\begin{aligned} \rho(E_x, J, \Pi) &= \frac{1}{2} R_F(E_x, J) \rho_T^{\text{tot}}(E_x), \text{ if } E_x \leq E_M, \\ &= \rho_F(E_x, J, \Pi), \text{ if } E_x \geq E_M. \end{aligned} \tag{240}$$

Note that the spin distribution of Eq. (231) is also used in the constant temperature region, including the low-energy behaviour for the spin cut-off parameter as expressed by Eq. (238).

For the Fermi gas regime, TALYS uses the effective excitation energy $U = E_x - \Delta^{\text{CTM}}$, where the energy shift is given by

$$\Delta^{CTM} = \chi \frac{12}{\sqrt{A}}, \tag{241}$$

with

$$\begin{aligned} \chi &= 0, \ \text{ for } \ \text{odd} - \text{odd}, \\ &= 1, \ \text{ for } \ \text{odd} - \text{even}, \\ &= 2, \ \text{ for } \ \text{even} - \text{even}. \end{aligned} \tag{242}$$

The constant temperature part of the total level density reads

$$\rho_T^{\text{tot}}(E_x) = \frac{dN(E_x)}{dE_x} = \frac{1}{T} \exp\left(\frac{E_x - E_0}{T}\right), \tag{243}$$

while for higher energies the total level density is given by Eq. (225). Ref. [122] gives the details of the matching problem between the two parts and the resulting parameters for the CTM model. When the levels N_L and N_U are chosen such that $\rho_T(E_x)$ gives the best description of the observed discrete states, the matching energy E_M between the constant temperature part and the Fermi gas part as well as the parameters E_0 and T can be found by an iterative procedure.

For nuclides for which no, or not enough, experimental discrete levels are available, TALYS relies on empirical formula for the temperature. For the effective model,

$$T = -0.22 + \frac{9.4}{\sqrt{A(1 + \gamma \delta W)}}, \tag{244}$$

and for the collective model to be discussed in Sect. 11.1.6

$$T = -0.25 + \frac{10.2}{\sqrt{A(1+\gamma\delta W)}}, \tag{245}$$

where γ is taken from Eq. (228). Next, we directly obtain E_M and E_0 solving the matching problem, see Ref. [122]. Again, Eqs. (244) and (245) were obtained by fitting all individual values of the nuclides for which sufficient discrete level information exists. In a few cases, the global expression for T leads to a value for E_M which is clearly off scale. In that case, we resort to empirical expressions for the matching energy. For the effective model

$$E_M = 2.33 + 253/A + \Delta^{CTM}, \tag{246}$$

and for the collective model

$$E_M = 2.67 + 253/A + \Delta^{CTM}, \tag{247}$$

after which T can be obtained.

11.1.5 The Back-shifted Fermi gas Model

In the BFM [129], the pairing energy is treated as an adjustable parameter and the Fermi gas expression is used all the way down to zero energy. Hence the total level density is given by Eq. (225) and the level density by Eq. (223). For the BFM, these expressions, as well as the energy-dependent expressions for a and σ^2, contain the effective excitation energy $U = E_x - \Delta^{\mathrm{BFM}}$, where the energy shift is given by

$$\Delta^{BFM} = \chi\frac{12}{\sqrt{A}} + \delta, \tag{248}$$

with

$$\begin{aligned}\chi &= -1, \text{ for odd} - \text{odd},\\ &= 0, \text{ for odd} - \text{even},\\ &= 1, \text{ for even} - \text{even},\end{aligned} \tag{249}$$

and δ is a free parameter adjusted on experimental data, if available.

A problem of the original BFM, which may have hampered its use as the default level density option in nuclear model analyses, is the divergence of Eq. (223) when U goes to zero. A solution to this problem has been provided by Grossjean and Feldmeier [130], and has been put into a practical form by Demetriou and Goriely [131], and is adopted in TALYS. The expression for the total BFM level density is

$$\rho^{\mathrm{tot}}_{\mathrm{BFM}}(E_x) = \left[\frac{1}{\rho^{\mathrm{tot}}_F(E_x)} + \frac{1}{\rho_0(t)}\right]^{-1}, \tag{250}$$

where ρ_0 is given by

$$\rho_0(t) = \frac{\exp(1)}{24\sigma}\frac{(a_n+a_p)^2}{\sqrt{a_n a_p}}\exp(4a_n a_p t^2), \tag{251}$$

where $a_n = a_p = a/2$ and t is given by Eq. (234).

With the usual spin distribution, the level density reads

$$\rho_{\mathrm{BFM}}(E_x, J, \Pi) = \frac{1}{2}\frac{2J+1}{2\sigma^2}\exp\left[-\frac{(J+\frac{1}{2})^2}{2\sigma^2}\right] \times \rho^{\mathrm{tot}}_{\mathrm{BFM}}(E_x). \tag{252}$$

In sum, there are two adjustable parameters for the BFM, a and δ.

11.1.6 Collective effects in the level density

All the previously described models do not explicitly account for collective effects. However, it is well known that generally the first excited levels of nuclei result from coherent excitations of the fermions it contains. The Fermi gas model is not appropriate to describe such levels. Nevertheless, the models presented so far can still be applied successfully in most cases since they incorporate collectivity in the level density in an effective way through a proper choice of the energy-dependent level density parameters.

In some calculations, especially if the disappearance of collective effects with excitation energy plays a role (e.g. in the case of fission), one would like to model the collective effects in more detail. It can be shown that the collective effects may be accounted for explicitly by introducing collective enhancement factors on top of an intrinsic level density $\rho_{F,\mathrm{int}}(E_x, J, \Pi)$. Then, the deformed Fermi gas level density $\rho_{F,\mathrm{def}}(E_x, J, \Pi)$ reads

$$\rho_{F,\mathrm{def}}(E_x, J, \Pi) = K_{\mathrm{rot}}(E_x)K_{\mathrm{vib}}(E_x) \times \rho_{F,\mathrm{int}}(E_x, J, \Pi). \tag{253}$$

K_{rot} and K_{vib} correspond to the rotational and vibrational enhancement factors, respectively. If K_{rot} and K_{vib} are explicitly accounted for, $\rho_{F,\mathrm{int}}(E_x, J, \Pi)$ should now describe purely single-particle excitations, and can be determined again by using the Fermi gas formula. Obviously, the level density parameter a of $\rho_{F,\mathrm{int}}$ will be different from that of the effective level density described before. More precisely, as illustrated in Fig. 16, the level density parameter is much lower when collective effects are explicitly treated than it is without an explicit treatment.

The vibrational enhancement of the level density is approximated [9], by

$$K_{\mathrm{vib}} = \exp[\delta S - (\delta U/t)], \tag{254}$$

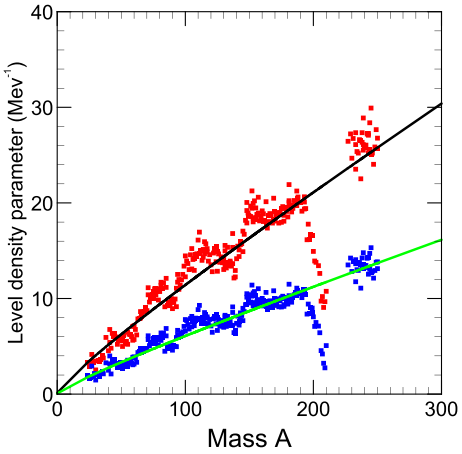

Fig. 16 Level density parameter required to fit D_0 values at S_n as function of the mass for the BFM model with (blue squares) and without (red squares) an explicit treatment of collective effects. The black and green lines represent the asymptotic limit (Eq. (227) for the two situations.)

where δS and δU are changes in the entropy and excitation energy, respectively, resulting from the vibrational modes and t is the nuclear temperature given by Eq. (234). These changes are described by the Bose gas relationships, i.e

$$\delta S = \sum_i (2\lambda_i + 1)\Big[(1+n_i)\ln(1+n_i) - n_i \ln n_i\Big],$$
$$\delta U = \sum_i (2\lambda_i + 1)\omega_i n_i, \tag{255}$$

where ω_i are the energies, λ_i the multipolarities, and n_i the occupation numbers for vibrational excitations at a given temperature. The disappearance of collective enhancement of the level density at high temperatures can be taken into account by defining the occupation numbers in terms of the equation

$$n_i = \frac{\exp(-\gamma_i/2\omega_i)}{\exp(\omega_i/t) - 1}, \tag{256}$$

where γ_i are the spreading widths of the vibrational excitations. This spreading of collective excitations in nuclei should be similar to the zero-sound damping in a Fermi liquid, and the corresponding width can be written as

$$\gamma_i = C(\omega_i^2 + 4\pi^2 t^2). \tag{257}$$

The value of $C = 0.0075\, A^{1/3}$ was obtained from the systematics of the neutron resonance densities of medium-weight nuclei [132]. TALYS adopts a modified systematics [133], which includes shell effects to estimate the phonon energies (in MeV), namely

$$\omega_2 = 65 A^{-5/6}/(1 + 0.05\delta W), \tag{258}$$

for the quadrupole vibrations and

$$\omega_3 = 100 A^{-5/6}/(1 + 0.05\delta W), \tag{259}$$

for the octupole excitations.

An alternative estimation of the vibrational collective enhancement factor is given by Iljinov et al. [134]

$$K_{\rm vib}(E_x) = \exp\left(0.0555 A^{\frac{2}{3}} t^{\frac{4}{3}}\right). \tag{260}$$

A more important contribution to the collective enhancement of the level density originates from rotational excitations. Its effect is not only much stronger ($K_{\rm rot} \sim 10 - 100$ whereas $K_{\rm vib} \sim 3$), but the form for the rotational enhancement depends on the nuclear shape as well. This makes it crucial, among others, for the description of fission cross sections.

The expression for the rotational enhancement factor depends on the deformation, see Capote et al. [9,135]. Basically, $K_{\rm rot}$ is equal to the perpendicular spin cut-off parameter $\sigma_\perp^2$,

$$\sigma_\perp^2 = I_\perp t, \tag{261}$$

with the rigid-body moment of inertia perpendicular to the symmetry axis given by

$$I_\perp = I_0\left(1 + \frac{\beta_2}{3}\right) = 0.01389 A^{5/3}\left(1 + \frac{\beta_2}{3}\right), \tag{262}$$

where β_2 is the ground-state quadrupole deformation, which is consistently taken from TALYS nuclear structure database. Hence,

$$\sigma_\perp^2 = 0.01389 A^{5/3}\left(1 + \frac{\beta_2}{3}\right)\sqrt{\frac{U}{a}}. \tag{263}$$

For high excitation energies, it is known that the rotational behavior vanishes. To take this into account, it is customary to introduce a phenomenological damping function $f(E_x)$ which is equal to 1 in the purely deformed case and 0 in the spherical case. The expression for the level density is then

$$\rho(E_x, J, \Pi) = K_{\rm rot}(E_x) K_{\rm vib}(E_x) \rho_{F,\rm int}(E_x, J, \Pi), \tag{264}$$

where

$$K_{\rm rot}(E_x) = \max([\sigma_\perp^2 - 1] f(E_x) + 1, 1). \tag{265}$$

The function $f(E_x)$ is taken as a Fermi function,

$$f(E_x) = \frac{1}{1 + \exp(\frac{E_x - E_{col}^{g.s.}}{d_{col}^{g.s.}})}, \tag{266}$$

which yields the desired property of $K_{\rm rot}$ going to 1 for high excitation energy. Little is known about the parameters that govern this damping, although attempts have been made (see e.g. Ref. [136]). By default, the values of $E_{col}^{g.s.} = 30$ MeV, $d_{col}^{g.s.} = 5$ MeV are adopted by TALYS though these parameters are adjustable.

Finally, these collective enhancement expressions can be applied to the various phenomenological level density models. The CTM formalism can be extended with explicit collective enhancement, i.e. the total level density reads

$$\begin{aligned}\rho^{\rm tot}(E_x) &= \rho_T^{\rm tot}(E_x), \quad \text{if } E_x \le E_M,\\ &= K_{\rm rot}(E_x)K_{\rm vib}(E_x)\rho_{F,\rm int}^{\rm tot}(E_x),\\ &\quad \text{if } E_x \ge E_M,\end{aligned} \tag{267}$$

and similarly for the level density $\rho(E_x, J, \Pi)$. Note that the collective enhancement is not applied to the constant temperature region, since collectivity is assumed to be already implicitly included in the discrete levels. The matching problem is completely analogous to that described before, although the resulting parameters E_M, E_0 and T will of course be different.

The BFM can also be extended with explicit collective enhancement, i.e.

$$\rho_{\rm BFM}^{\rm tot}(E_x) = K_{\rm rot}(E_x)K_{\rm vib}(E_x)\left[\frac{1}{\rho_{F,\rm int}^{\rm tot}(E_x)} + \frac{1}{\rho_0(t)}\right]^{-1}, \tag{268}$$

and similarly for the level density $\rho(E_x, J, \Pi)$.

Since phenomenological level densities need to be generated from analytical expressions for the total level density, spin distribution, collective enhancement, shell effects, etc. they come with a large number of models and adjustable parameters.

11.2 Microscopic level densities

Besides the phenomenological models that are used in TALYS, there is also an option to employ more microscopic approaches. All these models include detailed structure ingredients, in particular a mean-field single-particle level scheme and associated pairing, to estimate the nuclear level density, contrary to the analytical approaches described before. Therefore, the shell and pairing effects are intrinsically and coherently taken into account.

Three options are available. The first one estimates the level densities on the basis of the microscopic statistical model [131]. The statistical calculations are performed using the deformed Hartree-Fock-BCS (HF-BCS) predictions of the ground-state structure properties. The microscopic model includes a consistent treatment of the shell effects, pairing correlations, deformation effects and collective excitations. However, it does not account for possible deviations from a Gaussian law for the spin distribution and keeps the assumption of a parity equipartition. It predicts the experimental neutron resonance spacings with a degree of accuracy comparable to that of the phenomenological back-shifted Fermi-gas-type formulae. The microscopic level densities are renormalized to the existing experimental data, namely the s-wave neutron resonance spacings and the cumulative number of low-lying levels. Level densities for more than 8000 nuclei from the proton drip line to the neutron drip line are available for excitation energies up to 150 MeV and for the 30 first spins.

To go beyond the limitations inherent to the statistical model, two other models have been included in TALYS; both are based on the combinatorial approach. The first one is based on Skyrme-HFB calculations [106] and the second one on temperature-dependent HFB calculations [137] using the D1M Gogny force (Gogny-HFB). In both cases, the starting point is the HFB single-particle level scheme upon which all possible particle-hole excitations are counted. This intrinsic non-collective particle-hole state density is then folded with a vibrational state density to provide total state densities in the nucleus intrinsic frame. The level density is then finally obtained going from the intrinsic nucleus frame to the laboratory frame. If we denote by $\omega(U, M, \pi)$ the state density in the intrinsic frame, the level density is given by

$$\rho(U, J, \pi) = \omega(U, M = J, \pi) - \omega(U, M = J + 1, \pi), \tag{269}$$

for a spherical nucleus while, for an axially symmetric deformed nucleus it reads

$$\begin{aligned}\rho(U, J, \pi) = \frac{1}{2}&\sum_{K=-J, K\neq 0}^{J} \omega(U - E_{rot}^{J,K}, K, \pi)\\ &+\delta_{(J\ even)}\,\delta_{(\pi=+)}\,\omega(U - E_{rot}^{J,0}, 0, \pi)\\ &+\delta_{(J\ odd)}\,\delta_{(\pi=-)}\,\omega(U - E_{rot}^{J,0}, 0, \pi).\end{aligned} \tag{270}$$

with $E_{rot}^{J,K} = \dfrac{J(J+1) - K^2}{2I_\perp}$ where $I_\perp$ is the moment of inertia perpendicular to the symmetry axis for a deformed nucleus. In Eq. (270), the 1/2 factor accounts for the fact that, for axially symmetric nuclei, states with spin projections K and $-K$ belong to the same rotational band and the two remaining terms account for the fact that the rotational bands generated by 0^+ states have a level sequence $0^+, 2^+, 4^+, \ldots$ while those built on a 0^- band head are $1^-, 3^-, 5^-, \ldots$. It is worth recalling that the HFB moment of inertia is usually in good agreement with experiment and increases with excitation energy to reach the rigid body value.

An important aspect of the combinatorial approach stemming from the different treatment of spherical and deformed nuclei concerns the transitional region where the nuclear deformation is small and non-zero. For such cases, in order to avoid a sharp transition between Eq. (269) and Eq. (270), an empirical procedure based on a simple Fermi function is applied. Hence, the final combinatorial level density reads

$$\rho(U, J, \pi) = [1-f]\rho_{\rm sph}(U, J, \pi) + f\rho_{\rm def}(U, J, \pi). \quad (271)$$

However, the f function is different in the two models. In the Skyrme HFB case, it depends on the excitation energy and plays a role similar to that of Eq. (266), i.e. enables to account for the vanishing of deformation with excitation energy. In the temperature-dependent HFB approach, since the disappearance of deformation is accounted for by the temperature dependence of the single-particle levels, the f function only depends on the deformation.

The default, and in our opinion currently the most robust, option is the Skyrme-HFB model. For both models, level densities for more than 8500 nuclei are made available in tabular format, for excitation energies up to 200 MeV and for spin values up to $J = 49$. Since these tabulated microscopic combinatorial level densities have not been adjusted to experimental data, we add adjustment flexibility through Eq. (230). For microscopic models in particular, Eq. (230) allows to tune the nuclear level densities to experimental data from low-lying levels at low-energy and s-wave resonance spacings at energies in the vicinity of the neutron separation energy. The c and δ parameters of Eq. (230) have been systematically adjusted on experimental and made available in TALYS structure database. They guarantee the user to make use of nuclear level densities in agreement with data.

For the microscopic level density models, tables for level densities on top of the fission barriers are also available in the TALYS structure database, as discussed in Sect. 13. For nuclides outside the tabulated microscopic database, the default CTM level densities are used.

12 Photon strength functions and transmission coefficients

PSF are important for the description of any transition involving gamma rays in nuclear reactions [138,139]. The best known reaction channels which are governed by the PSF are the (n, γ) and (γ, n) reaction channels, but the PSF can be regarded as an important universal entity in reaction modeling since gamma rays in general may accompany emission of any other particle, and gamma transitions occur for both the continuum and discrete levels. And as discussed in Sect. 10, PSF are also used to estimate branching ratios between experimental discrete levels, when this information is not available experimentally.

Before we describe the PSF models implemented in TALYS, we first give the basic relations which establish their parameters, constraints and use in reaction models.

The transmission of a gamma ray at an energy E_γ is described by the PSF $f_{X\ell}(E_\gamma)$. Here X denotes either electric (E) or magnetic (M) radiation; and ℓ is the radiation multipolarity. In general, dipole $(\ell = 1)$ radiation dominates over radiation of higher multipolarity for a given E_γ, i.e. $f_{E1}(E_\gamma) >> f_{E2}(E_\gamma)$. Also E transitions are generally stronger than M transitions for a given multipolarity, i.e. $f_{E1}(E_\gamma) > f_{M1}(E_\gamma)$, though this might not be true at all energies.

One distinguishes between

- upward PSF $\overrightarrow{f_{X\ell}}(E_\gamma)$, related to the cross section for gamma absorption such as for (γ, n) reactions
- downward PSF $\overleftarrow{f_{X\ell}}(E_\gamma)$, related to the average width of the gamma decay and thus of particular interest in radiative capture.

The essential relation between the total photoabsorption cross section and the upward PSF is

$$\sigma_{(\gamma,abs)}(E_\gamma) = \sum_{X\ell} \sigma_{X\ell}(E_\gamma), \quad (272)$$

where,

$$\overrightarrow{f_{X\ell}}(E_\gamma) = K_{X\ell} \frac{\sigma_{X\ell}(E_\gamma)}{E_\gamma^{2\ell-1}}, \quad (273)$$

and

$$K_{X\ell} = \frac{1}{(2\ell+1)\pi^2\hbar^2c^2}. \quad (274)$$

Eq. (273) means that the PSF can be extracted from the photoabsorption cross section $\sigma_{X\ell}$ summed over all spins and parities. In practice, with other components being negligible near the peak of the PSF, this means that $\overrightarrow{f_{E1}}$ is directly determined by the (γ, n) cross section in the region of the giant dipole resonance (GDR).

The downward PSF is related to the deexcitation of the nucleus. Like the particle transmission coefficients that emerge from the optical model, photon transmission coefficients enter the Hauser-Feshbach model for the determination of the competition between photon emission and emission of other particles. The relation between the photon transmission coefficient and downward PSF is given by

$$T_{X\ell}(E_\gamma) = 2\pi \overleftarrow{f_{X\ell}}(E_\gamma) E_\gamma^{2\ell+1}. \quad (275)$$

The average radiation width $\langle\Gamma_\gamma\rangle$, for which experimental data are available, is obtained by integrating the gamma-ray transmission coefficients over the density of final states that may be reached in the first step of the gamma-ray cascade. This leads to the essential relation for the downward PSF,

$$\frac{2\pi\langle\Gamma_\gamma\rangle}{D_0} = \sum_{J,\Pi,X\ell}\sum_{I'=|J-\ell|}^{J+\ell}\sum_{\Pi'}\int_0^{S_n} dE_\gamma \; T_{X\ell}(E_\gamma)\rho(S_n - E_\gamma, I', \Pi')F(X, \Pi', \ell), \tag{276}$$

where D_0 is the average resonance spacing derived from the level density ρ. The J, Π sum runs over the compound nucleus states with spin J and parity Π that can be formed with s-wave incident particles, and I', Π' denote the spin and parity of the final states. The multipole selection rules are $F(E, \Pi', \ell) = 1$ if $\Pi = \Pi'(-1)^\ell$, $F(M, \Pi', \ell) = 1$ if $\Pi = \Pi'(-1)^{\ell+1}$, and 0 otherwise. The integral over dE_γ includes a summation over discrete states.

At the same time, $\overleftarrow{f_{X\ell}}(E_\gamma)$, and thus $T_{X\ell}(E_\gamma)$, is directly linked to the (n, γ) cross section just above the resonance range, before the opening of the inelastic channel. Since the transmission coefficient for neutrons is much larger than that of photons, $T_n >> T_\gamma$, the Hauser-Feshbach formula for this energy range can be stated in a compact way,

$$\sigma(n, \gamma) = \frac{T_n T_\gamma}{T_n + T_\gamma} \approx T_\gamma \; . \tag{277}$$

Both $\langle\Gamma_\gamma\rangle$ and Maxwellian-averaged (n, γ) cross sections (MACS) around 30 keV, have been experimentally determined for more than 200 nuclides, and are therefore important observables to constrain the PSF model and its parameters though both also depend on the nuclear level densities. Ideally, one and the same set of PSF parameters should predict both observables with the same accuracy. However, it was concluded that there may be up to a $\sim$ 20 % difference between the two predictions on a global scale [139,140].

Most of the PSF studies, be it experimental or theoretical, make the assumption that the average electromagnetic decay process (i.e. the photo-deexcitation) can be directly related to the inverse photoexcitation, i.e. $f_{X\ell} = \overleftarrow{f_{X\ell}} = \overrightarrow{f_{X\ell}}$, and essentially depends only on the energy of the emitted γ-ray, and not on the absolute excitation energy of the initial or final states, or the specific nuclear properties (such as the spin and parity) of the nuclear states involved. This assumption is known as the Brink hypothesis [141] that has played a key role in the description of the photo-deexcitation process, especially in reaction theory. While the Brink hypothesis is well established in the GDR energy region, at low energies, in particular below the neutron threshold, its validity is still open to debate and is under both theoretical as well as experimental investigation. For example, studies within the Fermi liquid theory [142] have found that photo-deexcitation PSF is a function of the excitation energy of the final state, which in turn depends on the excitation energy of the initial state and the γ-ray energy E_γ. In contrast, the photo-excitation process only depends on the γ-ray energy. Experimentally, the Brink hypothesis was investigated and shown to be valid to a good approximation, for γ-ray transitions between states in the quasicontinuum region below the particle separation energy, from a variety of experiments [143,144], though photon scattering (γ,γ') technique have found indications that the Brink hypothesis is at least partially violated below the neutron separation energy (see e.g. Refs. [145–147]). In TALYS, depending on the PSF model adopted, a temperature dependence may be included, hence the deexcitation PSF may differ from the photo-excitation one. The PSF can also be fine-tuned by using directly experimental information, as compiled in the reference IAEA PSF database [139].

Various phenomenological and microscopic models for the PSF are implemented in TALYS. We describe them all below. Figures 17 and 18 illustrate their description of the $E1$ and $M1$ modes, respectively, for the stable ^{96}Mo isotope, together with available experimental data, while Figs. 19, 20 compare their predictions for the exotic neutron-rich $N = 82$ Mo isotope ^{124}Mo. The ^{96}Mo GDR region is relatively well reproduced by all models, since all of them have been tuned in a way or another in this energy region through a local or global adjustment on photoabsorption data for stable nuclei. However, in the low-energy GDR tail and to some extent above the GDR, significant differences can be observed leading inevitably to different predictions of radiative capture cross sections. In the case of ^{124}Mo, major differences are found even in the GDR region. For the $M1$ component, only a few global models are available. Four of them, as implemented in TALYS, are illustrated in Figs. 18 and 20.

We need to stress that two models are more specifically recommended. They concern the phenomenological model, the Simplified Modified Lorentzian (SMLO) model [148, 149], and the microscopic QRPA model based on the D1M Gogny interaction (hereafter D1M+QRPA). Both models were developed and validated against experimental data during an IAEA coordinated research project on PSFs [139] and photonuclear cross sections [150]. They are regarded, by us at least, as the two best options for PSF, from a consistent physics point of view. Note that both models include the $E1$ and $M1$ PSFs and a phenomenological account of the low-energy enhancement (the so-called upbend), as discussed in Sect. 12.3.1. After the description of the various PSF models, we will outline in Sect. 12.4 how a proper normalization of PSF's to experimental data can be achieved.

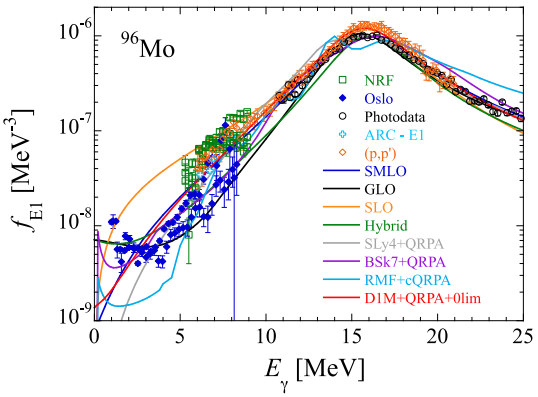

Fig. 17 Comparison between the 8 $E1$ PSFs for ^{96}Mo, as included in TALYS. Note that the $E1$ non-zero limit at zero energy (see Sect. 12.3.1) is included in the models prescribing it, see text for more details. The predictions are compared with existing data, as compiled in the 2019 IAEA PSF database [151], stemming from nuclear resonance fluorescence (NRF), Oslo method, photoabsorption data, average resonance capture (ARC) or (p, p') scattering data

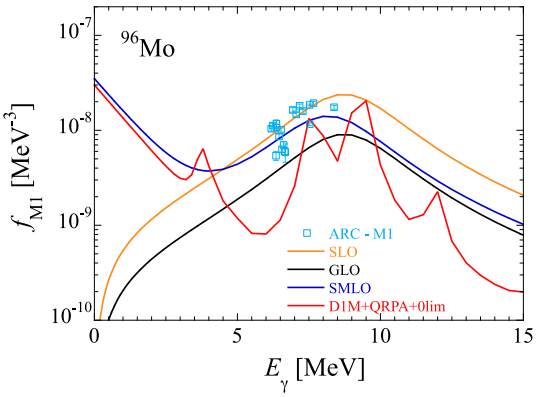

Fig. 18 Same as Fig. 17 for the $M1$ PSFs of ^{96}Mo. Note that the $M1$ upbend (see Sect. 12.3.1) is included in the models prescribing it

12.1 Analytical Lorentzian-type models for PSFs

The phenomenological models are generally parameterized in terms of Lorentzian forms with giant resonance parameters:

- $\sigma_{X\ell}$: cross section of the giant resonance at the peak energy,
- $E_{X\ell}$: centroid energy of the giant resonance,
- $\Gamma_{X\ell}$: width of the giant resonance.

Note that the PSF for deformed nuclei exhibits two peaks and consequently is described by two Lorentzian functions i.e.

$$f_{X\ell}(E_\gamma) = \sum_{i=1}^{2} f^i_{X\ell}(E_\gamma, \sigma^i_{E1}, E^i_{E1}, \Gamma^i_{E1}) \,. \tag{278}$$

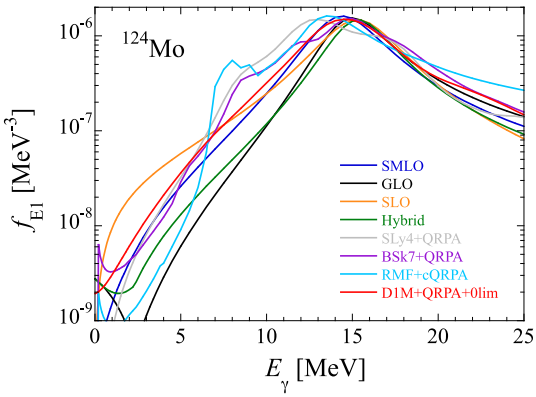

Fig. 19 Same as Fig. 17 for the $E1$ PSFs of ^{124}Mo

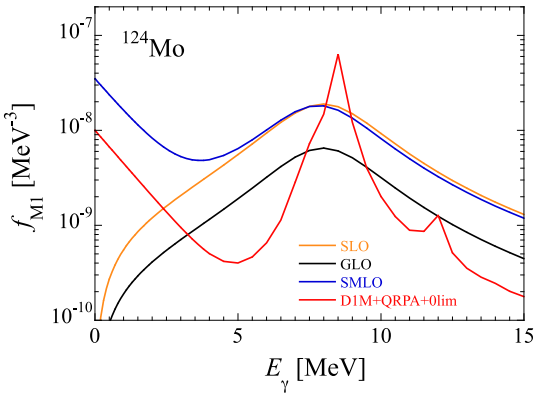

Fig. 20 Same as Fig. 18 for the $M1$ PSFs of ^{124}Mo

12.1.1 Standard Lorentzian model

The first, and oldest, model is the so-called Brink-Axel option [141,152], for which a standard Lorentzian (SLO) form describes the GDR shape, i.e.

$$f_{X\ell}(E_\gamma) = K_{X\ell} \frac{\sigma_{X\ell} E_\gamma \Gamma^2_{X\ell}}{(E^2_\gamma - E^2_{X\ell})^2 + E^2_\gamma \Gamma^2_{X\ell}} . \tag{279}$$

The standard Lorentzian option is usually used for all multipoles higher than 1 ($\ell > 1$).

12.1.2 Generalized Lorentzian model

For $E1$ radiation, an option which has been used as a default for many years in TALYS is the Generalized Lorentzian (GLO) form of Kopecky and Uhl [153,154],

$$f_{E1}(E_\gamma, T) = K_{E1} \left[\frac{E_\gamma \tilde{\Gamma}_{E1}(E_\gamma, T)}{(E^2_\gamma - E^2_{E1})^2 + E^2_\gamma \tilde{\Gamma}^2_{E1,T}(E_\gamma)} + \frac{0.7 \Gamma_{E1} 4\pi^2 T^2}{E^5_{E1}} \right] \sigma_{E1} \Gamma_{E1}, \tag{280}$$

where the energy-dependent and temperature-dependent damping width $\tilde{\Gamma}(E_\gamma, T)$ is given by

$$\tilde{\Gamma}_{E1}(E_\gamma, T) = \Gamma_{E1} \frac{E_\gamma^2 + 4\pi^2 T^2}{E_{E1}^2}, \tag{281}$$

and T the nuclear temperature given by

$$T = \sqrt{\frac{E_n + S_n - \Delta - E_\gamma}{a(S_n)}}, \tag{282}$$

where S_n is the neutron separation energy, E_n the incident neutron energy, Δ the pairing correction and a the level density parameter at S_n (see Sect. 11). Note that in the GLO model, a non-zero limit of the $E1$ deexcitation (i.e. $T > 0$) PSF at $E_\gamma \rightarrow 0$ is ensured through the second term of Eq. (280).

12.1.3 Hybrid model

The hybrid model [155] is a variant of the GLO model which includes a energy- and temperature-dependent width but also a low-energy (i.e. below S_n) behaviour inspired from the Fermi liquid theory [142] and reads

$$f_{E1}(E_\gamma, T) = K_{E1}\sigma_{E1}\Gamma_{E1} \left[\frac{E_\gamma \tilde{\Gamma}_{E1}(E_\gamma, T)}{(E_\gamma^2 - E_{E1}^2)^2 + E_\gamma^2 \Gamma_{E1} \tilde{\Gamma}_{E1}(E_\gamma, T)} \right] \tag{283}$$

with the energy- and temperature-dependent width

$$\tilde{\Gamma}_{E1}(E_\gamma, T) = 0.7\ \Gamma_{E1}\ \frac{E_\gamma^2 + 4\pi^2 T^2}{E_\gamma\ E_{E1}}\quad . \tag{284}$$

Note that in the hybrid model (like in the GLO model), a non-zero limit of the $E1$ deexcitation PSF at $E_\gamma \rightarrow 0$ is found through the above temperature dependence.

12.1.4 Parameters for the SLO, GLO and hybrid models

For $E1$-transitions, GDR parameters for various individual nuclides have been extracted from photoabsorption data [9, 148]. These are stored in the nuclear structure database of TALYS. If not available experimentally, the resonance parameters for any $X\ell$ transition can be taken from global systematic formulae [9]. More precisely,

- For $E1$ transitions for which no nuclide-specific data exist, we use

$$\begin{aligned} \sigma_{E1} &= 1.2 \times 120 NZ/(A\pi\Gamma_{E1})\ \text{mb}, \\ E_{E1} &= 31.2A^{-1/3} + 20.6A^{-1/6}\ \text{MeV}, \\ \Gamma_{E1} &= 0.026 E_{E1}^{1.91}\ \text{MeV}. \end{aligned} \tag{285}$$

- for $E2$ transitions,

$$\begin{aligned} \sigma_{E2} &= 0.00014 Z^2 E_{E2}/(A^{1/3}\Gamma_{E2})\ \text{mb}, \\ E_{E2} &= 63.A^{-1/3}\ \text{MeV}, \\ \Gamma_{E2} &= 6.11 - 0.012A\ \text{MeV}, \end{aligned} \tag{286}$$

- for multipole electric radiation higher than $E2$

$$\begin{aligned} \sigma_{E\ell} &= 8.10^{-4}\sigma_{E(\ell-1)}, \\ E_{E\ell} &= E_{E(\ell-1)}, \\ \Gamma_{E\ell} &= \Gamma_{E(\ell-1)}, \end{aligned} \tag{287}$$

- for $M1$ transitions within the SLO approach

$$\begin{aligned} f_{M1} &= 1.58\ 10^{-9} A^{0.47}\ \text{at}\ 7\ \text{MeV}, \\ E_{M1} &= 41.A^{-1/3}\ \text{MeV}, \\ \Gamma_{M1} &= 4\ \text{MeV}, \end{aligned} \tag{288}$$

  where Eq. (279) thus needs to be applied at 7 MeV to obtain the σ_{M1} value. Similarly, within the GLO model [153], the same centroid and width are considered, but the strength of the $M1$ channel is estimated with respect to the $E1$ channel at 7 MeV through the expression $f_{M1} = f_{E1}/(0.0588\ A^{0.878})$.
- for multipole magnetic radiation higher than $M1$, we use

$$\begin{aligned} \sigma_{M\ell} &= 8.10^{-4}\sigma_{M(\ell-1)}, \\ E_{M\ell} &= E_{M(\ell-1)}, \\ \Gamma_{M\ell} &= \Gamma_{M(\ell-1)}. \end{aligned} \tag{289}$$

12.1.5 SMLO model

The SMLO model was developed to provide an improved estimate of the $E1$ and $M1$ PSFs [148,149] for all nuclei with $8 \leq Z \leq 124$. It is the default phenomenological PSF model in TALYS. Details on the $E1$ PSF formulation and systematics can be found in Refs. [148,149] and will not be repeated here. Concerning the M1, the SMLO model adopts simple SLO expressions for both the low-energy scissors (sc) mode and the spin-flip (sf) components, i.e.

$$\begin{aligned} \overrightarrow{f_{M1}}(\varepsilon_\gamma) = &\frac{1}{3\pi^2\hbar^2c^2}\sigma_{sc}\frac{\varepsilon_\gamma\ \Gamma_{sc}^2}{(\varepsilon_\gamma^2 - E_{sc}^2)^2 + \varepsilon_\gamma^2\Gamma_{sc}^2} \\ &+ \frac{1}{3\pi^2\hbar^2c^2}\sigma_{sf}\frac{\varepsilon_\gamma\ \Gamma_{sf}^2}{(\varepsilon_\gamma^2 - E_{sf}^2)^2 + \varepsilon_\gamma^2\Gamma_{sf}^2} \end{aligned} \tag{290}$$

where $\sigma_i = f_i E_i$ is the peak cross section, E_i the energy at the peak and Γ_i the width at half maximum for both the spin-

flip ($i = sf$) or the scissors mode ($i = sc$). The following parameters for both $M1$ modes, i.e. for

- the spin-flip resonance: $\sigma_{sf} = 0.03A^{5/6}$ mb, $E_{sf} = 18A^{-1/6}$ MeV and $\Gamma_{sf} = 4$ MeV;
- the scissors mode: $\sigma_{sc} = 10^{-2}|\beta_2|A^{9/10}$ mb, $E_{sc} = 5 \times A^{-1/10}$ MeV and $\Gamma_{sc} = 1.5$ MeV;

where the spin-flip and the scissors mode components are tuned on experimental (average resonance capture and nuclear resonance fluorescence) data and inspired both from axially deformed QRPA and shell-model calculations [149].

Such expressions present the advantage of being easily tuned on experimental data, but also adjustable to reproduce measured cross sections. The prescription applied to the photoabsorption strength has been extended to the determination of the deexcitation PSF by adding a temperature dependence to the $E1$ GDR width and an $M1$ upbend at the lowest energies (see Sect. 12.3.1). Both $E1$ and $M1$ SMLO PSFs have been adjusted on a large number of experimental data, as described in Ref. [139].

12.2 Microscopic models for PSFs

Various microscopic options for the $E1$ PSF have been included in TALYS. They are all based on the relativistic or non-relativistic mean-field plus QRPA approach. Only one of these models, the so-called D1M+QRPA model [140], also provides the $M1$ PSF. The models provide the PSF as a function of the photon energy E_γ and possibly as a function of the temperature, or equivalently the excitation energy, of the final state. In all cases, the PSFs are stored as tables in TALYS structure database and, as discussed in Sect. 12.4, all these tabulated values can be adjusted for fitting purposes.

12.2.1 Skyrme-Hartree-Fock plus QRPA model

One of the models corresponds to the spherical Hartree-Fock-BCS plus QRPA model of Ref. [156] based on the SLy4 interaction where a folding procedure is applied to the QRPA strength distribution to take the damping of the collective motion into account. Deformation effects are included phenomenologically. This model was shown to lead to $E1$ PSF in fair agreement with the experimental data, such as photoreaction data and PSFs extracted from resolved-resonance and thermal-capture measurements at low energies (typically between 4 and 8 MeV).

The above-mentioned model was improved in Ref. [157] where a spherical Hartree-Fock-Bogoliubov (HFB) model plus QRPA calculation was performed on the basis of the BSk7 interaction. In addition, a temperature-dependent correction factor was introduced in the folding procedure to take the collision of quasiparticles into account. Energy- and temperature-dependent tables are provided in this case. No large-scale $M1$ PSFs has been derived yet within these approaches.

12.2.2 Relativistic Mean Field plus QRPA model

$E1$ PSF tables from the large-scale temperature-dependent RMF plus QRPA calculation of Ref. [158] are included in TALYS structure database. Calculations are based on the point coupling PCF1 force. While the coupling to the single-particle continuum is taken into account in an explicit and self-consistent way, additional corrections like the coupling to complex configurations and the temperature and deformation effects are included in a phenomenological way to account for a complete description of the nuclear dynamical problem.

12.2.3 Gogny-Hartree-Fock-Bogoliubov plus QRPA model

Large-scale calculations of the $E1$ and $M1$ absorption PSF were also obtained in the framework of the axially symmetric deformed HFB plus QRPA model based on the finite-range D1M Gogny force [140] and are included in TALYS. This so-called D1M+QRPA photoabsorption strength has been complemented with a phenomenological low-energy contribution inspired from shell-model results and existing experimental data to describe the deexcitation PSF (see Sect. 12.3.1 for the expression of the corresponding $M1$ upbend). The resulting D1M+QRPA+0lim PSF has been extensively compared and tested against experimental data directly or indirectly related to PSF [139].

12.3 Additional dipole contribution

12.3.1 The low-energy enhancement

When considering the deexcitation strength function, deviations from the photoabsorption strength can be expected, especially for γ-ray energies approaching the zero limit. When a temperature dependence is included in the $E1$ PSF (e.g. in the GLO, SMLO, Hybrid or T-dependent mean-field plus QRPA models), such a low-energy feature is included. However, other models may need to be complemented by a non-zero limit. In the specific case of the D1M+QRPA approach, an additional $E1$ low-energy contribution to the deexcitation PSF has been proposed, so that the PSF reads

$$\overleftarrow{f_{E1}}(E_\gamma) = \overrightarrow{f_{E1}^{QRPA}}(E_\gamma) + f_0 U/[1 + e^{(E_\gamma - \varepsilon_0)}] \qquad (291)$$

where $\overrightarrow{f_{E1}^{QRPA}}$ is the D1M+QRPA $E1$ strength at the photon energy E_γ, U is the excitation energy of the initial de-exciting state and $f_0 = 10^{-10}$ MeV^{-4}, $\varepsilon_0 = 3$ MeV [139,140].

The SMLO or D1M+QRPA $M1$ PSF is also complemented by an additional low-energy enhancement. In particular, shell-model calculations [159–161] predict an exponential increase of the $M1$ deexcitation strength function at decreasing energies approaching zero. This so-called upbend of the strength function, also observed experimentally [162, 163], has therefore been assumed to be of $M1$ nature, though no experimental evidence exists for the moment. Therefore, when dealing with the deexcitation $M1$ strength function, a low-energy enhancement, inferred from shell-model calculations [160,161,164], the analysis of experimental multi-step cascade spectra [165] and Oslo measurements [162,163], should be added to the photoabsorption expression, leading to

$$\overleftarrow{f_{M1}}(E_\gamma) = \overrightarrow{f_{M1}}(E_\gamma) + C\exp(-\eta E_\gamma), \tag{292}$$

where $\eta = 0.8\ \mathrm{MeV}^{-1}$ and for the SMLO model $C = 3.5 \times 10^{-8}\ \exp(-6\beta_2)\ \mathrm{MeV}^{-3}$ while for the D1M+QRPA model $C = 1 \times 10^{-8}\ \mathrm{MeV}^{-3}$ for all nuclei with $A \geq 105$ and $C = 3 \times 10^{-8} \exp(-4\beta_2)\ \mathrm{MeV}^{-3}$ for lighter nuclei (see Ref. [139] for more details).

The low-energy $M1$ upbend can give a significant contribution to the (n, γ) cross section. Generally the $M1$ contribution is much lower than $E1$ near the peak of the GDR, but at the lowest gamma energies may become comparable to that of $E1$. The impact on low-energy neutron capture is then given by Eq. (276) and similarly by the Hauser-Feshbach formula.

12.3.2 Pygmy resonances

In addition to the $E1$ contribution described above, a pygmy resonance of a given multipolarity $X\ell$ can be included by adding to the adopted PSF an additional component of the SLO form (Eq. 279). Despite such an option, by default, no pygmy resonance is included in cross section calculation and TALYS does not provide any global systematics for such a contribution. More information on the pygmy resonance can be found in Ref. [166,167].

12.4 Adjustment of the PSF

Regardless of the PSF model adopted, it is quite likely that an optimal fit to e.g. $\sigma(n, \gamma)$, MACS or $\langle\Gamma_\gamma\rangle$ can only be obtained with some adjustment of the PSF. The simple Lorentzian models like SLO or GLO have ready-to-use parameters for that, but this is not the case for tabulated PSFs coming from SMLO or QRPA calculations. It is however straightforward to bring all PSF models to the same practical level. If we denote the original, analytical or tabulated, PSF as $f_{X\ell}(E_\gamma)$ then we can add adjustment flexibility through

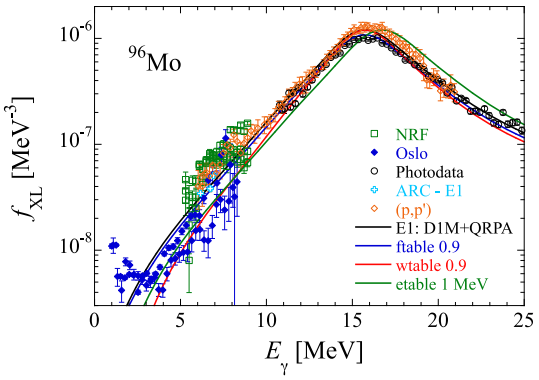

Fig. 21 Illustration of the possible adjustments of the $E1$ D1M+QRPA PSF offered by TALYS in the case of ^{96}Mo. The original D1M+QRPA PSF is given by the black solid line; a modification of the PSF through the f^{table} (by a factor 0.9), w^{table} (by a factor 0.9), and E^{table} (by 1 MeV)(see Eq. 293) are shown by the blue, red and green solid lines, respectively. Experimental data are taken from the 2019 IAEA PSF database [151]. See text for more details

scaling parameters to obtain the final PSF as follows,

$$f^{\mathrm{final}}_{X\ell}(E_\gamma) = f^{\mathrm{table}} f_{X\ell}(E^c_{X\ell} + w^{\mathrm{table}}(E_\gamma - E^c_{X\ell}) + E^{\mathrm{table}}) \tag{293}$$

where by default $f^{\mathrm{table}} = 1$, $E^{\mathrm{table}} = 0$, $w^{\mathrm{table}} = 1$, i.e. unaltered values from the original table or analytical function, and $E^c_{X\ell}$ is the centroid energy at the middle of the PSF which can be numerically determined. Here, f^{table} scales the entire PSF up or down, E^{table} allows to shift in energy the entire PSF and w^{table} can be used to increase or reduce the width of the giant resonance. The most effective adjustment parameter for (n, γ) cross sections is w^{table}. It leaves the PSF practically untouched near its peak while it has a significant effect below S_n. In addition, since the majority of adjusted values of w^{table} needed to fit (n, γ) lies within 15% of 1, the resulting PSF is usually not in disagreement with measurements for PSF's near S_n.

Figure 21 shows the w^{table} values for PSF's adjusted to the experimental (n, γ) cross section around 30 keV using the D1M+QRPA+0lim PSF and the HFB+combinatorial level density model. Note that the adjustment flexibility of the (less physical) phenomenological models is somewhat higher, since in addition one may adjust the parameters for a possible second peak as well. Microscopic PSFs certainly predict such double peaks, but we have to accept the relative position of the two peaks as they come from the calculated tables.

TALYS also allows an automatic adjustment of the PSF to the experimental [9] or systematic [168] value of the average radiative width $\langle\Gamma_\gamma\rangle$ as given by Eq. (276). The $\langle\Gamma_\gamma\rangle$ values are, when available, read from TALYS nuclear structure database. This effect is similar to the adjustment of the above-mentioned f^{table} parameter. However, such an approach should be followed with care since the low-energy (n, γ) cross section is essentially sensitive to the low-energy

tail of the PSF below S_n. A too large adjustment of f^{table} may destroy the agreement of the PSF fitted to (γ,n)-based data near the GDR peak. Artificially increasing or decreasing the PSF amplitude may affect the (n, γ) at higher energies.

An example is provided for ^{101}Mo in Fig. 22 where the GLO strength gives $\langle\Gamma_\gamma\rangle_{\text{GLO}} = 0.015$ eV, i.e. a factor of 6 lower than the experimental value $\langle\Gamma_\gamma\rangle_{\text{exp}} = 0.09 \pm 0.01$ eV [9]. As seen in Fig. 22b, such a low dipole strength leads to a neutron capture cross section a factor of about 4–5 lower than experimental data. Multiplying artificially the overall $E1$ strength by a factor $f^{\text{table}} = \langle\Gamma_\gamma\rangle_{\text{exp}}/\langle\Gamma_\gamma\rangle_{\text{GLO}} = 6$ provides, however, a cross section in good agreement at low energies with experimental data. Such a renormalization has become a default procedure in most of the reaction codes. In contrast, the D1M+QRPA+0lim PSF gives an average radiative width of 0.082 eV in agreement with experiments and therefore does not need to be renormalized. It is seen in Fig. 22a to be relatively close to the renormalized GLO strength at low energies, hence giving rise to relatively similar cross section for keV neutrons. However, at neutron energies above 1 MeV, significant deviations between the cross sections obtained with the renormalized GLO and D1M+QRPA+0lim strengths can be observed since both strengths differ now in the energy region of relevance, i.e. in the GDR region. The long-standing problem between the compatibility of the predicted radiative width and experimental capture and photoabsorption data is largely solved with the present D1M+QRPA+0lim model where both the average radiative width and neutron capture cross sections are consistently estimated and globally in agreement with experimental data, including photoabsorption and photo-deexcitation data [139,140]. Such a conclusion holds regardless of the nuclear level density model adopted.

12.4.1 Photoabsorption cross section

TALYS requires an estimate of the photoabsorption cross sections to estimate photonuclear reactions and pre-equilibrium gamma-ray emission. Obviously, for low energies this can be directly related to the above-discussed PSF. However, at higher energies, typically above 20 MeV, the dipole strength may be dominated by the non-resonant process in the pre-equilibrium mode, the so-called quasi-deuteron component [169]. A general expression for the photoabsorption cross section reads

$$\sigma_{abs}(E_\gamma) = \sigma_{GDR}(E_\gamma) + \sigma_{QD}(E_\gamma). \tag{294}$$

where the quasi-deuteron component σ_{QD} is given by

$$\sigma_{QD}(E_\gamma) = L\frac{NZ}{A}\sigma_d(E_\gamma)f(E_\gamma). \tag{295}$$

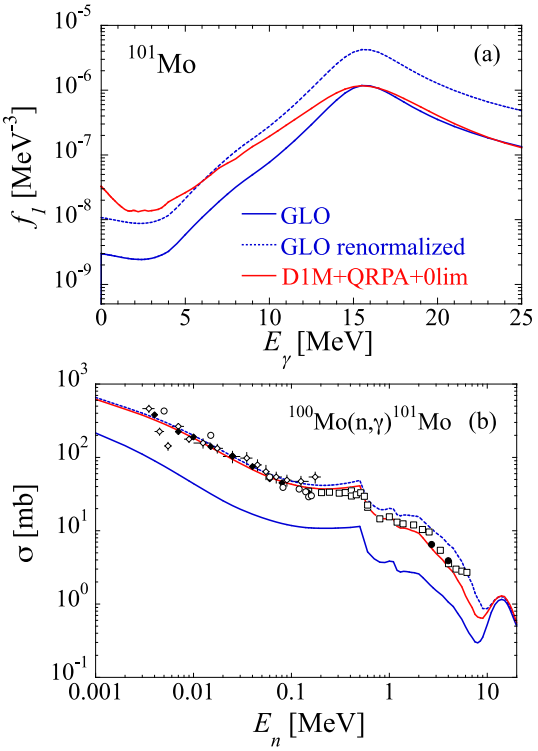

Fig. 22 **a** $E1 + M1$ PSF of ^{101}Mo calculated with the GLO model [9,153] (solid blue line), with the GLO after renormalizing the $E1$ PSF by a factor of $f^{\text{table}} = 6$ (dotted line) and with D1M+QRPA+0lim (solid red line). **b** ^{100}Mo$(n, \gamma)^{101}$Mo cross sections calculated with the GLO (solid blue line), renormalized GLO (dotted line) and D1M+QRPA+0lim (red solid line) dipole PSFs. Also shown are the experimental data extracted from EXFOR database [80]

Here, $\sigma_d(E_\gamma)$ is the experimental deuteron photo-disintegration cross section, parameterized as

$$\sigma_d(E_\gamma) = 61.2\frac{(E_\gamma - 2.224)^{3/2}}{E_\gamma^3}, \tag{296}$$

for $E_\gamma > 2.224$ MeV and zero otherwise. The so-called Levinger parameter is $L = 6.5$ and the Pauli-blocking function is approximated by the polynomial expression

$$\begin{aligned} f(E_\gamma) = {} & 8.3714.10^{-2} - 9.8343.10^{-3}E_\gamma \\ & +4.1222.10^{-4}E_\gamma^2 - 3.4762.10^{-6}E_\gamma^3 \\ & +9.3537.10^{-9}E_\gamma^4 \end{aligned} \tag{297}$$

for $20 < E_\gamma < 140$ MeV,

$$f(E_\gamma) = \exp(-73.3/E_\gamma) \tag{298}$$

for $E_\gamma < 20$ MeV, and

$$f(E_\gamma) = \exp(-24.2348/E_\gamma) \tag{299}$$

for $E_\gamma > 140$ MeV.

For the Hauser–Feshbach calculations in TALYS, the associated photon transmission coefficients are normalized as follows,

$$T_{X\ell}^{\text{final}}(E_\gamma) = T_{X\ell}(E_\gamma)\frac{\sigma_{abs}(E_\gamma)}{\sigma_{abs}(E_\gamma) - \sigma_{QD}(E_\gamma)}. \quad (300)$$

12.5 Isospin forbidden transitions

The Hauser–Feshbach formalism implicitly assumes complete isospin mixing which is valid except in the region of self-conjugate ($Z_{CN} = N_{CN}$) compound nuclei where isospin effects affect the dipole emission [170,171]. In particular, the isospin selection rule for dipole transitions is $T = 0, 1$ with transitions $0 \rightarrow 0$ being forbidden. Isospin forbidden transition has two major impacts on statistical cross section calculations, namely the reduction of the transmission coefficient for reactions involving self-conjugate nuclei and the suppression of the neutron emission in proton-induced reactions. For example, the α capture on $N = Z$ ($T = 0$) targets populates states with isospin $T = 0$ in the compound system which, through the strong suppression of the γ transitions in the compound nucleus, leads to a significant reduction of the radiative α-capture cross section. In TALYS cross section calculations, such a suppression is treated phenomenologically, as in Ref. [172], by dividing the total photon strength function (and thus the transmission coefficient) by a factor of 5 for (α, γ) reactions leading to self-conjugate residual nuclei, by a factor of 2 for radiative proton and neutron capture reactions proceeding into self-conjugate nuclei, and by a factor of 1.5 for all reactions proceeding into nuclei one unit away from self-conjugate nuclei, i.e. $Z_{CN} = N_{CN} \pm 1$. Similarly, isospin mixing effects also affect the reverse reactions, including in particular photoreactions. These isospin forbidden transitions corrections are accounted for both in the single and multiple particle emission channels.

13 Fission

The probability that a nucleus fissions can be estimated by TALYS on both phenomenological and microscopic grounds. In both cases, the modeling is based on the combination of Bohr's transition state hypothesis with the concept of fission barrier penetrability. Even if the most advanced models of fission describe the path to fission with a multidimensional landscape whose degrees of freedom correspond to several nuclear deformations (among which elongation and asymmetry are believed to be the dominant ones), in actual reaction codes, this path is reduced to a one dimensional potential energy surface (PES) which displays at least one barrier and often more (see Fig. 23). In TALYS a maximum of three barriers can be considered.

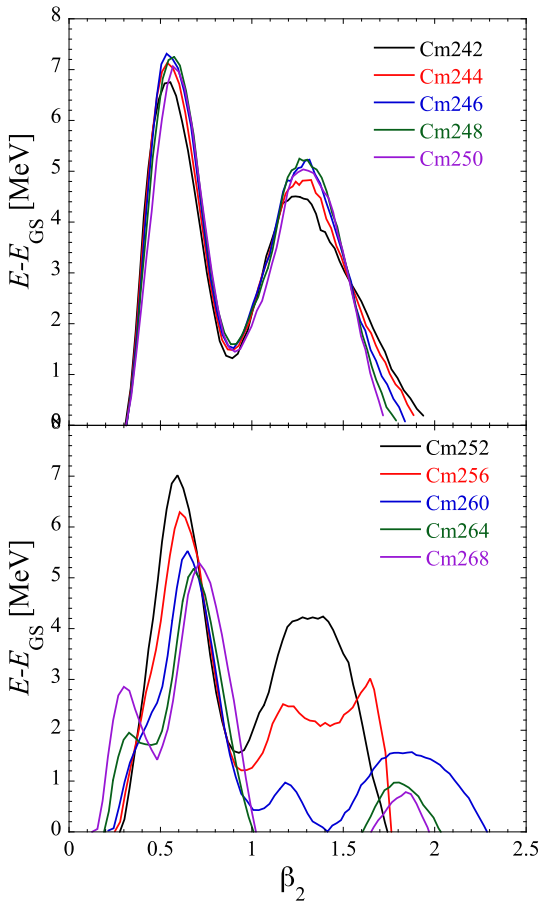

Fig. 23 HFB-14 PES [173] for Cm isotopes close to the valley of stability (top) and for neutron rich Cm isotopes (bottom)

The competition between fission, particle emission and photo-deexcitation is treated within the Hauser-Feshbach model, and thus requires the computation of fission transmission coefficients.

13.1 Fission transmission coefficients

The calculation of fission transmission coefficients requires several nuclear quantities depending on each barrier considered in the modeling. In order to define them, we start with a single humped barrier.

13.1.1 Single humped barrier

The phenomenological model implemented in TALYS is based on the Hill-Wheeler expression which gives the probability of tunneling through a barrier of height B_f and width $\hbar\omega_f$ for a compound nucleus with excitation energy E_x. The

transmission coefficient reads

$$T_f(E_x) = \frac{1}{1+\exp\left[-2\pi\frac{(E_x-B_f)}{\hbar\omega_f}\right]}. \quad (301)$$

Similarly, for a transition state of excitation energy ε_i above the top of this barrier, one has

$$T_f(E_x,\varepsilon_i) = \frac{1}{1+\exp\left[-2\pi\frac{(E_x-B_f-\varepsilon_i)}{\hbar\omega_f}\right]}, \quad (302)$$

which means that the barrier is simply shifted up by ε_i.

For a compound nucleus with excitation energy E_x, spin J, and parity Π, the total fission transmission coefficient is given by the sum of the individual transmissions coefficients for each barrier through which the nucleus may tunnel, and thus reads in terms of the previously introduced $T_f(E_x,\varepsilon_i)$

$$T_f^{J,\Pi}(E_x) = \sum_i T_f(E_x,\varepsilon_i) f(i,J,\Pi) + \int_{E_{th}}^{E_x} \rho(\varepsilon,J,\Pi) T_f(E_x,\varepsilon) d\varepsilon. \quad (303)$$

The summation runs over all discrete transition states on top of the barrier and E_{th} marks the beginning of the continuum. In this equation, $f(i,J,\Pi) = 1$ if the spin and parity of the transition state equal that of the compound nucleus and 0 otherwise. Moreover, $\rho(\varepsilon,J,\Pi)$ is the density of the transition states with spin J and parity Π for an excitation energy ε relative to the top of the fission barrier. The main difference with the usually employed expressions is that the upper limit in the integration is finite. This choice enables to define the number of fission channels by replacing $T_f(E_x,\varepsilon_i)$ by 1 in Eq. (303) and to treat fission transmission coefficients as a particle continuum transmission coefficient for the width fluctuation calculations [69] (see also Sect. 5.2).

A microscopic alternative based on the WKB approximation [174] is also available to replace the phenomenological Hill-Wheeler expression. In this case, the aforementioned transmission coefficient T_f can be written as

$$T_f(E_x) = \frac{1}{1+\exp(2K)} \quad (304)$$

in terms of the momentum integrals for the hump, i.e.

$$K = \pm\int_a^b [2\mu(E_x - V(\beta)/\hbar^2]^{1/2} d\beta \quad (305)$$

where V is the potential energy for the hump under consideration, and a and b the deformations corresponding to the intercepting points of the PES at the energy E_x. The + sign is taken when the excitation energy is lower than the hump and the − sign when it is higher. In the latter case, the intercepts (a and b) are complex conjugate ($b = a^*$) and the WKB approximation is valid when their imaginary parts are small, i.e. for energies slightly higher than the hump. The inertial mass μ is approximated by the semi-empirical expression $\mu = 0.054\, A^{5/3}$ MeV^{-1} and assumed to be independent of the deformation parameter β. In the case of a single parabolic barrier, $V(\beta) = B_f - 1/2\mu\omega_f^2\beta^2$, the transmission coefficient is reduced to the Hill-Wheeler expression (Eq. 301). TALYS includes about 3000 one-dimensional HFB fission paths based on the HFB-14 PES [173], as illustrated in Fig. 23, for which the WKB method to estimate the fission transmission coefficients can be consistently applied. More details on the method and its implementation can be found in Refs. [175–177].

13.1.2 Multiple-humped barriers

As mentioned above, the fission PES often displays more than one barrier. For double humped barriers, the generally employed expression is based on an effective transmission coefficient T_{eff} defined by

$$T_{eff} = \frac{T_A T_B}{T_A + T_B}, \quad (306)$$

where T_A and T_B are the transmission coefficients for barrier A and B respectively, calculated with Eq. (303). This expression is very similar to the Hauser-Feshbach formula meaning that the fission penetrability through a double humped barrier is given by the probability to tunnel through the first barrier multiplied by the probability to tunnel through the second one given the fact that it is possible to tunnel back through the first one.

If a triple humped barrier needs to be considered, the expression for T_{eff} is a generalization of Eq. (306) [55] which reads

$$T_{eff} = \frac{T_{AB} T_C}{T_{AB} + T_C}, \quad (307)$$

where T_{AB} is given by Eq. (306) and T_C by Eq. (303). Consequently, the expression used in TALYS reads

$$T_{eff} = \frac{T_A T_B T_C}{T_A T_B + T_A T_C + T_B T_C}. \quad (308)$$

For any number of barriers, the effective number of fission channels is calculated as in the case for one barrier [69].

13.2 Fission barrier parameters

As mentioned above, when fission barriers are described using an inverted parabola, the determination of the fission transmission coefficients depends on the number of fis-

sion barriers whose heights and widths have to be specified. Another important piece of information concerns the broken symmetries for each individual barrier. For instance, when the fission yield distribution is asymmetric, this means that the left-right symmetry is broken at least on top of the outer barrier. As discussed in Sect. 13.3, this information plays a role in the definition of the nuclear level densities on top of each individual barrier.

In TALYS several options are included for the fission barrier parameters, namely:

- Experimental parameters [9] corresponding to a set of actinide fission barrier heights and widths, for both the inner and outer barriers, extracted from a fit to experimental neutron-induced fission cross sections. Moreover, this compilation contains information on head band transition states, class-II states as well as the nature of the broken symmetries on top of each barrier.
- ETFSI parameters [178]: set of double-humped fission barrier heights for numerous isotopes derived from the so-called Extended Thomas-Fermi plus Strutinsky Integral calculations.
- Rotating-Finite-Range Model (RFRM) [179]: single-humped fission barrier heights are determined within a rotating liquid drop model, extended with finite-range effects in the nuclear surface energy and finite surface-diffuseness effects in the Coulomb energy.
- Rotating-Liquid-Drop Model (RLDM) [180].

In the current version of TALYS, the dependence on angular momentum of the fission barriers is discarded. If barriers obtained within the liquid drop model (LDM) are employed in the calculation, they are corrected for the difference between the ground state and fission barrier shell correction energy:

$$B_f^{LDM}(T) = B_f^{LDM}(0) - (\delta W_{ground} - \delta W_{barrier}) * g(T). \tag{309}$$

In this expression, the function $g(T)$ accounts for the gradual disappearance of the shell effects with increasing temperature [181]. One has $g(T) = 1$ for $T < 1.65$ MeV and $g(T) = 5.809 \exp(-1.066\ T)$ otherwise.

Shell corrections on top of the fission barrier are generally unknown. They obviously play an important role for the level density as well. Default values are adopted: for subactinides $\delta W_{barrier} = 0$ MeV while for actinides $\delta W_{barrier} = 2.5$ MeV for the inner barrier and $\delta W_{barrier} = 0.6$ MeV for the outer one [9]. Concerning the broken symmetries on top of fission barriers, default choices are also adopted depending on the neutron number. Inner barriers for nuclei with a number of neutron $N \leq 144$ are assumed to be axial otherwise to be triaxial. Outer barriers are generally considered as left-right asymmetric.

13.3 Fission barrier level densities

The level density formulae given in Sect. 11 for the ground state of the nucleus can all be applied to the fission barriers. In general, only the ingredients entering the level density definition change as compared to the ground-state case. These changes stem from the fact that the level densities for fission concern the transition states on top of each barrier and thus correspond to a nuclear deformation different from that of the ground state. Hence, shell and pairing effects, as well as collective enhancement are different for each barrier.

In TALYS, two methods for fission level densities are programmed. The first one explicitly describes each barrier level density with all its components, while the second one just account for a relative rotational enhancement for the fission barrier level density with respect to the ground state level density.

13.3.1 Explicit treatment of collective effects

Since the fission barriers are deformed, a rotational enhancement factor is used to increase the level density chosen for each barrier. As already mentioned before, the expression for this enhancement factor depends on the symmetries considered as broken on top of each barrier.

For axially symmetric barriers, Eq. (265) holds, replacing however the ground state deformation entering its definition by the barrier deformation. This concerns, by default, inner barriers with neutron number $N \leq 144$. If the axial symmetry is broken, the rotational enhancement reads

$$\begin{aligned} K_{rot}(E_x) &= K_{rot}^{asym}(E_x, \beta_2) \\ &= \max([g(\beta_2)\sigma_\perp^2\sigma_\parallel - 1]f(E_x) + 1, 1), \end{aligned} \tag{310}$$

with $g(\beta_2) = \sqrt{\frac{\pi}{2}}(1 - \frac{2\beta_2}{3})$ and $f(E_x)$ is given by Eq. (266). This occurs by default for inner barriers with $N > 144$.

For barriers generally considered as mass asymmetric, we apply an extra factor of 2 to $K_{\rm rot}$.

For all fission barriers, the default parameters for the damping function f of Eq. (266) are $U_f^{bar} = 45$ MeV, $C_f^{bar} = 5$ MeV. The shell correction is also different: For the inner barrier, $\delta W = 1.5$ MeV for an axially symmetric barrier, and 2.5 MeV otherwise. For the other barriers, we take 0.6 MeV in general. As usual, all these default choices can be modified using appropriate keywords in the input file.

13.3.2 Effective treatment of collective effects

Despite being of a more "effective" nature than the approach described above, this second method has been successful in

the description of fission cross sections, see e.g. Ref. [182]. An essential aspect is that the damping of collective effects are taken into account in a phenomenological way through the level density parameter a. The asymptotic level density parameter $\tilde{a}$ (Eq. 227) is damped from its effective limit $\sim A/8$ to its intrinsic limit $\sim A/13$ as follows

$$\tilde{a}^{\text{eff}} = \frac{A}{13} f(E_x) + \tilde{a}(1 - f(E_x)), \tag{311}$$

where

$$f(E_x) = \frac{1}{1 + \exp -(\frac{E_x - E_{col}^{g.s.}}{d_{col}^{g.s.}})}, \tag{312}$$

with the same values as mentioned below Eq. (266). Next, the resulting $a(E_x)$ is used in all equations. The term "effective limit" for the level density parameter stems from the fact that if collective enhancements are not explicitly treated, they are included in an effective way in the value of the level density parameter which is then of the order of $A/8$ while it is behaves rather like $A/13$ otherwise. This second approach also implies that the collective enhancement to be considered is not the one defined in Sect. 11. One has to distinguish two situations:

1. When analytical expression are used, the collective enhancement is defined with respect to that of the ground state. In other words, it implies that for an axially symmetric barrier, the collective enhancement is a constant value in principle close to the ratio between the ground state moment of inertia of Eq. (262) and the moment of inertia given by the same definition but with the fission barrier quadrupole deformation. Since this ratio is generally close to one, no enhancement is considered by default for axially symmetric barrier.
   For triaxial barriers, an extra rotational enhancement needs to be taken into account. Instead of Eq. (265), this is taken as

$$K_{rot}(E_x) = \left(\frac{U}{a_{\text{eff}}}\right)^{1/4} (1 - f(E_x)) + f(E_x), \tag{313}$$

   where $a_{\text{eff}} = 8a_{\text{GS}}/13$ and

$$f(E_x) = \frac{1}{1 + \exp(-\frac{1}{2}(E_x - 18)}. \tag{314}$$

   Again, this enhancement is the result of the ratio between the rotational enhancement for an axially asymmetric nucleus and that of axially symmetric one. There is no vibrational enhancement in this model since it is assumed to be accounted for with the level density parameter a_{GS} of the nucleus with the ground state deformation. Concerning the shell correction, one has for all barriers $\delta W = \frac{2}{3} \mid \delta W_{ground} \mid$. Finally, the spin cut-off parameter (Eq. 238) is multiplied by $\left(1 + \frac{\beta_2}{3}\right)$ as done in Eq. (262) for the perpendicular spin cut-off parameter.
2. When the level densities at the fission saddle points are taken from microscopic HFB calculations (see Sect. 11.2), the underlying idea is the same. Since the combinatorial method is only applied within the axially symmetric approximation, to account for extra broken symmetries, a rotational enhancement is included by multiplying the tabulated values by the ratio between the rotational enhancement for the considered broken symmetry (see above) and the one accounted for while computing the tables.

13.4 Class II/III states

Class II (resp. III) states may be introduced when double (resp. triple) humped barriers are considered. In the particular situation where the excitation energy E_{CN} of the compound nucleus is lower than the barrier heights, fission transmission coefficients display resonant structures which are due to the presence of nuclear excited levels in the second (class II), or in the third (class III) well of the PES. When such resonant structures occur, the expression for the effective fission transmission coefficient has to be modified (generally enhanced).

The way this resonant effect is determined depends on the number of barriers that are considered.

13.4.1 Double humped fission barrier

For two barriers, the effective fission transmission coefficient T_{eff} can be re-written as

$$T_{eff} = \frac{T_A T_B}{T_A + T_B} \times F_{AB}(E_{CN}), \tag{315}$$

where $F_{AB}(E_{CN})$ is a factor whose value depends on the energy difference between the excitation energy of the nucleus and that of the class II state located in the well between barrier A and B. It has been shown [183] that the maximum value of $F_{AB}(E)$ reaches $\frac{4}{T_A + T_B}$ and gradually decreases over an energy interval defined as the width Γ_{II} of the class II state with excitation energy E_{II}. This is accounted for by the empirical quadratic expression

$$F_{AB}(E) = \frac{4}{T_A + T_B} + \left(\frac{E - E_{II}}{0.5\Gamma_{II}}\right)^2 \times \left(1 - \frac{4}{T_A + T_B}\right), \tag{316}$$

if $E_{II} - 0.5\Gamma_{II} \leq E \leq E_{II} + 0.5\Gamma_{II}$ and $F_{AB} = 1$ otherwise.

Theoretically, this expression is valid for the tunneling through a single double humped barrier whereas in realistic situations, both T_A and T_B are obtained from a summation over several transition states. One may thus have large T_A and T_B values so that Eq. (316) may give $F_{AB}(E) \leq 1$. Such a situation can only occur for high enough excitation energies for which the individual Hill-Wheeler contributions in Eq. (303) are large enough. However, in TALYS, we only consider class II states with excitation energies lower than the height of the first barrier. Consequently, the resonant effect can only occur if the compound nucleus energy E_{CN} is (i) lower than the top of the first barrier and (ii) close to a resonant class II state ($E_{II} - 0.5\Gamma_{II} \leq E_{CN} \leq E_{II} + 0.5\Gamma_{II}$). With such requirements, the individual Hill-Wheeler terms are clearly small, and $T_A + T_B \ll 1$.

13.4.2 Triple humped fission barrier

If three barriers A, B and C are considered, the situation is more complicated. In this case, three situations can occur depending on the positions of the class II and class III states. Indeed the enhancement can be due either to a class II state or to a class III state, but on top of that, a double resonant effect can also occur if both class II and class III states have an excitation energy close to the compound nucleus energy. In all cases, the enhancement is first calculated for the first and second barriers giving the transmission coefficient

$$T_{eff}^{AB} = T_{AB} \times F_{AB}, \tag{317}$$

with F_{AB} given by Eq. (316) as in the previous double humped case.

Next, the eventual coupling with a class III state with energy E_{III} of width Γ_{III} is accounted for by generalizing Eq. (315) i.e.

$$T_{eff}^{ABC} = \frac{T_{eff}^{AB} T_C}{T_{eff}^{AB} + T_C} \times F_{ABC}(E), \tag{318}$$

where $F_{ABC}(E)$ is given by generalizing Eq. (316) writing

$$F_{ABC}(E) = \frac{4}{T_{eff}^{AB} + T_C} + \left(\frac{E - E_{III}}{0.5\Gamma_{III}}\right)^2 \times \left(1 - \frac{4}{T_{eff}^{AB} + T_C}\right), \tag{319}$$

if $E_{III} - 0.5\Gamma_{III} \leq E \leq E_{III} + 0.5\Gamma_{III}$ and $F_{ABC} = 1$ otherwise. Class III states can introduce an anti-resonance effect [55].

14 Fission yields and neutron and gamma observables

TALYS contains various models to describe the decay of highly excited fission fragments directly after scission into fission products, while book-keeping the associated neutron and gamma observables such as the average neutron multiplicity, prompt fission neutron spectrum, etc. The first implemented models in TALYS attempted to describe the complete description of all fission yield and neutron observables, at the expense of approximations in the calculation of neutron and gamma evaporation from the excited fission fragments. Examples of the use of TALYS for such fission product yield estimates were published for the Brosa model [184]. More recently, the advance in computer power has enabled more physical and exact methods. One can feed TALYS with a distribution of excited fission fragments coming from a specific projectile plus target fission event, and perform Hauser–Feshbach decay on each of these fission fragments, after which all fission product yields and neutron and gamma observables become available.

14.1 Fission fragment distribution models

As a starting point for the Hauser–Feshbach calculations, the fission fragment distributions are provided by different microscopic or phenomenological nuclear structure models. Each fission fragment pair is described by a yield $Y_{\rm ff}(Z, A, E_x, J, \Pi)$ which implicitly contains an excitation energy, spin and parity distribution. This excitation energy distribution is directly connected to the total excitation energy TXE, which is shared between the light (l) and heavy (h) fragments. This specific sharing may differ per fission fragment model. TXE is related to the total kinetic energy TKE and can be written for a neutron-induced fission reaction leading to two fragments only as follows,

$$\begin{aligned} \mathrm{TXE}(A_l, Z_l; A_h, Z_h) &= Q_f(A_l, Z_l; A_h, Z_h) \\ &\quad -\mathrm{TKE}(A_l, Z_l; A_h, Z_h) \\ &= [M_n(A_{CN}, Z_{CN}) - M_n(A_l, Z_l) - M_n(A_h, Z_h)]\, c^2 \\ &\quad + E_{inc} + S_n - \mathrm{TKE}(A_l, Z_l; A_h, Z_h), \end{aligned} \tag{320}$$

where Q_f is the Q value of the fission reaction, M_n the nuclear mass, and E_{inc} the incident neutron energy. Currently, the TALYS database contains fission fragment distribution for three models, GEF, HF^{3}D, and SPY for many nuclides, as detailed below. The $Y_{\rm ff}(Z, A, E_x, J, \Pi)$ yields are given in a table format on a sufficiently dense excitation energy grid, after which TALYS loops over all excited fission fragments.

14.1.1 GEF model

The GEF fission model [185] is based on the statistical population of states in the fission valley at the moment of dynamical freeze-out, which is specific to each collective degree of freedom. A macroscopic approach is utilized by deriving global fit parameters to a large set of experimental data such as fission mass and charge yields, prompt fission neutrons, and gamma rays. Most parameters are fixed from independent sources, only about 20 parameters have specifically been adjusted. The good reproduction of measured data by the code makes it useful for applications in nuclear technology and complement the use of purely empirical models. The code estimates fission barrier heights from the topographic theorem [185] and derives fission fragment yields by utilizing the Brosa model with Gaussian fitting. It further employs statistical mechanics and the law of entropy to share the excitation energy between the fragments. The TXE partitioning is determined according to a probability distribution that is given by the product of the level densities of the individual fragments.

For TALYS, Nordström et al. [186] used GEF as a fission event generator and performed 1,000,000 random samplings per fissioning system. With this, the average TKE and TXE of the fission fragment pairs, as well as the mean $E_{l,h}$ and standard deviations $W_{l,h}$ of the TXE distribution for both the light and heavy fragments were obtained for 738 isotopes in the $76 < Z < 107$ range.

14.1.2 HF^{3}D model

The Hauser–Feshbach fission fragment decay model (HF^{3}D) [187] is based on a full deterministic model to calculate fission observables. The primary fission fragment yield $Y(A)$ and TKE are determined by fitting experimental data with simple analytical functions. In order to generate the charge distribution $Y(A, Z)$, the so-called Z_P model [188] is employed, and the excitation energy division is made by the anithothermal model to reproduce the average neutron multiplicity $\overline{\nu}(A)$. For the TALYS fission fragment distribution parameters, three data sets are provided for the compound nuclides, ^{235}U, ^{238}U, and ^{239}Pu, for which some experimental data exist. A few important details of the HF^{3}D model are explained below.

The fission fragment mass distribution $Y(A)$ is made of the sum of multiple (5 or 7) Gaussian functions.

$$Y(A) = \sum_{i=1}^{5} \frac{Y_i}{\sqrt{2\pi}\sigma_i} \exp\left\{-\frac{(A - A_m + \Delta_i)^2}{2\sigma_i^2}\right\}, \tag{321}$$

where σ_i and Δ_i are the Gaussian parameters, A_m ($= A_{CN}/2$) is the symmetry point of the mass distribution, and Y_i is the yield component. The Y_i's are divided into the principal ($Y_{1,5}$), the inner ($Y_{2,4}$), and the central (Y_3) peak curves. Further details of the build-up of the fission fragment distribution can be found in Ref. [187]. The TXE is distributed over the light and heavy fragment using the R_T parameter which is defined as the ratio of effective temperatures in the fission fragments,

$$R_T = \frac{T_l}{T_h} = \sqrt{\frac{E_l}{E_h}\frac{a_h(E_h)}{a_l(E_l)}}, \tag{322}$$

where $a_{l,h}(E_{l,h})$ are the level density parameters at $E_{l,h}$. Therefore, the energies are given by

$$E_h = \mathrm{TXE}\frac{a_h}{R_T^2 a_l + a_h},\ E_l = \mathrm{TXE}\frac{R_T^2 a_l}{R_T^2 a_l + a_h}. \tag{323}$$

The TXE distribution G is also represented by a Gaussian,

$$G(E_x) = \frac{1}{\sqrt{2\pi}W_{l,h}} \exp\left\{-\frac{(E_x - E_{l,h})^2}{2W_{l,h}^2}\right\}, \tag{324}$$

where

$$W_{l,h} = \frac{W_{\mathrm{TXE}}}{\sqrt{E_l^2 + E_h^2}} E_{l,h},\ (W_{\mathrm{TXE}} = W_{\mathrm{TKE}}). \tag{325}$$

14.1.3 SPY model

The SPY model [189,190] is a static and statistical scission-point model that assumes a statistical equilibrium at scission. This model is based on microscopic inputs, computed within the constrained Hartree-Fock-Bogoliubov (HFB) mean-field model using the Skyrme BSk27 nucleon-nucleon effective interaction [191]. This interaction can predict all the 2457 experimental masses [111] with a root-mean-square deviation of 0.51 MeV. The main advantage of using the HFB model is it can describe nuclear structure properties for a wide range of nuclei without phenomenological parameters apart from those of the effective interaction (see Sect. 9).

In the SPY model, the scission configuration is defined by the proton density at the scission neck of the fissioning nucleus. The fission fragment yields are obtained by counting the number of available states at scission for all possible fragmentations. Currently, fission fragment distributions for more than 800 nuclides are available in TALYS.

14.1.4 TALYS applications

Preliminary results from the Hauser-Feshbach loop over all excited fission fragments have been reported in Ref. [192]. A complete publication with all the calculational details and results for a wide range of nuclides and observables is underway, and here we merely give a small preview of some results for ^{235}U. While all fission fragments are evaporated, TALYS

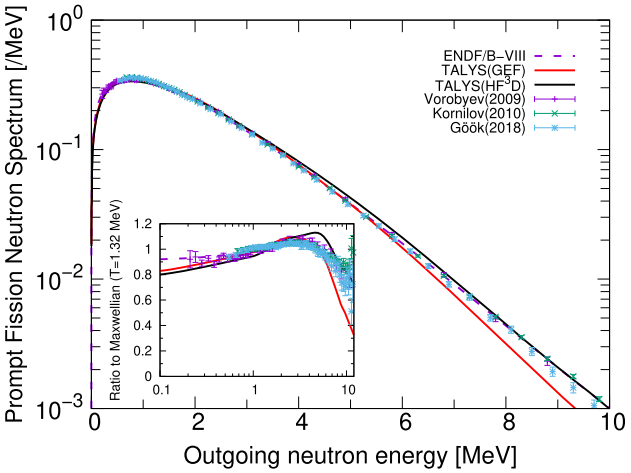

Fig. 24 Comparison of prompt fission neutron spectra for thermal neutrons on ^{235}U calculated by TALYS using the GEF and HF^{3}D fission fragment distributions as a starting point, with experimental data and the ENDF/B-VIII data library [193]. The inset shows the ratio over the Maxwellian distribution. The experimental data are from the EXFOR database [80]

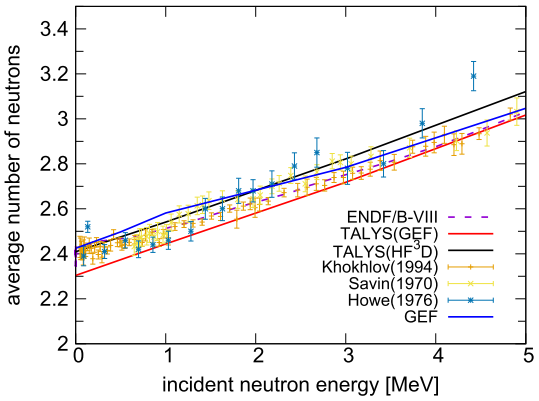

Fig. 25 Comparison of the average neutron multiplicity as a function of neutron incident energy for ^{235}U calculated by TALYS using the GEF (red solid line) and HF^{3}D (black solid line) fission fragment distributions, with experimental data from the EXFOR database [80], and the ENDF/B-VIII data library [193]. The GEF calculation by the original code (blue solid line) is also shown

collects the data of all emitted particles and residual fission products. Figure 24 shows the prompt fission neutron spectrum for thermal neutron-induced fission. It is clear that TALYS results cannot yet match the accuracy of experiment-based evaluation of ENDF/B-VIII [193]. This is especially visible upon comparison with the Maxwellian ratio, which shows a deviation at the lowest and highest energies for both the GEF and HF^{3}D sets of fission fragments. Figure 25 shows the average neutron multiplicity, which shows an interesting difference coming from full Hauser-Feshbach decay by TALYS versus the built-in neutron evaporation model in GEF. Figure 26 shows the final fission product yield.

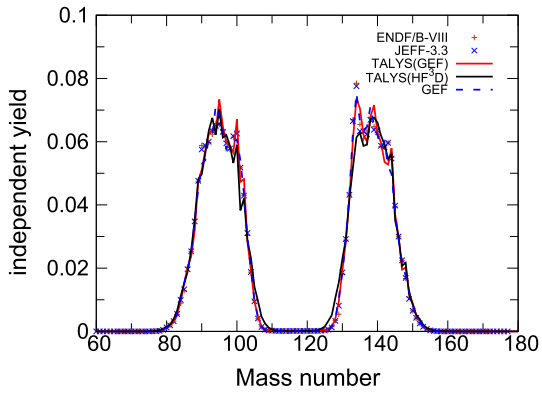

Fig. 26 Comparison of fission product yield for thermal neutrons on ^{235}U calculated by TALYS using the GEF (red solid line) and HF^{3}D (black solid line) fission fragment distributions, with the ENDF/B-VIII [193] and JEFF−3.3 [194] data libraries. The GEF calculation (blue dashed line) is also shown

14.2 High energies: temperature-dependent Brosa model

The description of fission fragment and product yields follows the procedure outlined in Ref. [184]. The Hauser-Feshbach formalism gives a fission cross section per excitation energy bin for each fissioning system. The fission fragment masses and charges are, subsequently, determined per given excitation energy bin E_x, in a fissioning system (FS), characterised by (Z_{FS}, A_{FS}, E_x), for which the fission cross section exceeds some minimum value. The total fragment mass distribution is given by a sum over all contributing bins weighted with the corresponding fission cross sections:

$$\sigma(A_{FF}) = \sum_{Z_{FS},A_{FS},E_x} \sigma_f(Z_{FS}, A_{FS}, E_x) \times Y(A_{FF}; Z_{FS}, A_{FS}, E_x), \quad (326)$$

where $Y(A_{FF}; Z_{FS}, A_{FS}, E_x)$ is the relative yield of a fission fragment with mass A_{FF} originating from a fissioning system. Combining this expression with the result of a fission fragment charge distribution calculation gives the final production cross section of a fission fragment with mass A_{FF} and charge Z_{FF}:

$$\sigma_{prod}(Z_{FF}, A_{FF}) = \sum_{Z_{FS},A_{FS},E_x} \sigma_f(Z_{FS}, A_{FS}, E_x) \times Y(A_{FF}; Z_{FS}, A_{FS}, E_x) \times Y(Z_{FF}; A_{FF}, Z_{FS}, A_{FS}, E_x), \quad (327)$$

where $Y(Z_{FF}; A_{FF}, Z_{FS}, A_{FS}, E_x)$ is the relative yield of a fission fragment with charge Z_{FF} given its mass A_{FF} and the fissioning system characterised by (Z_{FS}, A_{FS}, E_x).

The fission fragment mass distribution is determined with a revised version of the multi-modal random neck-rupture model. The original model has been developed by Brosa et

al. [195] to calculate properties of fission fragments at zero temperature. However, fission calculations within TALYS require fragment mass distributions up to higher temperatures. In the version of the model of Ref. [184] the temperature is added to the calculation of the potential energy landscape of the nucleus.

15 Astrophysical reaction rates

In view of the huge amount of nuclear data needed for nuclear astrophysics applications [196], TALYS has been and is still used extensively in many different branches of astrophysics (see Fig. 1). Although significant effort has been devoted in the past decades to measuring reaction cross sections of astrophysical interest, experimental data only covers a minute fraction of the entire data set required for such a nuclear physics application. Reactions of interest often concern unstable or even exotic (neutron-rich, neutron-deficient, superheavy) species for which no experimental data exist. Some astrophysical applications, such as nucleosynthesis also involve a large number (thousands) of unstable nuclei for which many different properties have to be determined. The energy range for which experimental data is available is also restricted to the small range that can be studied by present experimental setups. Finally, a thermonuclear reaction in an astrophysical plasma also depends on some specific properties of this plasma, in particular its temperature. To fill the gaps, only theoretical predictions can be used [196].

A thermodynamic equilibrium holds locally to a good approximation inside stellar interiors. Consequently, the energies of both the targets and projectiles, as well as their relative energies E, obey a Maxwell-Boltzmann distribution corresponding to the temperature T at that location (or a black-body Planck spectrum for photons). In such conditions, the astrophysical rate is obtained by integrating the cross section over a Maxwell-Boltzmann distribution of energies at the given temperature T. In addition, in hot astrophysical plasmas, the target nucleus exists in its ground as well as excited states. In a thermodynamic equilibrium situation, the relative populations of the various levels of nucleus I^μ with excitation energies E_x^μ and spin I^μ obey a Maxwell-Boltzmann distribution. The effective stellar rate per pair of particles in the entrance channel at a temperature T, taking account of the contributions of various target excited states, is finally expressed in a classical notation (see Sect. 5) as

$$N_A\langle\sigma v\rangle^*_{\alpha\alpha'}(T) = \left(\frac{8}{\pi m}\right)^{1/2}\frac{N_A}{(kT)^{3/2}\,G_I(T)} \times\int_0^\infty\sum_\mu\frac{(2I^\mu+1)}{(2I^0+1)}\sigma^\mu_{\alpha\alpha'}(E) \times E\exp\left(-\frac{E+E_x^\mu}{kT}\right)dE, \tag{328}$$

where k is the Boltzmann constant, m the reduced mass of the $I^0 + a$ system, $\mu = 0$ denotes the target ground state, N_A the Avogadro number, and

$$G_I(T) = \sum_\mu (2I^\mu+1)/(2I^0+1)\exp(-E_x^\mu/kT) \tag{329}$$

the T-dependent normalized partition function. In the specific case of the radiative neutron captures, the Maxwellian-averaged reaction rate is traditionally expressed by the Maxwellian-averaged cross section (MACS)

$$\langle\sigma\rangle = \langle\sigma v\rangle/v_T \tag{330}$$

where $v_T = \sqrt{2kT/m}$ is the thermal velocity at the temperature T.

Reverse reactions can also be estimated on the basis of the reciprocity theorem [172]. In particular, the stellar photodissociation rates for astrophysical applications have until now been derived mainly from radiative capture rates by the expression

$$\lambda^*_{(\gamma,a)}(T) = \frac{(2I^0+1)(2j_a+1)}{(2I'^0+1)}\frac{G_I(T)}{G_{I'}(T)} \times\left(\frac{mkT}{2\pi\hbar^2}\right)^{3/2}\langle\sigma v\rangle^*_{(a,\gamma)}\,\mathrm{e}^{-Q_{a\gamma}/kT}, \tag{331}$$

where $Q_{a\gamma}$ is the Q-value of the $I^0(a,\gamma)I'^0$ capture. We note that, in stellar conditions, the reaction rates for targets in thermal equilibrium are usually believed to obey reciprocity since the forward and reverse channels are expected to be symmetrical, in contrast to the situation that would be experienced by targets in their ground state only [172]. The total stellar photodissociation rate can also be determined directly from

$$\lambda^*_{(\gamma,a)}(T) = \frac{\sum_\mu(2I^\mu+1)\;\lambda^\mu_{(\gamma,a)}(T)\;\exp(-E_x^\mu/kT)}{\sum_\mu(2I^\mu+1)\;\exp(-E_x^\mu/kT)}, \tag{332}$$

where the photodissociation rate $\lambda^\mu_{(\gamma,a)}$ of state μ with excitation energy E_x^μ is given by

$$\lambda^\mu_{(\gamma,a)}(T) = \int_0^\infty c\,n_\gamma(E,T)\,\sigma^\mu_{(\gamma,a)}(E)\,dE\,, \tag{333}$$

where c is the speed of light, $\sigma^\mu_{(\gamma,a)}(E)$ is the photodisintegration cross section at energy E estimated within the above-described reaction formalism, and $n_\gamma(E,T)$ is the stellar γ-ray distribution described by the black-body Planck spectrum at the given temperature T. Concerning the calculation of Maxwellian-averaged reaction rates of astrophysical interest, the TALYS code has some clear advantages over previous codes developed for astrophysical applications, such

as MOST [197] or NON-SMOKER [198]. As detailed in Ref. [199], these concern:

- the inclusion of the pre-equilibrium and direct capture reaction mechanisms,
- the detailed description of the decay scheme, including the description of γ-delayed particle emission and the possible particle emission from all residual nuclei,
- the inclusion of multi-particle emission,
- the inclusion of detailed width fluctuation corrections [200, 201] in contrast to the approximation of [202,203] usually applied in other astrophysical codes,
- the inclusion of parity-dependent level densities,
- the inclusion of a coupled channel description for deformed nuclei, while other astrophysical codes consider spherically equivalent optical potentials for deformed targets, and
- the inclusion of the fission channel for the compound as well as the residual nuclei. Fission is often neglected in astrophysical codes, and if included, insufficiently tested on experimental data and not consistently taken into account in the full decay scheme.

16 Illustration of TALYS calculations

All nuclear reaction models outlined in this paper are driven by parameters. During the two decades of TALYS development, global trends and systematic formulae for all these parameters have been established. Hence, TALYS can be used for entirely global calculations, being agnostic to the experimental data from a particular nucleus, or as a fitting code, where it is assumed that the functional forms provided by the physics of TALYS only needs to be altered by adjusting the nuclear model parameters to obtain a good fit to experimental data. In this Section, both approaches will be demonstrated by several examples.

16.1 Radiative neutron capture

Figure 27 shows a simple example of the flexibility offered by level density adjustment given by Eq. (230) to tune cross sections. In this case, both parameters c and δ of Eq. (230) are adjusted to improve the description of the low-energy discrete levels of ^{90}Y (as shown in the upper panel of Fig. 27). This results in an improved description of the ^{89}Y capture cross section (lower panel of Fig. 27). In this illustration, the PSF has also been tuned on experimental radiative width once the level density is adjusted on experimental data. The default calculation corresponds to setting both parameters entering Eq. (230) to zero ($c = 0, \delta = 0$).

Sect. 12 explained how the PSF can be altered by means of the three adjustable parameters introduced through Eq. (293),

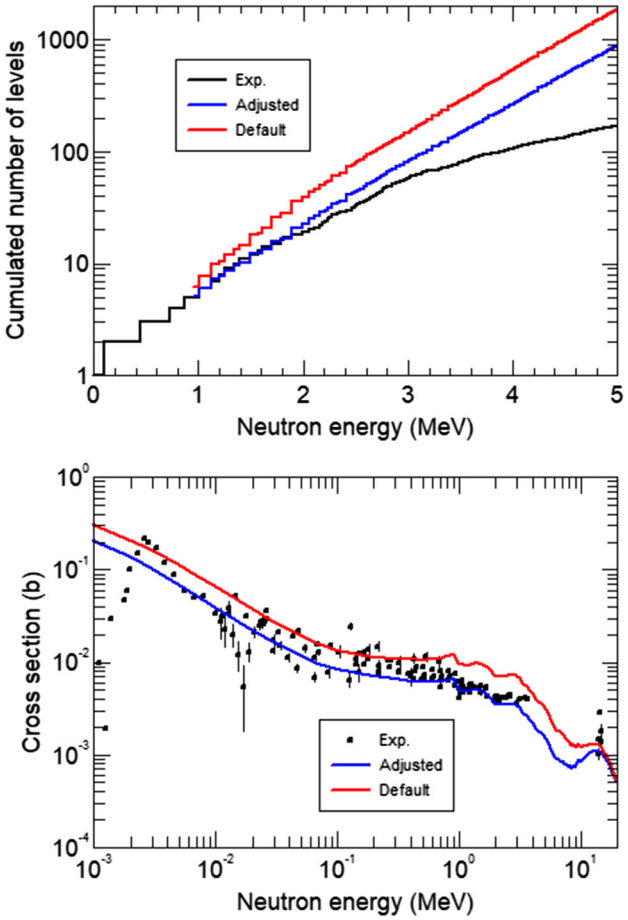

Fig. 27 Impact of the level density adjustment (Eq. 230) on the cumulative number of low-lying levels in ^{90}Y (upper panel) and the ^{89}Y(n, γ) cross section (lower panel). The black symbols correspond to experimental data taken from the EXFOR library [80]

as illustrated in Fig. 21. An important application of this parameter adjustment is to obtain an optimal calculation of (n, γ) cross sections over the entire energy range. Figure 28 shows a calculation performed with the QRPA PSF and the HFB plus combinatorial microscopic level densities. For this combination of models, the w^{table} parameter has been optimized to all nuclides for which experimental (n, γ) cross sections are available. The resulting values of w^{table} are plotted in Fig. 29. This means that by only changing the width of the PSF, leaving its absolute strength and position the same, the (n, γ) excitation function can be shifted in absolute value until the best agreement with measurement is obtained. The global value of w^{table} i.e. averaged over the optimized values for all nuclides is equal to 1.017, i.e. a slight increase compared to purely microscopic tabulated values (given by $w^{\text{table}} = 1$). For the particular case of ^{174}Yb(n, γ), this calculation leads to the global TALYS curve in Fig. 28. Reducing the value of w^{table} to 0.90 yields the fitted TALYS curve. This procedure has been automated for all nuclides: provided the

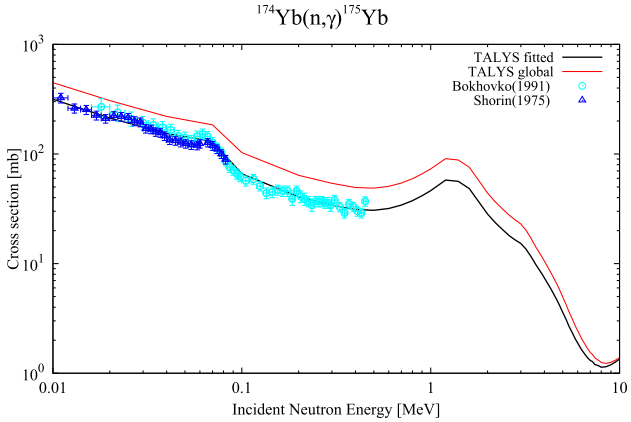

Fig. 28 Adjustment of the PSF with a $w^{\text{table}} = 0.9$ parameter to reproduce the ^{174}Yb(n, γ) cross section. The global cross section calculation corresponding to the default value $w^{\text{table}} = 1$ is shown by the solid red line. Experimental data are taken from the EXFOR library [80]

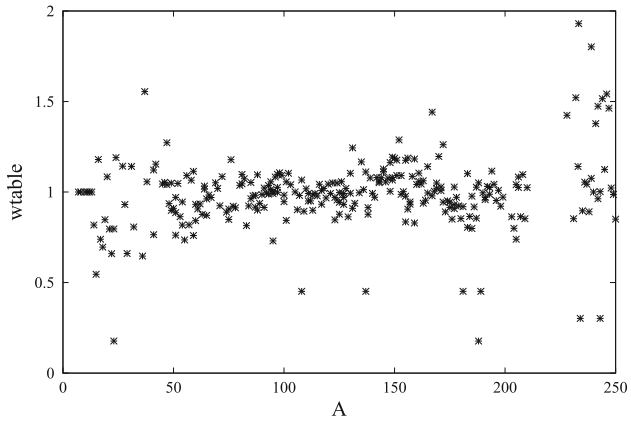

Fig. 29 Values of the w^{table} parameter providing optimal fit to (n, γ) cross sections in the fast neutron energy range as a function of target mass number A

correct experimental data are selected (which is not an obvious task), the optimal value of w^{table} is readily obtained. It should be mentioned that other experimental data need to be simultaneously taken into account to constrain the calculation. Often, the average radiative capture width, $\langle\Gamma_\gamma\rangle$, and the MACS are also measured. Table 2 illustrates, for the ^{174}Yb(n, γ) case, the agreement between experiment and theoretical values obtained with the global and adjusted values of w^{table}. The combined picture of the three different types of observables is often seen in nuclear data evaluation: they do not all point to the same optimal nuclear model parameter. Although the adjusted value of w^{table}, optimized to differential (n, γ) cross sections is confirmed by the comparison with the experimental MACS value, the $\langle\Gamma_\gamma\rangle$ seems to favor the global value for w^{table}.

16.2 Photoneutron cross sections

Figure 30 compares TALYS prediction of photoneutron cross sections for stable Sm isotopes with experimental data [204–207]. TALYS calculations are obtained with the D1M+QRPA [140] or the BSk7+QRPA [157] PSF models. Both are PSF models that have been globally adjusted on photodata. Improved adjustment can be obtained using TALYS capabilities to modify locally the PSF, as described in Sect. 12.4. Using the same PSF, the inverse radiative neutron capture cross sections have been calculated and compared with experimental data in Fig. 31. In this case the D1M+QRPA PSF is used to estimate the cross section calculation. Since the cross section also depends on the adopted level densities, two models are considered, namely the Skyrme-HFB plus combinatorial model [140] and the temperature-dependent Gogny-HFB plus combinatorial [137]. Both of them are normalized to the experimental s-wave resonance spacing D_0 values [9] whenever available. More details can be found in Ref. [204].

Table 2 Comparison for ^{174}Yb(n, γ) MACS and ^{175}Yb $\langle\Gamma_\gamma\rangle$ between experimental data and TALYS predictions obtained with the global model or the model adjusted to (n, γ) cross sections with $w^{\text{table}} = 0.90$, as illustrated in Fig. 28. The C/E value gives the theoretical deviation with respect to experiment

	MACS (mb)	$\langle\Gamma_\gamma\rangle$ (eV)
Exp.	151. ± 1.7	0.08 ± 0.02
Global	249.4 (C/E = 1.65)	0.0689 eV (C/E = 0.86)
Adjusted	172.9 (C/E = 1.14)	0.0415 eV (C/E = 0.52)

Figure 32 compares experimental and TALYS photoneutron cross sections for ^{181}Ta. It includes the total photoreaction cross section [208,209] as well as the partial cross section to the 9^- ^{180}Ta^m isomer only [209]. TALYS total and partial cross sections have been estimated with the SLy4+QRPA PSF and two level density models, namely the HFBCS plus statistical [131] or the HFB plus combinatorial [106] models. The weak partial cross section ^{181}Ta$(\gamma$,n$)^{180}$Ta^m is sensitive not only to the ^{181}Ta $E1$ PSF and ^{180}Ta – neutron optical potential (in a similar way as the total photoneutron cross section) but also to the detailed level spectrum in ^{180}Ta responsible for the $E1$ photon cascade. In this respect, the measured partial cross section is relatively sensitive to the spin- and parity-dependent nuclear level density of ^{180}Ta. More details can be found in Ref. [209].

16.3 $(n, xn\gamma)$ cross sections

The exact exclusive reaction decay scheme outlined in Sect. 2 allows to keep track of gamma-ray intensities between discrete levels, for either exclusive or residual production cross sections. Figure 33 shows four specific ^{238}U$(n, n'\gamma)$ cross sections of the ^{238}U ground state band. Such cross sections provide strong constraints on the total inelastic modeling, in particular in situations where (n, n') is hard to

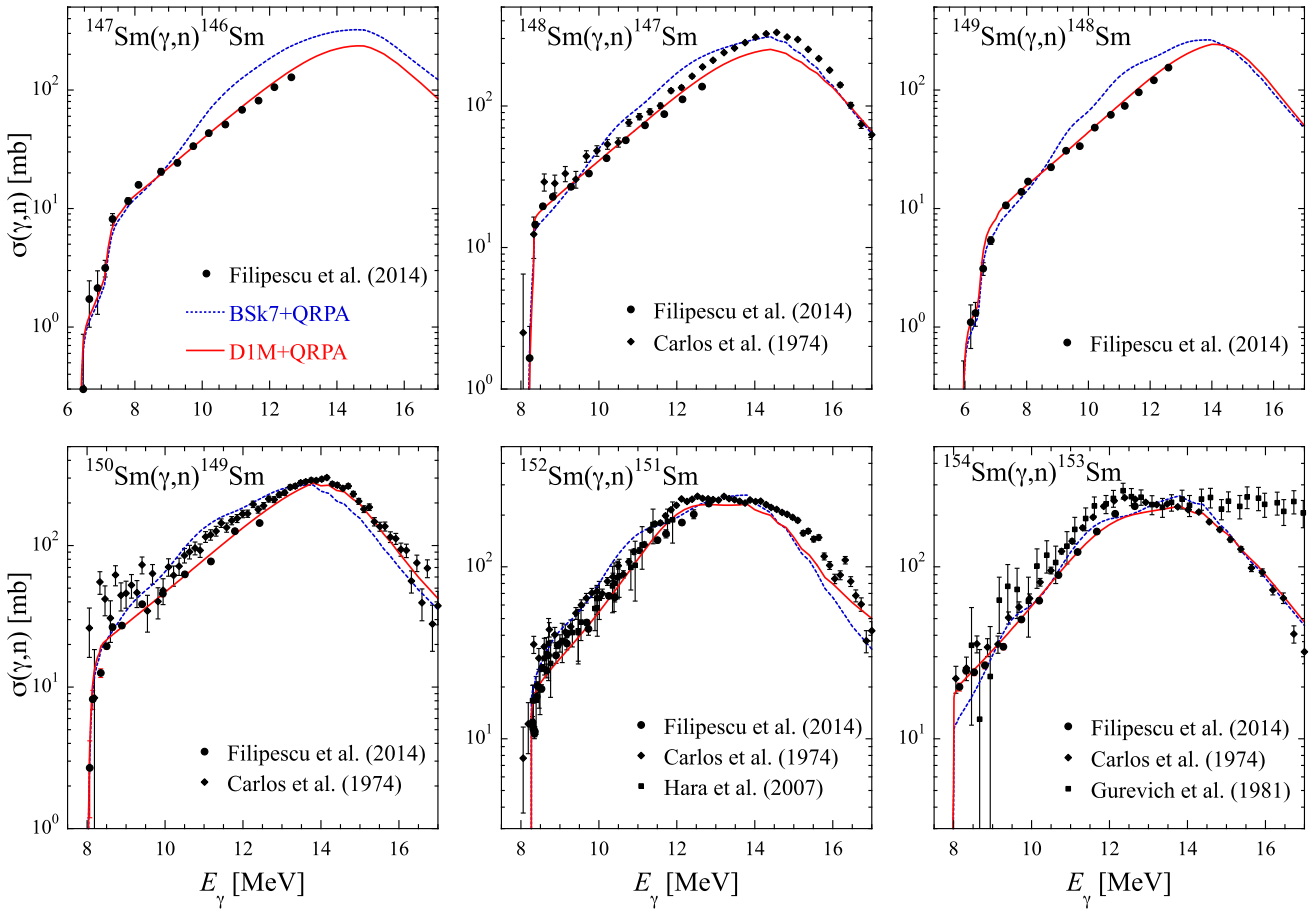

Fig. 30 Comparison between experimental [204–207] and TALYS photoneutron cross sections for Sm isotopes. The predictions are obtained with D1M+QRPA (solid red line) [140] or the BSk7+QRPA (dashed blue line) [157] PSF models

measure. The underlying idea is that if the nuclear reaction models succeed in describing individual transitions, this gives a better confidence in the predictive power regarding more global cross sections. In this illustration, two models are considered for the pre-equilibrium spin distribution (see Sect. 6.3). The red curves correspond to the usual definition of the pre-equilibrium spin cut-off factor of Eq. (177) using $C_p = 0.24$. while the green curves are obtained using $C_p = 0.04$, as suggested in a much detailed analysis reported in Ref. [93]. As can be observed, the agreement, even if it is not perfect, is much better with this latter choice. This stems from the fact that the initial spin distribution which precedes the pre-equilibrium process is predicted, by microscopic approaches, to be peaked at lower spins than what Eq. (177) with $C_p = 0.24$ prescribes. The consequence is that high spins are less populated leading to a reduction of the cross sections for the highest spin transitions.

16.4 Actinides and fission cross sections

A proper description of the fission channel poses one of the largest challenges of nuclear reaction modeling. Often, one can be satisfied if a fission calculation is descriptive, with respect to experimental data, while being predictive is beyond the current capabilities of nuclear theory. For TALYS, we have considered the following interesting challenge: Can we build a systematic evaluation approach which gives a simultaneous reasonable description for all actinides for which experimental data exist, i.e. from ^{227}Ac to ^{252}Cf. It turns out that this is indeed possible to some extent, of course at the expense of using several adjustable parameters. The objective is then to consistently use the same type of model parameters to adjust for each fissioning nuclide. As mentioned in Sect. 3, TALYS can include all the OMP's from the RIPL database and has as default the dispersive OMP of Capote et al. [35], which gives a good description of all OMP-related observables over the whole actinide range. The other global settings we use are a rotational band up to the 5th excited state to be included in the coupled-channels equations, the SMLO PSF

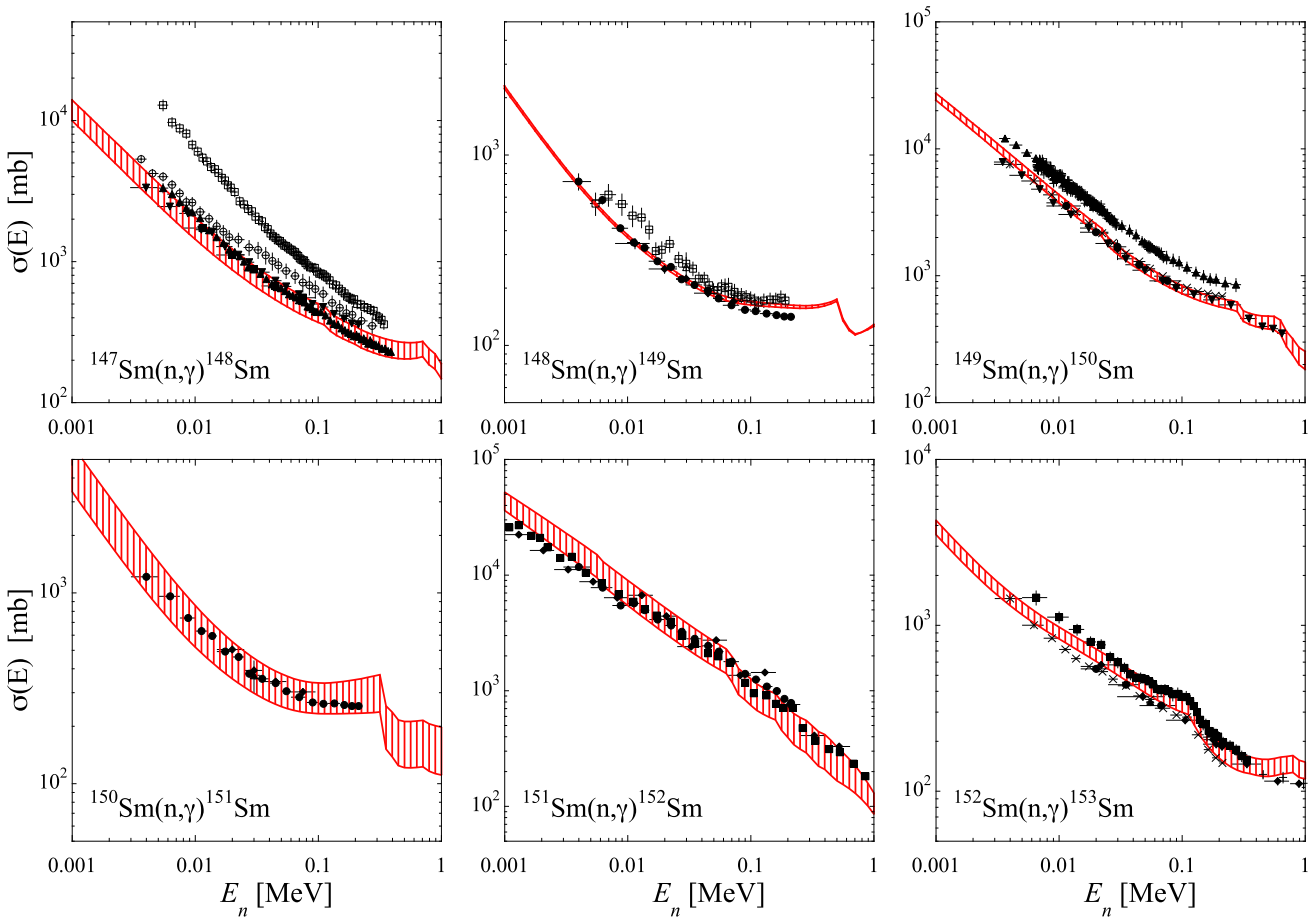

Fig. 31 Comparison between experimental and theoretical radiative neutron capture cross sections for Sm isotopes. The TALYS calculation is based on the D1M+QRPA PSF [140], as shown in Fig. 30. The hashed area corresponds to the sensitivity to the nuclear level densities obtained with the HFB plus combinatorial model [106] or the temperature-dependent HFB plus combinatorial model [137]. Experimental data (black symbols) are taken from the EXFOR library [80]

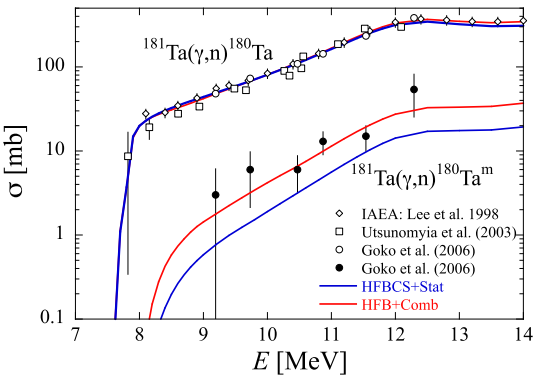

Fig. 32 Comparison between experimental and theoretical photoneutron cross sections for ^{181}Ta. The open squares, diamonds and circles correspond to the experimental total ^{181}Ta photoreaction cross section [208–210] while the lower full circles correspond to the partial cross section to the 9^- ^{180}Ta^m isomer only [209]. The blue and red lines correspond to TALYS predictions of the total and partial cross sections, respectively, using the HFBCS plus statistical [131] or the HFB plus combinatorial [106] level densities, respectively

model including an $M1$-upbend of which the parameters have been adjusted first to the (n, γ) cross sections, microscopic HFB plus combinatorial level densities (both for the ground state and saddle points, and HFB-based fission paths using the WKB approach to calculate fission transmission coefficients. For the first chance fission cross section, there are 7 parameters to be adjusted, in case of two fission barriers. The height of the fission barriers is adjusted by one global factor, while the relative shape of the barriers is given by the HFB fission paths. Next for the level density for each fission barrier, three parameters can be adjusted, one for the absolute value of the level density, one for the pairing, see Eq. (230), and one for the spin distribution. Obviously, for this case, we should not expect that the best possible evaluation for the "big 3" actinides ^{235,238}U and ^{239}Pu comes from this approach (which would require a much larger number of adjustable parameters), but eventually for several minor actinides the current evaluation method may approach the quality of the others. Figure 34 shows the result for the fission cross sec-

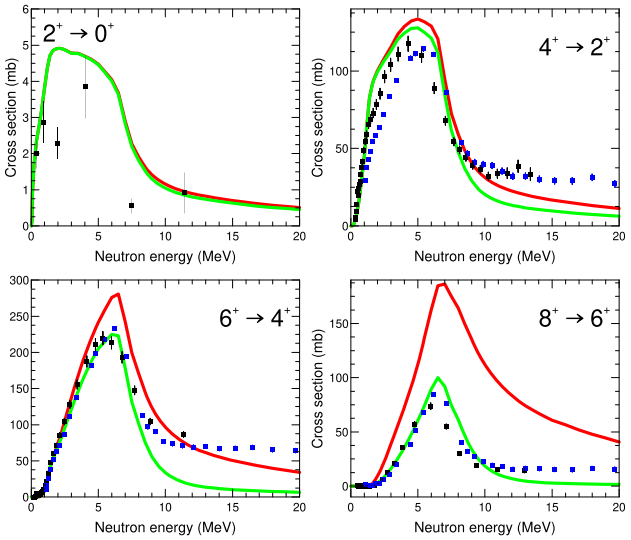

Fig. 33 ^{238}U$(n, n'\gamma)$ cross sections for 4 transitions within the ground state rotational band. Spin and parity of the initial and final states are reported in each panel. Black and blue squares correspond to Ref. [93] and Ref. [211] respectively. The red and green lines correspond to two options for the pre-equilibrium spin distribution of the exciton model (see text for more details)

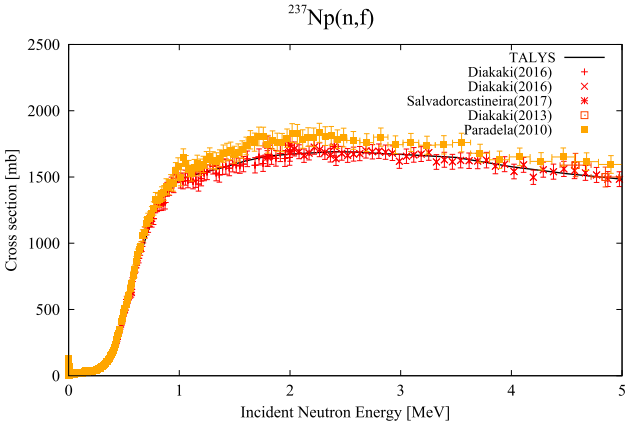

Fig. 34 TALYS calculation for the ^{237}Np(n, f) reaction. Experimental data (symbols) are taken from EXFOR database [80]

tion of ^{237}Np up to the threshold for second chance fission. Similar quality of fits are obtained for all other actinides. A future challenge will be to enforce consistency between fission nuclides and first, second etc. chance fission, so that good evaluations up to 20 MeV can be obtained with the WKB method. For U isotopes and phenomenological models this has already been accomplished with TALYS [55].

Microscopic inputs have also been used to determine fission cross sections on a larger scale [176,177]. Figure 35 illustrates the ^{240}Pu neutron-induced fission cross section obtained with HFB fission path [173] and HFB plus combinatorial level densities both in the ground state and at the fission saddle points [106]. The default HFB barriers are relatively

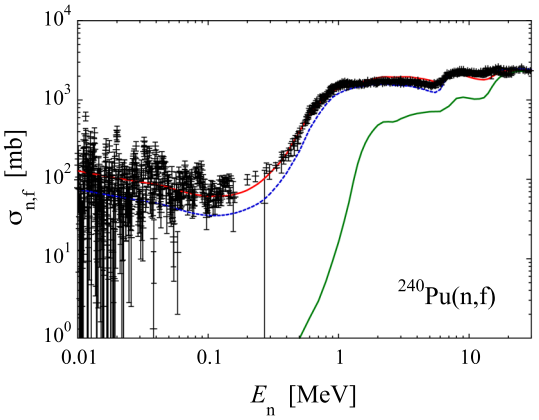

Fig. 35 ^{240}Pu neutron-induced fission cross section. The green curve corresponds to the TALYS default calculation with a microscopic HFB fission path [173] and HFB plus combinatorial level densities both in the ground state and at the fission saddle points [106]. The red curve is obtained adjusting the microscopic fission barrier by a nuclide-specific multiplication factor. The blue curve is obtained using a global normalization for the fission barriers. Experimental data (symbols) are taken from EXFOR database [80]. See Ref. [176] for details

high, so that the cross section is severely underestimated at low energies. However, a simple overall decrease of the fission path obtained from systematics [176] can already significantly improve the agreement with data. A specific adjustment of the fission path can further improve the description, as shown in Fig. 35.

If in addition to the fission path adjustment, the nuclear level densities at the fission saddle points are tuned, an excellent fit to the cross section can be achieved, This is illustrated in Fig. 36 where the ^{238}U neutron-induced fission cross section is compared to experimental data. In this case, the fit obtained with microscopic models is found to be relatively similar to that with more macroscopic models for the PSF, level densities and fission paths (see Ref. [177] for more details). However, if fission cross sections are described in one unique coherent framework for all U isotopes, such a high accuracy may be compromised, as shown in Fig. 36.

16.5 Astrophysical rates

Figure 37 compares the 240 experimental MACS [212] at 30 keV (assuming the target in its ground state only) for nuclei with $20 \leq Z \leq 83$ with the TALYS predictions obtained with the D1M+QRPA+0lim model of the PSF [140] and the HFB+combinatorial level density model [106]. Note that in the TALYS calculation, the PSF is not renormalized for reproducing the experimental average radiative width. Only nuclei with $Z \geq 20$ are considered in the comparison to ensure the validity of the Hauser-Feshbach approach, the cross section for lighter nuclei being affected by the direct capture contribution and the resolved resonance range.

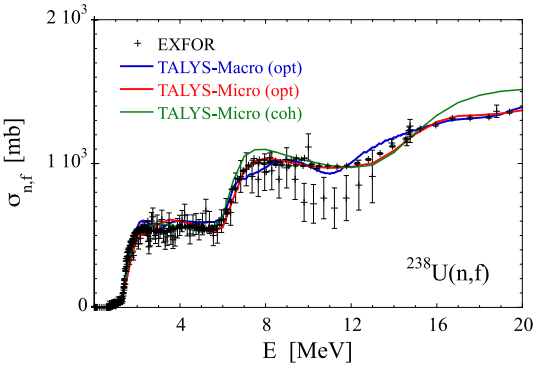

Fig. 36 ^{238}U neutron-induced fission cross section. The blue curve is obtained optimizing the parameter of macroscopic models [55] while the red curve is a fit on the basis of microscopic models [177] regardless of constrained stemming from neutron-induced fission cross section on the other U isotopes. The green fit is obtained tuning the microscopic model to reproduce, at best, all experimental data along the U chain in one unique coherent framework [177]

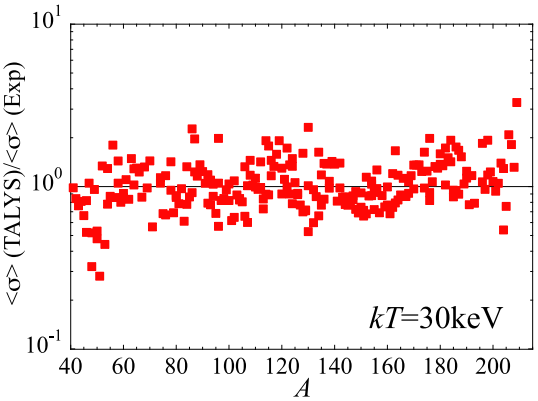

Fig. 37 Ratio of the theoretical to experimental (n, γ) MACS at $kT = 30$ keV as a function of the atomic mass A for all the 240 nuclei between Ca and Bi for which experimental MACS exist [212]. The theoretical MACS are obtained with the D1M+QRPA+0lim PSF [140] and the HFB+combinatorial model of level densities [106]

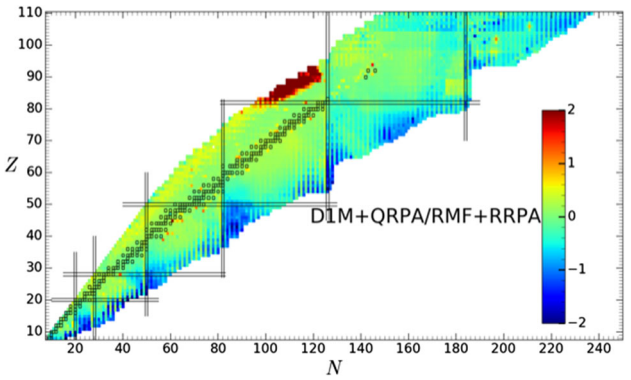

Fig. 38 Representation in the (N, Z) plane of the ratio between the theoretical (n, γ) MACS at a temperature $T = 10^9$ K obtained with two different PSF models, namely the D1M+QRPA [140] and the RMF plus QRPA [158] (see Sect. 12). The color code gives the logarithmic value of the ratio

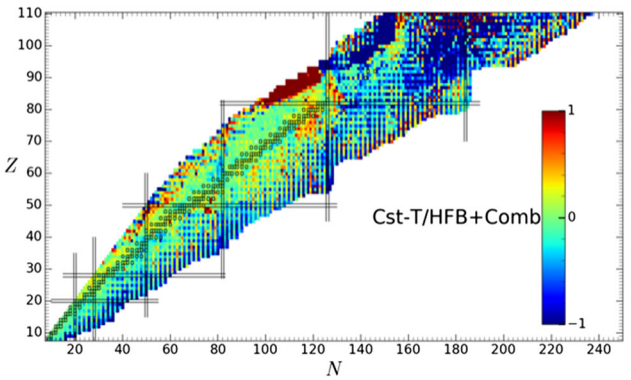

Fig. 39 Representation in the (N, Z) plane of the ratio between the theoretical (n, γ) MACS at a temperature $T = 10^9$ K obtained with two different level density models, namely the constant-temperature [122] and the HFB+Combinatorial [106] models (see Sect. 11). The color code gives the logarithmic value of the ratio

Different nuclear inputs may lead to relatively different predictions when dealing with exotic neutron-rich or neutron-deficient nuclei. This is illustrated on the (n, γ) MACS in Figs. 38–39 obtained with different PSFs, namely the D1M+QRPA+0lim [140] and the RMF plus QRPA [158] (see Sect. 12) or different level density models, namely the constant-temperature [122] and the HFB+Combinatorial [106] models (see Sect. 11). Global variations are found, in particular when varying the PSF, but also local variations, and more specifically odd-even or shell effects are observed, in particular when changing the level densities.

16.6 Radionuclide production

A popular application of TALYS is to predict the production of radioisotopes for medical applications. Up to now, approximately 600 papers have been published in which TALYS was used to estimate cross section excitation functions, often in combination with new cross section measurements. The resulting excitation functions can then be combined with the characteristics of a dedicated irradiation source, often a reactor or a cyclotron, to estimate the final radioactive yield as a function of the irradiation time. The majority of those cases concern proton-induced reactions, although there are also a significant number of TALYS analyses with photon-, deuteron- and alpha-induced reactions.

The predictive power of TALYS for excitation functions is determined by the quality of the optical model, the pre-equilibrium model and its parameters, level densities and the accuracy of the multiple emission Hauser-Feshbach model. The combination of these models generally give a reasonable to a good description of measured residual production cross sections from 10 to 200 MeV.

Figure 40 illustrates the excitation function of ^{123}Te(p, n). It shows the difference between a global TALYS calculation, with all nuclear model parameters at their default values, and a calculation with adjusted values for the most sensitive parameters in the 5–20 MeV energy range for (p, n) reactions, which are often used as a production route for medical isotopes. The TASMAN code [11] has been used to (a) determine the most important TALYS parameters from sensitivity profiles and (b) to optimize these parameters in a multi-dimensional parameter search. For the optimal result, the following parameters take on values within 10% of their default values:

- radius of real volume potential r_V for protons, see Eq. (71),
- radius of imaginary surface potential r_D for protons, see Eq. (71),
- radius of real volume potential r_V for neutrons, see Eq. (71),
- single-particle state density parameter for the compound nucleus, see Eq. (167),
- single-particle state density parameter for the residual (p, n) nucleus, see Eq. (167),
- total level density parameter for the residual (p, n) nucleus, see Eq. (230).

which amounts to 3 OMP parameters, 2 pre-equilibrium parameters and 1 compound nucleus parameter. It turns out that these 6 parameters can be used to get a good (p, n) fit for all nuclides for which experimental data exist. It is also important to filter the experimental data set for obvious outliers: in the current case the data from Barrall et al. [213] has been excluded from the optimization, while those of Mahunka et al. [214] and Scholten et al. [215] have been included. It is interesting to see that both the global and fitted TALYS calculations, as well as the JENDL−5.0 evaluation [216] follow the Mahunka et al. data in the rising part of the excitation function, regardless of the inclusion of the Scholten et al. data in the optimization of the fitted TALYS results. Apparently, the nuclear model does not allow a shift to the higher energies, regardless of its parameters. The IAEA evaluation [217] generally comes from least-squares fitting by means of a Pade approximation.

Similar sets of about 2 to 7 sensitive parameters can be identified to automatically optimize other excitation functions such as (n, γ), the combination of the three correlated channels (n, n'), $(n, 2n)$ and (n, p), (n, α), (n, f), (α, n) etc. for all nuclides for which experimental data exist. Of course, one should always remember that there are model limitations which currently make it impossible to reproduce the required shape of the experimental excitation functions (assuming these represent reality), even if we allow the parameter values to move away quite far from the default values.

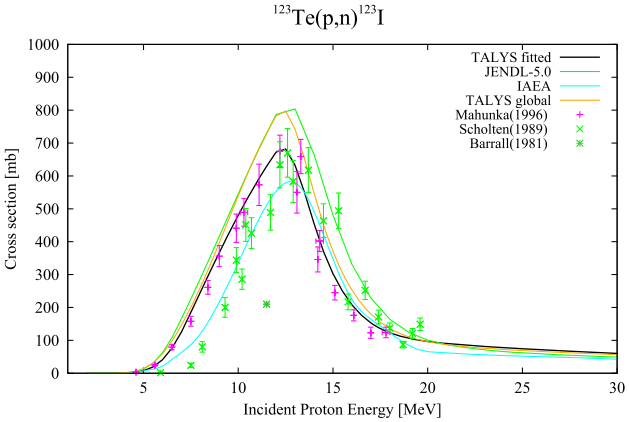

Fig. 40 Excitation function of ^{123}Te(p, n), calculated with global and adjusted TALYS parameters compared with existing nuclear data evaluations, such as JENDL−5.0 [216] or IAEA [217], and experimental data [213–215]

Trends in nuclear model parameters are also being investigated at higher energies. Fox et al. [90] measured residual production cross sections for protons incident on spherical nuclides and performed an analysis of the various nuclear model parameters that play an important role in the 30–100 MeV range.

For radioisotope production with charged particles, TALYS contains a built-in module to estimate the radioactive yields on the basis of accelerator characteristics such as power, energy, irradiation time, and basic production and depletion equations for activation. For this, the radioactive decay paths to the produced isotopes need to be known. Therefore, the JEFF−3.1.1 Radioactive Decay Data File [194,218] is included in the nuclear structure database. We give in Fig. 41 an example of the production of ^{99m}Tc via proton irradiation of ^{100}Mo, which is one of the production routes considered as an alternative for production with a reactor. First, Fig. 41 gives a comparison between an optimized TALYS calculation, experimental data and a few evaluated data libraries. The fit is obtained by optimizing the same 6 parameters as mentioned before, with an additional reduction of the spin cutoff parameter of the residual level density, to obtain a good agreement with the isomeric ratio. The excitation function can then be inserted into the module for radioisotope production and the result for a typical cyclotron set-up is given in Fig. 42. Extending this capability to photon and neutron irradiations (with e.g. a reactor) is under construction.

16.7 High-energy models

In the nuclear data community, energies beyond 50 MeV are often called “intermediate” or even “high”. As the models built in TALYS should cover incident energies up to (at least) 200 MeV a few examples for this energy range are given below.

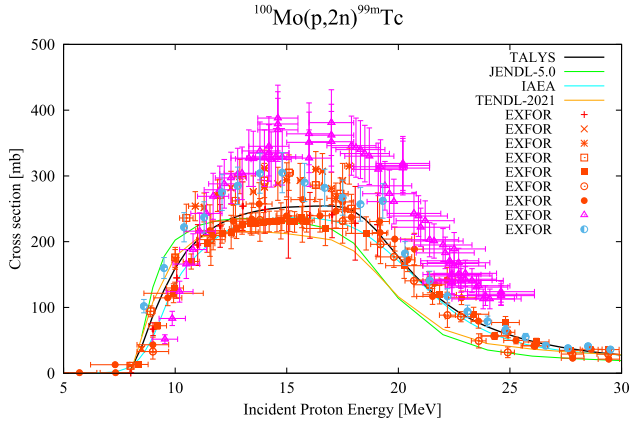

Fig. 41 Comparison of the ^{100}Mo(p,2n)^{99m}Tc excitation function obtained with an optimized TALYS calculation with existing nuclear data evaluations [11,193,216,217] and experimental data taken from EXFOR library [80]

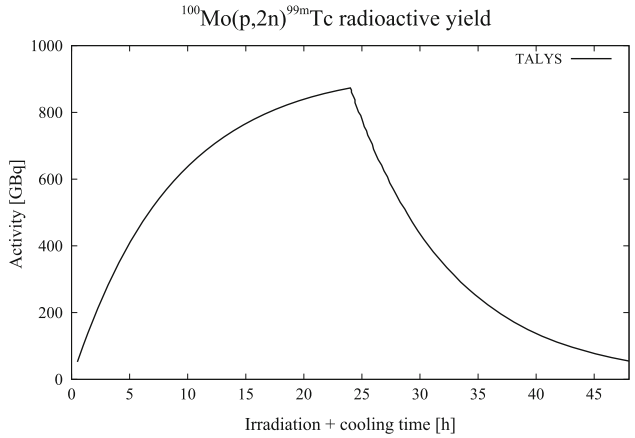

Fig. 42 Total activity of ^{99m}Tc produced by a 24 MeV proton accelerator of 150 μA and a ^{100}Mo target with an energy of 10 MeV at the back of the target, for an irradiation time of 24 h and a cooling time of 24 h

First, we argued in Sect. 8 that the multiple pre-equilibrium process is indispensable for incident energies above 50 MeV or so. The situation is similar to that presented in Fig. 12 for the primary pre-equilibrium process: the highly excited nucleus contains so much energy that more than one fast particle can be emitted from the non-equilibrated nucleus. If this process would not exist, particle evaporation would take place much deeper in the isotopic chain of every residual nucleus, since the evaporating system would only lose energy through sequential compound emission. Figure 43 shows a TALYS prediction for high-energy protons on ^{209}Bi with the default calculation compared with one where multiple pre-equilibrium emission is deactivated. The excitation function without multiple pre-equilibrium decreases much faster since more reaction flux can go to the lighter Bi isotopes. In general, one observes that omitting multiple pre-equilibrium leads to significant deviations from experiment.

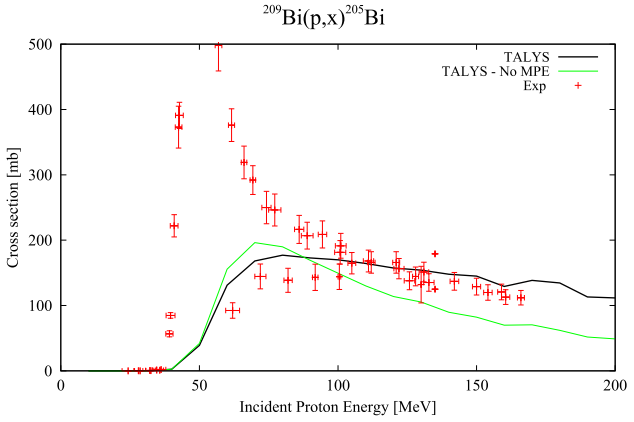

Fig. 43 Excitation function for ^{209}Bi(p,x)^{205}Bi compared with experimental data from the EXFOR database [80]. Two calculations are shown: one default TALYS calculation, and one with the multiple pre-equilibrium process turned off (No MPE)

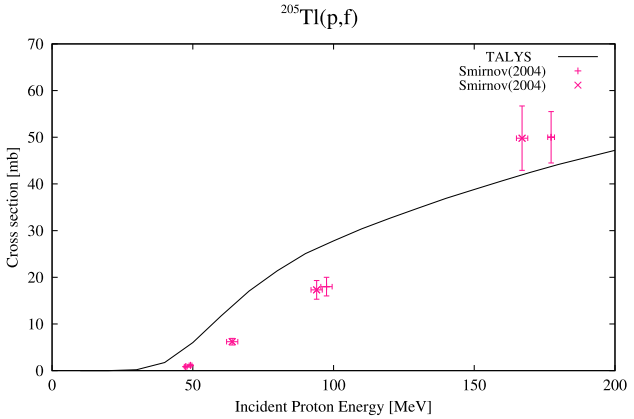

Fig. 44 Subactinide fission: ^{205}Tl(p, f) TALYS calculation compared with experimental data [219]

The last example is high-energy fission. This may fall into two categories: (1) actinide fission, where the "normal" fissioning process of actinides is simply extended to higher energies, with multi-chance fission now coming from several residual nuclides, (2) subactinide fission, observed in the W-Bi range, where the fission contribution comes from multi-chance fission of unstable residual nuclides far away from the target nucleus. Figure 44 gives the example of ^{205}Tl(p, f). For subactinides, these calculations are based on the RFRM fission barriers [179], as described in Sect. 13.

17 TALYS in a larger system

This paper concerns the nuclear physics implemented in TALYS and a description of the observables it can simulate. A paper of similar size could be devoted to the impact of the code on many important nuclear fundamental or technological applications. Instead of adding all that to the current

paper, we merely mention some of the most important examples. Also the current paper does not go into detail on the computational structure of the code.

An important aspect of TALYS is consistent and user-friendly input and output. Versatile interfacing of data is essential for basically all use of TALYS, from making the simplest plot to full-scale automation in larger software systems.

There are two important satellite programs for TALYS that have appeared many times in the literature already:

- TASMAN [11], statistical software for TALYS. The most used function of TASMAN is the generation of probability distributions for all the outputs of TALYS such as cross sections, spectra, angular distributions etc. and their related first moments such as averages, variances and covariances. It does this on the basis of Bayesian Monte Carlo sampling of the TALYS input parameters while looping over TALYS. Generally, after a few hundred TALYS runs all converged statistical information is available. TASMAN can also create parameter sensitivity profiles for all cross sections, spectra etc. and it can automatically fit TALYS results to experimental data through deterministic or stochastic search methods on the model parameters.
- TEFAL [11], for translating the results of TALYS into ENDF-6 data libraries. TEFAL was constructed to avoid any error-prone human interference in the creation of nuclear data files: the whole ENDF-6 file is created at once, on the basis of all nuclear reaction information that we feed it with. Hence, the idea is to first run TALYS for a projectile-target combination and a range of incident energies, and then to obtain a ready to use nuclear data library from the TEFAL code through processing of the TALYS results, if needed by merging it with experimental data or data from existing data libraries. For all this, a significant part of the ENDF-6 formats manual [10] was implemented in TEFAL.

The combination of TALYS, TASMAN and TEFAL lies at the basis of two important applied developments of the past 15 years: Total Monte Carlo uncertainty propagation [220] and the TALYS Evaluation Nuclear Data Library, known as TENDL [11].

18 Outlook

We note that various extensions are possible for the physics included in TALYS, and some will be mentioned below. Obviously, we cannot guarantee that these will be included in a future release. This will depend on the required effort, future careers of the authors, the user's willingness to share code updates with us, our willingness to implement them, and in the case of significant extensions, financial input from research programs that require nuclear data.

By now the reader should have an overview of the nuclear reaction simulations provided by TALYS. It is always wise to limit expectations, and warn the user that there are several important quantities in nuclear physics and nuclear data which TALYS cannot handle. If TALYS cannot do it, then either we have developed other software to take care of it, or it falls outside the scope of the physics included in TALYS, and software by other groups should be considered. Some of TALYS restrictions are listed below.

- The heaviest projectile or emitted particle considered is an α-particle. Hence, TALYS is not (yet) an heavy-ion collision code. Many of the essential mechanisms like pre-equilibrium and compound nucleus decay are however in place. A proper OMP for heavy-ion reactions needs to be implemented to describe the fusion cross section, at least, while direct reaction effects for heavy ions would probably be beyond the scope of what TALYS is supposed to cover.
- The so-called Engelbrecht-Weidenmüller transformation has not been implemented yet. It allows us to treat more in-depth the interplay between elastic and inelastic channels via interfering compound and direct reactions, see Refs. [61,62] for recent progress. An implementation for TALYS is underway.
- Primary γ-rays from the compound nucleus directly to discrete states or the ground state could be taken from a combination of experimental and evaluated data from the Evaluated Gamma-ray Activation File (EGAF) database [221] and simulations, such as currently done by the code Dicebox [222].
- Quantum-mechanical pre-equilibrium models could be implemented. Concerning continuum reactions, there exists microscopic multi-step direct software for quantum-mechanical pre-equilibrium calculations (Multi-step direct/Multi-step compound) [223], which still needs to be merged with TALYS.
- Individual resonance reactions are not modeled. This is the domain of R-matrix theory (or its more or less approximate versions) that can be handled by codes like SAMMY [224] or CONRAD [225]. TALYS does however reconstruct cross sections from resonance parameters as provided by the TARES code [73].
- Light-nuclide physics, as implemented in R-matrix codes is missing. TALYS is in essence a statistical model code, and that statistics starts to break down for systems with less than typically 20 nucleons.
- An explicit microscopic treatment of stripping and pick-up mechanisms for e.g. (d, p) reactions is not included.

There are a few codes, like FRESCO [226] and DEURACS [227], which handle that.
- Optical potential model to handle the fission-absorption competition far below the barrier could be implemented [228].

In general, the nuclear structure database can still be extended with more tables based on microscopic nuclear structure calculations that have proven their capacity to reproduce associated observables accurately. Through a trivial change in the TALYS code, the impact of these ingredients on reaction calculations can immediately be tested.

TALYS is already being used with microscopic OMPs, but only with the spherical JLMB method. An extension to deformed JLMB has been made available, but is not yet implemented. A few direct reaction items, such as the prediction of the isobaric analogue state, are also yet to be completed.

A general analysis of all actinides simultaneously should result in a stable, ready-to-use fission database. It is clear that the theoretical fission models themselves are also not yet mature, even though microscopic fission paths are now included.

Coupling TALYS with high-energy intranuclear cascade (INC) codes is possible, now that TALYS is able to take a pre-defined excitation population distribution as the starting point. The INC code would take care of energies above e.g. 200 MeV, while TALYS takes over below that cutoff energy. The well-validated pre-equilibrium and Hauser-Feshbach approach at lower energies may then lead to more precise simulated data (including isomer production), even for reactions in the GeV region.

As for computational possibilities, the current day computer power enables to use nuclear model codes in ways that were previously thought impossible. Activities that have already proven to be possible are the generation of nuclear-model based covariances with Monte Carlo methods, automatic multi-parameter fitting of all partial cross sections to the existing experimental data, and dripline-to-dripline generation of all cross sections over the entire energy and projectile range, see e.g. the TENDL link on the TALYS website (https://www.talys.eu). The applications range from fundamental science (e.g. astrophysics) to the production of nuclear data libraries for existing and future nuclear technologies.

The development of TALYS has initially followed the "first completeness, then quality" principle. This merely means that, in our quest for completeness, we tried to divide our effort equally among all nuclear reaction types. We think that, with the exception of a few issues the code is indeed *complete* in terms of predicted quantities. We now hope that TALYS also qualifies for "completeness and quality". Nevertheless, it is certain that future theoretical improvements as suggested above are needed to bring our computed results even closer to reality.

Acknowledgements It is impossible to list all the people who have in one way or another contributed to the current status of TALYS, so we will refrain from that. We wish to dedicate this paper to the memory of our friend and colleague Eric Bauge. SG is F.R.S.-FRNS research associate. This work has been supported by the Fonds de la Recherche Scientifique (FNRS, Belgium) and the Research Foundation Flanders (FWO, Belgium) under the EOS Project nr O022818F and O000422.

Data Availability Statements This manuscript has no associated data or the data will not be deposited. [Authors' comment: There is no additional data for this paper. All figures are in the manuscript.]

References

1. P.G. Young, E.D. Arthur, M.B. Chadwick, The GNASH nuclear model code. Workshop on Computation and Analysis of Nuclear Data Relevant to Nuclear Energy and Safety, edited by M.K. Mehta and J.J. Schmidt, Feb. 10 - March 13 1992, Trieste, Italy, 622 (1993)
2. M. Blann, Recent progress and current status of pre-equilibrium reaction theories and computer code ALICE. Workshop on Computation and Analysis of Nuclear Data Relevant to Nuclear Energy and Safety, edited by M.K. Mehta and J.J. Schmidt, Feb. 10 - March 13 1992, Trieste, Italy, 622 (1993)
3. M. Uhl, B. Strohmaier, Computer code for particle induced activation cross sections and related quantities. IRK Vienna report **76/01** (1976)
4. M. Herman, R. Capote, B.V. Carlson, P. Oblozinsky, M. Sin, A. Trkov, H. Wienke, V. Zerkin, EMPIRE: Nuclear reaction model code system for data evaluation. Nucl. Data Sheets **108**, 2655 (2007)
5. J. Raynal, Notes on ECIS94. CEA Saclay Report **CEA-N-2772** (1994)
6. T. Kawano, CoH3: The coupled-channels and Hauser-Feshbach code. Proceedings of the 6th International Workshop on Compound-Nuclear Reactions and Related Topics CNR*18 (2021)
7. O. Iwamoto, N. Iwamoto, S. Kunieda, F. Minato, K. Shibata, The CCONE code system and its application to nuclear data evaluation for fission and other reactions. Nuclear Data Sheets **131**, 259–288 (2016). https://doi.org/10.1016/j.nds.2015.12.004. Special Issue on Nuclear Reaction Data
8. W.E. Ormand, K. Kravvaris, YAHFC: A code framework to model nuclear reactions and estimate correlated uncertainties. LLNL-TR-821653, Lawrence Livermore Nationa Laboratory (2021)
9. R. Capote, M. Herman, P. Oblozinsky, P.G. Young, S. Goriely, T. Belgya, A.V. Ignatyuk, A.J. Koning, S. Hilaire, V.A. Plujko, M. Avrigeanu, O. Bersillon, M.B. Chadwick, T. Fukahori, Z. Ge, Y. Han, S. Kailas, J. Kopecky, V.M. Maslov, G. Reffo, M. Sin, E.S. Soukhovitskii, P. Talou, RIPL - Reference Input Parameter Library for calculation of nuclear reactions and nuclear data evaluations. Nucl. Data Sheets **110**, 3107 (2009)
10. A. Trkov, M. Herman, D.A. Brown, ENDF-6 Formats Manual, Data Formats and Procedures for the Evaluated Nuclear Data Files ENDF/B-VI, ENDF/B-VII and ENDF/B-VIII. CSEWG Document ENDF-102, Report BNL-203218-2018-INRE, SVN Commit: revision 215 (2012)
11. A.J. Koning, D. Rochman, J.-C. Sublet, N. Dzysiuk, M. Fleming, S. van der Marck, TENDL: Complete nuclear data library for

innovative nuclear science and technology. Nucl. Data Sheets **155**, 1 (2019)
12. A.M. Baldin, *Kinematics of Nuclear Reactions* (Oxford University Press, Oxford, 1961)
13. M.B. Chadwick, P.G. Young, S. Chiba, S.C. Frankle, G.M. Hale, H.G. Hughes, A.J. Koning, R.C. Little, R.E. MacFarlane, R.E. Prael, L.S. Waters, Cross-Section Evaluations to 150 MeV for Accelerator-Driven Systems and Implementation in MCNPX. Nucl. Sci. Eng. **131**(3), 293–328 (1999). https://doi.org/10.13182/NSE98-48
14. M.B. Chadwick, P.G. Young, R.E. Macfarlane, A.J. Koning, High energy nuclear data libraries for accelerator-driven technologies: Calculational method for heavy recoils. Second International Conference on Accelerator-Driven Transmutation Technologies and Applications, Kalmar, Sweden, June 3-7 1996, 483 (1996)
15. A.J. Koning, J.P. Delaroche, Local and global nucleon optical models from 1 keV to 200 MeV. Nucl. Phys. A **713**(3), 231–310 (2003). https://doi.org/10.1016/S0375-9474(02)01321-0
16. C. Mahaux, H. Ngo, G.R. Satchler, Causality and the threshold anomaly of the nucleus-nucleus potential. Nucl. Phys. A **449**(2), 354–394 (1986). https://doi.org/10.1016/0375-9474(86)90009-6
17. C. Mahaux, R., S., Single-particle motion in nuclei. Adv. Nucl. Phys. **20**, 1–223 (1991)
18. C. Mahaux, R. Sartor, Dispersion relation approach to the mean field and spectral functions of nucleons in 40Ca. Nucl. Phys. A **528**(2), 253–297 (1991). https://doi.org/10.1016/0375-9474(91)90090-S
19. B. Morillon, P. Romain, Dispersive and global spherical optical model with a local energy approximation for the scattering of neutrons by nuclei from 1 keV to 200 MeV. Phys. Rev. C **70**, 014601 (2004). https://doi.org/10.1103/PhysRevC.70.014601
20. B. Morillon, P. Romain, Bound single-particle states and scattering of nucleons on spherical nuclei with a global optical model. Phys. Rev. C **76**, 044601 (2007). https://doi.org/10.1103/PhysRevC.76.044601
21. J.P. Jeukenne, A. Lejeune, C. Mahaux, Many-body theory of nuclear matter. Phys. Rep. **25**(2), 83–174 (1976). https://doi.org/10.1016/0370-1573(76)90017-X
22. J.-P. Jeukenne, A. Lejeune, C. Mahaux, Optical-model potential in nuclear matter from Reid's hard core interaction. Phys. Rev. C **10**, 1391–1401 (1974). https://doi.org/10.1103/PhysRevC.10.1391
23. J.-P. Jeukenne, A. Lejeune, C. Mahaux, Microscopic calculation of the symmetry and Coulomb components of the complex optical-model potential. Phys. Rev. C **15**, 10–29 (1977). https://doi.org/10.1103/PhysRevC.15.10
24. J.-P. Jeukenne, A. Lejeune, C. Mahaux, Optical-model potential in finite nuclei from Reid's hard core interaction. Phys. Rev. C **16**, 80–96 (1977). https://doi.org/10.1103/PhysRevC.16.80
25. E. Bauge, J.P. Delaroche, M. Girod, Semimicroscopic nucleon-nucleus spherical optical model for nuclei with $A >= 40$ at energies up to 200 MeV. Phys. Rev. C **58**, 1118 (1998)
26. E. Bauge, J.P. Delaroche, M. Girod, Lane-consistent, semimicroscopic nucleon-nucleus optical model. Phys. Rev. C **63**, 024607 (2001). https://doi.org/10.1103/PhysRevC.63.024607
27. S. Goriely, J.-P. Delaroche, The isovector imaginary neutron potential: a key ingredient for the r-process nucleosynthesis. Phys. Lett. B **653**, 178 (2007)
28. F. Maréchal, T. Suomijärvi, Y. Blumenfeld, A. Azhari, E. Bauge, D. Bazin, J.A. Brown, P.D. Cottle, J.P. Delaroche, M. Fauerbach, M. Girod, T. Glasmacher, S.E. Hirzebruch, J.K. Jewell, J.H. Kelley, K.W. Kemper, P.F. Mantica, D.J. Morrissey, L.A. Riley, J.A. Scarpaci, H. Scheit, M. Steiner, Proton scattering by short lived sulfur isotopes. Phys. Rev. C **60**, 034615 (1999). https://doi.org/10.1103/PhysRevC.60.034615
29. H. Scheit, F. Maréchal, T. Glasmacher, E. Bauge, Y. Blumenfeld, J.P. Delaroche, M. Girod, R.W. Ibbotson, K.W. Kemper, J. Libert, B. Pritychenko, T. Suomijärvi, Proton scattering by the unstable neutron-rich isotopes ^{42,44}Ar. Phys. Rev. C **63**, 014604 (2000). https://doi.org/10.1103/PhysRevC.63.014604
30. E. Khan, T. Suomijärvi, Y. Blumenfeld, N.V. Giai, N. Alamanos, F. Auger, E. Bauge, D. Beaumel, J.P. Delaroche, P. Delbourgo-Salvador, A. Drouart, S. Fortier, N. Frascaria, A. Gilibert, M. Girod, C. Jouanne, K.W. Kemper, A. Lagoyannis, V. Lapoux, A. Lépine-Szily, I. Lhenry, J. Libert, F. Maréchal, J.M. Maison, A. Mussumara, S. Ottini-Hustache, P. Piattelli, S. Pita, E.C. Pollaco, P. Roussel-Chomaz, D. Santonocito, J.E. Sauvestre, J.A. Scarpacci, T. Zerguerras, Proton scattering from the unstable nuclei 30S and 34Ar: structural evolution along the sulfur and argon isotopic chains. Nucl. Phys **A694**, 103 (2001)
31. E. Bauge, J.P. Delaroche, M. Girod, G. Haouat, J. Lachkar, Y. Patin, J. Sigaud, J. Chardine, Neutron scattering from the ^{155,156,157,158,160}Gd isotopes: Measurements and analyses with a deformed, semimicroscopic optical model. Phys. Rev. C **61**, 034306 (2000). https://doi.org/10.1103/PhysRevC.61.034306
32. A.J. Koning, D. Rochman, S.C. van der Marck, Extension of TALYS to 1 GeV. Nucl. Data Sheets **118**, 187–190 (2014). https://doi.org/10.1016/j.nds.2014.04.033
33. S. Typel, O. Riedl, H.H. Wolter, Elastic proton-nucleus scattering and the optical potential in a relativistic mean field model. Nucl. Phys. A **709**(1), 299–318 (2002). https://doi.org/10.1016/S0375-9474(02)01031-X
34. S. Chiba, K. Niita, T. Fukahori, T. Maruyama, T. Maruyama, A. Iwamoto, The isovector/isoscalar ratio of the imaginary part of the intermediate-energy nucleon optical model potential studied by the quantum molecular dynamics. Spec. Meet. on the nucleon nucleus optical model up to 200 MeV, Bruyeres-le-Chatel (1996)
35. R. Capote, S. Chiba, E.S. Soukhovitskii, J.M. Quesada, E. Bauge, A global dispersive coupled-channel optical model potential for actinides. J. Nucl. Sci. Tech. **45**, 333–340 (2009)
36. S. Watanabe, High energy scattering of deuterons by complex nuclei. Nucl. Phys. **8**, 484–492 (1958). https://doi.org/10.1016/0029-5582(58)90180-9
37. D.G. Madland, Recent results in the development of a global medium-energy nucleon-nucleus optical model potential. Proceedings of a Specialists' Meeting on preequilibrium nuclear reactions, Semmering, Austria, February 10-12 1988, 103
38. W.W. Daehnick, J.D. Childs, Z. Vrcelj, Global optical model potential for elastic deuteron scattering from 12 to 90 MeV. Phys. Rev. C **21**, 2253–2274 (1980). https://doi.org/10.1103/PhysRevC.21.2253
39. J. Bojowald, H. Machner, H. Nann, W. Oelert, M. Rogge, P. Turek, Elastic deuteron scattering and optical model parameters at energies up to 100 MeV. Phys. Rev. C **38**, 1153–1163 (1988). https://doi.org/10.1103/PhysRevC.38.1153
40. Y. Han, Y. Shi, Q. Shen, Deuteron global optical model potential for energies up to 200 MeV. Phys. Rev. C **74**, 044615 (2006). https://doi.org/10.1103/PhysRevC.74.044615
41. H. An, C. Cai, Global deuteron optical model potential for the energy range up to 183 MeV. Phys. Rev. C **73**, 054605 (2006). https://doi.org/10.1103/PhysRevC.73.054605
42. L. McFadden, G.R. Satchler, Optical-model analysis of the scattering of 24.7 MeV alpha particles. Nucl. Phys. **84**(1), 177–200 (1966). https://doi.org/10.1016/0029-5582(66)90441-X
43. M. Nolte, H. Machner, J. Bojowald, Global optical potential for α particles with energies above 80 MeV. Phys. Rev. C **36**, 1312–1316 (1987). https://doi.org/10.1103/PhysRevC.36.1312
44. V. Avrigeanu, P.E. Hodgson, M. Avrigeanu, Global optical potentials for emitted alpha particles. Phys. Rev. C **49**, 2136–2141 (1994). https://doi.org/10.1103/PhysRevC.49.2136

45. P. Demetriou, C. Grama, S. Goriely, Improved global alpha-optical model potentials at low energies. Nucl. Phys. A **707**(1), 253–276 (2002). https://doi.org/10.1016/S0375-9474(02)00756-X
46. V. Avrigeanu, M. Avrigeanu, C. Mihaelescu, Further explorations of the α-particle optical model potential at low energies for the mass range A$\approx$ 45–209. Phys. Rev. C **90**, 044612 (2014). https://doi.org/10.1103/PhysRevC.90.044612
47. G.R. Satchler, *Direct nuclear reactions* (Clarendon Press, Oxford, 1983)
48. T. Tamura, Analyses of the scattering of nuclear particles by collective nuclei in terms of the coupled-channel calculation. Rev. Mod. Phys. **37**, 679–708 (1965). https://doi.org/10.1103/RevModPhys.37.679
49. J.P. Delaroche, Use of coupled-channel optical model calculations in nuclear data evaluations for incident energies up to 1 GeV. Proceedings of the International Symposium on *Nuclear Data Evaluation Methodology*, C.L. Dunford (Ed.), October 12-16 1992, Brookhaven, USA, 347 (1992)
50. N. Olsson, E. Ramström, B. Trostell, Neutron elastic and inelastic scattering from Mg, Si, S, Ca, Cr, Fe and Ni at En = 21.6 MeV. Nucl. Phys. A **513**, 205–238 (1990). https://doi.org/10.1016/0375-9474(90)90096-5
51. B.V. Carlsson, Optical model calculations with the code ECIS95. Workshop on Nuclear Reaction Data and Nuclear Reactors: Physics, Design and Safety, edited by N. Paver, M. Herman and A. Gandini, March 13 - April 14 2000, Trieste Italy, 61 (2001)
52. E.S. Soukhovitskii, R. Capote, J.M. Quesada, S. Chiba, D.S. Martyanov, Nucleon scattering on actinides using a dispersive optical model with extended couplings. Phys. Rev. C **94**, 064605 (2016). https://doi.org/10.1103/PhysRevC.94.064605
53. P.P. Guss, R.C. Byrd, C.R. Howell, R.S. Pedroni, G. Tungate, R.L. Walter, J.P. Delaroche, Optical model description of the neutron interaction with ^{116}Sn and ^{120}Sn over a wide energy range. Phys. Rev. C **39**, 405–414 (1989). https://doi.org/10.1103/PhysRevC.39.405
54. M.J.L. Jimenez, B. Morillon, P. Romain, Triple-humped fission barrier model for a new 238U neutron cross-section evaluation and first validations. Ann. Nucl. Energy **32**(2), 195–213 (2005). https://doi.org/10.1016/j.anucene.2004.08.005
55. P. Romain, B. Morillon, H. Duarte, Bruyères-le-Châtel neutron evaluations of actinides with the TALYS code: The fission channel. Nuclear Data Sheets **131**, 222–258 (2016). https://doi.org/10.1016/j.nds.2015.12.003. Special Issue on Nuclear Reaction Data
56. P.E. Hodgson, *Nuclear reactions and nuclear structure* (Clarendon Press, Oxford, 1971)
57. A. van der Woude, Electric and magnetic giant resonances in nuclei, 99–232 (1991)
58. C. Kalbach, Surface and collective effects in preequilibrium reactions. Phys. Rev. C **62**, 044608 (2000). https://doi.org/10.1103/PhysRevC.62.044608
59. W. Hauser, H. Feshbach, The inelastic scattering of neutrons. Phys. Rev. **87**, 366–373 (1952). https://doi.org/10.1103/PhysRev.87.366
60. J.M. Blatt, L.C. Biedenharn, The angular distribution of scattering and reaction cross sections. Rev. Mod. Phys. **24**, 258–272 (1952). https://doi.org/10.1103/RevModPhys.24.258
61. T. Kawano, R. Capote, S. Hilaire, P. Chau Huu-Tai, Statistical Hauser-Feshbach theory with width-fluctuation correction including direct reaction channels for neutron-induced reactions at low energies. Phys. Rev. C **94**, 014612 (2016). https://doi.org/10.1103/PhysRevC.94.014612
62. T. Kawano, Unified description of the coupled-channels and statistical Hauser-Feshbach nuclear reaction theories for low energy neutron incident reactions. European Physical Journal A **57**, 1–16 (2021)
63. J.W. Tepel, H.M. Hofmann, H.A. Weidenmueller, Hauser-Feshbach formulas for medium and strong absorption. Phys. Lett. B **49**(1), 1–4 (1974). https://doi.org/10.1016/0370-2693(74)90565-6
64. H.M. Hofmann, J. Richert, J.W. Tepel, H.A. Weidenmueller, Direct reactions and Hauser-Feshbach theory. Ann. Phys. **90**(2), 403–437 (1975). https://doi.org/10.1016/0003-4916(75)90005-6
65. H.M. Hofmann, T. Mertelmeier, M. Herman, J.W. Tepel, Hauser-Feshbach calculations in the presence of weakly absorbing channels with special reference to the elastic enhancement factor and the factorization assumption. Zeit. Phys. A **297**, 153 (1980)
66. P.A. Moldauer, Evaluation of the fluctuation enhancement factor. Phys. Rev. C **14**, 764–766 (1976). https://doi.org/10.1103/PhysRevC.14.764
67. P.A. Moldauer, Statistics and the average cross section. Nucl. Phys. A **344**(2), 185–195 (1980). https://doi.org/10.1016/0375-9474(80)90671-5
68. J.J.M. Verbaarschot, H.A. Weidenmueller, M.R. Zirnbauer, Grassmann integration in stochastic quantum physics: The case of compound-nucleus scattering. Phys. Rep. **129**(6), 367–438 (1985). https://doi.org/10.1016/0370-1573(85)90070-5
69. S. Hilaire, C. Lagrange, A.J. Koning, Comparisons between various width fluctuation correction factors for compound nucleus reactions. Ann. Phys. **306**(2), 209–231 (2003). https://doi.org/10.1016/S0003-4916(03)00076-9
70. M. Ernebjerg, M. Herman, Assessment of approximate methods for width fluctuation corrections. AIP Conf. Proc. **769**, 1233–1236 (2005)
71. T. Kawano, P. Talou, Numerical simulations for low energy nuclear reactions to validate statistical models. Nucl. Data Sheets **118**, 183–186 (2014). https://doi.org/10.1016/j.nds.2014.04.032
72. H. Gruppelaar, G. Reffo, Some properties of the width fluctuation factor. Nucl. Sci. Eng. **62**(4), 756–763 (1977). https://doi.org/10.13182/NSE77-A15219
73. D. Rochman, J.-C.S.A.J. Koning, A statistical analysis of evaluated neutron resonances with TARES for JEFF-3.3, JENDL-4.0, ENDF/B-VIII.0 and TENDL-2019. Nucl. Data Sheets **163**, 163 (2020)
74. J. Kopecky, M.G. Delfini, H.A.J. van der Kamp, D. Nierop, Revisions and extensions of neutron capture cross-sections in the European Activation File EAF-3. ECN-C–92-051, July 1992 (1992)
75. S.F. Mughabghab, *Atlas of Neutron Resonances*, 6th edn. (Elsevier, The Netherlands, 2018)
76. S.I. Sukhoruchkin, Z.N. Soroko, *Neutron Resonance Parameters*, 5th edn. (Landolt-Bornstein, Germany, 2015)
77. D.E. Cullen, PREPRO 2021 - ENDF/B6 Pre-processing codes. Technical report IAEA-NDS-0238, IAEA (2021)
78. D. Rochman, S. Goriely, A.J. Koning, H. Ferroukhi, Radiative neutron capture: Hauser Feshbach vs. statistical resonances. Phys. Lett. B **764**, 109–113 (2017). https://doi.org/10.1016/j.physletb.2016.11.018
79. C. Kalbach, Systematics of continuum angular distributions: Extensions to higher energies. Phys. Rev. C **37**, 2350–2370 (1988). https://doi.org/10.1103/PhysRevC.37.2350
80. N. Otuka, E. Dupont, V. Semkova, B. Pritychenko, A.I. Blokhin, M. Aikawa, S. Babykina, M. Bossant, G. Chen, S. Dunaeva et al., Towards a more complete and accurate experimental nuclear reaction data library (EXFOR): International collaboration between nuclear reaction data centres (NRDC). Nucl. Data Sheets **120**, 272–276 (2014)
81. A.J. Koning, M.C. Duijvestijn, A global pre-equilibrium analysis from 7 to 200 MeV based on the optical model potential. Nucl. Phys. A **744**, 15–76 (2004). https://doi.org/10.1016/j.nuclphysa.2004.08.013
82. H. Gruppelaar, P. Nagel, P.E. Hodgson, Pre-equilibrium processes in nuclear reaction theory. Riv. Nuovo Cimento **9**(7), 1 (1986)

83. E. Gadioli, P.E. Hodgson, Pre-equilibrium nuclear reactions (1992)
84. C. Kalbach, Two-component exciton model: Basic formalism away from shell closures. Phys. Rev. C **33**, 818–833 (1986). https://doi.org/10.1103/PhysRevC.33.818
85. C.K. Cline, M. Blann, The pre-equilibrium statistical model: Description of the nuclear equilibration process and parameterization of the model. Nucl. Phys. A **172**(2), 225–259 (1971). https://doi.org/10.1016/0375-9474(71)90713-5
86. J. Dobeš, E. Běták, Two-component exciton model. Zeit. Phys. **A310**, 329 (1983)
87. E. Běták, J. Dobeš, The finite depth of the nuclear potential well in the exciton model of preequilibrium decay. Zeit. Phys. A **279**, 319 (1976)
88. C.Y. Fu, Implementation of on advanced pairing correction for particle-hole state densities in precompound nuclear reaction theory. Nucl. Sci. Eng. **86**, 344 (1984)
89. C. Kalbach, Surface effects in the exciton model of preequilibrium nuclear reactions. Phys. Rev. C **32**, 1157–1168 (1985). https://doi.org/10.1103/PhysRevC.32.1157
90. M.B. Fox, A.S. Voyles, J.T. Morrell, L.A. Bernstein, A.M. Lewis, A.J. Koning, J.C. Batchelder, E.R. Birnbaum, C.S. Cutler, D.G. Medvedev, F.M. Nortier, E.M. O'Brien, C. Vermeulen, Investigating high-energy proton-induced reactions on spherical nuclei: Implications for the preequilibrium exciton model. Phys. Rev. C **103**, 034601 (2021). https://doi.org/10.1103/PhysRevC.103.034601
91. J.M. Akkermans, H. Gruppelaar, Analysis of continuum gamma-ray emission in precompound-decay reactions. Phys. Lett. B **157**(2), 95–100 (1985). https://doi.org/10.1016/0370-2693(85)91524-2
92. H. Gruppelaar, Level density in unified preequilibrium and equilibrium models. IAEA Advisory Group Meeting on Basic and Applied Problems on Nuclear Level Densities, (Brookhaven National Laboratory report, Report BNL-NCS-51694), **143** (1983)
93. M. Kerveno, M. Dupuis, A. Bacquias, F. Belloni, D. Bernard, C. Borcea, M. Boromiza, R. Capote, C. De Saint Jean, P. Dessagne, J.C. Drohé, G. Henning, S. Hilaire, T. Kawano, P. Leconte, N. Nankov, A. Negret, M. Nyman, A. Olacel, A.J.M. Plompen, P. Romain, C. Rouki, G. Rudolf, M. Stanoiu, R. Wynants, Measurement of ^{238}U$(n, n'\gamma)$ cross section data and their impact on reaction models. Phys. Rev. C **104**, 044605 (2021). https://doi.org/10.1103/PhysRevC.104.044605
94. C. Kalbach, Preequilibrium reactions with complex particle channels. Phys. Rev. C **71**, 034606 (2005). https://doi.org/10.1103/PhysRevC.71.034606
95. C. Kalbach, Phenomenological model for light-projectile breakup. Phys. Rev. C **95**, 014606 (2017). https://doi.org/10.1103/PhysRevC.95.014606
96. M. Avrigeanu, V. Avrigeanu, Additive empirical parametrization and microscopic study of deuteron breakup. Phys. Rev. C **95**, 024607 (2017). https://doi.org/10.1103/PhysRevC.95.024607
97. A.J. Koning, J.M. Akkermans, Randomness in multi-step direct reactions. Ann. Phys. **208**(1), 216–250 (1991). https://doi.org/10.1016/0003-4916(91)90345-9
98. G.R. Satchler, *Introduction to Nuclear Reactions* (Macmillan press ltd., USA, 1980)
99. A. Mengoni, T. Otsuka, M. Ishihara, Direct radiative capture of p-wave neutrons. Phys. Rev. C **52**, 2334 (1995)
100. P. Descouvemont, *Theoretical Models for Nuclear Astrophysics* (Nova Science Publishers, New York, USA, 2003)
101. P. Descouvemont, Cluster models in nuclear astrophysics. J. Phys. G: Nucl. Part. Phys. **35**, 014006 (2008)
102. Y. Xu, S. Goriely, Systematic study of direct neutron capture. Phys. Rev. C **86**, 045801 (2012). https://doi.org/10.1103/PhysRevC.86.045801
103. Y. Xu, S. Goriely, A.J. Koning, S. Hilaire, Systematic study of neutron capture including the compound, pre-equilibrium, and direct mechanisms. Phys. Rev. C **90**, 024604 (2014). https://doi.org/10.1103/PhysRevC.90.024604
104. S. Goriely, Direct neutron captures and the r-process nucleosynthesis. Astron. Astrophys. **325**, 414 (1997)
105. S. Goriely, Radiative neutron captures by neutron-rich nuclei and the r-process nucleosynthesis. Phys. Lett. B **436**, 10 (1998)
106. S. Goriely, S. Hilaire, A.J. Koning, Improved microscopic nuclear level densities within the Hartree-Fock-Bogoliubov plus combinatorial method. Phys. Rev. C **78**, 064307 (2008). https://doi.org/10.1103/PhysRevC.78.064307
107. K. Sieja, S. Goriely, Shell-model based study of the direct capture in neutron-rich nuclei. Eur. Phys. J. A **57**, 110 (2021)
108. M. Blann, M.B. Chadwick, New precompound decay model: Angular distributions. Phys. Rev. C **57**, 233–243 (1998)
109. M.B. Chadwick, P.G. Young, D.C. George, Y. Watanabe, Multiple preequilibrium emission in Feshbach-Kerman-Koonin analyses. Phys. Rev. C **50**, 996–1005 (1994). https://doi.org/10.1103/PhysRevC.50.996
110. A.J. Koning, M.B. Chadwick, Microscopic two-component multistep direct theory for continuum nuclear reactions. Phys. Rev. C **56**, 970–994 (1997). https://doi.org/10.1103/PhysRevC.56.970
111. M. Wang, W.J. Huang, F.G. Kondev, G. Audi, S. Naimi, The AME2020 atomic mass evaluation (II). Chin. Phys. C **45**, 030003 (2021)
112. D. Lunney, J.M. Pearson, C. Thibault, Recent trends in the determination of nuclear masses. Rev. Mod. Phys. **75**(3), 1021 (2003)
113. K. Blaum, S. Eliseev, S. Goriely, Masses of exotic nuclei. In: Toki, H. Tanihata, T. Kajino, (eds.) Handbook of Nuclear Physics, pp. 1–38. Springer, (2023)
114. S. Goriely, N. Chamel, J.M. Pearson, Further explorations of Skyrme-Hartree-Fock-Bogoliubov mass formulas. XIII. the 2012 atomic mass evaluation and the symmetry coefficient. Phys. Rev. C **88**, 024308 (2013)
115. S. Goriely, S. Hilaire, M. Girod, S. Péru, First Gogny Hartree-Fock-Bogoliubov nuclear mass model. Phys. Rev. Lett. **102**, 242501–242504 (2009)
116. P. Moller, A.J. Sierk, T. Ichikawa, H. Sagawa, Nuclear ground-state masses and deformations: FRDM(2012). Chin. Phys. **109**, 1–204 (2016)
117. J. Duflo, A.P. Zuker, Microscopic mass formulas. Phys. Rev. C **52**, 23–27 (1995). https://doi.org/10.1103/PhysRevC.52.R23
118. N. Wang, M. Liu, X. Wu, J. Meng, Surface diffuseness correction in global mass formula. Phys. Lett. B **734**, 215 (2014)
119. ENSDF: Evaluated Nuclear Structure Data File. Source: Nuclear Structure and Decay Data Evaluators Network. https://www.nndc.bnl.gov/ensdf/
120. F.G. Kondev, M. Wang, W.J. Huang, S. Naimi, G. Audi, The NUBASE2020 evaluation of nuclear physics properties. Chin. Phys. C **45**(3), 030001 (2021). https://doi.org/10.1088/1674-1137/abddae
121. S. Goriely, S. Hilaire, M. Girod, S. Péru, The Gogny-Hartree-Fock-Bogoliubov nuclear-mass model. European Physical Journal A **52**, 202 (2016)
122. A.J. Koning, S. Hilaire, S. Goriely, Global and local level density models. Nucl. Phys. A **810**(1), 13–76 (2008). https://doi.org/10.1016/j.nuclphysa.2008.06.005
123. A.V. Ignatyuk, G.N. Smirenkin, A.S. Tishin, Phenomenological description of energy dependence of the level density parameter. Sov. J. Nucl. Phys. **21**(3), 255 (1975)

124. A.V. Ignatyuk, K.K. Istekov, G.N. Smirenkin, The role of collective effects in the systematics of nuclear level densities. Sov. J. Nucl. Phys. **29**(4), 450 (1979)
125. T. Ericson, The statistical model and nuclear level densities. Adv. Phys. **9**, 425–511 (1960)
126. H. Baba, A shell-model nuclear level density. Nucl. Phys. A **159**(2), 625–641 (1970). https://doi.org/10.1016/0375-9474(70)90862-6
127. A. Mengoni, Y. Nakajima, Fermi-gas model parametrization of nuclear level density. J. Nucl. Sci. Techn. **31**, 151–162 (1994)
128. A. Gilbert, A.G.W. Cameron, A composite nuclear-level density formula with shell corrections. Can. J. Phys. **43**, 1446–1496 (1965)
129. W. Dilg, W. Schantl, H. Vonach, M. Uhl, Level density parameters for the Back-Shifted Fermi gas model in the mass range $40 < A < 250$. Nucl. Phys. A **217**(2), 269–298 (1973). https://doi.org/10.1016/0375-9474(73)90196-6
130. M.K. Grossjean, H. Feldmeier, Level density of a Fermi gas with pairing interactions. Nucl. Phys. A **444**(1), 113–132 (1985). https://doi.org/10.1016/0375-9474(85)90294-5
131. P. Demetriou, S. Goriely, Microscopic nuclear level densities for practical applications. Nucl. Phys. A **695**(1), 95–108 (2001). https://doi.org/10.1016/S0375-9474(01)01095-8
132. O.T. Grudzevich, A.V. Ignatyuk, V.I. Plyaskin, A.V. Zelenetsky, Consistent systematics of level density for medium and heavy nuclei. Proc. Nuclear Data for Science and Technology (Mito, JAERI), **187** (1988)
133. S. Hilaire, S. Goriely, Global microscopic nuclear level densities within the HFB plus combinatorial method for practical applications. Nucl. Phys. A **779**, 63–81 (2006). https://doi.org/10.1016/j.nuclphysa.2006.08.014
134. A.S. Iljinov, M.V. Mebel, N. Bianchi, E. De Sanctis, C. Guaraldo, V. Lucherini, V. Muccifora, E. Polli, A.R. Reolon, P. Rossi, Phenomenological statistical analysis of level densities, decay widths and lifetimes of excited nuclei. Nucl. Phys. A **543**(3), 517–557 (1992). https://doi.org/10.1016/0375-9474(92)90278-R
135. A.R. Junghans, M. de Jong, H.-G. Clerc, A.V. Ignatyuk, G.A. Kudyaev, K.-H. Schmidt, Projectile-fragment yields as a probe for the collective enhancement in the nuclear level density. Nucl. Phys. A **629**(3), 635–655 (1998). https://doi.org/10.1016/S0375-9474(98)00658-7
136. G. Hansen, A.S. Jensen, Energy dependence of the rotational enhancement factor in the level density. Nucl. Phys. A **406**(2), 236–256 (1983). https://doi.org/10.1016/0375-9474(83)90459-1
137. S. Hilaire, M. Girod, S. Goriely, A.J. Koning, Temperature-dependent combinatorial level densities with the D1M Gogny force. Phys. Rev. C **86**, 064317 (2012). https://doi.org/10.1103/PhysRevC.86.064317
138. M.N. Harakeh, A. Van der Woude, Giant Resonances: Fundamental High-frequency Modes of Nuclear Excitation. Oxford studies in nuclear physics. Oxford Univ. Press, Oxford (2002). https://cds.cern.ch/record/579269
139. S. Goriely, P. Dimitriou, M. Wiedeking, T. Belgya, R. Firestone, J. Kopecky, M. Krticka, V. Plujko, R. Schwengner, S. Siem, H. Utsunomiya, S. Hilaire, S. Péru, Y.S. Cho, D.M. Filipescu, N. Iwamoto, T. Kawano, V. Varlamov, R. Xu, Reference database for photon strength functions. Eur. Phys. J. A **55**, 172 (2019)
140. S. Goriely, S. Hilaire, S. Péru, K. Sieja, Gogny-HFB+QRPA dipole strength function and its application to radiative nucleon capture cross section. Phys. Rev. C **98**, 014327 (2018). https://doi.org/10.1103/PhysRevC.98.014327
141. D.M. Brink, Individual particle and collective aspects of the nuclear photoeffect. Nucl. Phys. **4**, 215–220 (1957). https://doi.org/10.1016/0029-5582(87)90021-6
142. S.G. Kadmenskii, V.P. Markushev, V.I. Furmann, Dynamical enhancement of parity violation effects for compound states and giant 0- resonances. Sov. J. Nucl. Phys. **37**, 165 (1983)
143. M. Guttormsen, A.C. Larsen, A. Görgen, T. Renstrøm, S. Siem, T.G. Tornyi, G.M. Tveten, Validity of the generalized Brink-Axel hypothesis in 238Np. Phys. Rev. Lett. **116**, 012502 (2016)
144. ...D. Martin, P. von Neumann-Cosel, A. Tamii, N. Aoi, S. Bassauer, C.A. Bertulani, J. Carter, L. Donaldson, H. Fujita, Y. Fujita, T. Hashimoto, K. Hatanaka, T. Ito, A. Krugmann, B. Liu, Y. Maeda, K. Miki, R. Neveling, N. Pietralla, I. Poltoratska, V.Y. Ponomarev, A. Richter, T. Shima, T. Yamamoto, M. Zweidinger, Test of the Brink-Axel hypothesis for the Pygmy dipole resonance. Phys. Rev. Lett. **119**(18), (2017). https://doi.org/10.1103/PhysRevLett.119.182503
145. C.T. Angell, S.L. Hammond, H.J. Karwowski, J.H. Kelley, M. Krtička, E. Kwan, A. Makinaga, G. Rusev, Evidence for radiative coupling of the Pygmy dipole resonance to excited states. Phys. Rev. C **86**, 051302 (2012)
146. J. Isaak, D. Savran, M. Krtička, M.W. Ahmed, J. Beller, E. Fiori, J. Glorius, J.H. Kelley, B. Loher, N. Pietralla, C. Romig, G. Rusev, M. Scheck, L. Schnorrenberger, J. Silva, K. Sonnabend, A.P. Tonchev, W. Tornow, H.R. Weller, M. Zweidinger, Constraining nuclear photon strength functions by the decay properties of photo-excited states. Phys. Lett. B **727**, 361 (2013)
147. J. Isaak, D. Savran, B. Löher, T. Beck, M. Bhike, U. Gayer, Pietralla, N. Krishichayan, M. Scheck, W. Tornow, V. Werner, A. Zilges, M. Zweidinger, The concept of nuclear photon strength functions: A model-independent approach via $(\gamma, \gamma'\gamma'')$ reactions. Phys. Lett. B **788**, 225 (2019)
148. V.A. Plujko, O.M. Gorbachenko, R. Capote, P. Dimitriou, Giant dipole resonance parameters of ground-state photoabsorption: Experimental values with uncertainties. At. Data Nucl. Data Tables **123**, 1 (2018)
149. S. Goriely, V. Plujko, Simple empirical E1 and M1 strength functions for practical applications. Phys. Rev. C **99**, 014303 (2019)
150. T. Kawano, Y.S. Cho, P. Dimitriou, D. Filipescu, N. Iwamoto, V. Plujko, X. Tao, H. Utsunomiya, V. Varlamov, R. Xu, R. Capote, I. Gheorghe, O. Gorbachenko, Y.L. Jin, T. Renstrom, M. Sin, K. Stopani, Y. Tian, G.M. Tveten, J.M. Wang, T. Belgya, R. Firestone, S. Goriely, J. Kopecky, M. Krticka, R. Schwengner, S. Siem, M. Wiedeking, IAEA photonuclear data library 2019. Nucl. Data Sheets **163**, 109–162 (2020). https://doi.org/10.1016/j.nds.2019.12.002
151. IAEA: Photon Strength Function Database (2019). www-nds.iaea.org/PSFdatabase
152. P. Axel, Electric dipole ground-state transition width strength function and 7-MeV photon interactions. Phys. Rev. **126**, 671–683 (1962). https://doi.org/10.1103/PhysRev.126.671
153. J. Kopecky, M. Uhl, Test of gamma-ray strength functions in nuclear reaction model calculations. Phys. Rev. C **41**, 1941–1955 (1990). https://doi.org/10.1103/PhysRevC.41.1941
154. J. Kopecky, M. Uhl, R.E. Chrien, Radiative strength in the compound nucleus ^{157}Gd. Phys. Rev. C **47**, 312–322 (1993). https://doi.org/10.1103/PhysRevC.47.312
155. S. Goriely, Radiative neutron captures by neutron-rich nuclei and the r-process nucleosynthesis. Phys. Lett. B **436**(1), 10–18 (1998). https://doi.org/10.1016/S0370-2693(98)00907-1
156. S. Goriely, E. Khan, Large-scale QRPA calculation of E1-strength and its impact on the neutron capture cross section. Nucl. Phys. A **706**(1), 217–232 (2002). https://doi.org/10.1016/S0375-9474(02)00860-6
157. S. Goriely, E. Khan, M. Samyn, Microscopic HFB + QRPA predictions of dipole strength for astrophysics applications. Nucl. Phys. A **739**(3), 331–352 (2004). https://doi.org/10.1016/j.nuclphysa.2004.04.105

158. I. Daoutidis, S. Goriely, Large-scale continuum random-phase approximation predictions of dipole strength for astrophysical applications. Phys. Rev. C **86**, 034328 (2012). https://doi.org/10.1103/PhysRevC.86.034328
159. K. Sieja, Electric and magnetic dipole strength at low energy. Phys. Rev. Lett. **119**, 052502 (2017)
160. K. Sieja, Low energy dipole strength from large scale shell model calculations. EPJ Web of Conferences **146**, 05004 (2017)
161. R. Schwengner, S. Frauendorf, B.A. Brown, Low-energy magnetic dipole radiation in open-shell nuclei. Phys. Rev. Lett. **118**, 092502 (2017)
162. A. Voinov, E. Algin, U. Agvaanluvsan, T. Belgya, R. Chankova, M. Guttormsen, G.E. Mitchell, J. Rekstad, A. Schiller, S. Siem, Large enhancement of radiative strength for soft transitions in the quasicontinuum. Phys. Rev. Lett. **93**, 142504 (2004)
163. M. Guttormsen, R. Chankova, U. Agvaanluvsan, E. Algin, L.A. Bernstein, F. Ingebretsen, T. Lönnroth, S. Messelt, G.E. Mitchell, J. Rekstad, A. Schiller, S. Siem, A.C. Sunde, A. Voinov, S. Ødegård, Radiative strength functions in Mo93-98. Phys. Rev. C **71**, 044307 (2005)
164. J.E. Midtbø, A.C. Larsen, T. Renstrøm, F.L.B. Garrote, E. Lima, Consolidating the picture of low-energy magnetic dipole decay radiation. Phys. Rev. C **98**, 064321 (2018)
165. M. Krtička, S. Goriely, S. Hilaire, S. Péru, S. Valenta, Constraints on the dipole photon strength functions from experimental multistep cascade spectra. Phys. Rev. C **99**, 044308 (2019)
166. D. Savran, T. Aumann, A. Zilges, Experimental studies of the Pygmy dipole resonance. Prog. Part. Nucl. Phys. **70**, 210 (2013)
167. A. Zilges, D.L. Balabanski, J. Isaak, N. Pietralla, Photonuclear reactions–from basic research to applications. Prog. Part. Nucl. Phys. **122**, 103903 (2022)
168. D.G. Gardner, Neutron radiative capture, 62 (1984)
169. M.B. Chadwick, P. Obloinský, P.E. Hodgson, G. Reffo, Pauli-blocking in the quasideuteron model of photoabsorption. Phys. Rev. C **44**, 814–823 (1991). https://doi.org/10.1103/PhysRevC.44.814
170. D. Robson, A. Richter, H.L. Harney, Consequences of isospin and other conserved quantum numbers for compound-nucleus reactions. Phys. Rev. C **8**, 153–160 (1973). https://doi.org/10.1103/PhysRevC.8.153
171. S.M. Grimes, Role of isospin in neutron- and alpha-induced reactions. Phys. Rev. C **46**, 1064–1068 (1992). https://doi.org/10.1103/PhysRevC.46.1064
172. J.A. Holmes, S.E. Woosley, W.A. Fowler, B.A. Zimmerman, Tables of thermonuclear-reaction-rate data for neutron-induced reactions on heavy nuclei. At. Data Nucl. Data Tables **18**, 305 (1976)
173. S. Goriely, M. Samyn, M.J. Pearson, Further explorations of Skyrme-Hartree-Fock-Bogoliubov mass formulas. VII. Simultaneous fits to masses and fission barriers. Phys. Rev. C **75**, 064312 (2007)
174. S. Bjørnholm, J.E. Lynn, The double-humped fission barrier. Rev. Mod. Phys. **52**, 725–931 (1980)
175. M. Sin, R. Capote, A. Ventura, M. Herman, P. Oblozinsky, Fission of light actinides: ^{232}Th(n, f) and ^{231}Pa(n, f) reactions. Phys. Rev. C **74**, 014608 (2006). https://doi.org/10.1103/PhysRevC.74.014608
176. S. Goriely, S. Hilaire, A.J. Koning, M. Sin, R. Capote, Towards a prediction of fission cross section on the basis of microscopic nuclear inputs. Phys. Rev. C **79**, 024612 (2009)
177. S. Goriely, S. Hilaire, A.J. Koning, R. Capote, Towards an improved evaluation of neutron-induced fission cross sections on actinides. Phys. Rev. C **83**, 034601 (2011). https://doi.org/10.1103/PhysRevC.83.034601
178. A. Mamdouh, J.M. Pearson, M. Rayet, F. Tondeur, Fission barriers of neutron-rich and superheavy nuclei calculated with the ETFSI method. Nucl. Phys. A **679**(3), 337–358 (2001). https://doi.org/10.1016/S0375-9474(00)00358-4
179. A.J. Sierk, Macroscopic model of rotating nuclei. Phys. Rev. C **33**, 2039–2053 (1986). https://doi.org/10.1103/PhysRevC.33.2039
180. S. Cohen, F. Plasil, W.J. Swiatecki, Equilibrium configurations of rotating charged or gravitating liquid masses with surface tension. Ann. Phys. **82**(2), 557–596 (1974). https://doi.org/10.1016/0003-4916(74)90126-2
181. A. D'Arrigo, G. Giardina, M. Herman, A.V. Ignatyuk, A. Taccone, Semi-empirical determination of the shell correction temperature and spin dependence by means of nuclear fission. Journ. Phys. G **20**, 365–376 (1994)
182. P. Romain, B. Morillon, A. Koning, Neutron actinides evaluations with the TALYS code. NEMEA-3 Neutron Measurements, Evaluations and Applications **25**, 113 (2006)
183. E.V. Gai, A.V. Ignatyuk, N.S. Rabotnov, G.N. Smirenkin, Two-bump barrier and the neutron-induced nuclear fission. Physics and Chemistry of Fission, IAEA, Vienna, 337 (1969)
184. M.C. Duijvestijn, A.J. Koning, F.-J. Hambsch, Mass distributions in nucleon-induced fission at intermediate energies. Phys. Rev. C **64**, 014607 (2001). https://doi.org/10.1103/PhysRevC.64.014607
185. K.-H. Schmidt, B. Jurado, Thermodynamics of nuclei in thermal contact. Phys. Rev. C **83**, 014607 (2011). https://doi.org/10.1103/PhysRevC.83.014607
186. F. Nordström, Benchmark of the fission channels in TALYS. UPTEC ES 21016, Uppsala University, 2021 (2021)
187. S. Okumura, T. Kawano, P. Jaffke, P. Talou, S. Chiba, 235U(n, f) independent fission product yield and isomeric ratio calculated with the statistical Hauser-Feshbach theory. J. Nucl. Sci. Technol. **55**, 1009–1023 (2018)
188. A. Wahl, Systematics of fission-product yields. Tech. Rep. LA-13928, Los Alamos National Laboratory, Los Alamos, NM, USA, May (2002) (2002)
189. J.-F. Lemaitre, S. Goriely, S. Hilaire, J.-L. Sida, Fully microscopic scission-point model to predict fission fragment observables. Phys. Rev. C **99**, 034612 (2019). https://doi.org/10.1103/PhysRevC.99.034612
190. J.-F. Lemaître, S. Goriely, A. Bauswein, H.-T. Janka, Fission fragment distributions and their impact on the r-process nucleosynthesis in neutron star mergers. Phys. Rev. C **103**, 025806 (2021)
191. S. Goriely, N. Chamel, J.M. Pearson, Hartree-Fock-Bogoliubov nuclear mass model with 0.50 MeV accuracy based on standard forms of Skyrme and pairing functionals. Phys. Rev. C **88**, 061302 (2013)
192. K. Fujio, S. Okumura, A.J. Koning, New development in TALYS - fission fragment statistical decay model. Proceedings of the 2021 Symposium on Nuclear Data, November 16-18 2021, JAEA, Japan JAEA-Conf 2022-001, 6 (2022)
193. D.A. Brown, M.B. Chadwick, R. Capote, A.C. Kahler et al., ENDF/B-VIII.0: The 8th Major Release of the Nuclear Reaction Data Library with CIELO-project Cross Sections, New Standards and Thermal Scattering Data. Nucl. Data Sheets **148**, 1 (2018)
194. A.J.M. Plompen, O. Cabellos, C.D.S. Jean, M. Fleming, A. Algora, M. Angelone, P. Archier, E. Bauge, O. Bersillon, A. Blokhin, F. Cantargi, A. Chebboubi, C. Diez, H. Duarte, E. Dupont, J. Dyrda, B. Erasmus, L. Fiorito, U. Fischer, D. Flammini, D. Foligno, M.R. Gilbert, J.R. Granada, W. Haeck, F.-J. Hambsch, P. Helgesson, S. Hilaire, I. Hill, M. Hursin, R. Ichou, R. Jacqmin, B. Jansky, C. Jouanne, M.A. Kellett, D.H. Kim, H.I. Kim, I. Kodeli, A.J. Koning, A.Y. Konobeyev, S. Kopecky, B. Kos, A. Krasa, L.C. Leal, N. Leclaire, P. Leconte, Y.O. Lee, H. Leeb, O. Litaize, M. Majerle, J.I.M. Damian, F. Michel-Sendis, R.W. Mills, B. Morillon, G. Noguere, M. Pecchia, S. Pelloni, P. Pereslavtsev, R.J. Perry, D. Rochman, A. Roehrmoser, P. Romain, P. Romojaro, D. Roubtsov, P. Sauvan, P. Schillebeeckx, K.H. Schmidt, O. Serot,

S. Simakov, I. Sirakov, H. Sjoestrand, A. Stankovskiy, J.C. Sublet, P. Tamagno, A. Trkov, S. van der Marck, F. Alvarez-Velarde, R. Villari, T.C. Ware, K. Yokoyama, G. Zerovnik, The joint evaluated fission and fusion nuclear data library. JEFF-3.3. European Physical Journal A **56**, 181 (2020)

195. U. Brosa, S. Grossmann, A. Müller, Nuclear scission. Phys. Rep. **197**(4), 167–262 (1990). https://doi.org/10.1016/0370-1573(90)90114-H
196. M. Arnould, S. Goriely, Astronuclear physics: A tale of the atomic nuclei in the skies. Prog. Part. Nucl. Phys. **112**, 103766 (2020)
197. Y. Xu, S. Goriely, A. Jorissen, G. Chen, M. Arnould, Databases and tools for nuclear astrophysics applications: BRUSsels Nuclear LIBrary (BRUSLIB), Nuclear Astrophysics Compilation of REactions II (NACRE II) and Nuclear NETwork GENerator (NETGEN). A&A **549**(10), A106 (2013)
198. T. Rauscher, F.-K. Thielemann, Table of cross sections and reaction rates. At. Data Nucl. Data Tables **79**, 47 (2001)
199. S. Goriely, S. Hilaire, A.J. Koning, Improved predictions of nuclear reaction rates with the TALYS reaction code for astrophysical applications. Astronomy & Astrophysics **487**(2), 767–774 (2008). https://doi.org/10.1051/0004-6361:20078825
200. P.A. Moldauer, Statistics and the average cross section. Nucl. Phys. A **344**, 185 (1980)
201. J.J.M. Verbaarschot, H.A. Weidenmüller, M.R. Zirnbauer, Grassmann integration in stochastic quantum physics: The case of compound-nucleus scattering. Phys. Rep. **129**, 367 (1985)
202. H.M. Hofmann, J. Richert, J.W. Tepel, H.A. Weidenmüller, Direct reactions and hauser-feshbach theory. Ann. Phys. **90**(2), 403–437 (1975). https://doi.org/10.1016/0003-4916(75)90005-6
203. H.M. Hofmann, T. Mertelmeier, M. Herman, J.W. Tepel, Hauser-feshbach calculations in the presence of weakly absorbing channels with special reference to the elastic enhancement factor and the factorization assumption. Zeit. Phys. A **297**, 153 (1980)
204. D.M. Filipescu, I. Gheorghe, H. Utsunomiya, S. Goriely, T. Renstrøm, H.-T. Nyhus, O. Tesileanu, T. Glodariu, T. Shima, K. Takahisa, S. Miyamoto, Y.-W. Lui, S. Hilaire, S. Péru, M. Martini, A.J. Koning, Photoneutron cross sections for samarium isotopes: Toward a unified understanding of (γ, n) and (n, γ) reactions in the rare earth region. Phys. Rev. C **90**, 064616 (2014). https://doi.org/10.1103/PhysRevC.90.064616
205. P. Carlos, H. Beil, R. Bergere, A. Lepretre, A.D. Miniac, A. Veyssière, The giant dipole resonance in the transition region of the samarium isotope. Nucl. Phys. A **225**, 171 (1974)
206. K.Y. Hara, H. Harada, F. Kitatani, S. Goko, S.-Y. Hohara, T. Kaihori, A. Makinaga, H. Utsunomiya, H. Toyokawa, K. Yamada, Measurements of the 152Sm(g, n) cross section with Laser-Compton scattering gamma-rays and the photon difference method. J. Nucl. Sci. Technol. **44**(7), 938–945 (2007). https://doi.org/10.1080/18811248.2007.9711333
207. G.M. Gurevich, L.E. Lazareva, V.M. Mazur, S.Y. Merkulov, G.V. Solodukhov, V.A. Tyutin, Total nuclear photoabsorption cross sections in the region $150 < A < 190$. Nucl. Phys. A **351**(2), 257–268 (1981). https://doi.org/10.1016/0375-9474(81)90443-7
208. IAEA: Handbook on photonuclear data for applications. cross-sections and spectra. TECDOC-1178 (2000)
209. S. Goko, H. Utsunomiya, S. Goriely, A. Makinaga, T. Kaihori, S. Hohara, H. Akimune, T. Yamagata, Y.-W. Lui, H. Toyokawa, A.J. Koning, S. Hilaire, Partial photoneutron cross sections for the isomeric state 180Ta-m. Phys. Rev. Lett. **96**, 192501 (2006)
210. H. Utsunomiya, H. Akimune, S. Goko, M. Ohta, H. Ueda, T. Yamagata, K. Yamasaki, H. Ohgaki, H. Toyokawa, Y.-W. Lui, T. Hayakawa, T. Shizuma, E. Khan, S. Goriely, Cross section measurements of the ^{181}Ta$(\gamma, n)^{180}$Ta reaction near neutron threshold and the p-process nucleosynthesis. Phys. Rev. C **67**, 015807 (2003). https://doi.org/10.1103/PhysRevC.67.015807
211. N. Fotiades, G.D. Johns, R.O. Nelson, M.B. Chadwick, M. Devlin, M.S. Wilburn, P.G. Young, J.A. Becker, D.E. Archer, L.A. Bernstein, P.E. Garrett, C.A. McGrath, D.P. McNabb, W. Younes, Measurements and calculations of ^{238}U$(n, xn\gamma)$ partial γ-ray cross sections. Phys. Rev. C **69**, 024601 (2004). https://doi.org/10.1103/PhysRevC.69.024601
212. I. Dillmann, T. Szücs, R. Plag, Z. Fülöp, F. Käppeler, A. Mengoni, T. Rauscher, The Karlsruhe Astrophysical Database of Nucleosynthesis in Stars Project - status and prospects. Nucl. Data Sheets **120**, 171–174 (2014). https://doi.org/10.1016/j.nds.2014.07.038
213. R.C. Barrall, J.E. Beaver, H.B. Hupf, F.F. Rubio, Production of Curie quantities of high purity I-123 with 15 MeV protons. Europ. J. of Nucl. Medicine and Molecular Imaging **6**, 411 (1981)
214. I. Mahunka, L. Ando, P. Mikecz, A.N. Tcheltsov, I.A. Suvorov, Iodine-123 production at a small cyclotron for medical use. J. of Radioanalytical and Nucl. Chem. Letters **213**, 135 (1996)
215. B. Scholten, S.M. Qaim, G. Stocklin, Excitation functions of proton induced nuclear reactions on natural tellurium and enriched Te-123: Production of I-123 via the Te-123(p, n)I-123 process at a low-energy cyclotron. Appl. Radiat. Isot. **40**, 127 (1989)
216. O. Iwamoto, N. Iwamoto, S. Kunieda, F. Minato, S. Nakayama, Y. Abe, K. Tsubakihara, S. Okumura, C. Ishizuka, T. Yoshida, S. Chiba, N. Otuka, J.-C. Sublet, H. Iwamoto, K. Yamamoto, Y. Nagaya, K. Tada, C. Konno, N. Matsuda, K. Yokoyama, H. Taninaka, A. Oizumi, M. Fukushima, S. Okita, G. Chiba, S. Sato, M. Ohta, S. Kwon, Japanese evaluated nuclear data library version 5: JENDL-5. Journal of Nuclear Science and Technology **1–60**, (2023). https://doi.org/10.1080/00223131.2022.2141903
217. F.T. Tarkanyi, A.V. Ignatyuk, A. Hermanne, R. Capote, B.V. Carlson, J.W. Engle, M.A. Kellett, T. Kibedi, G.N. Kim, F.G. Kondev, M. Hussain, O. Lebeda, A. Luca, Y. Nagai, H. Naik, A.L. Nichols, F.M. Nortier, S.V. Suryanarayana, S. Takacs, M. Verpelli, Recommended nuclear data for medical radioisotope production: diagnostic positron emitters. J. Rad. Nucl. Chem. **319**, 487–531 (2019)
218. M. Kellett, O. Bersillon, R. Mills, The JEFF-3.1/-3.1.1 radioactive decay data and fission yields sub-libraries. JEFF Report 20, NEA No. 6287, ISBN 978-64-99087-6 (2009)
219. A.N. Smirnov, V.P. Eismont, N.P. Filatov, S.N. Kirillov, J. Blomgren, H. Conde, N. Olsson, M. Duijvestijn, A. Koning, Measurement of neutron-induced fission cross section for Bi-209, Pb-nat, Pb-208, Au-197, W-nat and Ta-181 in the intermediate energy range. Proceedings of the International on Nuclear Data for Science and Technology, Santa Fe **2004**, 637 (2004)
220. A.J. Koning, D. Rochman, Towards sustainable nuclear energy: Putting nuclear physics to work. Ann. Nucl. Energy **35**(11), 2024–2030 (2008). https://doi.org/10.1016/j.anucene.2008.06.004
221. R. Firestone, G. Molnar, Z. Revay, T. Belgya, D. Mcnabb, B. Sleaford, The evaluated gamma-ray activation file (EGAF). AIP Conference Proceedings **769**, (2005). https://doi.org/10.1063/1.1944994
222. F. Becvar, Simulation of gamma cascades in complex nuclei with emphasis on assessment of uncertainties of cascade-related quantities. Nucl. Instrum. Methods Phys. Res., Sect. A **417**(2), 434–449 (1998). https://doi.org/10.1016/S0168-9002(98)00787-6
223. A.J. Koning, M.B. Chadwick, Microscopic two-component multistep direct theory for continuum nuclear reactions. Phys. Rev. C **56**, 970–994 (1997). https://doi.org/10.1103/PhysRevC.56.970
224. N.M. Larson, Updated users' guide for SAMMY: Multilevel R-matrix fits to neutron data using Bayes' equations. Technical Report ORNL/TM-9179/R6, Oak Ridge National Lab, TN (2003)
225. C. De Saint Jean, P. Tamagno, P. Archier, G. Noguere, CONRAD - a code for nuclear data modeling and evaluation. EPJ Nuclear Sci. Technol. **7**, 10 (2021)
226. I.J. Thompson, Coupled channels methods for nuclear physics. Computer Physics Reports **7**, 167–212 (1988)

227. O.I. Shinsuke Nakayama, Y. Watanabe, Recent progress of a code system DEURACS toward deuteron nuclear data evaluation. EPJ Web of Conferences **239**, 03014 (2020)
228. M. Sin, R. Capote, M.W. Herman, A. Trkov, Extended optical model for fission. Phys. Rev. C **93**, 034605 (2016). https://doi.org/10.1103/PhysRevC.93.034605